Molybdenum diimine tetracarbonyl complexes for the Electrocatalytic reduction of CO2

Carlos Garcia Bellido

DOCTORAT MATIERE BRETAGNE MOLECULES LOIRE ET MATERIAUX

UBO
Université de Bretagne Occidentale

THESE DE DOCTORAT DE

L'UNIVERSITE
DE BRETAGNE OCCIDENTALE

ECOLE DOCTORALE N° 596
Matière Molécules et Matériaux
Spécialité: *Chimie moléculaire et macromoléculaire*

Par
Carlos GARCIA BELLIDO

Molybdenum Diimine Tetracarbonyl Complexes for the Electrocatalytic Reduction of CO_2

Thèse présentée et soutenue à Brest, le 25 Juin 2021
Unité de recherche: UMR 6521, "Chimie, Electrochimie Moléculaires et Chimie Analytique"

Rapporteurs avant soutenance :

Jérôme FORTAGE, Chargé de recherche CNRS, Université Grenoble Alpes.

Laurent RUHLMANN, Professeur, Université de Strasbourg.

Composition du Jury :

Jérôme FORTAGE, Chargé de recherche CNRS, Université Grenoble Alpes.

Laurent RUHLMANN, Professeur, Université de Strasbourg.

Corinne LAGROST, Directrice de recherche CNRS, Institut des Sciences Chimiques de Rennes, Président de Jury.

Carole BAFFERT, Maître de Conférences CNRS, Aix-Marseille Université.

Nicolas LE POUL, Chargé de recherche CNRS, Université de Bretagne Occidentale, Directeur de thèse.

Frédéric GLOAGUEN, Directeur de Recherche CNRS, Université de Bretagne Occidentale, Directeur de thèse.

Acknowledgements

I would like to thank the members of this PhD examination. My sincere appreciation to Dr. Jérôme Fortage from the Université Grenoble Alpes, Laurent Ruhlmann from the University of Strasbourg, Dr. Corinne Lagrost from the Institut des Sciences Chimiques de Rennes and Dr. Carole Baffert from the Aix-Marseille Université for their participation as reviewers and examiners in this PhD dissertation.

I would like to emphasize that the last year of this thesis was performed during the COVID-19 pandemic. Considering this, I am grateful for the efforts of the Ecole Doctorale 3M and the Université de Bretagne Occidentale for allowing UMR-6521 PhD students the flexibility to continue their research as safely as possible.

After finishing my Master´s degree in Girona, I arrived in Brest without any knowledge of electrochemistry or French, naively expecting that my English and organometallic background could be enough. I could not have imagined how hard it would be to adapt to a new city so different from my hometown. But from the moment that I performed my first cyclic voltammetry without knowing what that "duck-shaped" graph was, to the first time that I could perform spectroelectrochemical experiments without any help, I was supported by the people of the UMR 6521´second floor.

Therefore, I will dedicate a few words to everyone that has been present during my PhD. I would like to thank the people of UMR 6521 second floor for supporting me since my arrival in 2017. First of all, thanks to my PhD supervisors, Dr. Nicolas Le Poul et Dr. Frédéric Gloaguen, for their support during this PhD stage. Thank you, Nicolas, for all the discussions about "where the electron goes in the molecule", all the advice during these long days of experiments and the support during these years that helped me to forget all the bad jokes that you usually made every time that I was working at the glovebox. I would also like to thank Fred for all the support given and for tolerating every email that I sent to him because I needed another DFT calculation (there were a lot of them). The accomplishment of this PhD thesis would not be possible without the help of either of you. Also, thanks to Noémie and Nolwenn that helped me in the early steps of my PhD thesis. Your advice and your help were totally necessary to develop this project and sorry for being such a mess sometimes!

But there were more people in the UMR 6521 besides my PhD supervisors! I have to start with Matthieu and Danny, my PhD colleagues in the student´s room! I couldn´t be more grateful for the help and support that they provided me during most of my stay in Brest, giving joy between each long experiment. I will not forget Matthieu´s love for maintaining a good orthography in every text that he found, nor how Danny helped me on any occasion no matter what. However, Laurianne should be also included in this PhD group! I am sure that without our talks at the laboratory the work would have been quite boring, and having you around was always a pleasure. Thanks for being so optimistic and cheerful every day of the year! To finish I want to thank the rest of the UMR 6521 second floor people, thanks for all the support.

Regarding the rest of the UMR 6521 group, I would like to thank Pr. Philippe Schollhammer, director of the UMR, and Pr. Paul-Alain Jaffrès, director of the Chemistry department, for allowing me to teach courses and the prolongation of my PhD contract due to the pandemic situation. I would like to especially thank my PhD colleagues from the first floor, Julie, Marie and Axia, for all the nice moments that we had inside and outside the lab! The last two years will not be the same without all the meetings at “Les Fauvettes” or “Tortuga”, and I will miss them a lot! Best of luck in your PhD thesis!

But not everything is working at the lab. Three years allowed for a lot of anecdotes and a lot of relationships. I would like to especially thanks my roommates during 2019, Marlene, Charles and Damien, as the people that helped me discover how to have fun in Brest (as it was not that obvious in the beginning!). The phrases “Yé suis bourréé!” and “Voisin Relou” will not be forgotten! Y, por supuesto, gracias a Eva y Sergi por todo el apoyo y la amistad que me habéis dado durante todo mi tiempo en Brest, no sé qué habría hecho sin vosotros.

Para acabar, me gustaría a toda la gente que me ha apoyado desde España. A Félix, que nunca pude visitarlo en Singapur; a todos los que me han acompañado durante la redacción de tesis telemáticamente como Rafa Marques, Santi, Juan, Rafa Ruiz… y todos los demás, ¡gracias a todos! Por último, agradecer a mi familia; tanto a mis padres, Manuel e Isabel María, como a mi hermana Isabel, gracias por todo el apoyo. ¡Y a mis abuelos Juana y Pepe junto con mi tía Pepi que me estarán esperando en Paterna, voy pronto para allá!

Gracias a todos, nunca podré agradecerlo lo suficiente.

Carlos

Abbreviations

ATP	Adenosine triphosphate
BDD	Boron-diamond doped
[Cat]	Catalyst
CCS	Carbon capture and storage
CODHs	Carbon monoxide dehydrogenase
CPE	Controlled-potential electrolysis
CV	Cyclic voltammetry
D	Diffusion coefficient
DCM	Dichloromethane
DFB	1,2-Difluorobenzene
DFT	Density functional theory
DMF	Dimethylformamide
E^0	Standard potential
$E_{1/2}$	Half-wave potential
EDG	Electron-donating group
EOR	Enhanced oil recovery
ET	Electron transfer
ETL	Emissions to liquid
EWG	Electron-withdrawing group
Fc	Ferrocene
Fc^+	Ferrocenium
FDHs	Formate dehydrogenases
FE	Faradaic efficiency
i_{cat}	Catalytic current peak
i_p	Current peak
GC	Glassy carbon
G	Free Gibbs energy
HAT	Hydrogen atom transfer
HER	Hydrogen evolution reaction
HOMO	Highest occupied molecular orbital
LUMO	Lowest unoccupied molecular orbital
MeCN	Acetonitrile
MLCT	Metal-to-ligand charge transfer
MTOE	Millions of tons of oil equivalents
MO	Molecular orbital
MWCNT	Multi-walled carbon nanotube
NADPH	Nicotinamide adenine dinucleotide phosphate
NBD	Norbornadiene
NHE	Normal hydrogen electrode
NMP	N-Methyl-2-pyrrolidone
NADPH	Nicotinamide adenine dinucleotide phosphate
Ox	Oxidation
PCET	Proton-coupled electron transfer
PhOH	Phenol
PT	Proton-transfer
Red	Reduction
SOMO	Single occupied molecular orbital
THF	Tetrahydrofuran
TOF	Turnover frequency
TON	Turnover number

Summary

Chapter I. Carbon dioxide reduction: a general introduction

Chapter II. Synthesis, characterization and reactivity towards CO_2 of $[Mo(CO)_4(bpy\text{-}(R)_2)]$ complexes

Chapter III. Synthesis, characterization and reactivity towards CO_2 of $[Mo(CO)_4(L)]$ complexes (L = bpy, phen, py-indz)

Résumé en français : Principaux résultats des travaux de thèse

Chapter I

Carbon dioxide reduction: a general introduction

I. Global warming: a general perspective

I.1. Global energy sources

Since the beginning of the 20th century, fossil fuels have become an essential resource for mankind in almost every aspect of life, having an essential role in transport, industries and technologies that we enjoy nowadays.

Fossil fuels still are the most important energy sources, having a 41% participation in the energy sources balance in 2018, which corresponds to 168 million of tons of oil equivalents (MTOE), meanwhile renewable sources constitute the 17% of the world energy consumption corresponding to 78 MTOE (Figure I.1). The current hegemony of fossil fuels is caused by the relative easiness of their extraction, transport, purification and transformation into available energy (heat) and valuable products, thanks to efficient and cheap processes.

Nevertheless, all of those technologies have the disadvantage of generating by-products which are toxic for most of living organisms on Earth. Moreover, the combustion of fossil fuels generates huge amounts of greenhouse gases which are now widely recognized as being the main factor of the increase of global temperature on Earth, achieving an increase of + 1°C in the last decade according to the IPCC - Intergovernmental Panel on Climate Change- in 2019.[1]

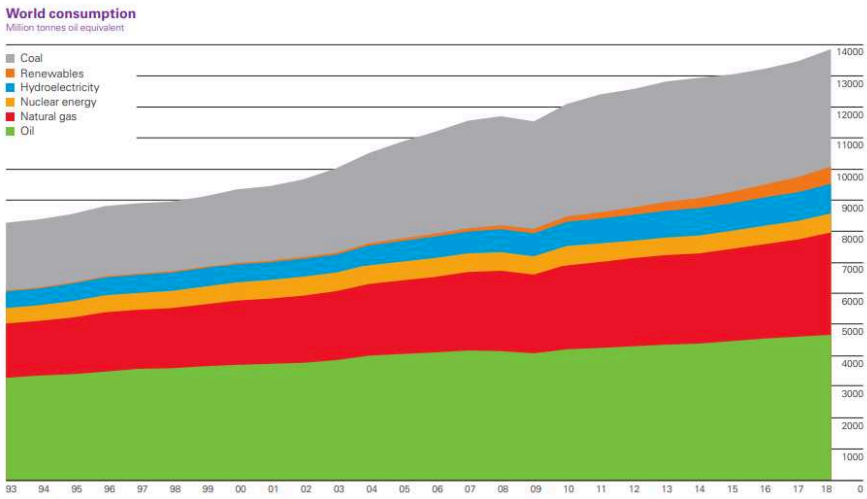

Figure I.1. Energetic world consumption in millions of tons of oil equivalents from 1993 to 2018, with an oil consumption increase of almost the double between 2010 and 2018, mostly due to the industrialization of countries such as China and India. Reproduced from Ref. [2].

Due to the direct consequences of global warming, such as melting glaciers[3] or shifting precipitation patterns,[4] different agreements have been made such as the Paris Agreement at COP 21 (Conference of the Parties) in 2015, where members of the UNFCCC (United Nations Framework Convention on Climate Change) agreed to participate in a global response to the climatic change in an effort to avoid a global 2°C temperature rise above preindustrial levels. Among the global actions proposed in these agreements, the decrease of the production/use of fossils fuels by the development of alternative technologies combined with a change of the industrial framework have been mainly targeted (Figure I.2).[5]

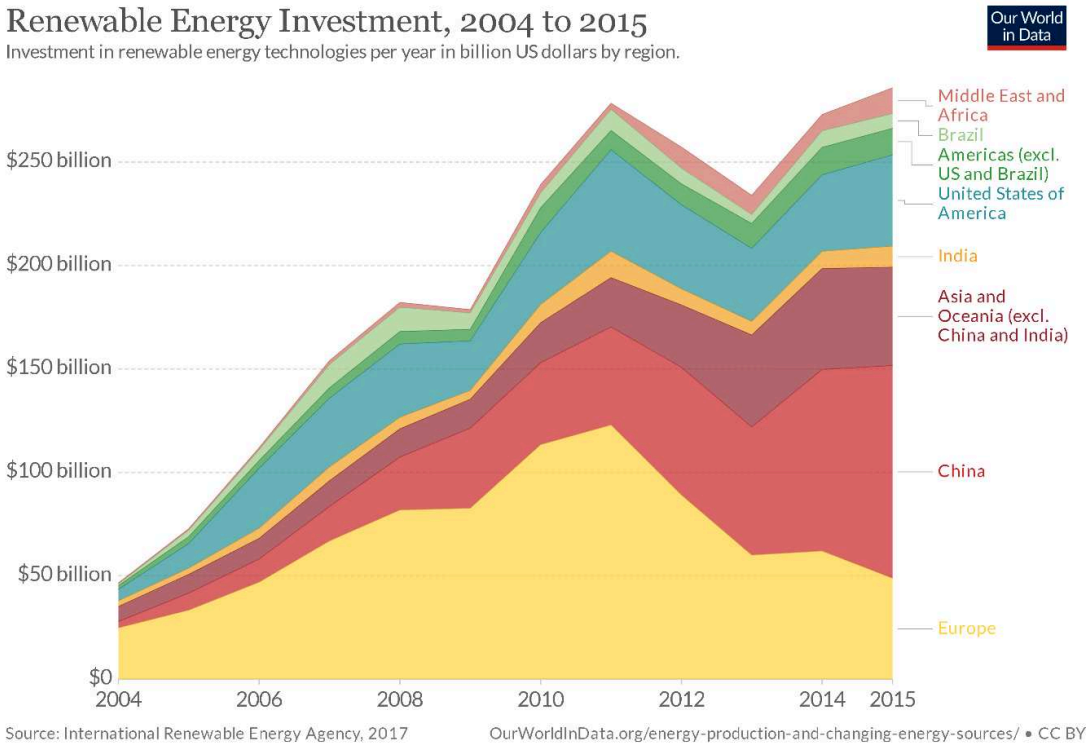

Figure I.2. Investment in billion US dollars per year and region from 2004 to 2015 in renewable energy technologies. Reproduced from Ref. [6].

I.2. The enhanced greenhouse effects

When sunlight that arrives to the Earth´s surface is absorbed, the Earth radiates back to space the same amount of thermal energy, mainly as infrared radiation. The absorption of a part of this thermal radiation by the atmosphere with a consequent re-radiation back to the Earth is what is called greenhouse effect, warming the surface of the planet much more than without atmosphere. Greenhouse gases are the ones responsible for this effect, including water vapor, CO_2, methane and ozone as the four major greenhouse gases that are identified by the overlap of the emission and absorption bands of the gases.[7]

The disruption of Earth´s climate equilibrium is influenced directly by the increase of the amount of anthropogenic greenhouse gases emitted in the atmosphere as they increase the back-radiation to Earth´s surface, consequently enhancing the greenhouse effect and increasing the temperature of the Earth´s surface (Figure I.3).

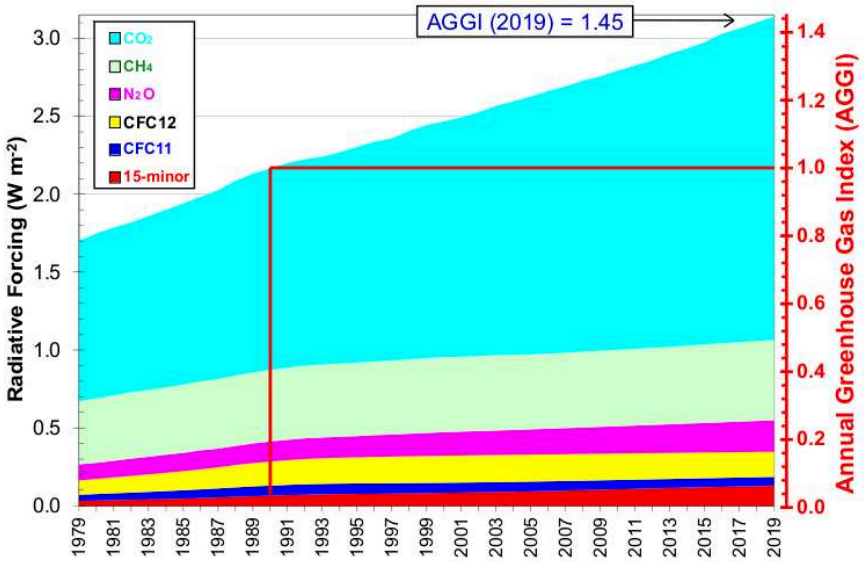

Figure I.3. Radiative forces of greenhouse gases until 2019. Reproduced from Ref. [8].

Concentration of greenhouse gases in the Earth atmosphere has been moderately varying between 200 and 300 ppm for the last 800 000 years. The anthropogenic emission of

"greenhouse" gases has dramatically increased since the industrialization of the business factory during the 19th century, to attain more than 400 ppm nowadays.[9],[10]

Among all greenhouse gases, one of the most impactful molecules is carbon dioxide, which, because of its high concentration in atmosphere, accounts for about 81% of total greenhouse effects in the US. CO_2 is an inert molecule that is being generated either by living organisms during aerobic respiration and by the combustion of carbon-based materials, such as fossils fuels, but also by deforestation, land clearing for agriculture and degradation of soils (Figure I.4).

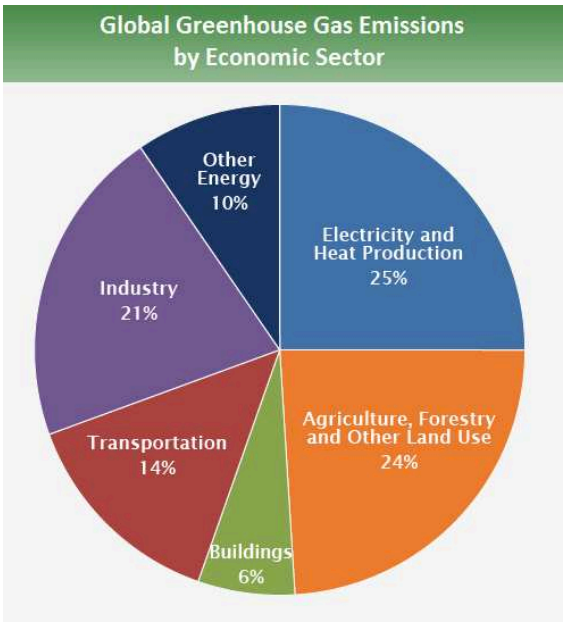

Figure I.4. Global gas emissions distribution in 2014 by economic sectors. Reproduced from Ref. [1].

From a chemical perspective, carbon dioxide has a linear geometry with two carbon-oxygen double bonds. Carbon dioxide possesses a longer C-O bond than carbon monoxide (1.163 Å *vs.* 1.128 Å, respectively). Moreover, C=O bond energy in CO_2 equals to 750 $kJ.mol^{-1}$, a higher value in comparison with other common bonds such as C-C or C-H (346 and 417 $kJ.mol^{-1}$ respectively), hence making carbon dioxide harder to be transformed, thus explaining its accumulation in the atmosphere.[11]

II. Strategies for CO_2 transformation

II.1. Industrial applications

CO_2 recycling has become one of the most urgent issues to be addressed in the last decades, motivating intensive scientific researches to find new technologies that could decrease the use of conventional methods that are fossil fuel dependent and still in use nowadays.

Traditional CO_2 transformation processes have been present since the 19th century, being possible to form methanol, formic acid, carbon monoxide and methane, among other hydrocarbons, as products. One of the first reactions described that uses carbon dioxide as a reagent was the Sabatier process (Scheme I.1), discovered in 1889 as the reaction of hydrogen and carbon dioxide at high temperature and pressure to produce methane and water, all in the presence of a nickel catalyst.[12]

$$CO_2 + 4\ H_2 \xrightarrow[400\ °C,\ 9\ atm]{[cat]} CH_4 + 2\ H_2O$$

Scheme I.1. Total reaction of the Sabatier process.

The use of Sabatier reaction for methane production is a very important step in a lot of industrial processes, such as the production of ammonia and synthetic natural gas.[13] Noteworthy, Sabatier reaction has been used in the International Space Station life recover service in order to recycle the CO_2 exhaled, recovering water that can be further used for dioxygen production by electrolysis.[14]

Another traditional process is the modified Fischer-Tropsch process, one of the most common hydrocarbon synthetic routes in the 20th century that use CO_2 as carbon source, reacting with H_2 at high temperatures and pressure to produce hydrocarbons. Iron oxides are typically used as catalysts, having a two-step process with CO as intermediate via CO_2 hydrogenation (Scheme I.2).[15]

$$CO_2 + H_2 \xrightarrow[600^oC,\ 1\ atm]{[cat]} CO + H_2O$$

$$n\ CO + 2n\ H_2 \xrightarrow[600^oC,\ 1\ atm]{[cat]} -[CH_2]_n- + n\ H_2O$$

Scheme I.2. Reaction scheme of the modified Fischer-Tropsch process.

An alternative process with a more focused carbon dioxide recycling perspective is the carbon capture and storage (CCS) technology that is used in critical points of CO_2 emissions, such as in cement factories, being able to recover the 90% of the carbon dioxide produced (Figure I.5).[16]

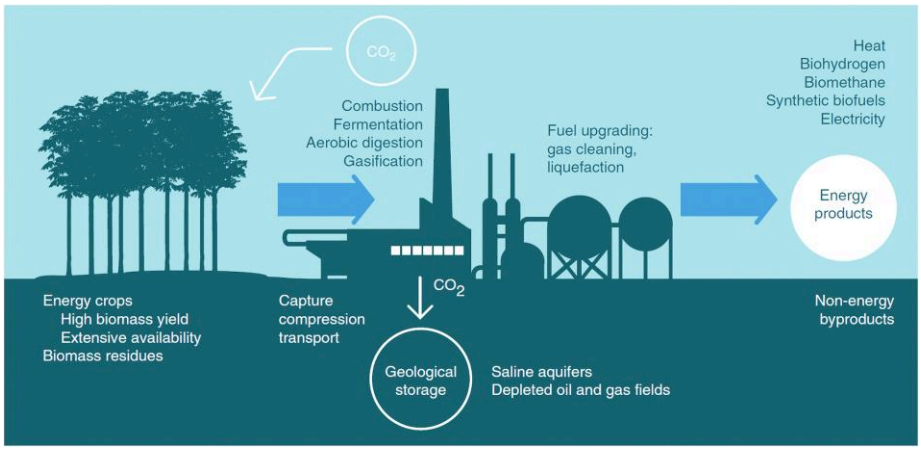

Figure I.5. General scheme of CCS technology. Reproduced from Ref. [17].

CCS involves three different processes, the efficiency of which are equally important and essential: capture, transport and storage of the carbon dioxide from the factories to the underground geological rock formations. Some of these processes also need energy, generally generated by combustion of fossil fuels. However, this issue can be solved by using technologies that combine renewable biomass and CCS (BECCS),[18] leading to a "carbon-negative" recycling of carbon dioxide.

Another example of a CO_2 recycling technology is the enhanced oil recovery (EOR) process in which CO_2 facilitates the extraction of crude oil,[19] even if nowadays this technique is in disuse due to economic factors. Alternatively, projects such as emissions-to-liquid (ETL) plants are becoming

attractive, as they allow the combination of CO_2 with H_2 to produce green methanol within a circular economy perspective.[20]

In conclusion, few industrial processes have been developed for the recycling and conversion of carbon dioxide into valuable products.

II.2. CO_2 in nature

Most of the technologies focused on the use of carbon dioxide have been developed to mitigate the increase of the anthropogenic CO_2 emission. But nature has different ways to deal with carbon dioxide. While approximately 25% of the CO_2 globally emitted is absorbed by plants and trees, another 25% is absorbed from some areas of the ocean, leaving the 50% remaining in the atmosphere.[21]

The most important natural process which uses CO_2 is photosynthesis, as it is able to convert 200 billion tons of CO_2 every year, making this process the most effective one to recycle all the anthropogenic carbon dioxide ever emitted.[22] It is performed by cyanobacteria and vegetation that convert solar energy into chemical energy in the form of organic molecules such as carbohydrates, only by the use of carbon dioxide and water.

The fundamental process of photosynthesis is shown in Scheme I.3. It involves two stages: light-driven reactions which produce adenosine triphosphate (ATP) and nicotinamide adenine dinucleotide phosphate (NADPH), and dark reactions that transform CO_2 into sugars, both of these processes being performed by chloroplasts in plants.

$$H_2O + CO_2 \xrightarrow{h\nu} CH_2O + O_2 \qquad \Delta G^0 = 473\ kJ{\cdot}mol^{-1}$$

Scheme I.3. Total chemical reaction of photosynthesis.

The first light-dependent reaction is water oxidation, which takes place in the Photosystem II, a protein complex existing in chloroplasts. Electrons which are generated upon charge separation by light input are transported through an electron transport chain, forming a proton gradient that

helps to the production of ATP, which is further used in the Calvin cycle (Figure I.6). Formation of another important molecule, NADPH, requires two excited electrons after passing through a second leg of the electron transport chain, according to the well-known "Z-Scheme".[23] Both ATP and NADPH products are involved in the Calvin Cycle in order to transform CO_2 into sugars.

The reaction is catalyzed by ribulose 1,5-biphosphate carboxylase (called rubisco) in the stroma, forming 2 molecules of 3-phosphoglycerate by adding CO_2 to ribulose 1,5-biphosphate, a sugar with 5 carbons.[24]

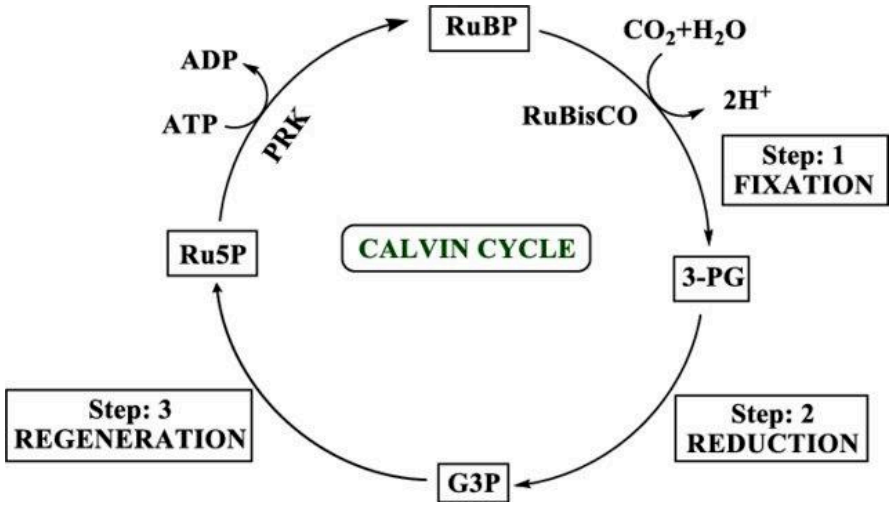

Figure I.6. Simplified representation of the Calvin cycle. Reproduced from Ref. [25].

Alternatively to photosynthesis, CO_2 can be transformed into formate and methanol by different enzymatic processes which occur in cells, bacteria and microbial organisms, helping to the regulation of CO_2 and CO levels in the atmosphere.[26] On one hand, carbon monoxide dehydrogenases (CODHs), which belong to the family of oxidoreductases, are able to catalyze the reversible oxidation of CO_2 into CO in anaerobic bacteria. In these enzymes, the active site displays $[NiFe_3S_4]$ and $[Fe_4S_4]$ clusters (Figure I.7, left). On the other hand, formate dehydrogenases (FDHs) can catalyze the two-electron reduction of CO_2 into formate with a molybdenum or tungsten active center in a trigonal pyramid geometry (Figure I.7, right).[27]

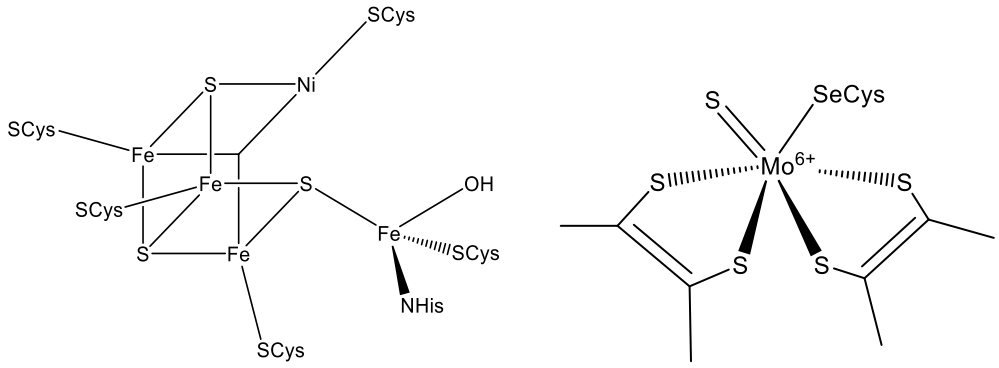

Figure I.7. Schematic representation of carbon dioxide dehydrogenase (left) and formate dehydrogenase (right) systems.

II.3. Photo-, electro, and photoelectro-catalytic strategies for reduction of CO_2

As previously mentioned, chemical conversion or fixation of CO_2 from the Earth atmosphere is a very complex issue. Even if different strategies for CO_2 transformation are constantly evolving, it is worth pointing out biomimetic approaches, which find inspiration from photosynthetic redox processes. As shown in Figure I.8, three main approaches have been developed so far: electrocatalysis, photocatalysis and photoelectro-catalysis.

Electrochemistry has been shown to be a powerful strategy to produce high-value chemicals through CO_2 electrocatalytic reduction.[28] The principle of electrocatalysis (Figure I.8, left) is to optimize in terms of energetics the electron transfer from/to the electrode to/from the substrate (here CO_2) by the use of a catalyst. The latter can diffuse freely from the bulk of the solution, or be immobilized onto the electrode surface. It can also be the electrode material itself. As explained in the next sections, various types of electrocatalytic systems have been reported for the CO_2 reduction. Although much progress has been achieved over the last 10 years, electrochemical reduction of carbon dioxide still presents several drawbacks, such as low selectivity and efficiency, which can be overcome by the use of molecular catalytic systems in presence of proton sources (Figure I.8, left).[29, 30] However, the poor solubility of most of molecular electrocatalysts in

aqueous media forces the use of organic solvents such as DMF or THF, less interesting towards achieving greener and cleaner technologies.

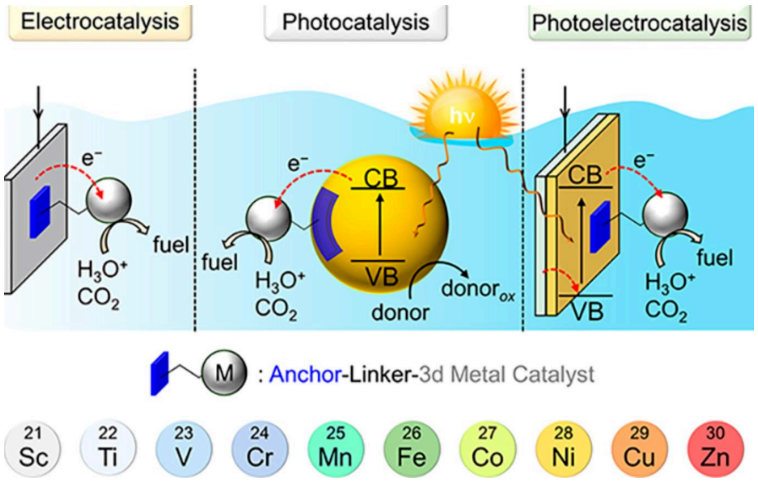

Figure I.8. Schematic representation of the electrocatalytic (left), photocatalytic (middle) and photoelectro-catalytic (right) strategies towards CO_2 transformation. Reproduced from Ref. [31].

Another interesting perspective is the transformation of carbon dioxide molecule *via* photocatalysis, which is classically performed by p-doped semi-conductor materials such as metallic oxides, e.g. TiO_2 (Figure I.8, middle).[32, 33] These materials are able to absorb sunlight, albeit most of them mainly in the UV region, to generate high-energetic holes and electrons that are transferred to the active species adsorbed over the surface of the catalyst, achieving great recyclability and high catalytic yields.[34] The main drawback regarding the use of photocatalytic systems is the complex interaction of the photocatalyst surface with the adsorbed active species hence making difficult to decipher the exact catalytic mechanism. Another disadvantage is the need for enough active sites over the surface of the photocatalyst to bind successfully the substrate, a feature that can be improved by attaching high surface area materials such as nanocrystals or surface atoms to the photocatalyst, allowing strong interactions with the active species formed during the catalysis (Figure I.8, right).[33]

Finally, photoelectro-catalysis which combines light-driven processes and electrochemistry (Figure I.8, right) appears as a very promising strategy to substitute to current technologies that use non-renewable feedstocks. Photoelectro-catalytic devices normally use semiconductors as materials for the photocathode. The latter has to be able to activate the attached molecular electrocatalyst, such as cobalt porphyrins and cobalt thiolates, on its surface.[35]

In the following section, we will focus on electrocatalytic systems for CO_2 transformation. This section starts with a brief summary of the fundamentals of carbon dioxide catalytic electroreduction, exploring the different approaches that have been explored in the last decades. It then discusses more precisely on metal molecular complexes which can be used as electrocatalysts for CO_2 conversion.

III. Electrocatalytic reduction of CO_2

III.1. General aspects of CO_2 electroreduction

Electrochemistry is commonly defined as the branch of chemistry which involves changes upon electron transfer reactions from or to electrodes immerged in solid or liquid solutions. The electrodes, which can be made of different materials (metals, semi-conductors…), are used to modulate the potential of the electrons at the electrode surface that can interact with the different chemical species of the solution. In order to reduce a molecule, the electrons on the electrode surface must display higher energy than the lowest unoccupied molecular orbital (LUMO) level of the molecule. Inversely, for an oxidation, the electrons should be lower in energy than the highest occupied molecular orbital (HOMO) level of the molecule (Figure I.9).[36]

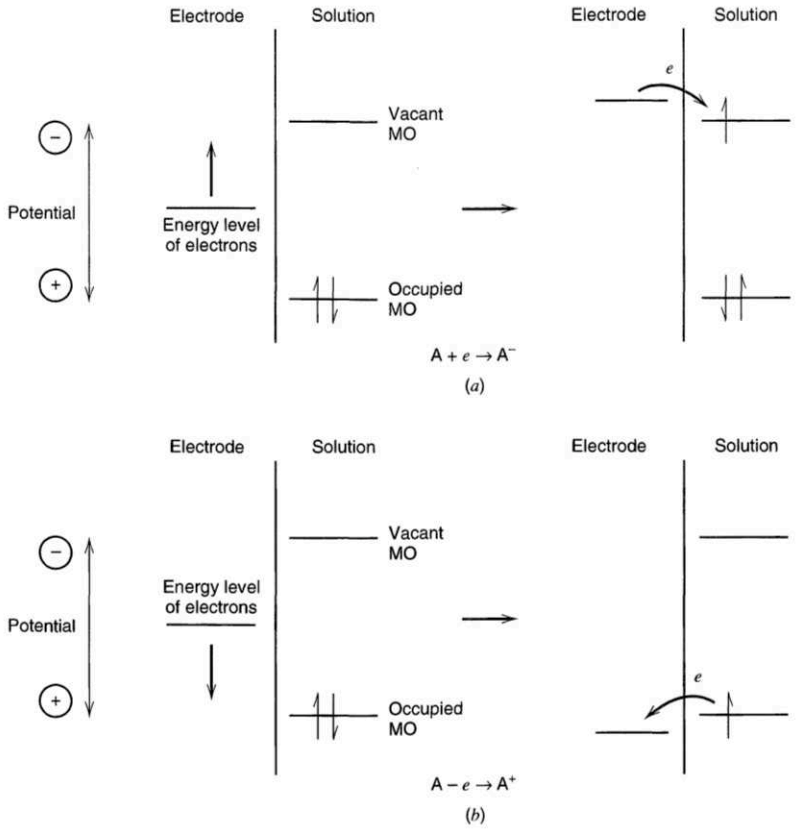

Figure I.9. Schematic representation of reduction (top) and oxidation (below) processes between the electrode and the frontier molecular orbitals of a molecule in solution. Reproduced from Ref. [37].

Consequently, the electrochemical behavior of a molecule is directly related to the nature of its frontier orbitals. CO_2 is a linear molecule in its ground state (belonging to $D_{\infty h}$ symmetry group) with sixteen valence electrons and two C-O double bonds, having lone pairs located in the oxygen atoms and an electrophilic carbon atom.

Carbon dioxide is an amphoteric oxide molecule as the carbon atom has a Lewis acid character meanwhile the oxygen atoms can act as Lewis bases. Even though, a study in the protonation affinity of carbon dioxide shows a value of 540.5 kJ/mol,[38] that is considerably lower than other molecules that present oxygen atoms, concluding that generally carbon dioxide presents a weak Lewis base character.[39, 40]

An interesting tool to understand the spectroscopic and electrochemical properties of carbon dioxide is its qualitative molecular orbital diagram, as shown in Figure I.10, where the relative energies and the symmetry of the molecular orbitals are displayed.

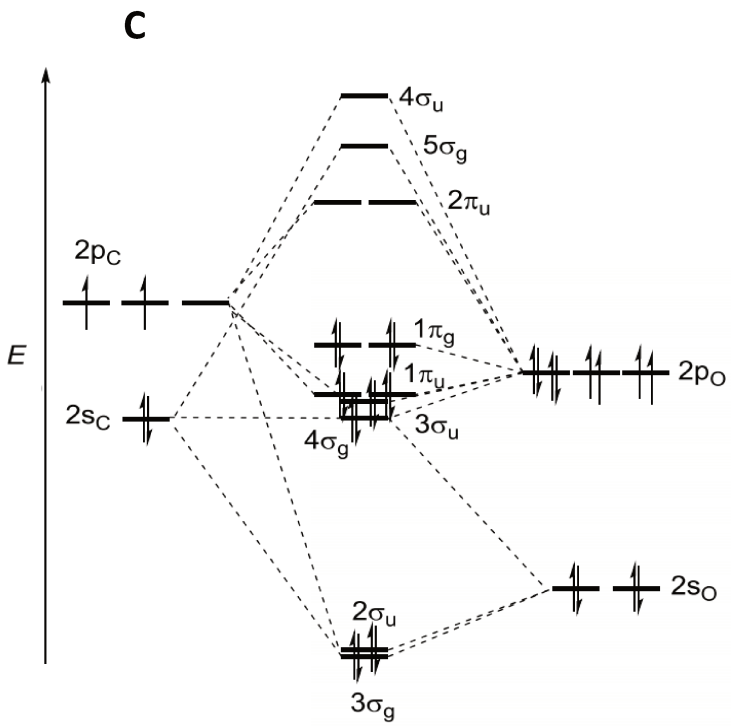

Figure I.10. Simplified MO diagram of the CO_2 molecule. Reproduced from Ref. [41].

Figure I.10 suggests that the HOMO for CO_2 ($1\pi_g$) is predominantly oxygen-centered and focused in the lone pairs, while the LUMO ($2\pi_u$) is localized on the carbon atom and presents an antibonding character, observing that a monoelectronic reduction process towards CO_2 induces half-filling of the LUMO $2\pi_u$ orbital. This reduction process causes a strong change in the geometry of the molecule, varying from a linear to a bent conformation, what has a drastic influence on the electronic energy of the molecular orbitals of carbon dioxide. This particularity is one of the drawbacks of the direct CO_2 electrochemical reduction in terms of energetics. [42]

Indeed, the high reorganization energy caused by the change of the geometry to a more bended conformation from the neutral to the anion radical during the direct one-electron reduction of CO_2 results in a slow electron transfer. In consequence, the generated anion is produced at a very

negative standard potential, $E^0(CO_2/CO_2^{\bullet-})$ = −1.9 V *vs*. NHE (normal hydrogen electrode).[28] The reduction potential becomes less negative when the redox process involves proton and electron transfers (*vide infra*). As shown in Table I.1, the standard potentials for the formation of different products, such as HCO_2H, CO, CH_3OH or CH_4, vary then from −0.61 V to −0.24 V *vs*. NHE in aqueous solution at pH 7.[28]

Table I.1. Reduction potentials of the transformation of carbon dioxide in CO, HCOOH, HCHO, CH_3OH and CH_4.

Reduction pathways	E^0 **(V *vs*. NHE)**
$CO_2 + 2H^+ + 2e^- \rightarrow HCOOH + H_2O$	−0.61
$CO_2 + 2H^+ + 2e^- \rightarrow CO + H_2O$	−0.53
$CO_2 + 4H^+ + 4e^- \rightarrow HCHO + H_2O$	−0.48
$CO_2 + 6H^+ + 6e^- \rightarrow CH_3OH + H_2O$	−0.38
$CO_2 + 8H^+ + 8e^- \rightarrow CH_4 + 2H_2O$	−0.24
$CO_2 + e^- \rightarrow CO_2^{\bullet-}$	−1.90

III.2. Homogeneous and heterogeneous CO_2 electrocatalysis

Experimentally, more negative potentials than those reported in Table I.1 are needed to drive these reactions at a measurable rate due to the slow kinetics of direct CO_2 reduction. Reaction rates and selectivity (i.e. products ratio) can be greatly improved by using redox-active catalytic species which can mediate the electron transfer to the substrate at the electrode surface, avoiding high energy barriers and being able to lower the overpotential of the catalytic reduction of the substrate.

For instance, Figure I.11 displays a generic redox catalytic cycle involving the catalytic homogeneous species $[Cat]_{ox}$. At a specific redox potential, $[Cat]_{ox}$ is reduced into its active form $[Cat]_{red}$ which reacts with carbon dioxide in presence of protons to yield products. This reaction

occurs in a thin portion of the diffusion layer, the "reaction-difussion layer", at the electrode-electrolyte interface.[43]

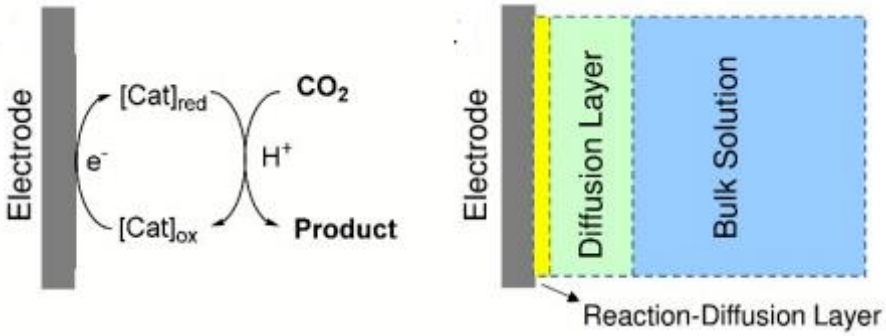

Figure I.11. Schematic representation of the CO_2 catalytic mechanism performed by a homogeneous electrocatalyst (left) and the steady-state layer distribution in solution (right). Reproduced from Ref. [43].

The electrocatalytic process can be homogenous or heterogeneous. In the homogeneous case, the catalyst is solubilized in solution and diffuses freely to the electrode for activation *via* an electron transfer reaction.[44] In heterogeneous catalysis, the catalyst is immobilized at the electrode surface through weak (e.g. Van de Wall) or strong (e.g. covalent) interactions with the electrode material. It can also be the electrode material itself.

One main advantage of heterogeneous *vs.* homogeneous catalysis is the possibility to achieve high product separation with a high rate of catalyst recyclability and no solubility issues. Moreover, harsh experimental conditions such as high temperatures and pressure can be used with no diffusion-dependence effects to consider.

So far, various materials have been described as efficient heterogeneous catalysts for CO_2 reduction: metals, metal alloys, transition metal oxides/chalcogenides and metal organic frameworks. Besides Ag and Pt, Cu has been amongst the most studied metals, which could serve as a heterogeneous catalyst for CO_2 reduction.[30] It is indeed the only metal which can generate CO and reduce it further into hydrocarbons and other organic compounds due to the strong binding of the CO molecule onto the Cu surface, hence favoring subsequent CO protonation in alcohols and formic acid upon electron transfer. The binding energy of the different intermediates

generated when using Cu catalysts was shown to be tunable by surface structure modulation, leading to better selectivity and overcoming thermodynamic and kinetic limitations. Cu nanoparticles have also brought particular attention due to their high versatility through variation of their shape and size (Figure I.12). Other strategies were reported such as the modification of the surface of Cu electrodes by addition of other metals, improving the product selectivity.[45]

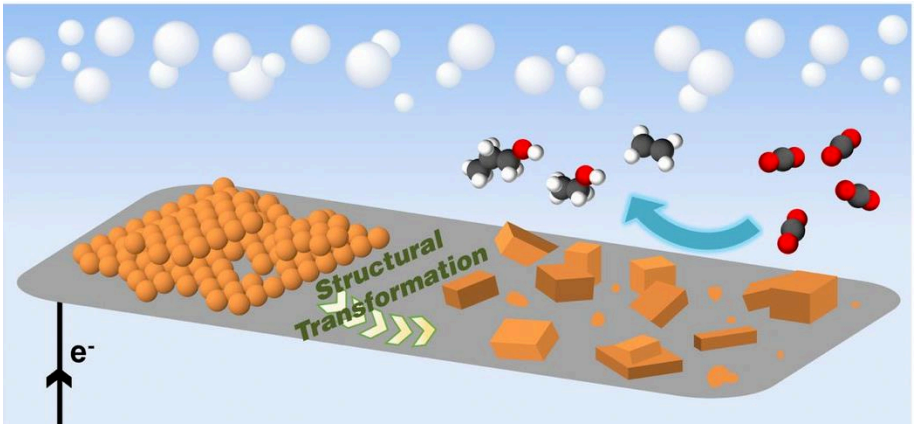

Figure I.12. General representation of the transformation of copper nanoparticles and their interaction with carbon dioxide. Reproduced from Ref. [46].

Deposition of metal oxides such as TiO_2 (or other oxides) have also been reported as efficient photo- and electrocatalytic systems.[32] For instance, Ramesha *et al.* deposited a thin film of TiO_2 on glassy carbon electrodes, observing that CO_2 reduction was occurring on Ti^{4+} sites.[47]

Alternatively, the material morphology was shown to play an important role in the catalytic activity of these systems, being possible to modulate the surface properties by suitable scavenging of the charge carriers as semiconductors are subjected to bandgap excitation. Many studies have emphasized that edges and defects could significantly improve CO_2 reduction, although being a drawback due to the difficulty to define the inhomogeneous structure of the interface of the materials. Current efforts are being focused on the development of single-atom catalysts.[33]

Several parameters are frequently considered for the electrocatalyst design:[48],[49]

- The turnover number (TON) is usually defined as the number of substrate-to-product conversion cycle that a catalyst in solution or immobilized on a surface can perform without being altered.
- The turnover frequency (TOF) corresponds to the turnover per time unit (s, min, h).
- The overpotential (η) is taken as the difference between the equilibrium potential for a given reaction and the potential at which the catalyst operates at a specific current. The lower the overpotential, the better the catalyst, even if other factors should be taken into account.[50] The equilibrium potential is often estimated as equivalent to the standard potential, although most of electrocatalytic reactions reported so far are not performed under standard conditions (1 M and 1 bar).
- The Faradaic efficiency (FE) is a ratio of the quantity of electricity calculated from products generation over the amount of electricity used to generate them.
- The selectivity defines the molar ratio of the different products obtained for a given electrocatalyst.[51, 52]

The nature of the interaction between the substrate and the electrocatalyst can be categorized according to two different approaches: redox-catalyzed electrochemical reactions that involve outer-sphere electron transfers (no bond created between the catalyst and the substrate), or chemically-catalyzed electrochemical reactions that are characterized by a more intimate contact (formation of a substrate-catalyst adduct), favoring an inner-sphere electron transfer.[53]

It is generally admitted that most of molecular metal electrocatalysts, which are constituted of a metal ion center bound to one or several ligands, perform substrate transformation through a chemically-catalyzed reaction involving a metal-substrate adduct. This is particularly true for the electrocatalytic reduction of CO_2 by metal complexes. The principal reason is that redox catalysis (*vs*. chemical catalysis) requires high reorganization energy for the formation of the $CO_2^{\bullet-}$ radical anion due to a geometry variation; instead, chemical catalysis induces an inner-sphere interaction that decreases the activation energy thanks to favorable binding interactions at the transition state as shown in Scheme I.4.

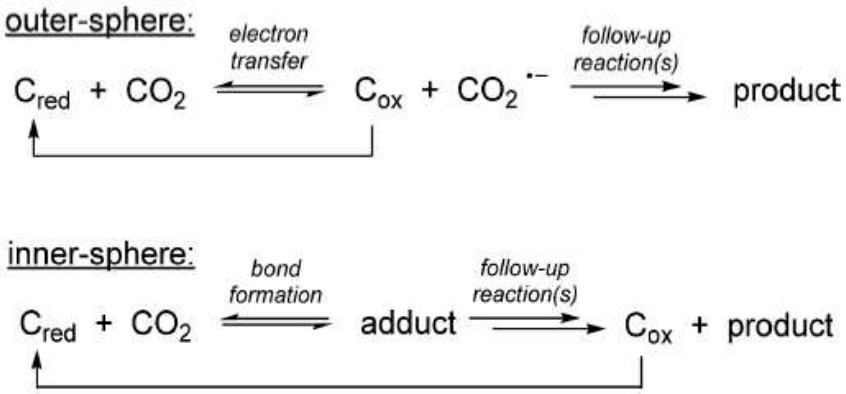

Scheme I.4. Schematic representation of an outer-sphere and inner-sphere interaction by an homogeneous catalyst with CO_2. Reproduced from Ref. [29].

III.3. Molecular metal catalysts for electrochemical reduction of CO_2

III.3.1. General aspects of molecular electrocatalysis for CO_2 reduction

Metal-CO_2 binding modes

Most of molecular catalysts able to perform homogeneous electrocatalytic reduction of CO_2 are organometallic/coordination compounds involving transition metals. This originates from the fact that metals can easily bind CO_2 because of partially filled *d* orbitals. Figure I.13 represents three main types of metal (M)-CO_2 binding modes: η^1-C, η^1-O or η^2-CO.[54] Other binding modes have been reported for transition-metal complexes such as μ_2-η^3 or μ_3-η^4 in bimetallic systems among others, but are less common.[55] η^1-C coordination causes a change in the geometry of the carbon dioxide molecule (linear to bent) and is generally observed for electron-rich metal centers due to the electrophilicity of the carbon atom while η^1-O coordination has a small effect onto the geometry of the substrate, maintaining its linearity or being weakly bent, as usually observed for electron-deficient metal centers.

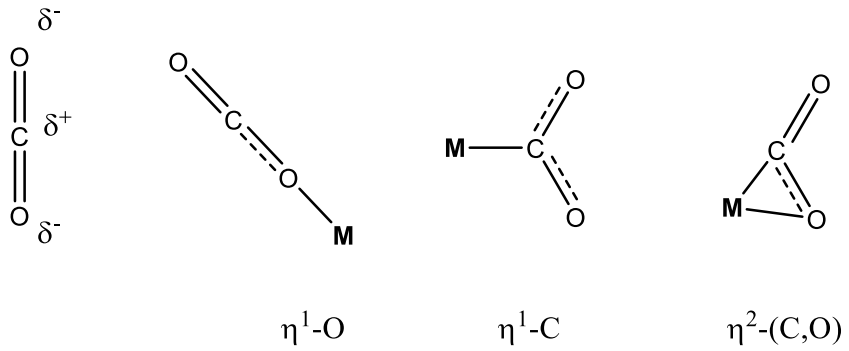

Figure I.13. Schematic representation of the CO_2 molecule and most common coordination modes with a metal center M.

Another mode of metal-carbon dioxide coordination is the insertion of CO_2 in a M-H bond. This reaction can be considered as an activation of carbon dioxide by a metal hydride, being the driving force the polarization of the M-H bond.[42]

Different routes can be undertaken depending on the insertion mode: Pathway B (known as abnormal insertion) is the classical route for low oxidation state metal complexes such as Mn.[56] Pathway A (normal insertion) implies the insertion of CO_2 into the M-H bond, the carbon atom being interacting with the hydride atom meanwhile one of the O atoms (with a nucleophilic character) interacts with the metal center (TS-1 in Figure I.14). Pathway A is normally observed for Rh and Ir complexes.[57]

Interestingly, Aresta *et al.* described how the charge distribution of the M-H bond can be altered by the nature of the metallic center and the ancillary ligands; for example, the presence of electron-donating ligands can increase the electron density on the metal center, inducing a more polarized M-H bond and increasing the efficiency of the catalyst.

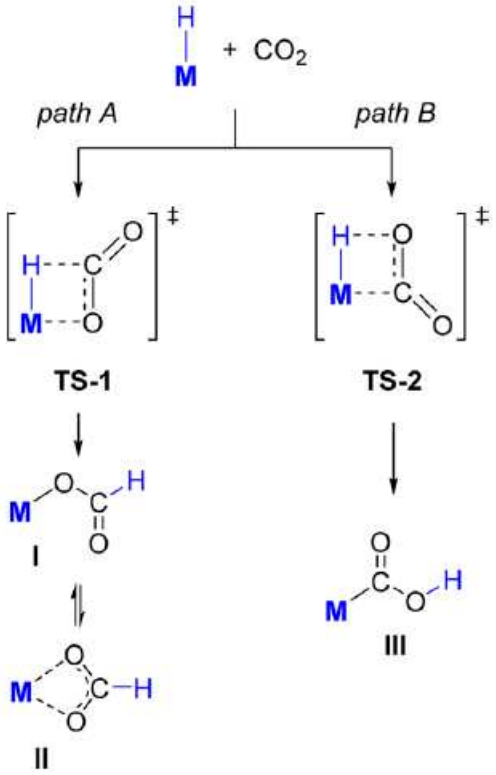

Figure I.14. Schematic representation of the different CO_2 insertion modes in a metal-hydride (M-H) bond. Reproduced from Ref. [29].

Proton sources

The presence of an external proton source in solution likely favors the protonation of the electrochemically reduced species. The role of the proton source in the formation of the catalytically active species for CO_2 reduction has been addressed by considering the free energy of the protonation of metal hydride species (equation I.1).[58]

$$\Delta G = -2.303RT(pK_{a(ext)} - pK_{a1}) \qquad \text{(I.1)}$$

where ΔG is the free energy of the protonation reaction between the proton source ($pK_{a(ext)}$) and the proton acceptor (pK_{a1}).

The selectivity is modulated by the pH of the medium. This is exemplified in Figure I.15 with the pH-diagram distribution of the various Ru species resulting from the reaction of $[Ru(bpy)_2(CO)_2]^{2+}$ with CO_2 in a water/DMF solution. According to this diagram, $[Ru(bpy)_2(CO)_2]^{2+}$, $[Ru(bpy)_2(CO)C(O)OH]^{+}$ and $[Ru(bpy)_2(COO^{-})]^{+}$ are in equilibrium, thus fine adjustment of the pH allows tuning of the selectivity. Additionally, the formation of $CO/HCOO^{-}$ can compete with the formation of H_2, even if the formation of H_2 depends on the proportion of water in solution and can be avoided by maintaining the pH at a value of 6.0.

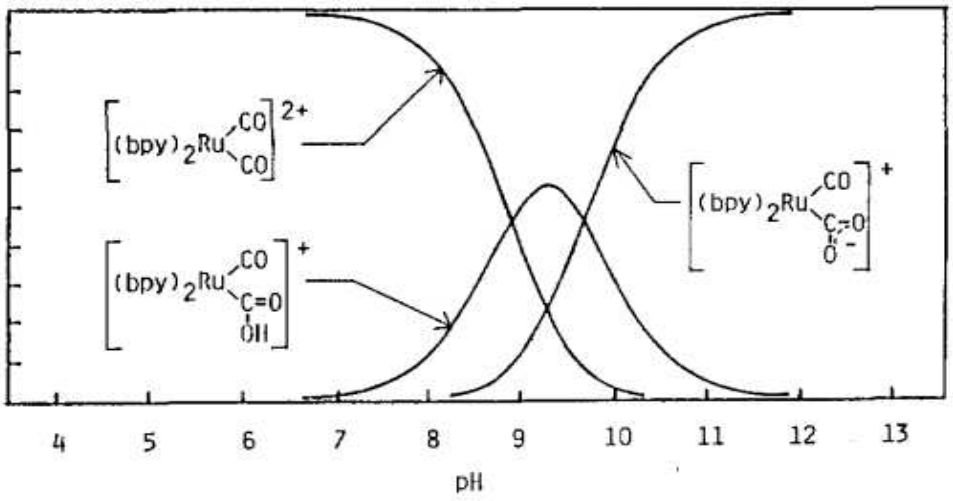

Figure I.15. Diagram distribution of the different Ru species in water at different pH values. Reproduced from Ref. [59].

In the case of η^1-C and η^2-CO coordination modes in protic conditions, activation of CO_2 by the proton source after coordination to the metal center can facilitate the cleavage of the C-O bond.

The intermediates detected in the activation of CO_2 by low-valent transition metals suggest that in the mechanism showed in Figure I.16 the molecule coordinated to the metal center is usually protonated, prioritizing the formation of a new η^1-COOH species that leads to the production of formate/formic acid.[44] In aprotic conditions, carbonate could be found as the main product, so the importance of the role of proton source gains importance due to the ability to enhance the product formation, ensuring new catalytic routes that can give extra stability to the catalytic system.[60]

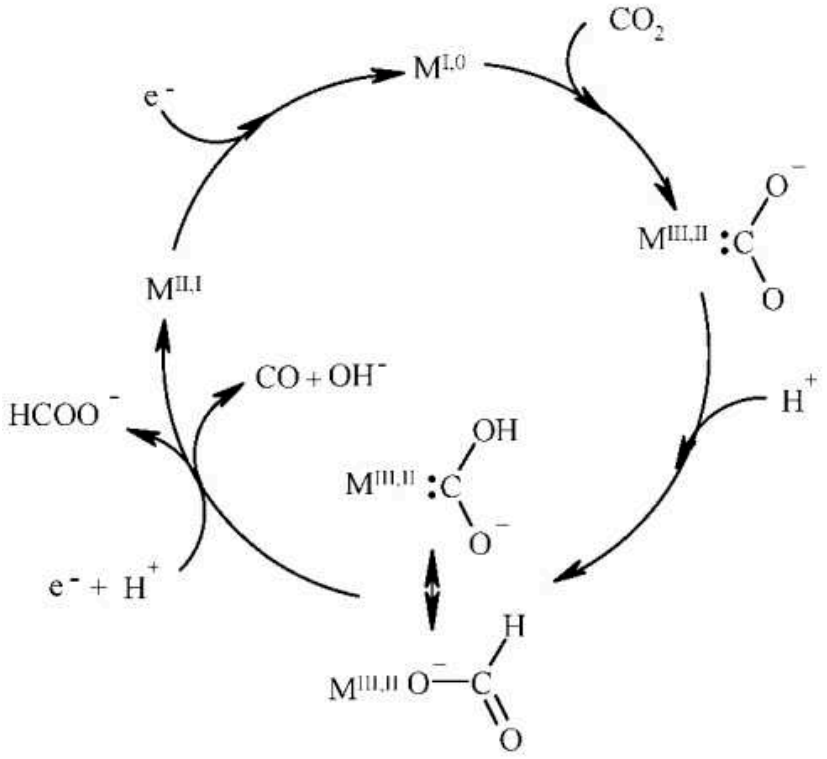

Figure I.16. General mechanism of formate formation by mediation of a transition metal system as a catalyst in a molecular CO_2 electroreduction reaction. Reproduced from Ref. [44].

Weak Brönsted acids, such as 2,2,2-trifluoroethanol (TFE) or methanol (MeOH), added in small quantities have been used as efficient proton sources. An excess of proton source could cause catalyst degradation and loss of effectiveness, promoting undesired reactions such as catalytic hydrogen evolution reaction (HER).

The choice of a solvent is also determined by different factors such as the solubility of the substrate, stability of the catalyst or reactivity with the proton source (undesired HER). Non-aqueous solvents such as acetonitrile (MeCN) or tetrahydrofuran (THF) are frequently used, presenting wide potential windows and fewer solubility issues than aqueous solutions. So far, only few examples of electrocatalytic CO_2 reduction by homogenous molecular electrocatalysts in water have been reported. [61]

III.3.2. Proton-coupled electron transfer in CO_2 electroreduction

In the precedent section, the different coordination modes between CO_2 and the metal complex have been discussed, as well as the role of a proton source in CO_2 electroreduction. These factors, among others, are directly related to the CO_2 electrocatalytic mechanism that these molecular catalysts follow.

However, an important mechanistic feature to consider is that the use of a proton source could cause a noticeable effect on the rate of the catalytic reactions, usually assigned to the presence of Proton-Coupled Electron Transfer (PCET) reactions.[62]

Proton-Coupled Electron Transfer (PCET) reactions have been extensively studied due to their relevance in the mechanism of catalytic electroreduction of small molecules[63-65] and biological processes.[66] Different definitions of PCET have been given, being troublesome to specify a single definition. In this work we will follow the definition given by Mayer,[64] defining PCET reactions as "a single chemical reaction step involving concerted transfer of both a proton and an electron without involving high-energy intermediates", causing a drastic drop of the energetic barrier of the reduction as in Figure I.17.

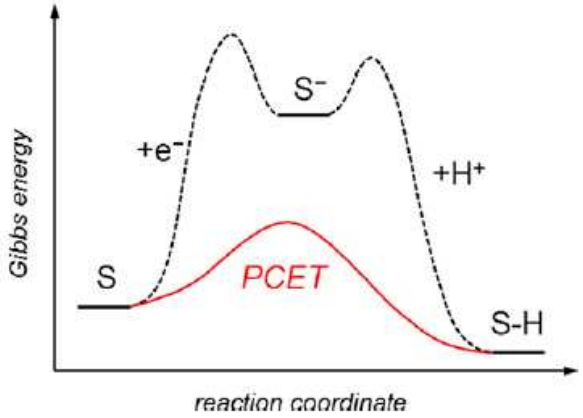

Figure I.17. General PCET energetic profile. Reproduced from Ref. [29].

PCET reactions can be differentiated by contemplating how electron transfer processes occur. Figure I.18.A depicts the transfer of a pure hydrogen atom from the donor to the acceptor group in a concerted process, being considered formally as a HAT reaction. Following the PCET definition

given by Mayer, Hydrogen atom transfer (HAT) reactions are considered as PCET reactions, being also defined as if both electron and proton "travel together" to the same molecular orbitals of the acceptor molecule,[67] or from the same chemical bond.[63]

Figure I.18.B considers the possibility of having both proton- and electron-transfers from different sources. The transfer of the proton occurs from the same acceptor molecule meanwhile the electron is provided by a different donor molecule, hence defining a "concerted PCET" (cPCET, also coined CPET) mechanism. DFT calculations overcome with an energetic difference between both mechanisms that lie on the orbital pathways followed by cPCET and HAT reactions.[68]

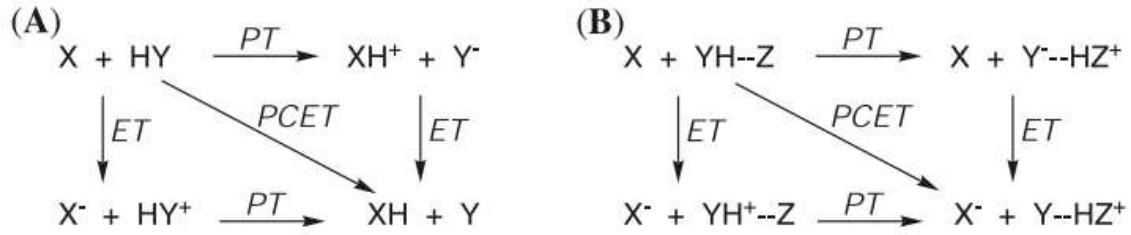

Figure I.18. Schematic representation of PCET (A) and concerted PCET (B) pathways. Reproduced from Ref. [64].

A typical example of the enhancement of electrocatalytic performance for CO_2 reduction by a PCET approach was reported by Savéant *et al.* in 1988. The authors investigated the electrochemical reduction of CO_2 by Fe(0) porphyrin complexes, forming CO as a main product. They demonstrated that addition of Lewis or Brönsted acids, such as phenol, as proton sources provided a boost in their catalytic activity, increasing their TOF and gaining stability.[60] This improvement was achieved due to the occurrence of PCET reactions in their catalytic mechanism.[69] Consequently, modulation of the porphyrin framework bearing -OH pendant groups in ortho position or a combination of fluorine atoms and -OH groups was performed, enhancing their activity towards CO_2 electroreduction with no proton addition (Figure I.19).[70, 71]

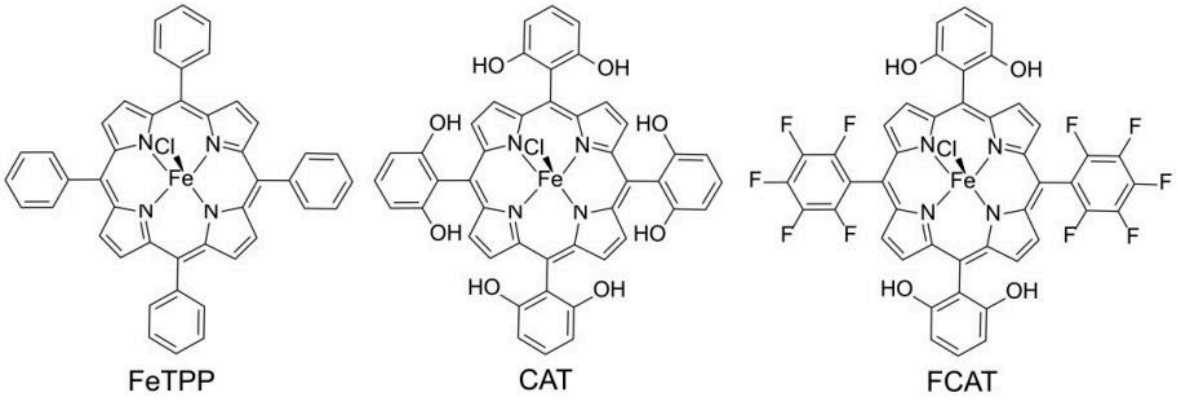

Figure I.19. Iron-substituted porphyrin complexes for PCET CO_2 reduction. Reproduced from Ref. [72].

III.3.3. Molecular metal electrocatalysts for CO_2: a general overview

Four major families of organic ligands are typically considered for the electrocatalytic reduction of carbon dioxide by molecular metal complexes: polypyridines, aza-macrocycles (including cyclam), phosphines and porphyrins. These ligands present P,N or C neutral donors in their framework, which can be bound to the metal center.[44] Supplementary monodentate ligands such as CO or halides can complete the first coordination sphere of metals and provide extra stability to the system or enhanced reactivity towards CO_2.

A great majority of the molecular metal-based electrocatalysts displays redox non-innocent ligands in their coordination sphere. Non-innocent redox ligands are known for playing an essential role in the metal-ligand interaction as they can improve the selectivity of the products, reducing the overpotential of the reduction process but also enhancing the affinity to the substrate with a good balance with products dissociation.[73, 74]

Lyaskovskyy *et al.* have proposed a classification of redox non-innocent ligands according to their main function during the catalytic cycle (Figure I.20):[75]

- In the Approach A, the redox non-innocent ligand acts as Lewis acid for the metal (**strategy I**) or electron reservoir after reduction (**strategy II**). This common approach allows stabilization of the oxidation states of the different intermediates during the catalytic cycle.[76]

- In the Approach B, the redox non-innocent ligand participates to bond making/breaking that involves the substrate. This can occur through substrate activation by the ligand (**strategy III**) or formation of substrate radicals (**strategy IV**).

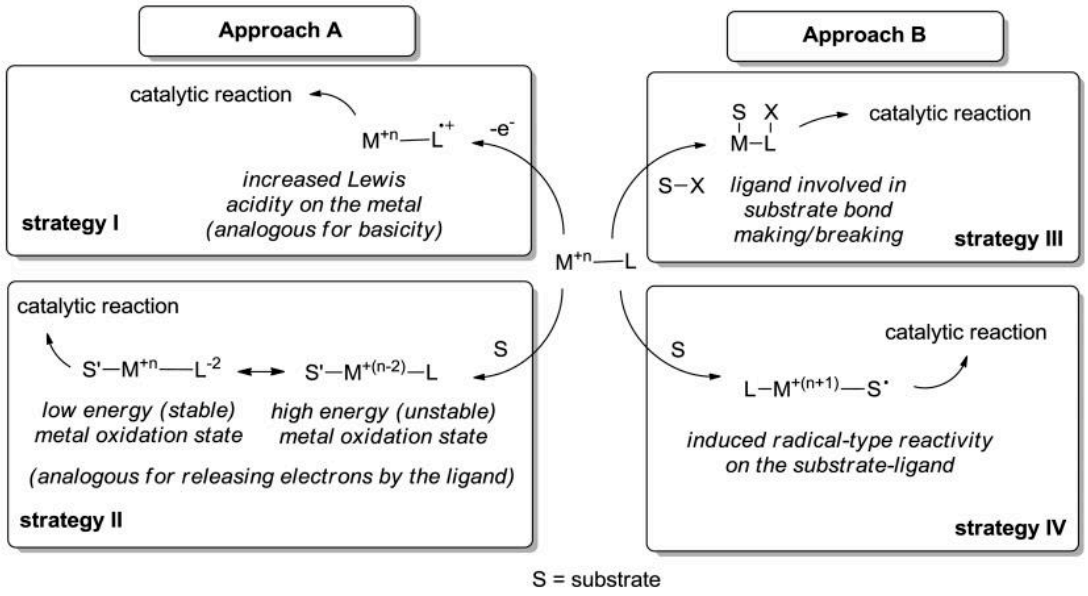

Figure I.20. Lyaskovskyy classification of non-innocent redox ligands by their interaction with the substrate. Reproduced from Ref. [75].

For a more general point of view, synergetic effects between the metal center and the ligand framework are also fundamental in the design of the complex. Hence, π-accepting ligands are prone to stabilize high energetic *d* orbitals from early transition metals while σ donors are more common among late transition metal centers as they can increase the nucleophilicity of the metal center.

The oxidation states of the active species formed during the catalytic cycle are also influenced by the position of the transition metal in the periodic table. Early transition metals have usually lower oxidation states during their catalytic cycles (as Mo or Mn) meanwhile group 8 to 10 metals show higher oxidation states such as for $Fe^{II}CO$ intermediate species in the case of Fe porphyrin.[77]

This effect is related to the relative energy of the d_{z2} orbital which is essential for the activation of the CO_2 molecule (Figure I.21). Consequently, d^6 metals such as Cr or Mo are not oxidized during catalytic cycles, and require "electron-reservoir" ligands such as bipyridine in the coordination sphere. Alternatively, d^7 metal-based complexes lead to mono-oxidized species.[78]

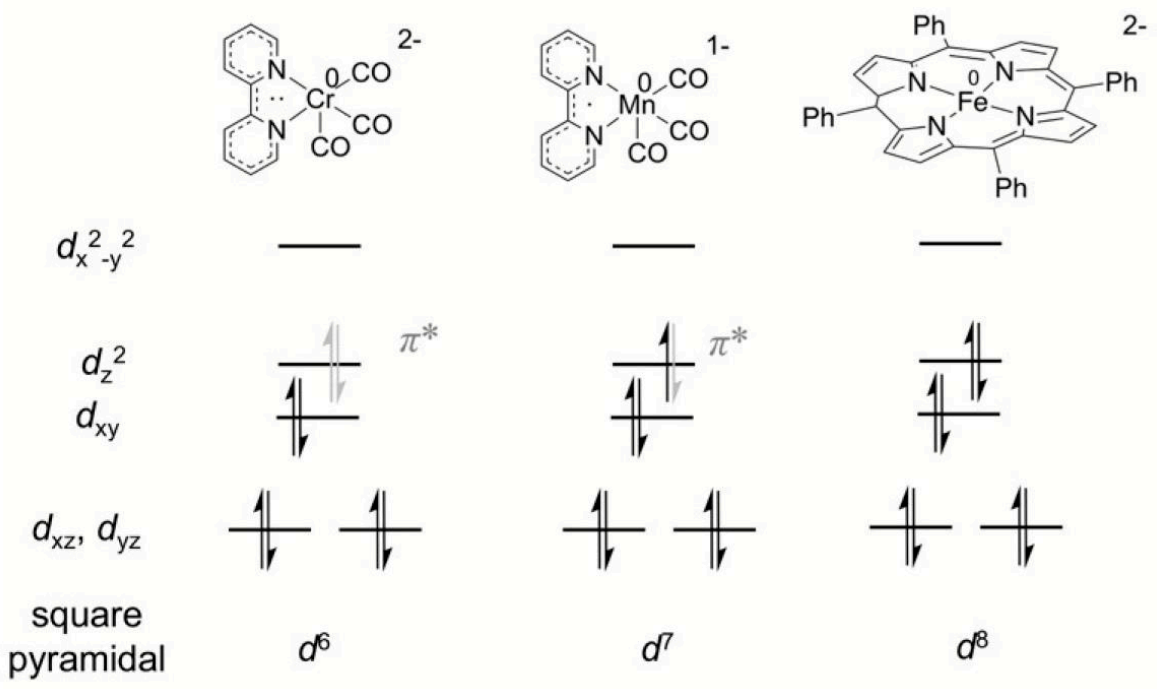

Figure I.21. Representation of metal d orbitals from group 6 to group 8, representing the localization of the electrons from the substrate based on symmetry. Reproduced from Ref. [43].

III.3.4. Homogeneous and heterogeneous molecular metal electrocatalysts

Table I.2 presents a list of molecular catalytic systems towards CO_2 electroreduction in homogenous phase. Values of TOF, TON and FE being acquired by the use of controlled-potential electrolysis (CPE) and cyclic voltammetry (CV) techniques are indicated, as well as experimental conditions.[69]

Table I.2. Selected examples of molecular transition metal CO_2 electrocatalysts (in homogenous phase) sorted by transition metal groups, detailing experimental conditions, TOF and efficiency obtained.

	Complexes	Electrolysis conditions: solvent, WE, proton source	TOF (s^{-1})	Products (FE in %)	Ref.
3d	[**Mn**(bpy)$(CO)_3$(Cl)]	MeCN, GC electrode, TFE	340 s^{-1}	CO (100)	[79]
	[**Ni**(cyclam)]$^{2+}$	1:4 H_2O/MeCN, GC electrode	90 s^{-1}	CO (90)	[61, 80]
	[**Ni**(CNC)]$^{2+}$	MeCN, GC electrode, H_2O	90 s^{-1}	CO	[81]
	[**Fe**(TPP)]	DMF, Hg pool electrode, PhOH	$3.8x10^3$ s^{-1}	CO (92)	[69, 82-84]
	[**Co**N_4H]$^{2+}$	MeCN, GC electrode, H_2O	-	CO (45), H_2 (30)	[85, 86]
4d	[**Ru**(bpy)$(CO)_2$(Cl)]$^+$	1:1 H_2O/DMF, GC electrode	5 s^{-1}	CO (67)	[59, 87]
	[**Pd**(triphosphine)(CH_3CN)]$^{2+}$	MeCN, GC electrode, HBF_4	154 s^{-1}	CO (86), H_2 (14)	[88]
	[**Mo**$(CO)_4$(bpy-(^{t}bu)$_2$]	THF, GC electrode	2 s^{-1}	CO (99)	[78]
	[**Rh**(Cp*)(bpy)Cl]$^+$	MeCN, GC electrode, H_2O	-	$HCOO/HCO_3^-$ (45), H_2 (15)	[89]
5d	[**Pt**$(dmpe)_2$]$^{2+}$	MeCN, GC electrode, PhOH	0.5 s^{-1}	$HCOO/HCO_3^-$ (100)	[90]
	[**Ir**(POCOP)H_2]	5% H_2O/MeCN, GC electrode	20 s^{-1}	$HCOO/HCO_3^-$ (85), H_2 (15)	[91, 92]
	[**Re**(bpy)$(CO)_3$(Cl)]	DMF/H_2O (9:1), GC electrode	570 s^{-1}	CO (99)	[93, 94]
	[**Re**(pyNHC-PhCF_3)$(CO)_3$]$^+$	MeCN, GC electrode, PhOH	100 s^{-1}	CO (100)	[95]

Several points can be taken from these data. The first one is that almost all homogenous electrocatalysts have been investigated in organic solvents (MeCN, THF, DMF), by using PhOH or H_2O as proton source. One main reason is that both CO_2 and molecular electrocatalysts are usually more soluble in organic media than in water. Moreover, hydrogen evolution reaction (HER) is more easily controlled and not competitive in organic media. A second observation is that CO appears as one of the main products of CO_2 electroreduction, unless the only one in certain cases. This suggests that the mechanistic pathways may be somewhat similar for these systems. At last, we observe that TOF and Faradaic efficiencies are varying over several ranges depending on the metal complexes. However, these values should be taken with caution as they are calculated by using different mathematical formula.[44, 69] From a more general view, it appears that these homogenous molecular catalysts among others are able to provide relative high selectivity rates towards catalytic reactions and easy modulation of the ligand framework.

From these results, one current challenge consists in immobilizing these molecular metal complexes onto electrodes to perform electrocatalytic reduction of CO_2 in heterogeneous phases. One main advantage is to overcome solubility issues present in homogeneous catalysis and providing higher recyclability rates.[96] Moreover, robustness, efficiency, selectivity and cost can be improved.[97, 98] Different strategies for immobilization of metal complexes onto surfaces have been developed these last years, including covalent grafting, $\pi-\pi$ or electrostatic interactions.[99, 100] For example, chemical modification of electrode surfaces by electrochemical polymerization of metal complexes was shown to inhibit deactivation pathways and enhance catalytic properties.[101] Alternatively, covalent grafting of molecular units using diazonium salts was described. For instance, Wenbin *et al*.[97] reported the grafting of [M(4-amino-bpy)$(CO)_3$X] (M = Mn, X = Br or M = Re, X = Cl) diazonium salts onto graphene oxide (Figure I.22), achieving a TOF of 4.4 s^{-1} in CO production in MeCN by using H_2O as a proton source.

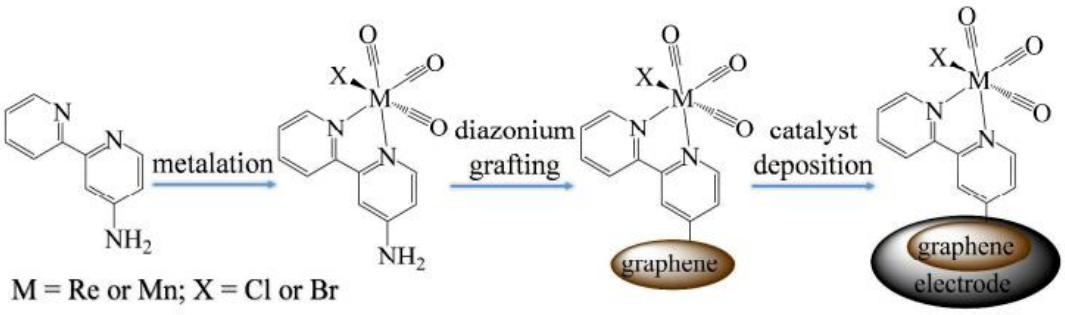

Figure I.22. Different stages during the immobilization process of [M(4-amino-bpy)$(CO)_3$X] in MeCN. Reproduced from Ref. [97].

Non-covalent strategies such as π-π interactions[102] or electrostatic interactions[103] have been also explored as no functionalization of the ligand framework is needed. A very promising technology is the incorporation of molecular catalysts onto the surface of multi-walled carbon nanotubes (MWCNTs) by π-π interactions[104] or incorporation into the MWCNTs structure,[105] which stands out due to its high active surface. For example, the complex [Re(4,4'-^{t}Bu-2,2'-bpy)$(CO)_3$Cl] showed excellent catalytic activity towards CO_2 electroreduction after immobilization over MWCNT electrodes, obtaining a TON > 5600 with no H_2 production in aqueous media with low overpotential values (–0.56 V *vs*. RHE).[106] High loading of the catalytic system in the MWCNT electrodes and inhibition of the interaction between H_2 and MWCNT surfaces were proposed to be factors that influence the efficiency and selectivity of [Re(4,4'-^{t}Bu-2,2'-bpy)$(CO)_3$Cl] as immobilized systems (Figure I.23). Noteworthy, no catalytic activity could be observed with the complex in homogeneous phase after addition of Brönsted acids such as phenol.[107]

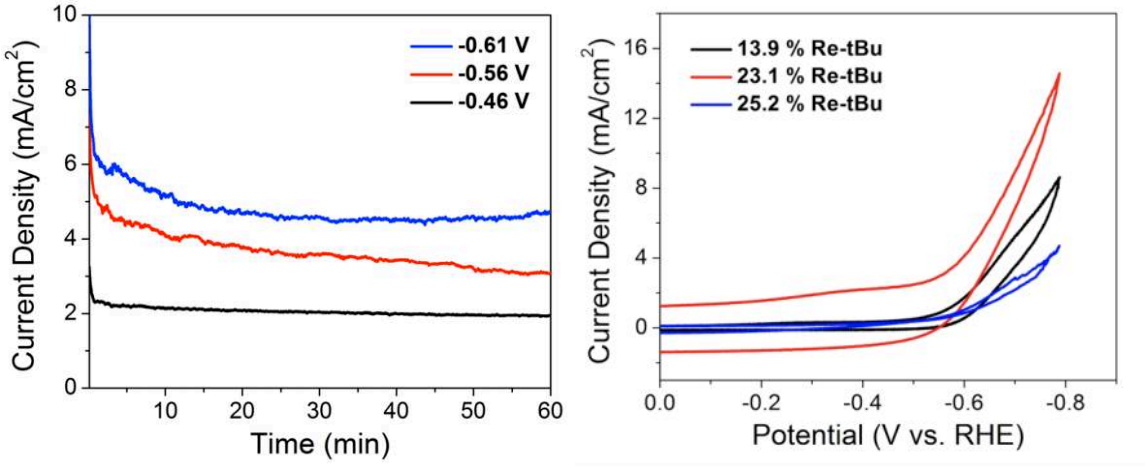

Figure I.23. Left: CPE responses at different potentials vs RHE under CO_2. Right: CV responses for different catalytic loading onto MWCNTs under CO_2. Reproduced from Ref. [106].

III.3.5. Group 6 Metal-$(CO)_4$(diimine) complexes for CO_2 electrocatalytic reduction

Diimine groups have been extensively explored as non-innocent redox ligands for molecular CO_2 electrocatalysts. Late transition metal centers such as for Re,[94, 108-110] Rh[89] and Ru[111, 112] were first investigated, but more earth-abundant metals such as Mn[56, 113] or Co[114] have drawn more attention these last years, showing high Faradaic efficiency towards CO or formate production.

However, very few examples of CO_2 electrocatalysts based on metals from the 6th group (Cr, Mo, W) have been reported, even if these two metals are present in the active site of enzymes that can carry out HCO_2H/CO_2 interconversion.[27] Most of group 6 catalysts are diimine tetracarbonyl systems, [$M(CO)_4$(diimine)].[78] One main reason for this trend is that the electronic reduction on these systems occurs merely on the non-redox innocent diimine moiety than on the metal, thus potentially providing a free binding site for CO_2 on the metal upon CO release. In addition, carbonyl ligands allow enhanced stabilization of the complexes upon reduction by back-bonding effects with the metal. So far, these complexes have been well studied for their photophysical properties, but remain poorly investigated as electrocatalysts.[115]

$[M(CO)_4(diimine)]$ complexes usually present a distorted pseudo-octahedral geometry (Figure I.24) with a C_{2v} or C_s symmetry depending on the nature of the diimine ligand. The axial C(O)-Mo-C(O) moiety is usually characterized by a slight bent towards the diimine ligand. This features a necessary distinction between equatorial and axial CO ligands in order to understand the reactivity of systems.[116]

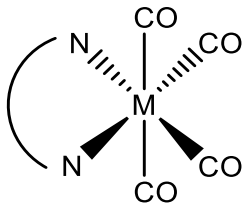

Figure I.24. General structure of $[M(CO)_4(diimine)]$ systems.

The first report of synthesis of group 6 tetracarbonyl bipyridine (bpy) systems was published by Hieber in 1935.[117] In the early 60s, Stiddart reported the synthesis of 2,2´-bipyridine tetracarbonyl systems $[M(CO)_4(bpy)]$ (M = W, Mo, Cr) by using $M(CO)_6$ as the main metallic source.[118] In the late 80s, Connor[119] reported the synthesis of ortho-functionalized 2,2´-bypiridine tetracarbonyl complexes $[M(CO)_4(bpy\text{-}(R_2)]$ (M = Mo, W, Cr ; R = NMe_2, OMe, NH_2, CMe_3, Ph, CO_2H, CO_2Me, NO_2, CH=CHPh) by using $[M(CO)_4(nbd)]$ (nbd = norbornadiene) as precursor instead of $Mo(CO)_6$.[120] This strategy has become the general procedure for the synthesis of 4,4-functionalized $[M(CO)_4(bpy\text{-}(R)_2]$ complexes.

Spectroscopic data of $[M(CO)_4(diimine)]$ systems is well documented. On one hand, infrared (IR) spectroscopy typically features four characteristic ν(CO) stretching bands ($2A_1+B_1+B_2$) in the 1800-2100 cm^{-1} region.[121] UV-Vis-NIR absorption spectra usually present several Metal-to-Ligand-Charge-Transfer (MLCT) transitions involving *d*-orbital from the metal to the diimine or CO orbitals, as demonstrated by TD-DFT studies.[122] Regarding more specifically the HOMO-LUMO gap, these systems show a LUMO that is mainly diimine-ligand based while the HOMO is centered on the metal center.

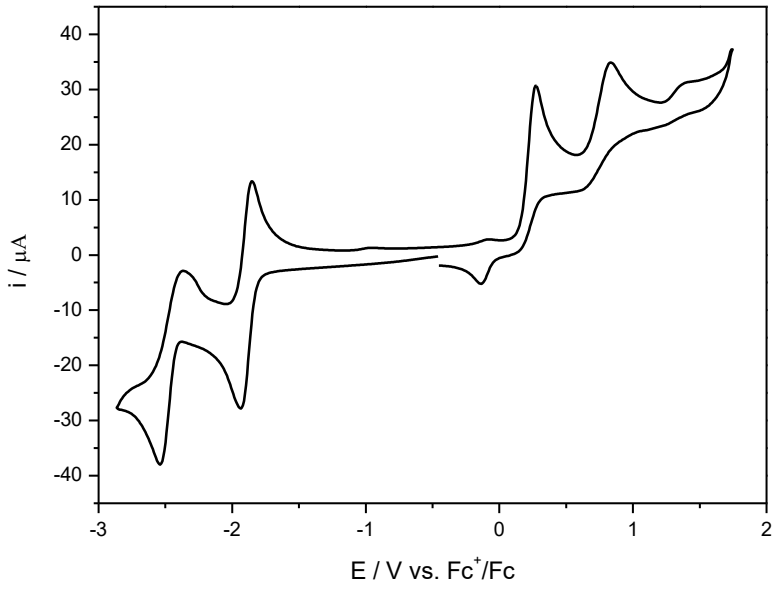

Figure I.25. CV (v = 100 V s^{-1}) of $[Mo(CO)_4(bpy)]$ (1 mM) at a glassy carbon working electrode in THF / NBu_4PF_6 (0.1 M).

Redox properties of $[M(CO)_4(diimine)]$ complexes have been for a great majority investigated by cyclic voltammetry (CV). For instance, the Figure I.25 displays the voltammetric signature of $[Mo(CO)_4(bpy)]$ in THF/NBu_4PF_6. In reduction, the complex shows two one-electron processes at moderate scan rate (v = 100 V s^{-1}). The first one is reversible and appears at $E_{1/2}$ = −1.90 V *vs*. Fc^+/Fc. Spectroscopic and DFT calculations have demonstrated that reduction occurs essentially on the diimine ligand, leading formally to the $[Mo^0(CO)_4(bpy)]^{\bullet-}$ species. Indeed, the formation of a radical diimine chromophore has been observed by NIR and UV-vis spectroscopic techniques, hence evidencing that the metal center is not implied into the redox process.[123] Moreover, the SOMO (Single Occupied Molecular Orbital) was shown to be extended over the diimine backbone with an increase of the π-retrodonation towards the CO ligands, especially to the equatorial ones.[116] The second reduction process occurs at −2.60 V *vs*. Fc^+/Fc. The partial reversibility of this process indicates a chemically coupled mechanism. IR and UV-Vis spectroscopic studies supported by theoretical studies have emphasized that the formation of bis-reduced species

$[Mo(CO)_4(bpy)]^{2-}$ is followed by a rapid loss of one of the axial CO ligands, forming a tricarbonyl $[Mo(CO)_{3(}bpy)]^{2-}$ species in that solvent (THF).

Noteworthy, the use of protic solvents such as MeCN inhibits CO loss but favors the protonation of the bis-reduced $[Mo(CO)_3(bpy)]^{2-}$, hence generating $[Mo(CO)_4(bpy\text{-}H^+)]^-$ after a rapid recoordination of a CO molecule. The anodic peaks observed on the back scan at potential values between the second and the first reduction potentials have been ascribed to the oxidation of bis-reduced complexes bearing 3 or 4 carbonyl groups.[124]

On the oxidation side, $[Mo(CO)_4(bpy)]$ is characterized by two monoelectronic processes at 0.26 V and 0.82 V *vs*. Fc^+/Fc in THF. These oxidation reactions were shown to be metal-centered. While the first system is reversible in THF (not shown in Figure I.25), the second is fully irreversible. Moreover, a loss of reversibility for the first oxidation peak is observed in presence of a coordinating solvent such as acetonitrile due to the substitution of one CO ligand by an acetonitrile molecule.[125]

Interestingly, the redox behavior of $[Mo(CO)_4(bpy)]$ is also affected by the nature of the working electrode material. Taylor *et al.* reported a positive shift of about 200 mV of the second reduction process by the use of gold instead of glassy carbon (GC) or a platinum working electrodes.[126] The adsorption of the mono-reduced $[Mo(CO)_4(bpy)]^-$ species onto the Au surface allows an ECE pathway (E = Electrochemical, C = Chemical) that facilitate the loss of one CO ligand during the first reduction process, leading to the tricarbonyl $[Mo(CO)_3(bpy)]^-$ species (Figure I.26). Remarkably, the latter is reduced at a more positive potential than its tetracarbonyl analogue $[Mo(CO)_4(bpy)]^-$.

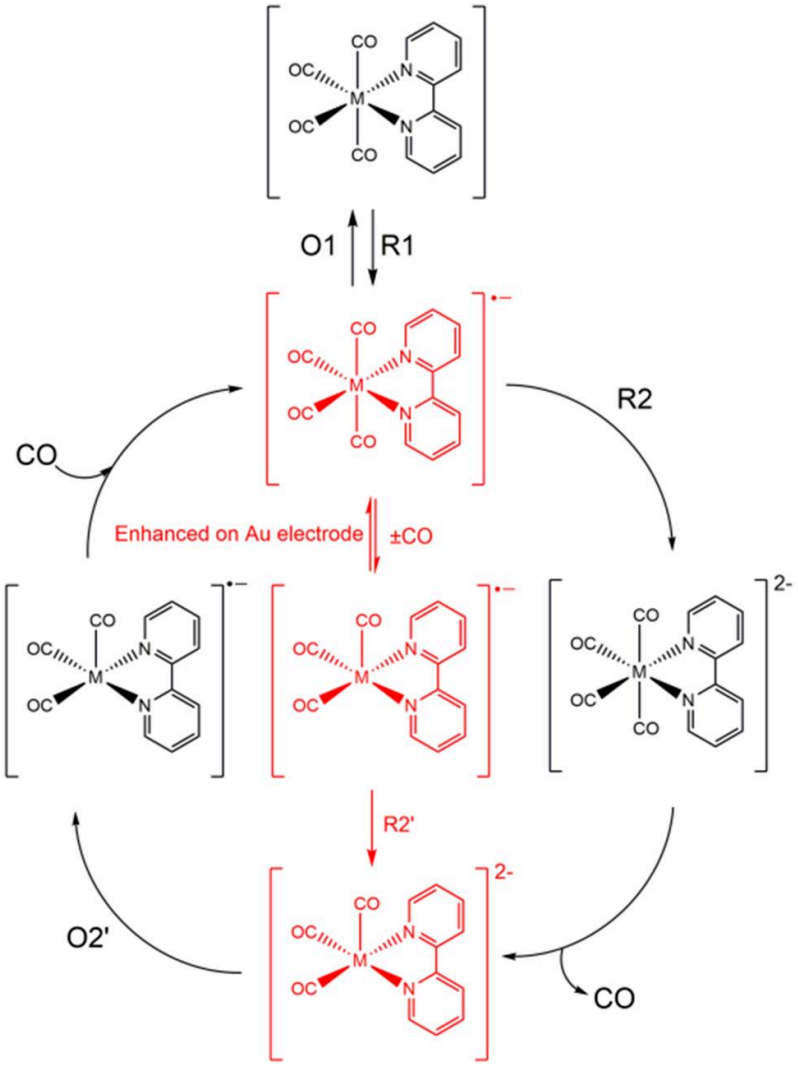

Figure I.26. Redox mechanism of $[M(CO)_4(bpy)]$ under Ar, showing in red a low energy ECE pathway when using Au as working electrode. Reproduced from Ref. [126].

As shown in Figure I.27, infrared spectroelectrochemical (IR-SEC) studies also allowed the characterization of the transient species generated by electrochemical reduction of $[Mo(CO)_4(bpy)]$. The monoanionic radical species $[Mo(CO)_4(bpy)]^{\bullet-}$ featured a negative shift of about 30 cm^{-1} lower than the neutral species as a consequence of the elongation of the CO bonds caused by an increase of the π* backbonding density towards the CO ligands.[124, 126] These results were consistent with those obtained by DFT calculations, which showed that the electron density

after the first reduction process was mainly localized on the bipyridine ring. For the second reduction process, both $[Mo(CO)_4(bpy\text{-}H^+)]^-$ (in MeCN) and $[Mo(CO)_3(bpy)]^{2-}$ (in THF) species were detected. $[Mo(CO)_4(bpy\text{-}H^+)]^-$ showed a small shift of 10 cm^{-1} comparing to the monoanionic species, meanwhile three bands at 1846, 1726 and 1706 cm^{-1} were detected for $[Mo(CO)_3(bpy)]^{2-}$, losing the signature of a tetracarbonyl species due to the disappearance of the peak usually found around 2000 cm^{-1} (Figure I.27).

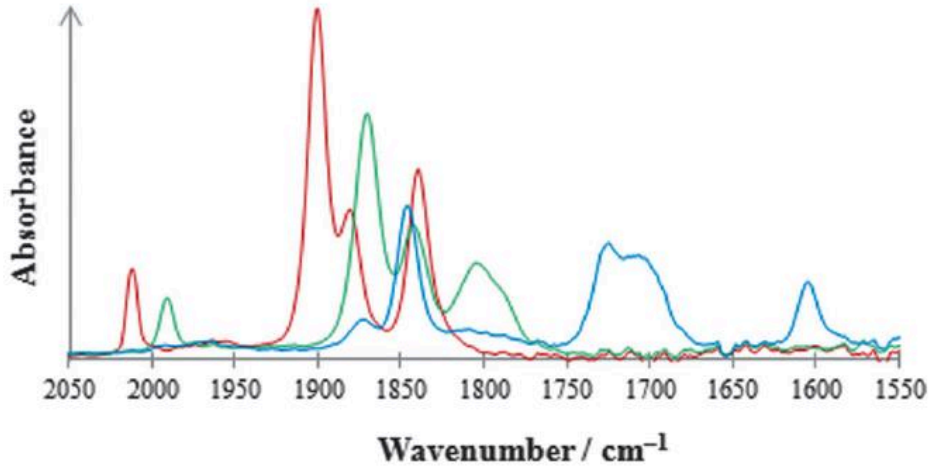

Figure I.27. IR-SEC spectra of $[Mo(CO)_4(bpy)]$ in THF under Ar, showing $[Mo(CO)_4(bpy)]$ (red), $[Mo(CO)_4(bpy)]^{\bullet-}$ (green) and $[Mo(CO)_3(bpy)]^{2-}$ (blue) species. Reproduced from Ref. [124].

Other techniques such as UV-Vis spectroelectrochemistry [124] and $^1H/^{13}C$ NMR experiments [127] were used to obtain additional information about the species formed and their interaction with carbon dioxide. Clark *et al.* reported the first study of the catalytic activity of $[M(CO)_4(bpy\text{-}(R)_2)]$ (M = Mo, W; R = H, ^{t}Bu) towards CO_2 electroreduction in THF (Figure I.28). A catalytic enhancement of the current was observed at potential values related to the formation of the doubly reduced species. Carbon monoxide was found to be the main product in MeCN,[78] while formate and carbonate were produced in THF.[126] Surprisingly, no proton source addition was necessary to promote the catalytic activity of group 6 $[M(CO)_4(diimine)]$ systems, in contrast to similar Mn systems.[79, 128] The presence of *tert*-butyl substituent groups in the bipyridine ring increased the catalytic activity of the system but displayed higher overpotential due to the electron donating character of the ^{t}Bu groups. Even though, the catalytic activity was very small compared to Fe

porphyrins[82] or group 7 [M(CO)$_3$(X)(bpy)] systems,[110, 129] that are known for being potentially the most active molecular systems towards catalytic CO_2 electroreduction to date.

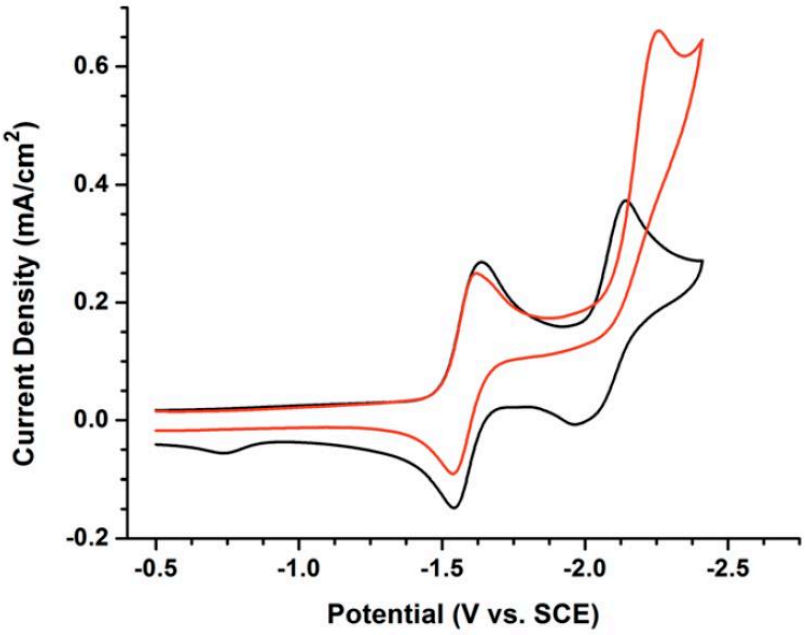

Figure I.28. CVs of [Mo(CO)$_4$(bpy)] under Ar (black) and CO_2 (red) recorded in THF/NBu_4PF_6 at GC working electrode and at a scan rate of 100 V s^{-1}. Reproduced from Ref. [78].

The effect of the steric factor in [Mo(CO)$_4$(bpy-4,4´-(R)$_2$)] complexes was investigated by Taylor *et al.* for R = Me. These authors compared the catalytic activity of different complexes only varying by the position of the methyl groups. They found an outstanding catalytic activity for the 6-6´derivative using a gold working electrode.[126]

Other interesting studies showed that all [Mo(CO)$_4$(diimine)] systems do not display the same electrocatalytic activity towards CO_2. For example, [M(CO)$_4$(dpa)] (M= Mo, W ; dpa = dipyridylamine) complexes presented only one reduction process at a more negative potential than the [M(CO)$_4$(bpy)] (M= Mo, W) first reduction.[78, 130] The irreversible character of the [M(CO)$_4$(dpa)] redox process indicated that a chemical reaction was occurring after the one-electron reduction, here a strong geometric rearrangement involving the loss of one H atom of the N-H amine group due to the excess of charge in the dpa ligand. As shown in Figure I.29, an

electrocatalytic wave was detected in presence of CO_2 at this first reduction potential, in strong contrast with [$M(CO)_4$(bpy)] systems which need double reduction to perform catalysis. As a matter of fact, DFT calculations suggested that the rearranged mono-reduced species underwent further electrochemical reduction at this potential hence inducing CO loss and CO_2 binding.

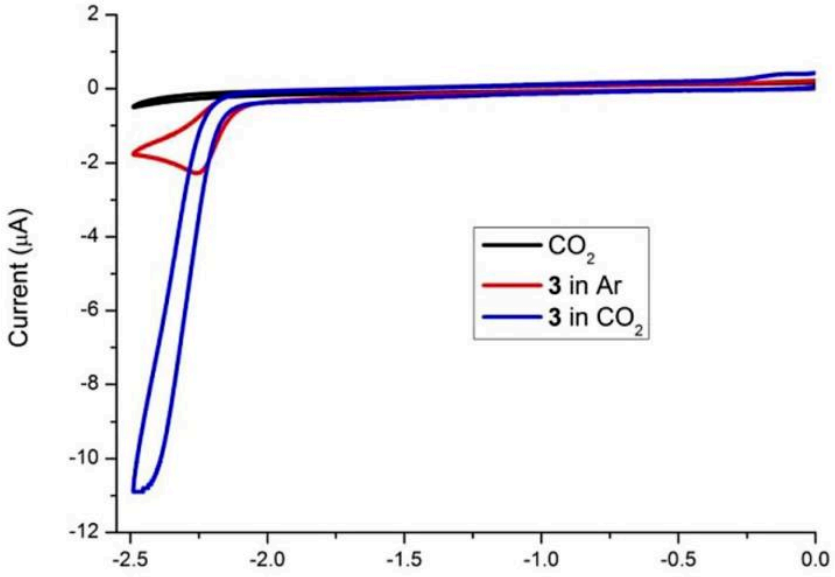

Figure I.29. CVs of [$Mo(CO)_4$(dpa)] under Ar (red) and CO_2 (blue) in comparison with CO_2 background (black) in MeCN. Reproduced from Ref. [130].

Most recent studies on group 6 diimine systems towards CO_2 electroreduction have focused on the modification of the ligand framework by adapting effective strategies used in other transition metal systems. For example, the design of the [$Mo(CO)_2$(SCN)(dimethyl-2,2´-bpy)(η^3-allyl)] system was built around the exchange of a CO ligand by an allyl group,[131] in an attempt to simulate the coordination sphere of the well-known group 7 [$M(CO)_3$(X)(bpy)] (X=halide) catalytic systems.[79, 129] Following this tendency, Machan *et al*.[132] reported the only known group 6 system, [Cr(^{tbu}dhbpy)Cl(H_2O)], whose catalytic activity towards CO_2 electroreduction was entirely dependent on the addition of a proton source such as phenol. A decrease of the overpotential in [Cr(^{tbu}dhbpy)Cl(H_2O)] system avoided an interference with the reduction of the acid present in solution, allowing the formation of CO and water according to a catalytic 2-electron process (Figure I.30).

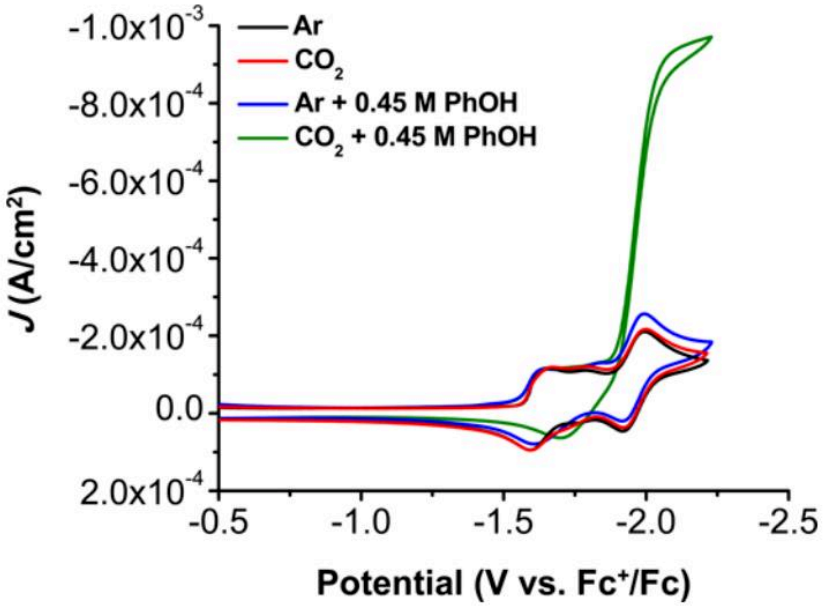

Figure I.30. CVs of [Cr(^{tbu}dhbpy)Cl(H_2O)] under Ar and CO_2 with and without phenol as a proton source in MeCN. Reproduced from Ref. [132].

IV. Objectives of the thesis

In conclusion, different perspectives have been contemplated in the last decades as a response to the issue of global warming. Transformation of carbon dioxide into value-added products has raised as one of the most interesting routes to follow, either by photochemical,[133] electrochemical[28] or chemical procedures.[13] Biomimicry has boosted the development of promising strategies to convert CO_2 into valuable products. On one hand, artificial photosynthesis[134] can combine light and electrochemical processes with the aim of developing a free-emission technology with the help of catalytic systems. On the other hand, electrocatalytic systems can transform carbon dioxide into carbonated products such as carbon monoxide or methanol, although they are often facing drawbacks such as lack of selectivity and high overpotentials.[53] Molecular catalysts involving transition metal have recently shown remarkable properties in terms of homogeneous electrocatalysis for CO_2 reduction. While Mn, Fe and Co complexes remain the most efficient electrocatalysts so far, group 6 (Mo, W, Cr) molecular systems have drawn more interest during the last five years.[29] The activity of these systems relays in the redox non-innocent character of the diimine moiety, being able to store electronic density enough to promote the reduction of molecules such as carbon dioxide.

From this state of the art, this doctoral work was aimed at developing and studying the redox properties of new $[Mo(CO)_4(diimine)]$ systems, by exploiting the modulation of the diimine ligand to obtain a better understanding on the interaction of the reduced species formed with carbon dioxide.

Different strategies have been explored and are gathered in the different chapters throughout this manuscript. In Chapter II, the study of the redox and catalytic properties of $[Mo(CO)_4(bpy\text{-}(\mathbf{R})_2)]$ systems (**R** = -H,-^{t}Bu,-OMe,-CO_2Me,-CF_3,-NO_2) was carried out, including the effects caused by electron-donor and electron-acceptor 4,4´-**R** substituents coordinated to the 2,2´-diimine ligand in the catalytic activity of these complexes towards CO_2 electroreduction (Figure I.31). Electrochemical and spectroelectrochemical techniques, along with DFT calculations, were used to develop a better understanding of the intermediates formed during the redox processes of the different derivatives tested.

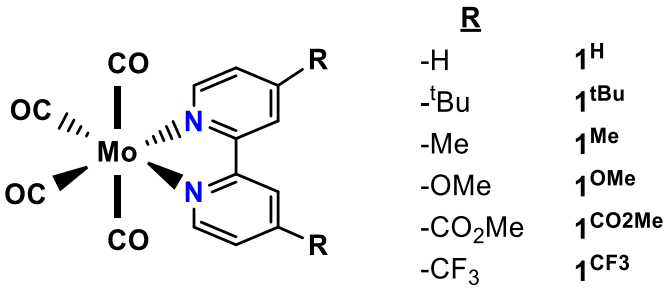

Figure I.31. General structure of $[Mo(CO)_4(bpy\text{-}(\mathbf{R})_2)]$ derivatives.

Another perspective that has been examined in Chapter III is the comparison of the redox and catalytic properties of $[Mo(CO)_4(bpy)]$ with two other analogues complexes, $[Mo(CO)_4(phen)]$ and $[Mo(CO)_4(py\text{-}indz)]$, since none of them was previously studied for CO_2 electroreduction, so far (Figure I.32). Meanwhile $[Mo(CO)_4(phen)]$, whose redox properties have been already reported without further extent (i.e. not for CO_2 reduction),[116] is a polypyridine system which has been well investigated for its photophysical properties,[135, 136] whereas $[Mo(CO)_4(py\text{-}indz)]$ is a novel complex whose redox and catalytic features have not been explored yet. $[Mo(CO)_4(py\text{-}indz)]$ is characterized by an antisymmetric diimine ligand that is formed by two different moieties, a pyridine and an indoziline group, being both of them able to store electronic density as redox non-innocent moieties. Chapter III is then focused on the study of the relationship between the framework of the diimine ligand and the interaction with carbon dioxide in $[Mo(CO)_4(diimine)]$ systems, using IR and UV-vis spectroelectrochemical techniques under Ar and CO_2 atmospheres, as well as DFT calculations.

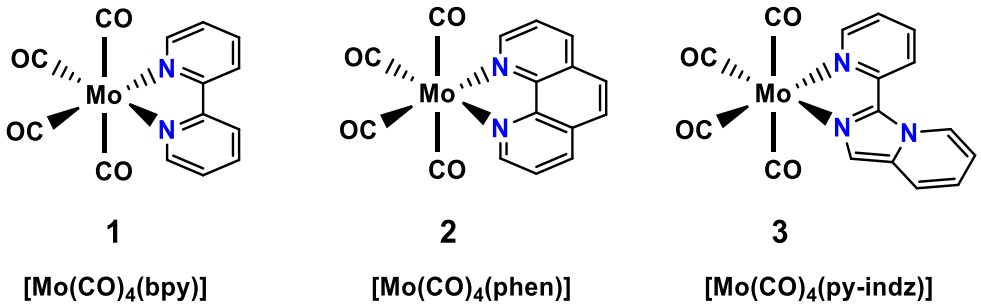

Figure I.32. From left to right, $[Mo(CO)_4(bpy)]$, $[Mo(CO)_4(py\text{-}indz)]$ and $[Mo(CO)_4(phen)]$ complexes.

In the last section (Chapter IV), the use of immobilization strategies is discussed, presenting our efforts in diminishing the overpotential and increasing the catalytic activity compared to homogeneous CO_2 electroreduction. The synthesis of the novel [$(Mo(CO)_4$(bpy-(C_5-pyrene,methyl)] and [$Mo(CO)_4$(4-$PhNH_2$-phen)] complexes has been carried out with the purpose of immobilizing these systems onto electrode surfaces by absorption through π-π interaction with MWCNTs (multi-walled carbon nanotubes) or by diazonium electrografting (Figure I.33), as previously done for other transition metal systems.[105, 137, 138]

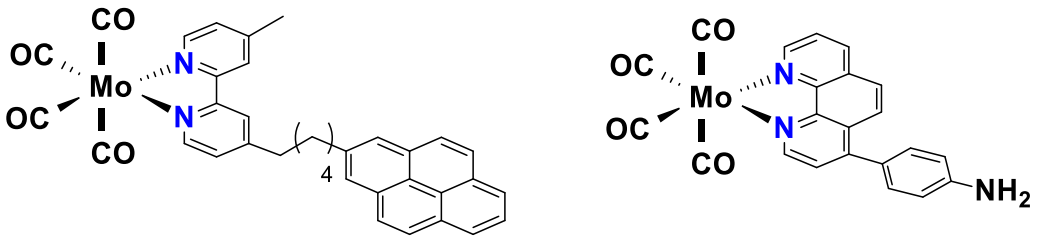

Complex **4** Complex **5**

Figure I.33. From left to right, [$(Mo(CO)_4$(bpy-(C_5-pyrene,methyl)] and [$Mo(CO)_4$(4-$PhNH_2$-phen)] complexes.

Bibliography

[1] *IPCC, 2019: Climate Change and Land*, **2019**.
[2] *BP Energy Outlook*, **2019**.
[3] The Imbie Team, *Nature* **2020**, *579*, 233-239.
[4] A. E. Putnam, W. S. Broecker, *Sci. Adv.* **2017**, *3*, e1600871.
[5] A. A. Lacis, G. A. Schmidt, D. Rind, R. A. Ruedy, *Science* **2010**, *330*, 356-359.
[6] H. Ritchie, Published online at OurWorldInData.org., **2017**.
[7] J. T. Kiehl, K. E. Trenberth, *Bull. Am. Meteorol. Soc.* **1997**, *78*, 197-208.
[8] J. H. Butler, S. A. Montzka, *Published online at esrl.noaa.gov*, **2020**.
[9] H. Ritchie, M. Roser, *Published online at OurWorldInData.org*, **2020**.
[10] G. De Leener, F. Evoung-Evoung, A. Lascaux, J. Mertens, A. G. Porras-Gutierrez, N. Le Poul, C. Lagrost, D. Over, Y. R. Leroux, F. Reniers, P. Hapiot, Y. Le Mest, I. Jabin, O. Reinaud, *J. Am. Chem. Soc.* **2016**, *138*, 12841-12853.
[11] M. North, *Carbon Dioxide Utilisation*, Elsevier, **2015**.
[12] S. Rönsch, J. Schneider, S. Matthischke, M. Schlüter, M. Götz, J. Lefebvre, P. Prabhakaran, S. Bajohr, *Fuel* **2016**, *166*, 276–296.
[13] J. Kopyscinski, T. J. Schildhauer, S. Biollaz, *Fuel* **2010**, *89*, 1763-1783.
[14] V. Kyriakou, I. Garagounis, E. Vasileiou, A. Vourros, M. Stoukides, *Catal. Today* **2017**, *286*, 2-13.
[15] W. Wang, S. Wang, X. Ma, J. Gong, *Chem. Soc. Rev.* **2011**, *40*, 3703-3727.
[16] A. Raza, R. Gholami, R. Rezaee, V. Rasouli, M. Rabiei, *Petroleum* **2019**, *5*, 335-340.
[17] M. Bui, *Energ. Environ. Sci.* **2018**, *11*, 1062-1176.
[18] C. Gough, P. Upham, *Greenh. Gases* **2011**, *1*, 324-334.
[19] G. Soloveichik, *Nature Catal.* **2019**, *2*, 377-380.
[20] M. J. Shaw, W. E. Geiger, *Organometallics* **1996**, *15*, 13-15.
[21] M. P. Johnson, *Essays Biochem.* **2016**, *60*, 255-273.
[22] H. Lodish, A. Berk, S. Zipursky, *Molecular Cell Biology, 4th edition*.
[23] M. Wada, S. G. Kong, *J. Cell Sci.* **2018**, *131*.
[24] J. Barber, *Chem. Soc. Rev.* **2009**, *38*, 185-196.
[25] D. Mondal, T. Sadhukhan, I. Latif, S. Datta, *J. Chem. Sci.* **2015**, *127*.
[26] I. Gamba, *Bioinorg. Chem. Appl.* **2018**, *2018*, 2379141.
[27] R. Hille, J. Hall, P. Basu, *Chem. Rev.* **2014**, *114*, 3963-4038.
[28] E. E. Benson, C. P. Kubiak, A. J. Sathrum, J. M. Smieja, *Chem. Soc. Rev.* **2009**, *38*, 89-99.
[29] R. Francke, B. Schille, M. Roemelt, *Chem. Rev.* **2018**, *118*, 4631-4701.
[30] R. Kortlever, J. Shen, K. J. Schouten, F. Calle-Vallejo, M. T. Koper, *J. Phys. Chem-US* **2015**, *6*, 4073-4082.
[31] K. E. Dalle, J. Warnan, J. J. Leung, B. Reuillard, I. S. Karmel, E. Reisner, *Chem. Rev.* **2019**, *119*, 2752-2875.
[32] K. Mori, H. Yamashita, M. Anpo, *RSC Adv.* **2012**, *2*, 3165.
[33] X. Su, X. F. Yang, Y. Huang, B. Liu, T. Zhang, *Acc. Chem. Res.* **2019**, *52*, 656-664.
[34] T. Kong, Y. Jiang, Y. Xiong, *Chem. Soc. Rev.* **2020**, *49*, 6579-6591.
[35] N. Queyriaux, N. Kaeffer, A. Morozan, M. Chavarot-Kerlidou, V. Artero, *J. Photoch. Photobio. A* **2015**, *25*, 90-105.
[36] N. Elgrishi, K. J. Rountree, B. D. McCarthy, E. S. Rountree, T. T. Eisenhart, J. L. Dempsey, *J. Chem. Educ.* **2017**, *95*, 197-206.
[37] A. J. Bard, *Electrochemical methods : fundamentals and applications*, Wiley, **1980**.

[38] E. Hunter, S. Lias, *J. Phys. Chem. Ref. Data* **1998**, *27*, 413-656.
[39] G. L. Gutsev, R. J. Bartlett, R. N. Compton, *J. Chem. Phys.* **1998**, *108*, 6756-6762.
[40] T. D. Märk, E. Hille, *J. Chem. Phys.* **1978**, *69*, 2492.
[41] A. Paparo, J. Okuda, *Coord. Chem. Rev.* **2017**, *334*, 136-149.
[42] M. Aresta, A. Dibenedetto, E. Quaranta, *Springer Berlin Heidelberg* **2016**.
[43] C. Jiang, A. W. Nichols, C. W. Machan, *Dalton Trans.* **2019**, *48*, 9454-9468.
[44] J. M. Saveant, *Chem. Rev.* **2008**, *108*, 2348-2378.
[45] C. W. Lee, K. D. Yang, D. H. Nam, J. H. Jang, N. H. Cho, S. W. Im, K. T. Nam, *Adv. Mater.* **2018**, *30*, 1704-1717.
[46] D. Kim, C. S. Kley, Y. Li, P. Yang, *P. Natl. A. Sci.* **2017**, *114*, 10560-10565.
[47] G. K. Ramesha, J. F. Brennecke, P. V. Kamat, *ACS Catal.* **2014**, *4*, 3249-3254.
[48] M. Boudart, *Chem. Rev.* **1995**, *95*, 661-666.
[49] S. Kozuch, J. M. L. Martin, *ACS Catal.* **2012**, *2*, 2787-2794.
[50] T. Newman J, *Wiley* **2004**, *3rd edn*.
[51] N. Elgrishi, M. B. Chambers, M. Fontecave, *Chem. Sci.* **2015**, *6*, 2522-2531.
[52] A. J. Morris, G. J. Meyer, E. Fujita, *Acc. Chem. Res.* **2009**, *42*, 1983-1994.
[53] C. Costentin, G. Passard, J. M. Saveant, *J. Am. Chem. Soc.* **2015**, *137*, 5461-5467.
[54] D. H. Gibson, *Chem. Rev.* **1996**, *96*, 2063-2096.
[55] X. Yin, J. R. Moss, *Coord. Chem. Rev.* **1999**, *181*, 27-59.
[56] C. Riplinger, M. D. Sampson, A. M. Ritzmann, C. P. Kubiak, E. A. Carter, *J. Am. Chem. Soc.* **2014**, *136*, 16285-16298.
[57] M. Hammouche, D. Lexa, M. Momenteau, J. M. Saveant, *J. Am. Chem. Soc.* **1991**, *113*, 8455-8466.
[58] J. M. Barlow, J. Y. Yang, *ACS Cent. Sci.* **2019**, *5*, 580-588.
[59] H. Ishida, K. Tanaka, T. Tanaka, *Organometallics* **1987**, *6*, 181-186.
[60] I. Bhugun, D. Lexa, J. M. Saveant, *J. Am. Chem. Soc.* **1996**, *118*, 1769-1776.
[61] J. D. Froehlich, C. P. Kubiak, *Inorg. Chem.* **2012**, *51*, 3932-3934.
[62] S. Hammes-Schiffer, A. A. Stuchebrukhov, *Chem. Rev.* **2010**, *110*, 6939-6960.
[63] M. H. V. Huynh, T. J. Meyer, *Chem. Rev.* **2007**, *107*, 5004-5064.
[64] J. M. Mayer, I. J. Rhile, *BBA-Bioenergetics* **2004**, *1655*, 51-58.
[65] Z. Thammavongsy, I. P. Mercer, J. Y. Yang, *Chem. Commun.* **2019**, *55*, 10342-10358.
[66] C. J. Chang, M. C. Y. Chang, N. H. Damrauer, D. G. Nocera, *BBA-Bioenergetics* **2004**, *1655*, 13-28.
[67] J. Klein, G. Knizia, *Angew. Chem. Int. Ed.* **2018**, *57*, 11913-11917.
[68] R. I. Cukier, *J. Phys. Chem. B* **2002**, *106*, 1746-1757.
[69] C. Costentin, S. Drouet, M. Robert, J. M. Saveant, *J. Am. Chem. Soc.* **2012**, *134*, 11235-11242.
[70] J. Bonin, A. Maurin, M. Robert, *Coord. Chem. Rev.* **2017**, *334*, 184-198.
[71] C. Römelt, J. Song, M. Tarrago, J. A. Rees, M. van Gastel, T. Weyhermüller, S. DeBeer, E. Bill, F. Neese, S. Ye, *Inorg. Chem.* **2017**, *56*, 4745-4750.
[72] C. Costentin, G. Passard, M. Robert, J. M. Saveant, *J. Am. Chem. Soc.* **2014**, *136*, 11821-11829.
[73] P. Kang, Z. Chen, M. Brookhart, T. J. Meyer, *Top. Catal.* **2015**, *58*, 30-45.
[74] C. Costentin, J. M. Saveant, C. Tard, *Proc. Natl. Acad. Sci. USA* **2018**, *115*, 9104-9109.
[75] V. Lyaskovskyy, B. de Bruin, *ACS Catal.* **2012**, *2*, 270-279.
[76] J. T. Muckerman, D. E. Polyansky, T. Wada, K. Tanaka, E. Fujita, *Inorg. Chem.* **2008**, *47*, 1787-1802.

[77] C. Costentin, M. Robert, J. M. Saveant, *Acc. Chem. Res.* **2015**, *48*, 2996-3006.
[78] M. L. Clark, K. A. Grice, C. E. Moore, A. L. Rheingold, C. P. Kubiak, *Chem. Sci.* **2014**, *5*, 1894-1900.
[79] F. Franco, C. Cometto, L. Nencini, C. Barolo, F. Sordello, C. Minero, J. Fiedler, M. Robert, R. Gobetto, C. Nervi, *Chem. Eur. J.* **2017**, *23*, 4782-4793.
[80] M. Beley, J. P. Collin, R. Ruppert, J. P. Sauvage, *J. Am. Chem. Soc.* **1986**, *108*, 7461-7467.
[81] M. Sheng, N. Jiang, S. Gustafson, B. You, D. H. Ess, Y. Sun, *Dalton Trans.* **2015**, *44*, 16247-16250.
[82] C. Costentin, G. Passard, M. Robert, J. M. Saveant, *Proc. Natl. Acad. Sci. USA* **2014**, *111*, 14990-14994.
[83] Eva M. Nichols, J. S. Derrick, S. K. Nistanaki, P. T. Smith, C. J. Chang, *Chem. Sci.* **2018**, *9*, 2952-2960.
[84] I. Bhugun, D. Lexa, J. M. Saveant, *J. Am. Chem. Soc.* **1994**, *116*, 5015-5016.
[85] D. C. Lacy, C. C. L. McCrory, J. C. Peters, *Inorg. Chem.* **2014**, *53*, 4980-4988.
[86] M. Zhang, M. El-Roz, H. Frei, J. L. Mendoza-Cortes, M. Head-Gordon, D. C. Lacy, J. C. Peters, *J. Phys. Chem. C* **2015**, *119*, 4645-4654.
[87] H. Ishida, K. Fujiki, T. Ohba, K. Ohkubo, K. Tanaka, T. Terada, T. Tanaka, *Dalton Trans.* **1990**, 2155-2160.
[88] D. L. DuBois, A. Miedaner, R. C. Haltiwanger, *J. Am. Chem. Soc.* **1991**, *113*, 8753-8764.
[89] C. Caix, S. Chardon-Noblat, A. Deronzier, *J. Electroanal. Chem.* **1997**, *434*, 163-170.
[90] B. M. Ceballos, J. Y. Yang, *Organometallics* **2020**, *39*, 1491-1496.
[91] P. Kang, C. Cheng, Z. Chen, C. K. Schauer, T. J. Meyer, M. Brookhart, *J. Am. Chem. Soc.* **2012**, *134*, 5500-5503.
[92] I. Osadchuk, T. Tamm, M. S. G. Ahlquist, *ACS Catal.* **2016**, *6*, 3834-3839.
[93] J. O. Taylor, G. Neri, L. Banerji, A. J. Cowan, F. Hartl, *Inorg. Chem.* **2020**, *59*, 5564-5578.
[94] J. Hawecker, J. M. Lehn, R. Ziessel, *Chem. Commun.* **1984**, 328-330.
[95] N. P. Liyanage, H. A. Dulaney, A. J. Huckaba, J. W. Jurss, J. H. Delcamp, *Inorg. Chem.* **2016**, *55*, 6085-6094.
[96] J. Qiao, Y. Liu, F. Hong, J. Zhang, *Chem. Soc. Rev.* **2014**, *43*, 631-675.
[97] X. Zhou, D. Micheroni, Z. Lin, C. Poon, Z. Li, W. Lin, *ACS Appl. Mater. Inter.* **2016**, *8*, 4192-4198.
[98] D. Gao, R. M. Arán-Ais, H. S. Jeon, B. Roldan Cuenya, *Nat. Catal.* **2019**, *2*, 198-210.
[99] D. Bélanger, J. Pinson, *Chem. Soc. Rev.* **2011**, *40*, 3995-4048.
[100] K. Torbensen, B. Boudy, D. Joulié, N. von Wolff, M. Robert, *Curr. Opin. Electrochem.* **2020**, *24*, 49-55.
[101] T. R. O'Toole, L. D. Margerum, T. D. Westmoreland, W. J. Vining, R. W. Murray, T. J. Meyer, *Chem. Commun.* **1985**, 1416.
[102] J. Shen, R. Kortlever, R. Kas, Y. Y. Birdja, O. Diaz-Morales, Y. Kwon, I. Ledezma-Yanez, K. J. P. Schouten, G. Mul, M. T. M. Koper, *Nat. Commun.* **2015**, *6*, 8177-8177.
[103] M. García, M. J. Aguirre, G. Canzi, C. P. Kubiak, M. Ohlbaum, M. Isaacs, *Electrochim. Acta* **2014**, *115*, 146-154.
[104] F. Li, B. Zhang, X. Li, Y. Jiang, L. Chen, Y. Li, L. Sun, *Angew. Chem. Int. Ed. Engl.* **2011**, *50*, 12276-12279.
[105] B. Reuillard, K. H. Ly, T. E. Rosser, M. F. Kuehnel, I. Zebger, E. Reisner, *J. Am. Chem. Soc.* **2017**, *139*, 14425-14435.
[106] A. Zhanaidarova, S. C. Jones, E. Despagnet-Ayoub, B. R. Pimentel, C. P. Kubiak, *J. Am. Chem. Soc.* **2019**, *141*, 17270-17277.

[107] M. L. Clark, P. L. Cheung, M. Lessio, E. A. Carter, C. P. Kubiak, *ACS Catal.* **2018**, *8*, 2021-2029.
[108] J. Hawecker, J. M. Lehn, R. Ziessel, *Helv. Chim. Acta* **1986**, *69*, 1990-2012.
[109] G. F. Manbeck, J. T. Muckerman, D. J. Szalda, Y. Himeda, E. Fujita, *Front. Chem.* **2015**, *119*, 7457-7466.
[110] J. M. Smieja, C. P. Kubiak, *Inorg. Chem.* **2010**, *49*, 9283-9289.
[111] S. Ramakrishnan, C. E. D. Chidsey, *Inorg. Chem.* **2017**, *56*, 8326-8333.
[112] S. Gonell, M. D. Massey, I. P. Moseley, C. K. Schauer, J. T. Muckerman, A. J. M. Miller, *J. Am. Chem. Soc.* **2019**, *141*, 6658-6671.
[113] L. Rotundo, E. Azzi, A. Deagostino, C. Garino, L. Nencini, E. Priola, P. Quagliotto, R. Rocca, R. Gobetto, C. Nervi, *Front. Chem.* **2019**, *7*.
[114] S. Dey, T. K. Todorova, M. Fontecave, V. Mougel, *Angew. Chem. Int. Ed.* **2020**, *59*, 15726-15733.
[115] D. J. Stufkens, *Coord. Chem. Rev.* **1990**, *104*, 39-112.
[116] I. R. Farrell, F. Hartl, S. Záliš, T. Mahabiersing, J. A. Vlček, *Dalton Trans.* **2000**, 4323-4331.
[117] Z. W. Hieber and F. Mühlbauer, *Anorg. Chem.* **1935**, *221*.
[118] M. H. B. Stiddard, *J. Chem. Soc.* **1962**, *0*, 4712-4715.
[119] J. O. Connor, C., *J. Organomet. Chem.* **1984**, *277*, 277-284.
[120] J. O. Connor, C., *J. Organomet. Chem.* **1983**, *249*, 165-174.
[121] A. Vlček, F. W. Grevels, T. L. Snoeck, D. J. Stufkens, *Inorg. Chim. Acta* **1998**, *278*, 83-90.
[122] L. Yang, J. K. Feng, A. M. Ren, *Synth. Met.* **2005**, *152*, 265-268.
[123] S. Ernst, W. Kaim, *J. Am. Chem. Soc.* **1986**, *108*, 3578-3586.
[124] J. Tory, B. Setterfield-Price, R. A. W. Dryfe, F. Hartl, *ChemElectroChem* **2015**, *2*, 213-217.
[125] R. Johnson, H. Madhani, J. P. Bullock, *Inorg. Chim. Acta* **2007**, *360*, 3414-3423.
[126] J. O. Taylor, R. D. Leavey, F. Hartl, *ChemElectroChem* **2018**, *5*, 3155-3161.
[127] D. Sieh, D. C. Lacy, J. C. Peters, C. P. Kubiak, *Chem. Eur. J.* **2015**, *21*, 8497-8503.
[128] J. M. Smieja, M. D. Sampson, K. A. Grice, E. E. Benson, J. D. Froehlich, C. P. Kubiak, *Inorg. Chem.* **2013**, *52*, 2484-2491.
[129] M. Bourrez, F. Molton, S. Chardon-Noblat, A. Deronzier, *Angew. Chem. Int. Ed. Engl.* **2011**, *50*, 9903-9906.
[130] F. Franco, C. Cometto, F. Sordello, C. Minero, L. Nencini, J. Fiedler, R. Gobetto, C. Nervi, *ChemElectroChem* **2015**, *2*, 1372-1379.
[131] J. O. Taylor, F. L. P. Veenstra, A. M. Chippindale, M. J. Calhorda, F. Hartl, *Organometallics* **2019**, *38*, 1372-1390.
[132] S. L. Hooe, J. M. Dressel, D. A. Dickie, C. W. Machan, *ACS Catal.* **2020**, *10*, 1146-1151.
[133] U. Ulmer, T. Dingle, P. N. Duchesne, R. H. Morris, A. Tavasoli, T. Wood, G. A. Ozin, *Nat. Commun.* **2019**, *10*, 3169.
[134] X. Sala, A. Llobet, *Eur. J. Inorg. Chem.* **2019**, *2019*, 2017-2019.
[135] S. Wieland, K. B. Reddy, R. Van Eldik, *Organometallics* **1990**, *9*, 1802-1806.
[136] D. M. Manuta, A. J. Lees, *Inorg. Chem.* **1986**, *25*, 1354-1359.
[137] S. Pugliese, N. T. Huan, J. Forte, D. Grammatico, S. Zanna, B. L. Su, Y. Li, M. Fontecave, *ChemSusChem* **2020**, *13*, 6449-6456.
[138] Y. Liu, X. Fan, A. Nayak, Y. Wang, B. Shan, X. Quan, T. J. Meyer, *Proc. Natl. Acad. Sci. USA* **2019**, *116*, 26353-26358.

Chapter II

Synthesis, characterization and reactivity towards CO_2 of $[Mo(CO)_4(bpy\text{-}(R)_2)]$ complexes

I. Introduction

Modulation of the electronic density over a catalytically-active system can affect the efficiency and selectivity of the complex. Among several strategies, the attachment of electro-donating or electro-attracting groups to the ligand framework has been extensively used for molecular metallic complexes.[1] Typically, the position or the nature of the substituent on the ligands are varied to modulate the catalytic properties. For example in the CO_2 chemistry, Taylor *et al*.[2] reported the enhanced activity of [Re(X,X´-bpy)(CO)$_3$Cl] (X = X' = 3,4,6) complexes *vs.* carbon dioxide, thanks to the modification of the bipyridine moiety with substituent groups in different positions. Another example was provided by Rotundo *et al*., who studied the electronic influence of several substituent groups coordinated in the ortho position for both [*fac*-M(bpy-(R)$_2$(CO)$_3$Cl] systems (M = Re and Mn).[3]

These strategies have also been explored for few group 6 diimine tetracarbonyl complexes, as mentioned in Chapter I. The Figure II.1 displays one example of a study performed on Mo and W substituted bipyridine complexes.[4, 5] The catalytic behavior of these complexes was shown to depend on the stability of the anionic species formed during the diimine-based reduction processes. In consequence, the study of the electronic effect provided by electron-withdrawing groups (EWG) and electron-donating groups (EDG) is of high interest for the enhancement of catalytic properties.

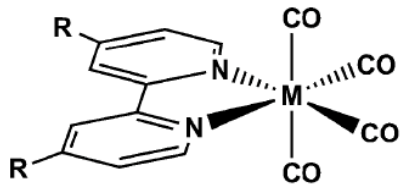

(**1**) M = Mo, R = H
(**2**) M = W, R = H
(**3**) M = Mo, R = *t*Bu
(**4**) M = W, R = *t*Bu

Figure II.1. Schematic representation of [M(CO)$_4$(bpy-R$_2$)] (M = W, Mo; R=H, ^{t}Bu) systems. Reproduced from Ref. [6].

Taking into consideration all the precedent results, our purpose has been to study a series of [Mo(CO)$_4$(bpy-4,4´-(**R**)$_2$)] systems as molecular catalysts towards CO_2 electroreduction, considering functionalized bipyridine ligands as redox-non innocent ligands (Figure II.2).

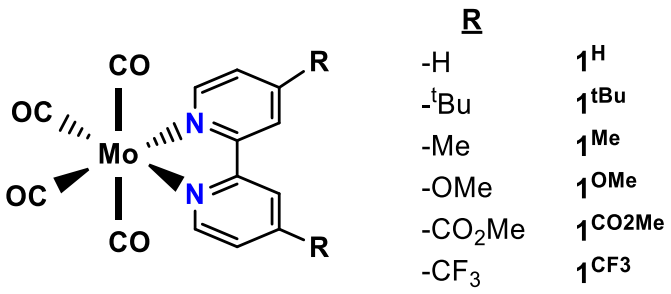

Figure II.2. General structure of $[Mo(CO)_4(bpy\text{-}(\mathbf{R})_2)]$ derivatives studied in the present work.

While the electrochemical properties of some of the systems that will be discussed in this chapter have been already reported,[7] no CO_2 electroreduction activity has been studied whatsoever except for complexes $\mathbf{1^H}$, $\mathbf{1^{tBu}}$ and $\mathbf{1^{Me}}$. The use of spectroelectrochemical techniques, supported with DFT calculations, has allowed us to correlate the electronic character of the **R** substituents with the spectroscopic and redox properties of the corresponding complexes.

II. Synthesis and characterization of $[Mo(CO)_4(bpy\text{-}(\mathbf{R})_2]$ systems

The syntheses of $[Mo(CO)_4(bpy\text{-}(\mathbf{R})_2)]$ (**R** = **H**, **^{t}Bu**, **Me**, **OMe**, **CO_2Me**, **CF_3**) complexes were carried out according to two different routes. Stiddard's procedure was used for $\mathbf{1^H}$ and $\mathbf{1^{tBu}}$ synthesis.[8] A solution of $Mo(CO)_6$ as metallic source with a small excess of the bipyridine was refluxed overnight in toluene, achieving a 81% and 70% yield, respectively (Scheme II.1). The product obtained was filtered and washed with cold toluene and petroleum ether to obtain a red crystalline solid.

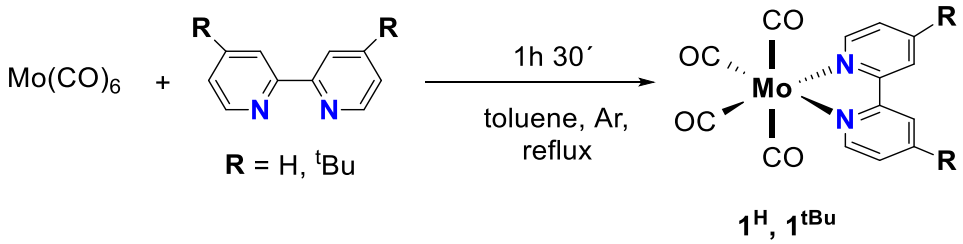

Scheme II.1. Synthetic pathway for $\mathbf{1^H}$ and $\mathbf{1^{tBu}}$.

The second synthetic route[9] used [$Mo(CO)_4$(nbd)] (nbd = norbornadiene) as metallic source (Scheme II.2). The latter was synthetised by reaction of [$Mo(CO)_6$] with an excess of norbornadiene in petroleum ether for 2 days in an inert atmosphere, giving a brown powder after extraction with boiling light petroleum (40% yield).[10] Hence, preparation of $\mathbf{1^{OMe}}$, $\mathbf{1^{Me}}$, $\mathbf{1^{CO2Me}}$ and $\mathbf{1^{CF3}}$ was performed by reaction of one equivalent of [$Mo(CO)_4$(nbd)] with a slight excess of the selected functionalized bipyridine in THF for 16 h at room temperature, to obtain orange to red solids with notable yields after recrystallization in CH_2Cl_2/petroleum ether. All the complexes were characterized via ^{1}H RMN and IR spectroscopic techniques (see Experimental part for further details).

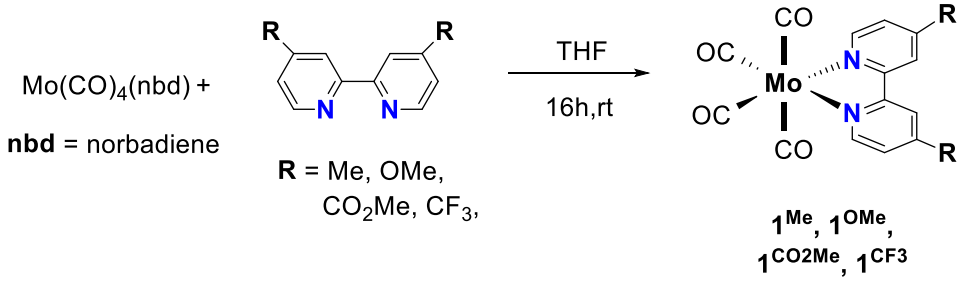

Scheme II.2. Synthetic pathway for $\mathbf{1^{Me}}$, $\mathbf{1^{OMe}}$, $\mathbf{1^{CO2Me}}$ and $\mathbf{1^{CF3}}$ complexes.

All [$Mo(CO)_4$(bpy-(**R**)$_2$)] complexes present a distorted octahedral geometry with slightly longer Mo-C(O) equatorial bonds than axial ones.[9] The IR wavenumber values of the carbonyl bands (ν_{CO}) of the [$Mo(CO)_4$(bpy-(**R**)$_2$)] complexes are gathered in Table II.1, correlated to A_1, B_1 and B_2 vibrational CO modes (Figure II.3). The positions of ν_{CO} bands are very slightly influenced by the nature of the substituent groups in the bipyridine ring. Electron-withdrawing substituent groups may induce a positive shift of the ν_{CO} bands (*vs.* $\mathbf{1^H}$) due to a smaller π-retrodonation contribution to the CO ligands from the metal center. Hence, the inverse effect is observed for electron-donating derivatives.

Table II.1. IR wavenumber values of the carbonyl bands (ν_{CO} / cm^{-1}) of [Mo(CO)$_4$(bpy-(**R**)$_2$)] complexes in THF and MeCN.

R	THF	MeCN
H	1840, 1882, 1890, 2012	1831, 1876, 1904, 2012
^{t}Bu	1846, 1889, 1908, 2015	1829, 1874, 1900, 2015
Me	1847, 1890, 1908, 2013	1829, 1874, 1901, 2015
OMe	1832, 1872, 1895, 2011	1827, 1870, 1899, 2015
CO_2Me	1845, 1889, 1910, 2013	1839, 1885, 1911, 2018
CF_3	1846, 1891, 1911, 2016	1838, 1885, 1911, 2017

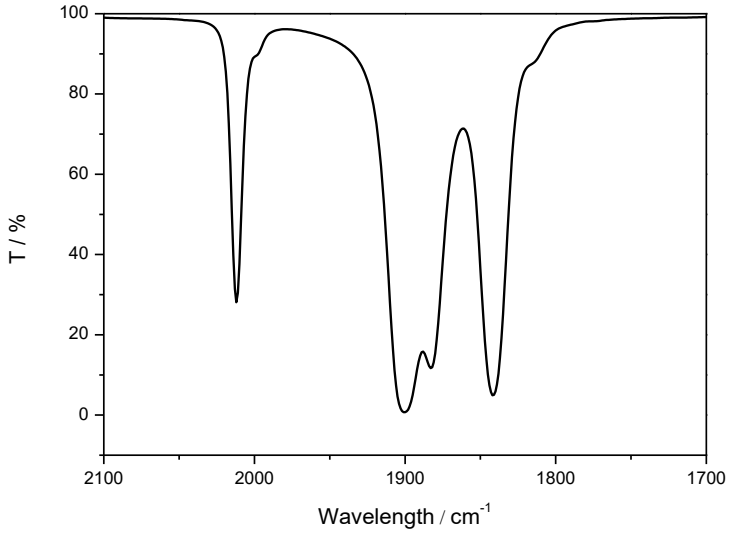

Figure II.3. Infrared spectrum of **1^H** in MeCN.

UV-vis absorption spectra of [Mo(CO)$_4$(bpy-(**R**)$_2$)] showed intense MLCT transitions in the 350-600 nm region. These transitions occur from d_{xz} metal orbitals to π* orbitals of the bipyridine / axial CO moieties, making these complexes very colorful in solution.[11, 12] The existence of low-lying MLCT transitions is confirmed by the influence of the nature of the substituent groups in the bipyridine moiety. The presence of electron donor substituents in [Mo(CO)$_4$(bpy-(**R**)$_2$)] bipyridine ring shifts

these bands to higher energies, while the inverse effect is observed for electron-withdrawing groups (Figure II.4).[13]

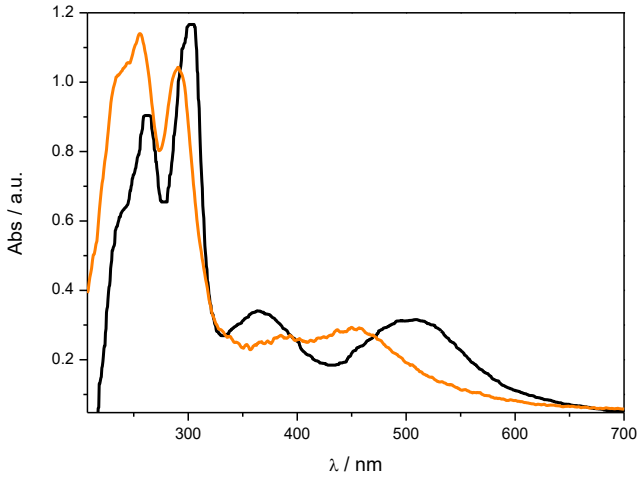

Figure II.4. UV-vis absorption spectra of **1^{H}** (orange) and **1^{CO2Me}** (black) in MeCN.

Theoretical calculations confirmed the nature of the main MLCT transition observed for [Mo(CO)$_4$(bpy-(**R**)$_2$)] complexes. The main contributor to this transition is the excitation of an electron from the b^1 HOMO-2, centered in the metal center with small contributions of axial CO and bipyridine ligands, to the b^1 LUMO orbital, with the latter displays an almost exclusive π* diimine character (see for comparison MO diagram of [Cr(CO)$_4$(bpy)], Figure II.5).[14]

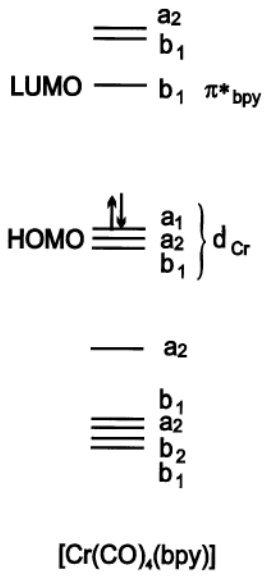

Figure II.5. Molecular orbital diagram of [Cr(CO)$_4$(bpy)], indicating the nature of the molecular orbitals involved in the observed MLCT transitions. Reproduced from Ref. [14].

The absorption maxima (λ_{max} / nm) of the [Mo(CO)$_4$(bpy-(**R**)$_2$)] complexes in THF and MeCN are gathered in Table II.2. A correlation between a more energetic MLCT transition with an increase of the polarity of the solvent was observed.[15]

Table II.2. Absorption maxima (λ_{max} / nm) of the MLCT band of [Mo(CO)$_4$(bpy-(**R**)$_2$)] in THF and MeCN.

R	THF	MeCN
H	470	452
^{t}Bu	468	449
Me	457	448
OMe	450	451
CO_2Me	529	502
CF_3	528	504

Hammett plots allowed us to visualize the influence of the electronic effect provided by the substituent groups present in the bipyridine ring.[16] Plotting both ν_{CO} and λ_{max} of [Mo(CO)$_4$(bpy-(**R**)$_2$)] *vs.* Hammett values corroborated the effect caused by a change of the electronic density. An excess of electronic density in the bipyridine ring leads to lower ν_{CO} wavenumbers together with a decrease of MLCT λ_{max} values. The reverse effect is obtained with electron-withdrawing groups.

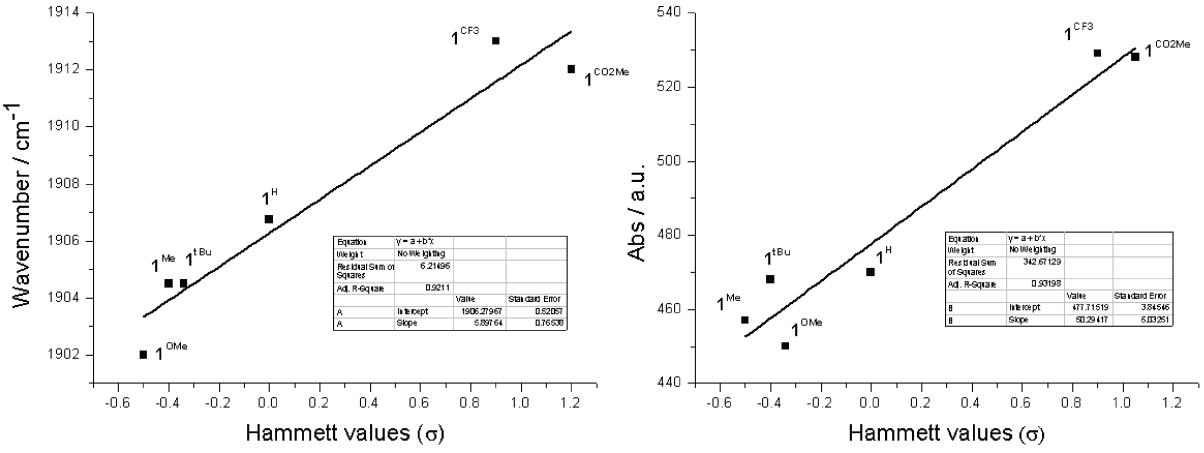

Figure II.6. Hammett plots of ν_{CO} (left) and λ_{max} (right) values versus σ_p Hammett parameters of the **R** groups in [Mo(CO)$_4$(bpy-(**R**)$_2$)] complexes.

III. Electrochemical studies of [Mo(CO)$_4$(bpy-(**R**)$_2$] systems under argon

Cyclic voltammetry (CV) experiments of [Mo(CO)$_4$(bpy-(**R**)$_2$)] complexes have been performed at room temperature in THF, a poor coordinating solvent, and in MeCN, a coordinating solvent, with 0.1 M NBu_4PF_6 as supporting electrolyte. A boron-diamond doped (BDD) or glassy carbon (GC) working electrode was used in a three-electrode configuration under an inert atmosphere (argon). All potentials are given against Fc^+/Fc redox potential. However, the choice of MeCN or THF as a solvent had no significant effects on the [Mo(CO)$_4$(bpy-(**R**)$_2$)] reduction potentials recorded during CV experiments.

The electrochemical studies of $\mathbf{1^H}$, $\mathbf{1^{tBu}}$ and $\mathbf{1^{Me}}$ have already been reported.[4-6] For these three complexes, a first ligand-localized reversible reduction was detected at ca. -1.9 V *vs.* Fc^+/Fc in THF and MeCN. A second irreversible reduction was found in the -2.4 to -2.7 V region, indicating that

the [Mo(CO)$_4$(bpy-(**R**)$_2$)]$^{2-}$ intermediate is not stable on the CV timescale. The [Mo(CO)$_4$(bpy-(**R**)$_2$)]$^{2-}$ complexes decay rapidly into other species depending on the nature of the solvent. Spectroelectrochemical techniques confirmed the formation of [Mo(CO)$_3$(bpy-(**R**)$_2$)]$^{2-}$ species in THF while [Mo(CO)$_4$(H$^+$-bpy-(**R**)$_2$)]$^-$ remains as major product in MeCN due to [Mo(CO)$_3$(bpy-(**R**)$_2$)]$^{2-}$ protonation by interaction with the solvent / large moisture content in the solvent with a rapid recoordination of a CO molecule (Scheme II.3). [5]

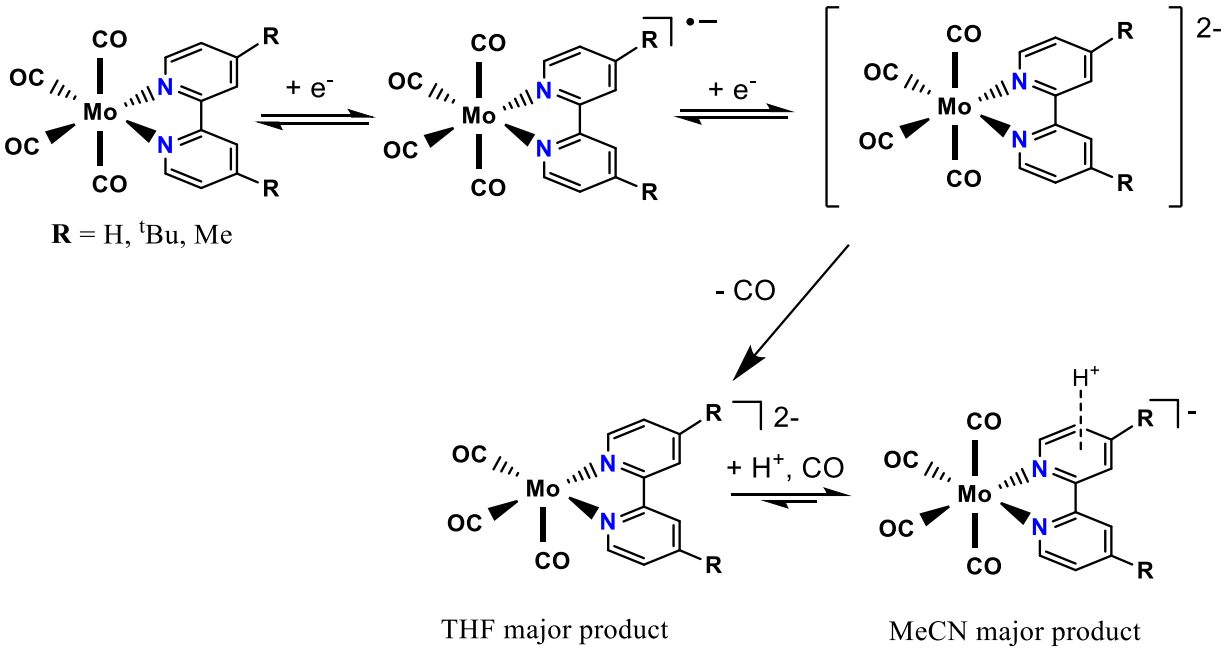

Scheme II.3. Reduction processes of **1^{H}**, **1^{tBu}** and **1^{Me}** systems in MeCN and THF.

Electrochemical characterization of the novel complex **1^{OMe}** (Figure II.7) showed a very similar redox signature as other electron-donating derivatives such as **1^{tBu}** and **1^{Me}**. Scan rate studies confirmed that the nature of the redox processes reported in Figure II.7 does not diverge with similar [Mo(CO)$_4$(bpy-(**R**)$_2$)] systems (Scheme II.3).[14]

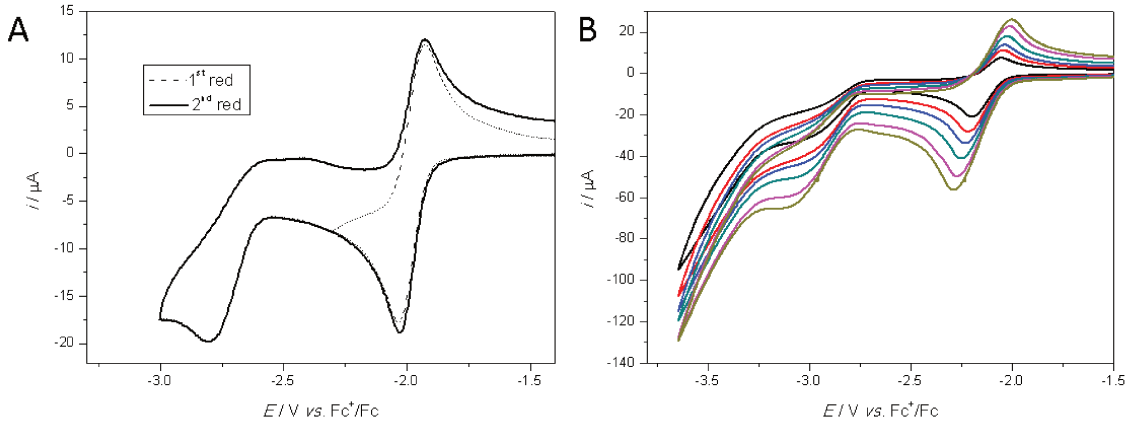

Figure II.7. CVs of the **1**$^{\mathbf{OMe}}$ complex for A) v = 0.1 V s^{-1} and B) 0.1 V s^{-1} < v < 5 V s^{-1} in THF / 0.1 M NBu_4PF_6 under Ar. Conditions: 1 mM of complex, BDD working electrode.

The Randles-Sevcik equation (equation II.1) was used to confirmed the diffusion-controlled and reversible nature of [Mo(CO)$_4$(bpy-(**OMe**)$_2$)] first reduction process from variation of the peak current i_p as a function of the scan rate v.

$$i_p = 0.446n^{3/2}FACD^{1/2}\left[\frac{F}{RT}\right]^{1/2}\nu^{1/2} \qquad \text{(II.1)}$$

[n = number of electrons, F = Faraday constant (C mol^{-1}), C = molar concentration (mol cm^{-3}), D = diffusion coefficient (cm^2 s^{-1}), R = universal gas constant (J K^{-1} mol^{-1}), T = temperature (K), v = scan rate (V s^{-1})]

Interestingly, a different voltammetric response was found for **1**$^{\mathbf{CO2Me}}$ and **1**$^{\mathbf{CF3}}$ complexes. Both systems bear an electron-withdrawing substituent group coordinated to the bipyridine ring in the ortho position. In the case of **1**$^{\mathbf{CO2Me}}$, a positive shift (*vs*. **1**$^{\mathbf{H}}$) of about 400 mV was detected for the first two reduction processes. A third reduction process was found at −2.70 V *vs*. Fc$^+$/Fc. The first reduction process at −1.54 V for **1**$^{\mathbf{CO2Me}}$ can be correlated to **1**$^{\mathbf{H}}$ first reduction process. However, both **1**$^{\mathbf{CO2Me}}$ second and third reduction processes displayed a loss of reversibility when MeCN was used as solvent instead of THF. For comparison, redox behavior of free ligand bpy-(CO_2Me)$_2$ showed two reversible systems in reduction at potential values close to those obtained for the

second and third reduction of complex **1**^{CO2Me} (Figure II.8). However, these comparative curves strongly suggest no ligand unbinding upon reduction for this complex.

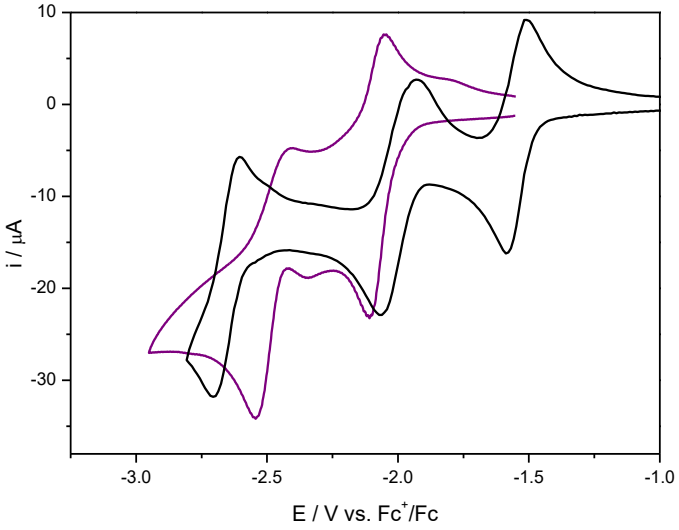

Figure II.8. CVs of A) **1**^{CO2Me} (black) and B) bpy-$(CO_2Me)_2$ ligand (purple) in THF / 0.1 M NBu_4PF_6 under Ar. Conditions: 1 mM of complex, BDD working electrode, v = 0.1 V s^{-1}.

As compared to **1**^{H}, the **1**^{CF3} complex displayed a 450 mV positive shift of the reduction potential values in a similar way as **1**^{CO2Me}**.** Even though, going to more negative potentials after the first reversible reduction process at $E_{1/2}$ = −1.55 V *vs*. Fc^+/Fc showed several irreversible peaks, differing from **1**^{CO2Me} redox behavior (Figure II.9).

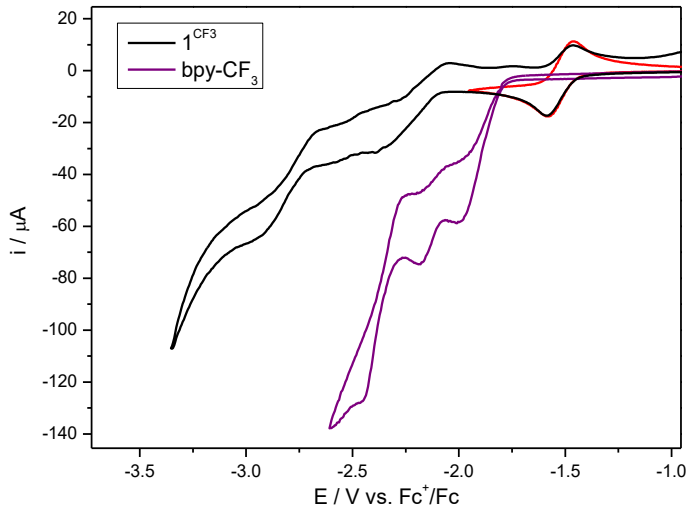

Figure II.9. CVs of A) **6-CF$_3$** (black) and B) bpy-(CF$_3$)$_2$ ligand (purple) in THF / 0.1 M NBu$_4$PF$_6$ under Ar. The red curve corresponds to the CV for the first reduction process only for the complex. Conditions: 1 mM of complex, BDD working electrode, v = 0.1 V s^{-1}.

Table II.3 gathers [Mo(CO)$_4$(bpy-(**R**)$_2$)] redox potential values in THF used to build Figure II.10. The potential values of the 3rd reduction process observed for **1^{CO2Me}** and **1^{CF3}** are also listed even if the origin of these reduction processes remains unknown.

Table II.3. Reduction half-wave potential of [Mo(CO)$_4$(bpy-(**R**)$_2$)] systems *vs*. Fc$^+$/Fc in THF.

$E_{1/2}$ *vs*. Fc$^+$/Fc	1st red	2nd red	3rd red
1^{H}	-1.90	-2.50[a]	-
1^{tBu}	-2.06	-2.70[a]	-
1^{Me}	-2.05	-2.65[a]	-
1^{OMe}	-2.06	-2.65[a]	-
1^{CO2Me}	-1.54	-1.98	-2.65
1^{CF3}	-1.55	-2.05[a]	-2.94[a]

[a] Irreversible cathodic peak

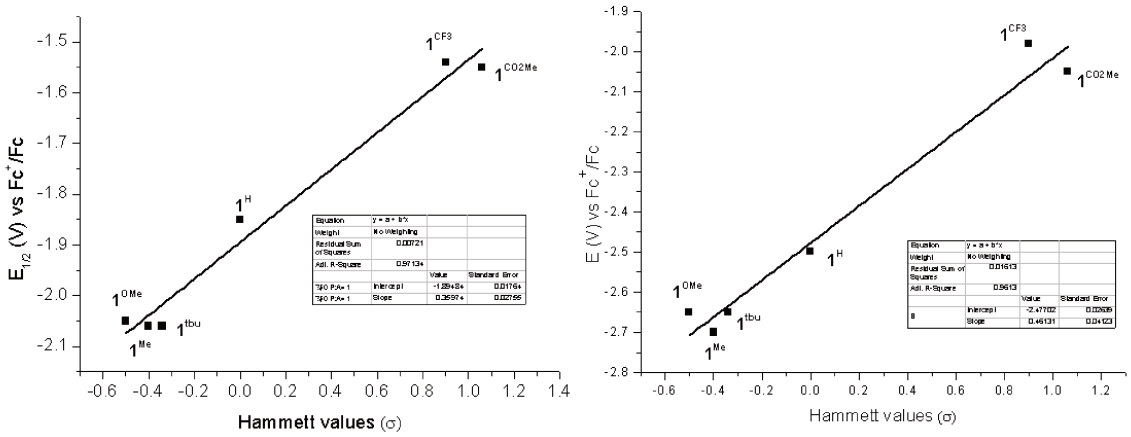

Figure II.10. Hammett plots of potential values for first (left) and second (right) reduction processes versus σ_p Hammett parameters of the **R** groups in [Mo(CO)$_4$(bpy-(**R**)$_2$)] complexes.

In conclusion, the presence of electron-donating groups in the bipyridine moiety of [Mo(CO)$_4$(bpy-(**R**)$_2$)] systems such as $\mathbf{1^{Me}}$ and $\mathbf{1^{OMe}}$ systems causes a negative shift of the redox potentials. However, redox behavior of $\mathbf{1^{CO2Me}}$ and $\mathbf{1^{CF3}}$ differed significantly from that of $\mathbf{1^{H}}$, especially after the first reduction process. As a result, spectroelectrochemical experiments became necessary to understand the redox behavior of $\mathbf{1^{CO2Me}}$ and $\mathbf{1^{CF3}}$ complexes.

IV. Spectroelectrochemical studies of [Mo(CO)$_4$(bpy-(**R**)$_2$)] systems under Ar

UV-Vis and IR-SEC setups were used to analyze the species generated under argon during the reduction of [Mo(CO)$_4$(bpy-(**R**)$_2$)] species.

IV.1. UV-Vis spectroelectrochemical studies under Ar

Absorption spectra between 200 and 800 nm of [Mo(CO)$_4$(bpy-(**R**)$_2$)] were recorded in MeCN and THF under thin layer conditions at room temperature (0.2 mm optical path). A modified three-electrode cell coupled with an UV-Vis probe was used, as described in appendix.

UV-vis spectra in dry THF of **1^H** in its initial (neutral) state and after the first reduction are presented in Figure II.11. An absorption band was detected at λ_{max} = 365 nm which can be ascribed to a π-π* transition for the bipyridine moiety, a feature related to mono-reduced radical bipyridine species.[4] Two absorption bands were also detected at 470 to 532 nm, which correspond to MLCT transitions [4]

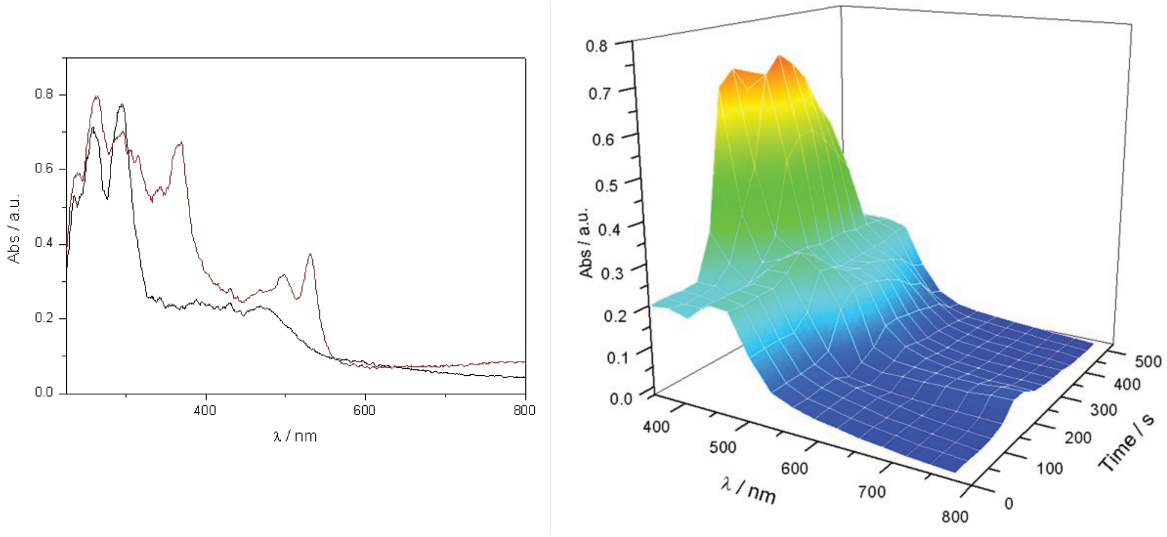

Figure II.11. Absorption spectra of mono-reduced (red) and neutral (black) species of complex **1^H** upon spectroelectrochemical experiments in THF / NBu_4PF_6 0.1 M (left) with its corresponding 3D monitoring graph (right). Conditions: 1 mM of complex, BDD (WE), thin layer condition, 0.2 mm optical path, under Ar.

For the other complexes, absorption spectra of mono-reduced species in THF displayed similar features as for $\mathbf{1}^{H}$ (Table II.4). Complexes $\mathbf{1}^{OMe}$ and $\mathbf{1}^{CO2Me}$ showed less intense MLCT bands compared to electron-richer derivatives such as $\mathbf{1}^{tBu}$ (Figure II.12). An additional weak absorption band at 795 nm was observed for $\mathbf{1}^{CO2Me}$, analogously to the band found at 760 nm for the corresponding mono-reduced ligand bpy-(CO_2Me)$_2$. The same experiments conducted in MeCN showed no significant change compared to THF, except for the electron-withdrawing groups $\mathbf{1}^{CO2Me}$ and $\mathbf{1}^{CF3}$ in the visible region (Table II.4).

Table II.4. UV-vis spectroscopic data of mono-reduced [Mo(CO)$_4$(bpy-(**R**)$_2$)] complexes in THF and MeCN.

R	THF	MeCN
H	365, 470, 532	367, 495, 533
^{t}Bu	366, 503, 536	363, 496, 536
Me	372, 509, 548	364, 482, 522
OMe	359, 485, 518	363, 487, 521
CO_2Me	377, 502, 538, 795	372, 606
CF_3	369, 493, 526	348, 635, 697

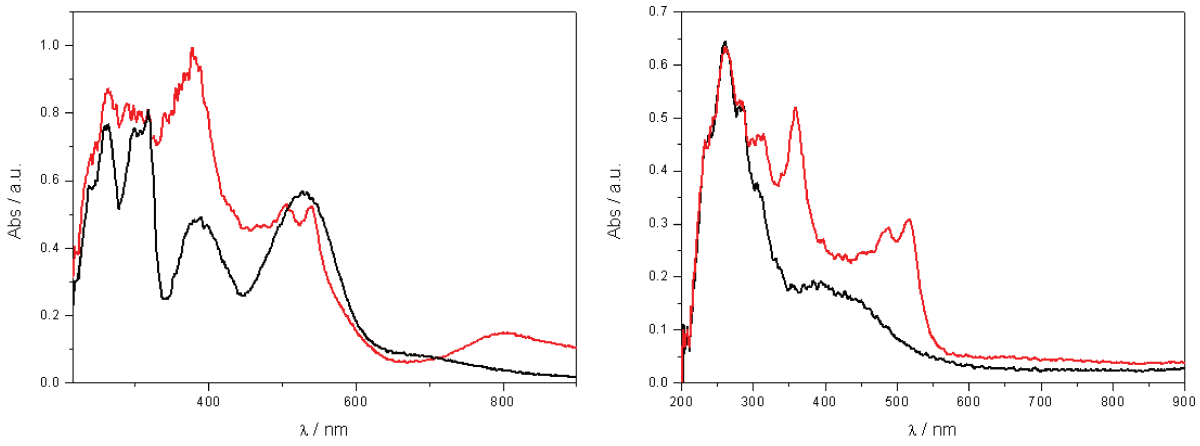

Figure II.12. Absorption spectra of mono-reduced (red) and neutral (black) species of complex $\mathbf{1}^{CO2Me}$ and $\mathbf{1}^{OMe}$ (right) upon spectroelectrochemical experiments in THF / NBu_4PF_6 0.1 M. Conditions: 1 mM of complex, BDD (WE), thin layer condition, 0.2 mm optical path, under Ar.

UV-Vis spectroelectrochemistry was then carried out for investigating the second reduction process under argon. As displayed in Scheme II.3, reduction of the $[Mo(CO)_4(bpy\text{-}(\mathbf{R})_2)]^{\bullet -}$ radical species may promote the formation of unstable bis-reduced species $[Mo(CO)_4(bpy\text{-}(\mathbf{R})_2)]^{2-}$. Consequently, a chemical transformation may occur depending on the solvent choice. Indeed, $[Mo(CO)_3(bpy\text{-}(\mathbf{R})_2)]^{2-}$ formation by loss of one axial CO ligand should be favored with non-protic solvents, such as THF. However, protonation of $[Mo(CO)_4(bpy\text{-}(\mathbf{R})_2)]^{2-}$ leading to $[Mo(CO)_4(H^+\text{-}bpy\text{-}(\mathbf{R})_2)]^-$ species should be promoted in more protic solvents, such as MeCN.[5]

As shown in Figure II.13 and Table II.5, the UV-vis spectrum of the bis-reduced species of $\mathbf{1^H}$ in dry THF displayed absorption bands at 407, 591 and 642 nm (blue curve). Although the assignment of these bands need the full support of IR-SEC and DFT studies, it likely corresponds to the $[Mo(CO)_3(bpy\text{-}(\mathbf{H})_2)]^{2-}$ species in agreement with literature data.[5] The absorption spectra of the same complex in MeCN presented noticeable differences, especially in the 500 nm region (green curve, Figure II.14 and Table II.6). Accordingly,[5] double reduction of $\mathbf{1^H}$ in this solvent leads to the formation of $[Mo(CO)_4(H^+\text{-}bpy\text{-}(\mathbf{H})_2)]^-$ which might be in equilibrium with $[Mo(CO)_3(bpy\text{-}(\mathbf{H})_2)]^{2-}$. The same effect was also obtained by working with "wet" THF (outside the glove or by addition of aliquots of water to dry THF), emphasizing the possible role of water in the equilibria between both bis-reduced species.

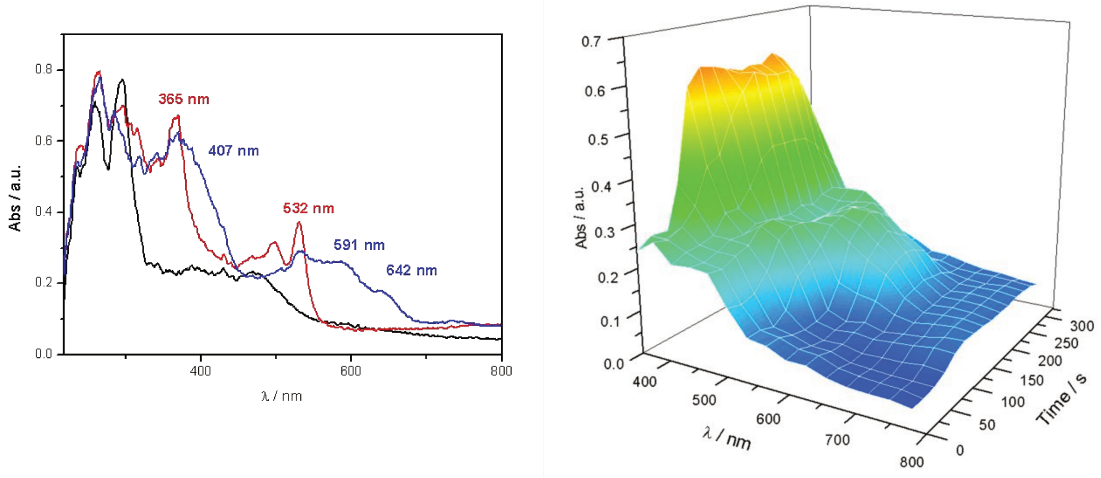

Figure II.13. Absorption spectra of bis-reduced (blue), mono-reduced (red) and neutral (black) species of complex $\mathbf{1^H}$ in THF / NBu_4PF_6 0.1 M (left) with its corresponding 3D monitoring graph (right). Conditions: 1 mM of complex, 0.1 M NBu_4PF_6, BDD (WE), thin layer condition, 0.2 mm optical path, under Ar.

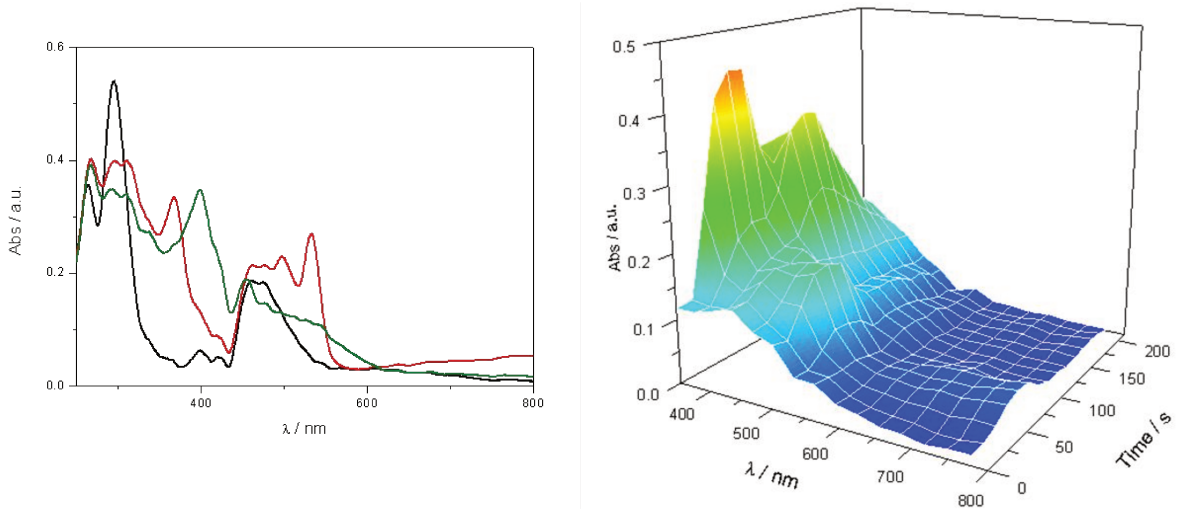

Figure II.14. Absorption spectra of bis-reduced (green), mono-reduced (red) and neutral (black) species of complex **1^{H}** in MeCN / NBu_4PF_6 0.1 M (left) with its corresponding 3D monitoring graph (right). Conditions: 1 mM of complex, 0.1 M NBu_4PF_6, BDD (WE), thin layer condition, 0.2 mm optical path, under Ar.

Table II.5. UV-Vis spectroscopic data for bis-reduced species of [Mo(CO)$_4$(bpy-(**R**)$_2$)] complexes in THF.

R	λ (nm) / MLCT
H	407, 591, 642
^{t}Bu	399, 583, 620
Me	393, 589, 625
OMe	383, 449
CO_2Me	456, 582, 803
CF_3	400, 449, 572

Table II.6. UV-Vis spectroscopic data for bis-reduced species of [Mo(CO)$_4$(bpy-(**R**)$_2$)] complexes in MeCN.

R	λ (nm) / MLCT
H	391, 575
^{t}Bu	390, 578
Me	396, 589
OMe	379, 436
CO_2Me	390, 585
CF_3	413, 578

For [Mo(CO)$_4$(bpy-(**R**)$_2$)] (**R** = Me, ^{t}Bu) complexes, the absorption maxima were similar to those obtained for **1^H** in THF and MeCN (Tables II.5 and II.6), demonstrating that the electron-donating substituents lead to the same bis-reduced species as **1^H**, i.e. [Mo(CO)$_3$(bpy-(**Me**)$_2$)]$^{2-}$ and [Mo(CO)$_3$(bpy-(**^{t}Bu**)$_2$)]$^{2-}$ in THF, as well as [Mo(CO)$_4$(H$^+$-bpy-(**Me**)$_2$)]$^-$ and [Mo(CO)$_4$(H$^+$-bpy-(**^{t}Bu**)$_2$)]$^-$ in MeCN.

As shown in Figure II.15 and Table II.6, double reduction of the complex **1^{OMe}** in MeCN showed the appearance of two main absorption bands at 379 nm and 436 nm, with a shoulder at 500 nm. A similar pattern was detected in THF (Table II.5).

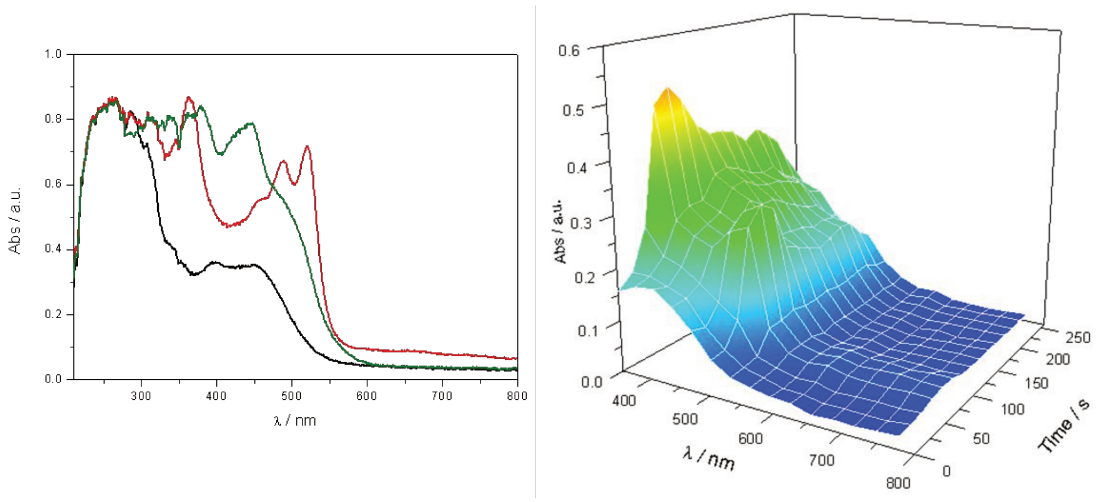

Figure II.15. Absorption spectra of bis-reduced (green), mono-reduced (red) and neutral (black) forms of complex $\mathbf{1}^{\mathbf{OMe}}$ in MeCN / NBu_4PF_6 0.1 M (left) with its corresponding 3D monitoring graph (right). Conditions: 1 mM of complex, 0.1 M NBu_4PF_6, BDD (WE), thin layer condition, 0.2 mm optical path, under Ar.

On one hand, the UV-vis signature of $\mathbf{1}^{\mathbf{CO2Me}}$ in THF was similar to other [$Mo(CO)_4$(bpy-(**R**)$_2$)] complexes (**R** = H, Me, ^{t}Bu) (Table II.5), although absorption bands were broad and not well-defined (Figure II.16.A). However, the well-resolved band at 795 nm detected at the first reduction process was found to be more intense when reaching the second reduction. No novel species were found in absorption spectra at the 3rd reduction potential, but an increase of the bands already present.

On the other hand, the UV-Vis spectroelectrochemical signature of $\mathbf{1}^{\mathbf{CF3}}$ in THF (Figure II.16.B, Table II.5) was similar to that of $\mathbf{1}^{\mathbf{CO2Me}}$, except that no characteristic band was detected at 800 nm. Further studies with IR-spectroelectrochemical techniques provided an insight of the species formed (see below).

As for the other complexes, the use of MeCN as solvent gave different results than those obtained in THF (Table II.6). While no significant differences could be detected for $\mathbf{1}^{\mathbf{CF3}}$, the absorption spectra of $\mathbf{1}^{\mathbf{CO2Me}}$ displayed a drastic diminution of the absorption bands related to the second and third reduced forms. This behavior could be related to a possible solvent interaction with the reduced species of $\mathbf{1}^{\mathbf{CO2Me}}$.

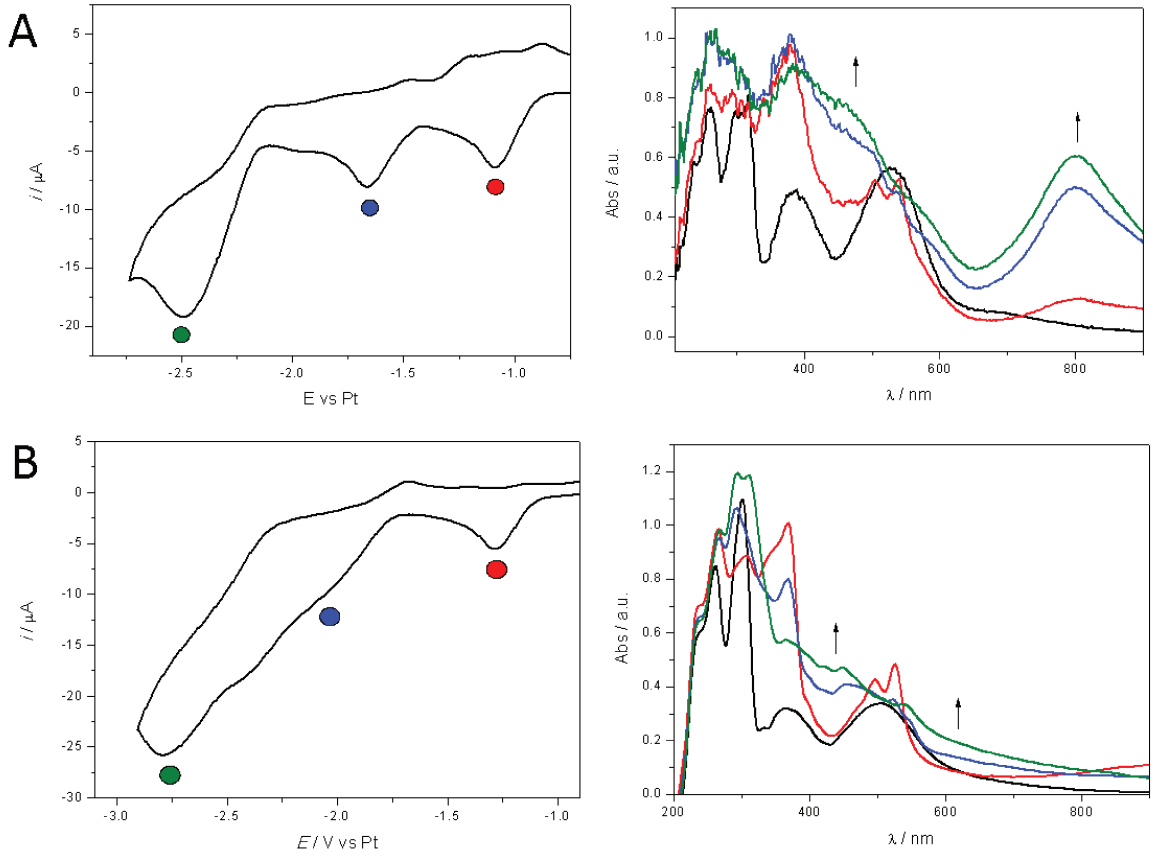

Figure II.16. CVs (v = 0.01 V s^{-1}) of $\mathbf{1}^{\mathbf{CO2Me}}$ (A) and $\mathbf{1}^{\mathbf{CF3}}$ (B) (left) and absorption spectra (right) of tri (green), bis (blue) and mono-reduced (red) and neutral (black) species of $\mathbf{1}^{\mathbf{CO2Me}}$ (A) and $\mathbf{1}^{\mathbf{CF3}}$ (B) in THF / 0.1 M NBu_4PF_6. Conditions: 1 mM of complex, BDD (WE), thin layer condition, 0.2 mm optical path, under Ar.

In summary, UV-vis spectroelectrochemical data for [$Mo(CO)_4$(bpy-(**R**)$_2$)] complexes under Ar suggest that the substituting group on the bipyridine moiety does not substantially affect the nature of the mono-reduced species formed during the reduction step, leading to [$Mo(CO)_4$(bpy-(**R**)$_2$)]$^{\bullet-}$ species in dry THF. Nevertheless, the broad peaks obtained for the second reduction did not afford clear discrimination between tetracarbonyl or tricarbonyl bis-reduced species. In consequence, complementary experimental data such as IR are necessary.

IV.2. IR spectroelectrochemical studies under Ar

Infrared spectroelectrochemical experiments in THF and MeCN solutions of Mo complexes (5mM) and NBu_4PF_6 (0.1 M) allowed for a structural characterization of [$Mo(CO)_4$(bpy-(**R**)$_2$)] reduced species. An ATR-IR probe was incorporated in a modified three-electrode cell such that thin-layer conditions could be obtained. A cone-dipped glassy carbon (GC) working electrode was used during chronoamperometry (CA) experiments at potentials values that promoted each [$Mo(CO)_4$(bpy-(**R**)$_2$)] reduction process.

As shown in Figure II.17.A, the infrared spectrum of complex **1^{H}** during the first reduction was recorded in THF under an inert atmosphere. The infrared signature remained unchanged regardless of the solvent used and displayed a 30 cm^{-1} negative shift of the ν_{CO} values compared to that of the neutral complex. The same trend was observed for the other [$Mo(CO)_4$(bpy-(**R**)$_2$)] complexes (Table II.7). This behavior was consistent with a weakening of the C-O bonds due to the increase of the electron density in the system, promoting a stronger π-retro-donation from the metal center to the CO π*-antibonding orbitals. The presence of a similar infrared signature for both mono-reduced and neutral species suggests no significant change in the coordination sphere of the system. Consequently, the aforementioned nature of the first reduction process corresponds to a simple one-electron transfer step, leading to [$Mo(CO)_4$(bpy-(**R**)$_2$)]$^{\bullet-}$ species. In the case of **1^{CO2Me}** complex, the band in the 1700-1750 region belongs to the C=O frequency mode of the CO_2Me group (Figure II.17.B)

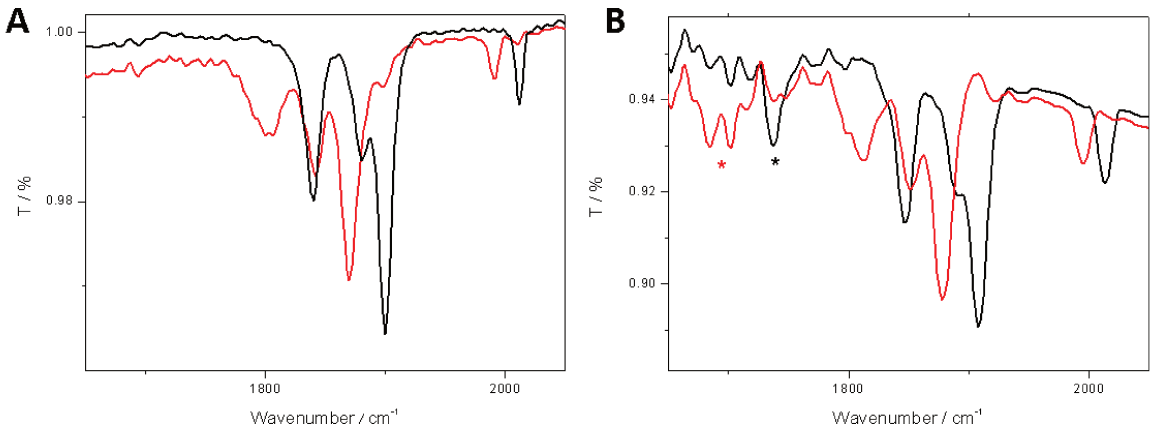

Figure II.17. Infrared spectra of neutral (black) and mono-reduced (red) forms of complex $\mathbf{1^{H}}$ (A) and $\mathbf{1^{CO2Me}}$ (B) under Ar in THF / 0.1 M NBu_4PF_6. Dots indicate the C=O frequency band of -CO_2Me group. Conditions: 5 mM of complex, GC working electrode, under Ar.

Table II.7. Values of the ν_{CO} bands of [Mo(CO)$_4$(bpy-(**R**)$_2$)]$^{\bullet-}$ in THF.

R	ν_{CO} (cm^{-1})
H	1803, 1841, 1870, 1991
^{t}Bu	1812, 1857, 1878, 1995
Me	1811, 1859, 1879, 1994
OMe	1801, 1845, 1866, 1991
CO_2Me	1813, 1856, 1878, 1994
CF_3	1812, 1860, 1881, 1997

Solvent-dependency of the second reduction process for [Mo(CO)$_4$(bpy-(**R**)$_2$)] complexes was studied by IR-SEC techniques. The nature of [Mo(CO)$_4$(bpy-(**R**)$_2$)] bis-reduced species was previously shown to be influenced by the moisture content on the solvent.[5, 6] The two possible bis-reduced species (unprotonated tricarbonyl or protonated tetracarbonyl) have indeed different IR signatures. As shown in Figure II.18.A, the spectrum of [Mo(CO)$_3$(bpy-(**H**)$_2$)]$^{2-}$ displayed ν_{CO} bands at 1707 and 1844 cm^{-1}, while that of [Mo(CO)$_4$(H^{+}-bpy-(**H**)$_2$)]$^{-}$ was very similar to that of the

corresponding neutral species, mainly due to a common tetracarbonyl structure (Figure II.18.B). The same behavior was observed for the IR-SEC studies of **1^{tBu}** and **1^{Me}** in THF and MeCN.

IR spectra of **1^{OMe}** for the second reduction process in THF remained comparable to that showed in Figure II.18.A for **1^{H}**, displaying two bands at 1700 and 1844 cm^{-1} that can be related to the [Mo(CO)$_3$(bpy-(**OMe**)$_2$)]$^{2-}$ intermediate. The presence of methoxy substituent group in the **1^{OMe}** bipyridine ring has an impact on the electronic transitions observed in its absorption spectra, but the redox behavior of **1^{OMe}** was similar to that of **1^{tBu}** and **1^{Me}**.

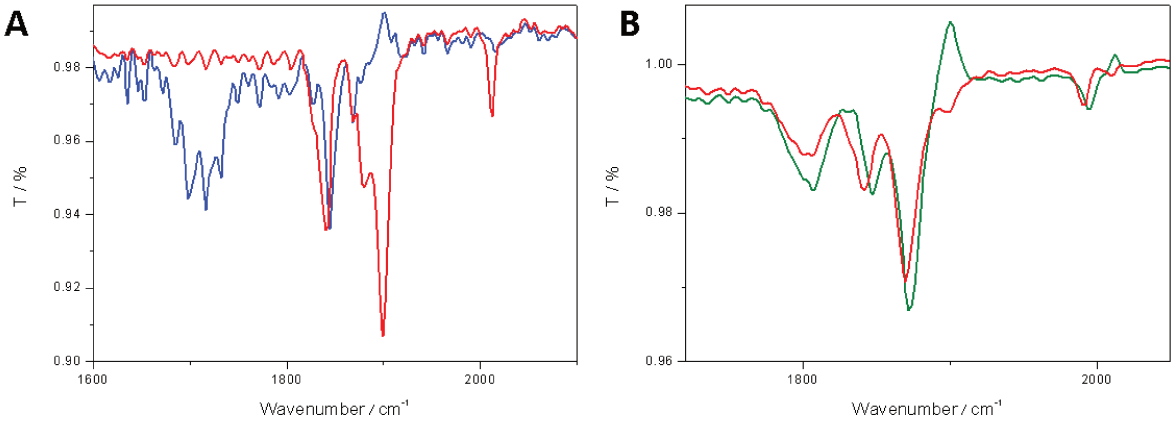

Figure II.18. A) Infrared spectra of the mono- (red) and bis-reduced (blue) forms of **1^{H}** in THF / 0.1 M NBu_4PF_6. B) Infrared spectra of the mono- (red) and bis-reduced (green) forms of **1^{H}** in MeCN / 0.1 M NBu_4PF_6. Conditions: 5 mM of complex, GC working electrode, under Ar.

Noteworthy, the IR-SEC spectrum of **1^{CO2Me}** upon reduction in THF at the second process displayed ν_{CO} bands at 1829, 1860, 1866 and 1974 cm^{-1} (Figure II.19). This infrared signature was not detected for the other [Mo(CO)$_4$(bpy-(**R**)$_2$)] complexes for the second reduction. In addition, the C=O band related to -CO_2Me group (1648 cm^{-1}) was negatively shifted. Possibly, electrochemical reduction of **1^{CO2Me}** at the second redox process may lead to the protonated [Mo(CO)$_4$(H$^+$-bpy-(**CO_2Me**)$_2$)]$^-$ species (Scheme II.3). This may result from the CO_2Me-substituted bipyridine moiety which can accommodate supplementary electron density by charge delocalization, as well as proton uptake. In consequence, the π-backbonding density towards the axial CO ligands is

decreased, thus shifting the ν_{CO} bands towards more positive values (compared to the mono-reduced species) as found experimentally.

IR-SEC studies of **1^{CO2Me}** for the third reduction process yielded ν_{CO} bands at 1708 cm^{-1} and 1851 cm^{-1} (Figure II.20), a behavior normally related to the formation of tricarbonyl species (see for example Figure II.17.A for **1^{H}**). A novel band at 1600 cm^{-1} was also detected, and may be ascribed to the -CO_2Me group.

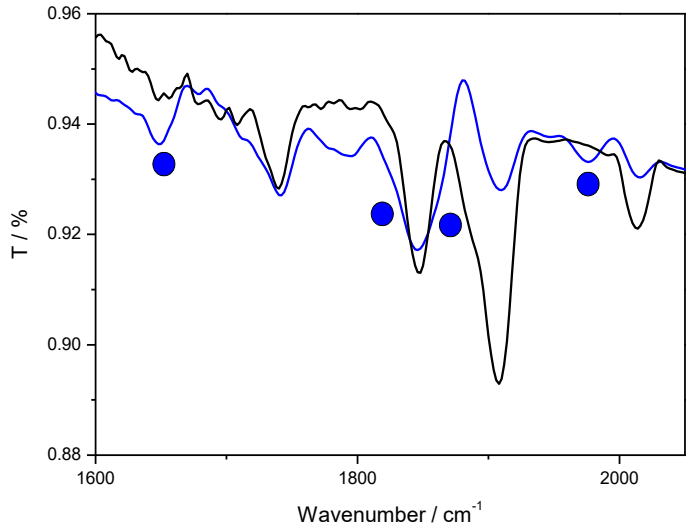

Figure II.19. Infrared spectra of the bis-reduced (blue) and neutral (black) species of **1^{CO2Me}** in THF/ 0.1 M NBu_4PF_6. Conditions: 5 mM of complex, GC working electrode, under Ar.

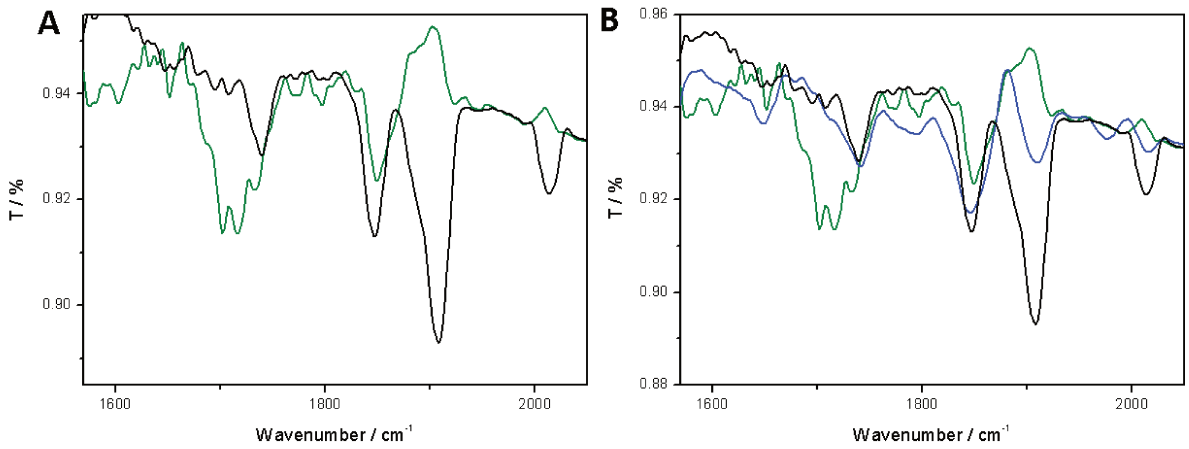

Figure II.20. Infrared spectra of the tris-reduced (green) and neutral (black) species of **1**^{CO2Me} in THF/ 0.1 M NBu_4PF_6. For B) the blue trace represents the bis-reduced form of **1**^{CO2Me}. Conditions: 5 mM of complex, GC working electrode, under Ar.

The IR-SEC study of **1**^{CF3} in THF revealed the appearance of two ν_{CO} bands at 1704 and 1842 cm^{-1} (Figure II.21) for the second reduction, which are likely assigned to [Mo(CO)$_3$(bpy-(**CF$_3$**)$_2$)]$^{2-}$. This result was similar to that obtained for all complexes except **1**^{CO2Me} (Table II.8). Since -CO_2Me and -CF_3 moieties display similar electronic (withdrawing) properties, their different IR-SEC spectra indicate that the CO_2Me group may also favor proton binding probably though oxygen atoms of the ester, leading to [Mo(CO)$_4$(H$^+$-bpy-(**CO$_2$Me**)$_2$)]$^-$.

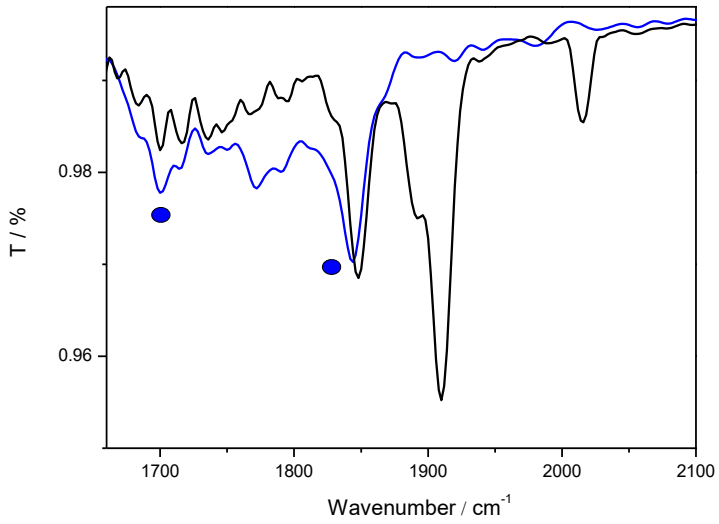

Figure II.21. Infrared spectra of the bis-reduced (blue) and neutral (black) species **1^{CF3}** in THF/ 0.1 M NBu_4PF_6. Conditions: 5 mM of complex, GC working electrode, under Ar.

Table II.8. IR data for [Mo(CO)$_4$(bpy-(**R**)$_2$)] in THF at the second reduction process (from IR-SEC).

R	ν_{CO} (cm^{-1})
H	1707, 1843
^{t}Bu	1712, 1860
Me	1714, 1865
OMe	1700, 1844
CO_2Me	1829, 1860, 1866, 1974
CF_3	1704, 1855

V. Electrocatalytic reduction of CO_2 by [Mo(CO)$_4$(bpy-(**R**)$_2$] complexes

*V.1. Cyclic voltammetry of [Mo(CO)$_4$(bpy-(**R**)$_2$)] systems under CO_2*

Electrochemical properties of [Mo(CO)$_4$(bpy-(**R**)$_2$)] were studied by cyclic voltammetry techniques under a CO_2 atmosphere. All experiments were performed under an inert atmosphere (glovebox), injecting carbon dioxide with a vacuum schlenk line after pre-purging. Boron-diamond doped (BDD) working electrode was used in each experiment. Solutions of [Mo(CO)$_4$(bpy-(**R**)$_2$)] (1 mM) in THF or MeCN with 0.1 M NBu_4PF_6 as supporting electrolyte were analyzed. As shown in Figure II.22, cyclic voltammetry of **1^H** recorded under carbon dioxide showed a current enhancement at potentials related to the second reduction process, compared to that under Ar. In agreement with spectroelectrochemical results, we can assign the active species to the bis-reduced form of **1^H**.

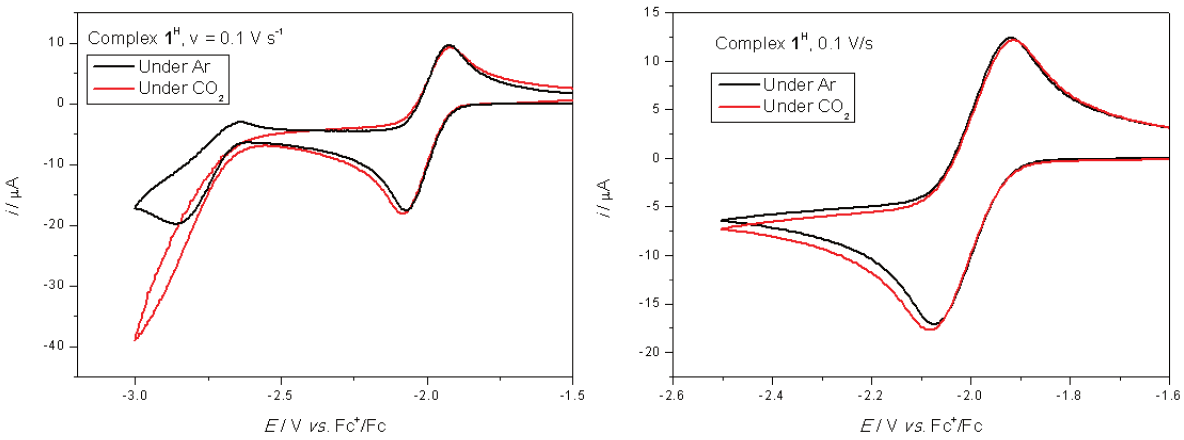

Figure II.22. CVs of complex **1^H** in THF/ 0.1 M NBu_4PF_6 under Ar (black) and CO_2 (red). Cyclic voltammetry of **1^H** first reduction process was studied separately. Conditions: 1 mM of complex, BDD working electrode, v = 0.1 V s^{-1}.

The same behavior as in Figure II.22. was also obtained for infrared-SEC studies of **1^{tBu}** and **1^{Me}**. However, a catalytic enhancement for the electron-donating [Mo(CO)$_4$(bpy-(**R**)$_2$)] derivatives was observed because of an easier reduction of the substrate (Figure II.23).

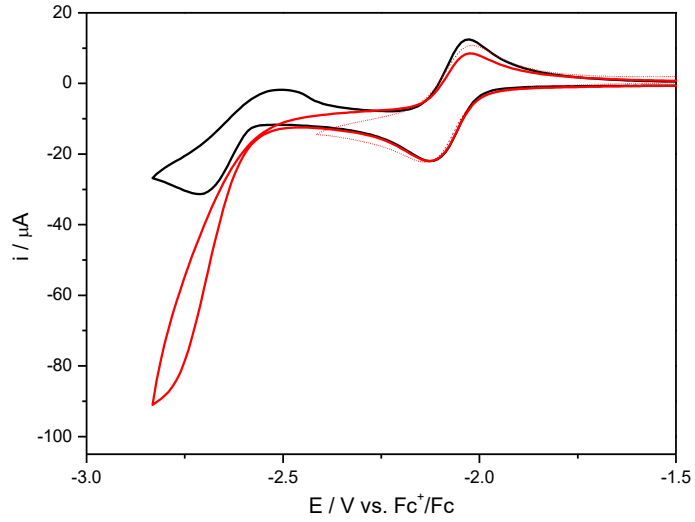

Figure II.23. CVs of complex **1^{tBu}** in THF/ 0.1 M NBu_4PF_6 under Ar (black) and CO_2 (red). Cyclic voltammetry of **1^{H}** first reduction process was studied separately. The dashed curve corresponds to the CV for the first reduction process only under carbon dioxide. Conditions: 1 mM of complex, BDD working electrode, v = 0.1 V s^{-1}.

The same behavior as in Figure II.22 was also obtained for infrared-SEC studies of **1^{tBu}** and **1^{Me}**. However, a higher catalytic current for the electron-donating [Mo(CO)$_4$(bpy-(**R**)$_2$)] derivatives was observed (Figure II.23). A small reversibility loss was found at the first reduction processes **1^{tBu}** in CO_2. This behavior suggests a possible chemical interaction of [Mo(CO)$_4$(bpy-(**R**)$_2$)]$^{\bullet-}$ with carbon dioxide. So far, electrocatalytic studies of CO_2 reduction by [Mo(CO)$_4$(bpy-(**R**)$_2$)] complexes have shown the inactivity of [Mo(CO)$_4$(bpy-(**R**)$_2$)]$^{\bullet-}$ in presence of carbon dioxide.[4, 6]

The catalytic peak current i_{cat} was determined for [Mo(CO)$_4$(bpy-(**R**)$_2$)] second reduction processes under CO_2. This value was compared to the non-catalytic response i_p under an inert atmosphere. Results obtained in MeCN/THF are displayed in Table II.9, considering i_{cat}/i_p ratio as main tool to evaluate the catalytic activity. Overall, the best activity was found for electron-donating [Mo(CO)$_4$(bpy-(**R**)$_2$)] derivatives. However, slightly smaller catalytic activities were obtained in MeCN. This effect could be caused by an interaction of [Mo(CO)$_3$(bpy-(**R**)$_2$)]$^{2-}$ species with an acetonitrile molecule. Another possibility could be the formation of [Mo(CO)$_4$(H$^+$-bpy-(**R**)$_2$)]$^-$ species in MeCN.

Table II.9. i_{cat}/i_p ratio for [Mo(CO)$_4$(bpy-(**R**)$_2$)] complexes at the second reduction potential in THF and MeCN.

R	i_{cat}/i_p in THF	i_{cat}/i_p in MeCN
H	1.8	1.6
^{t}Bu	2.3	1.7
Me	2.6	2.3
OMe	2.8	2.6
CO_2Me	1.3	1.1
CF_3	[a]	[a]

[a] Not detected

Surprisingly, electron-withdrawing [Mo(CO)$_4$(bpy-(**R**)$_2$)] systems displayed an unprecedented interaction with carbon dioxide. **1^{CO2Me}** presented discrete i_{cat}/i_p values, consistent with a smaller ability to reduce carbon dioxide (compared to **1^{H}**). This system showed indeed a slight current enhancement during its second reduction process in CO_2, accompanied with reversibility loss (Figure II.24). Nevertheless, a significant current enhancement was detected between the second and third process for this complex, suggesting the probable formation of a new CO_2 adduct after the second reduction. The lowest activity was recorded for **1^{CF3}**. These results indicate that the carbon dioxide reacted with the mono-reduced species since the bis-reduced complex was no longer detected (Figure II.24).

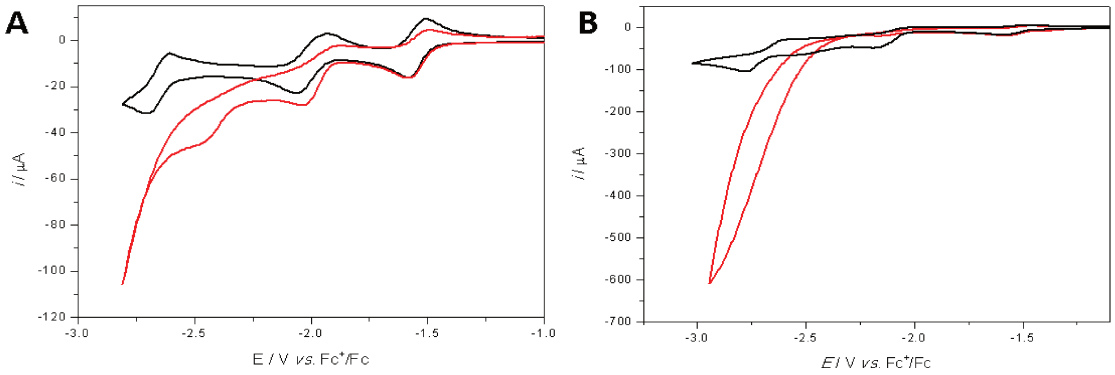

Figure II.24. CVs of A) **1^{CO2Me}** and B) **1^{CF3}** in THF/ 0.1 M NBu_4PF_6 under Ar (black) and CO_2 (red). Conditions: 1 mM of complex, BDD working electrode, v = 0.1 V s^{-1}.

*V.2. UV-vis spectroelectrochemical studies of [Mo(CO)$_4$(bpy-(**R**)$_2$)] systems under CO_2*

Studies of [Mo(CO)$_4$(bpy-(**R**)$_2$] systems under a saturated CO_2 atmosphere by UV-Vis time-resolved spectroelectrochemical techniques were performed in THF and MeCN.

Absorption spectra of [Mo(CO)$_4$(bpy-(**H**)$_2$] upon first reduction under CO_2 revealed smaller absorbance values than under Ar (Figure II.25). This absorbance loss was also found in the study of other [Mo(CO)$_4$(bpy-(**R**)$_2$] species, suggesting an interaction of [Mo(CO)$_4$(bpy-(**R**)$_2$]$^{\bullet-}$ with carbon dioxide. No additional information could be obtained by using UV-vis spectroelectrochemical techniques.

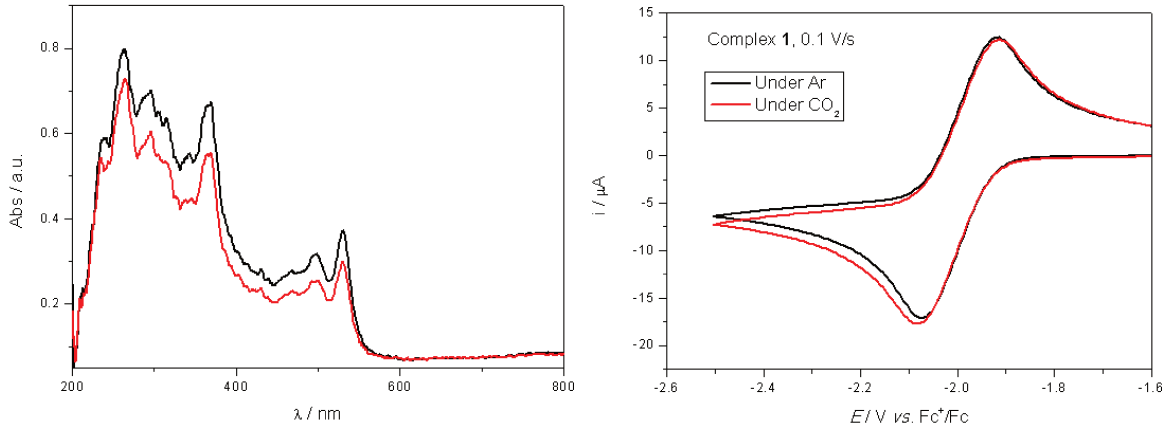

Figure II.25. [Mo(CO)$_4$(bpy-(**H**)$_2$)]$^{\bullet-}$ absorption spectra (left) and cyclic voltammetry (right) under Ar (black) and CO_2 (red) atmosphere in THF/ 0.1 M NBu_4PF_6. Conditions: 1 mM of complex, BDD working electrode, v = 0.1 V s^{-1}.

Study by UV-vis spectroelectrochemical techniques of the second reduction process for [Mo(CO)$_4$(bpy-(**H**)$_2$] under a saturated carbon dioxide atmosphere showed a drastic drop of the absorbance independently of the solvent used (Figure II.26). No adduct formation or novel absorption bands could be observed by UV-vis spectroscopic techniques.

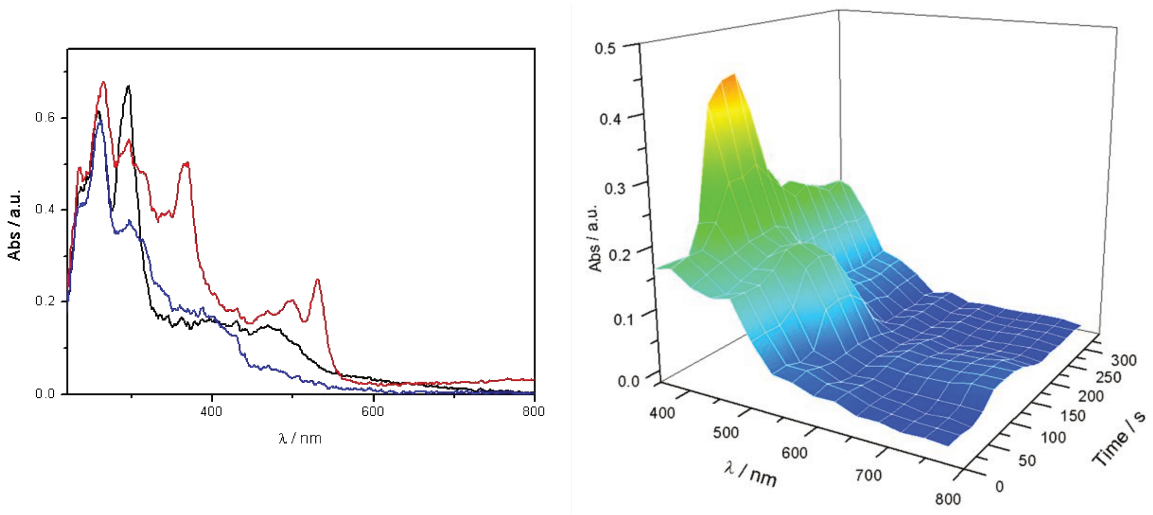

Figure II.26. Absorption spectra of bis-reduced (blue), mono-reduced (red) and neutral (black) species of **1^{H}** in THF / 0.1 M NBu_4PF_6 (left) with its corresponding 3D monitoring graph (right). Conditions: 1 mM of complex, BDD (WE), thin layer condition, 0.2 mm optical path, under CO_2.

The results shown in Figure II.26 can be extrapolated to most of the [Mo(CO)$_4$(bpy-(**R**)$_2$] systems. Nevertheless, a different behavior was observed for the second and third reduction processes for **1^{CO2Me}** under a CO_2 saturated atmosphere. The absorption spectra upon the second reduction showed two bands at 502 and 538 nm in THF together with the disappearance of the characteristic band at 800 nm, suggesting the formation of a new adduct with carbon dioxide. Even though, the absorption spectra obtained for the third reduction process was similar to that obtained for the second reduction for [Mo(CO)$_4$(bpy-(**R**)$_2$] complexes. Thus, the drastic drop of the absorbance bands (including that at 800 nm) was indicative of a catalytic interaction of a hypothetical tricarbonyl species with carbon dioxide (Figure II.27).

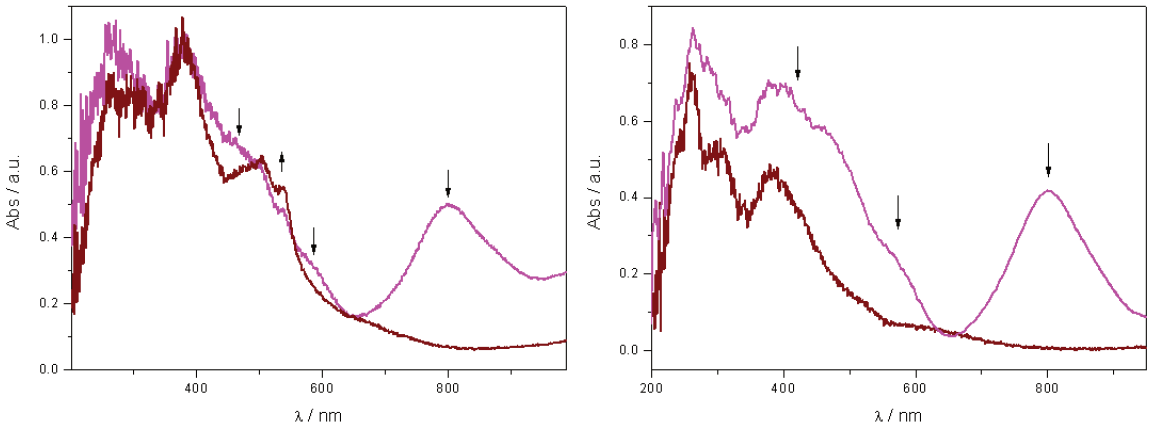

Figure II.27. UV-Vis-SEC spectra of **1**^{CO2Me} in THF during its 2nd reduction (left) and 3rd reduction (right) under Ar (pink) and CO_2 (brown) in THF/ 0.1 M NBu_4PF_6. Black arrows indicate the absorbance change under CO_2. Conditions: 1 mM of complex, BDD (WE), thin layer condition, 0.2 mm optical path.

*V.3. IR-SEC spectroelectrochemical studies of [Mo(CO)$_4$(bpy-(**R**)$_2$)] systems under CO_2*

Infrared spectroelectrochemical techniques were used in the study of [Mo(CO)$_4$(bpy-(**R**)$_2$)] complexes in a saturated CO_2 atmosphere. The formation of carbonated products was monitored by IR in the 1600-1700 cm^{-1} wavenumber range, such as formate (1610 cm^{-1}) and bicarbonate (1670 cm^{-1}) ions.[2, 17, 18] The consumption of carbon dioxide (ν_{CO} = 2320 cm^{-1}) could be also detected, a relevant factor to determine the reactivity of the reduced species formed.

First reduction process under CO_2

The Figure II.28 displayed the IR-SEC spectra of **1**^{H} upon first reduction under CO_2. The signature observed under Ar in Figure II.17, featured by a negative 30 cm^{-1} shift of the ν_{CO} values, remained unchanged. However, formation of carbonated products together with carbon dioxide consumption was detected. We could also confirm the consumption of [Mo(CO)$_4$(bpy-(**H**)$_2$)]$^{\bullet-}$ and carbon dioxide as already observed in the spectra in Figure II.25.

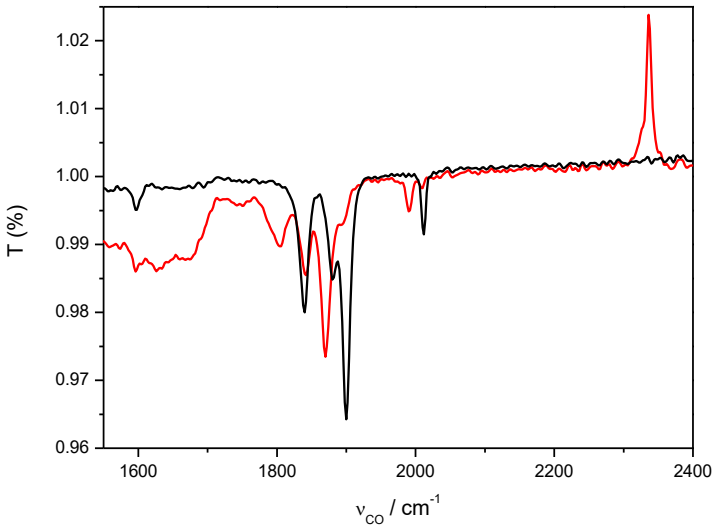

Figure II.28. IR-SEC spectra of complex **1^{H}** in THF/ 0.1 M NBu_4PF_6 at the neutral state (black) and after the first reduction (red) under CO_2. Conditions: 5 mM of complex, GC working electrode.

No result regarding the use of MeCN as a solvent has been discussed in this work due to an interaction of [Mo(CO)$_4$(bpy-(**R**)$_2$)]$^{\bullet-}$ with acetonitrile / 0.1 M NBu_4PF_6 solutions. Figure II.29 shows MeCN and CO_2 consumption during **1^{H}** first reduction process. This spectrum was recorded from a dry MeCN solution under an inert atmosphere. Surprisingly, no interaction with acetonitrile was observed under an inert atmosphere, suggesting that carbon dioxide plays an additional role in the interaction between [Mo(CO)$_4$(bpy-(**H**)$_2$)]$^{\bullet-}$ and the solvent molecule. This behavior was also found for the other [Mo(CO)$_4$(bpy-(**R**)$_2$] complexes. However, no solvent consumption was detected when dry THF was used instead of MeCN at the same experimental conditions.

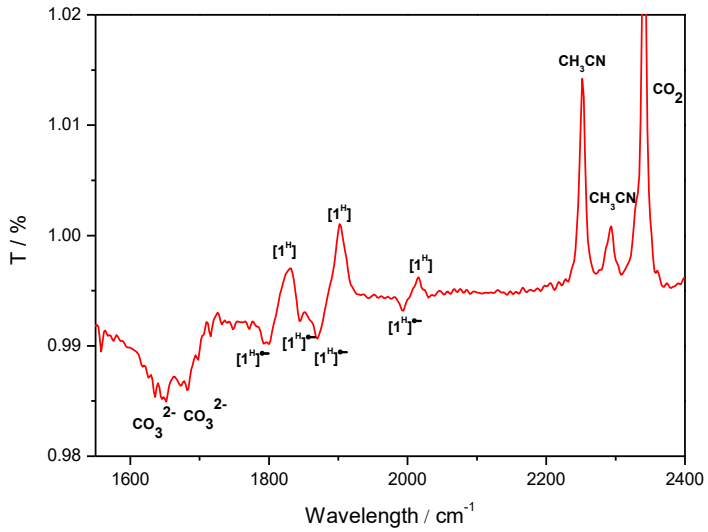

Figure II.29. $\mathbf{1^H}$ differential infrared spectra of [Mo(CO)$_4$(bpy-(**H**)$_2$)]$^{\bullet-}$ (red) under CO_2 in MeCN / 0.1 M NBu_4PF_6. Consumption of CO_2 and MeCN is observed in the 2200-2400 cm^{-1} region. Conditions: 5 mM of complex, GC (WE).

Second reduction process under CO_2

The proposed reactivity of [Mo(CO)$_4$(bpy-(**R**)$_2$)]$^{2-}$ species with carbon dioxide is described in Scheme II.4. Interestingly, the solvent can have an influence in the carbonated product formed. For instance, Clark *et al.* detected by gas chromatography (GC) the selective production of CO during the bulk electroreduction of [W(CO)$_4$(bpy-(**^{t}Bu**)$_2$)]$^{2-}$ in MeCN under a CO_2 atmosphere.[6] Nevertheless, Taylor *et al.* reported the formation of carbonate and formate in THF, under otherwise similar experimental conditions (Scheme II.4). [4, 5, 17]

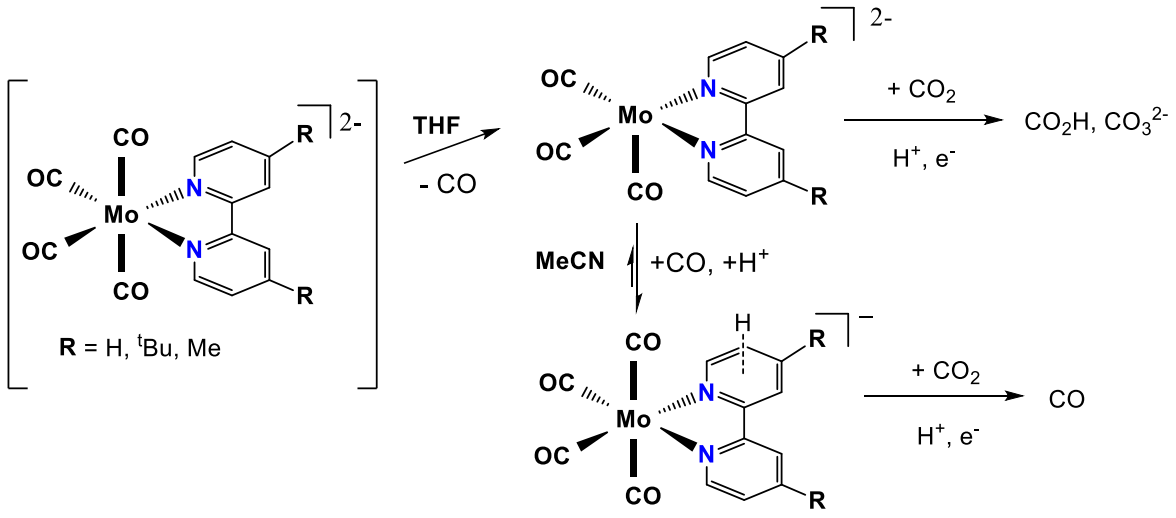

Scheme II.4. Reactivity of $[Mo(CO)_4(bpy\text{-}(\mathbf{R})_2)]^{2-}$ with carbon dioxide in different solvents.

Study by IR-SEC of the second reduction process for $[Mo(CO)_4(bpy\text{-}(\mathbf{H})_2]$ under a saturated carbon dioxide atmosphere in THF showed the formation of formate and carbonate. Surprisingly, the surge of a new ν_{CO} band at 1920 cm^{-1} featured the formation of a novel molybdenum species (Figure II.30).

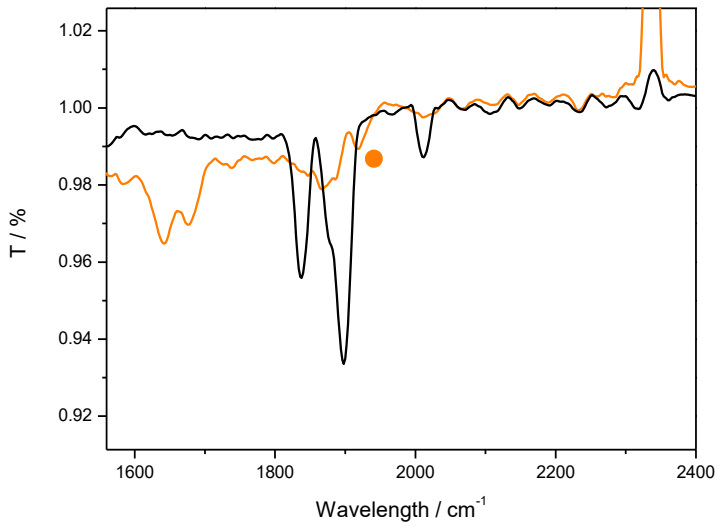

Figure II.30. IR-SEC spectra of complex $\mathbf{1^H}$ in THF/ 0.1 M NBu_4PF_6 at neutral state (black) and after the second reduction (orange) under CO_2. Conditions: 5 mM of complex, GC working electrode.

This behavior was replicated for every [$Mo(CO)_4$(bpy-(**R**)$_2$)] derivative for the second reduction process excepting $\mathbf{1^{CO2Me}}$. The nature of the interaction between bis-reduced species with CO_2 has not been defined yet. The novel ν_{CO} mode at 1920 cm^{-1} and the absence of any new absorbance bands during UV-vis spectroelectrochemical studies have already been reported for similar systems.[17] The formation of an adduct between [$Mo(CO)_3$(bpy-(**R**)$_2$]$^{2-}$ and carbon dioxide, or a formate / carbonate molecule could explain the spectroelectrochemical results obtained here, having no signature of a tetracarbonyl species that usually presents ν_{CO} modes in the 2000 cm^{-1} wavenumber region.

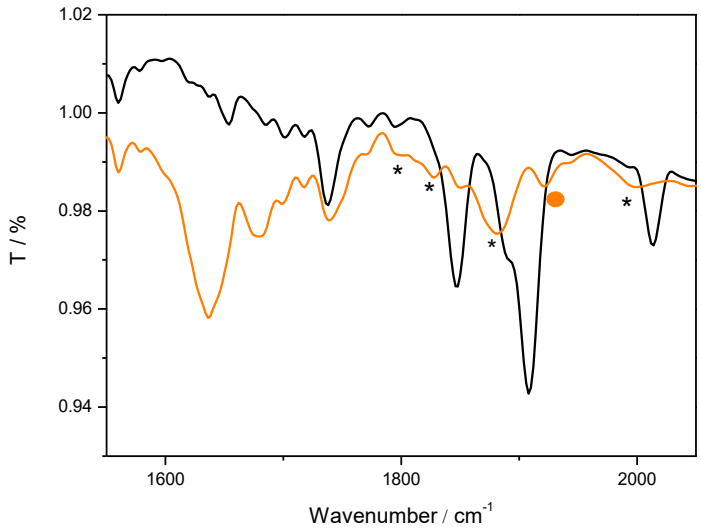

Figure II.31. IR-SEC spectra of complex $\mathbf{1^{tBu}}$ in THF/ 0.1 M NBu_4PF_6 at neutral state (black) and after the second reduction (orange) under CO_2. Conditions: 5 mM of complex, GC working electrode.

The study of the first reduction process for $\mathbf{1^{CO2Me}}$ indicated no interaction under a CO_2 atmosphere. Different conclusions can be drawn from the $\mathbf{1^{CO2Me}}$ second reduction process. An interaction with carbon dioxide can be suggested from the unassigned band at 1630 cm^{-1} (Figure

II.32). However, this band did not displayed the formate and carbonate signature usually observed for other [Mo(CO)$_4$(bpy-(**R**)$_2$)] processes, being more similar to the signature of free oxalate.[19]

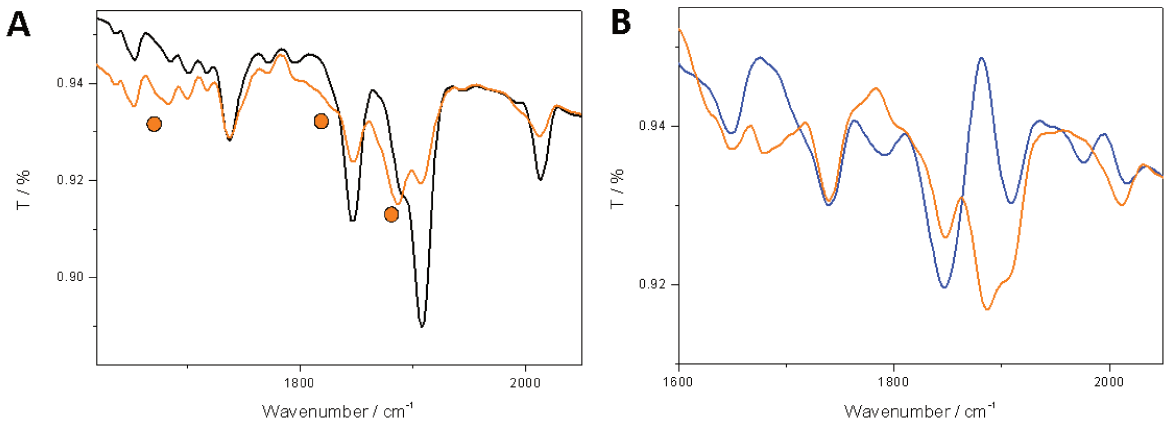

Figure II.32. Infrared spectra of the bis-reduced (orange) and neutral (black) forms of **1^{CO2Me}** in THF/ 0.1 M NBu_4PF_6 under CO_2. Orange dots indicate the ν_{CO} bands assigned to the new species formed under CO_2. For B) the blue trace represents the bis-reduced form of **1^{CO2Me}** under Ar. Conditions: 5 mM of complex, GC (WE).

We can conclude that, according to IR-SEC data, the complex **1^{CO2Me}** displays a different redox behavior as the rest of [Mo(CO)$_4$(bpy-(**R**)$_2$] complexes. However, this activity cannot be only related to the electron-withdrawing character of the -CO_2Me substituent groups by comparison with other electron-withdrawing derivatives such as **1^{CF3}**.

VI. Theoretical calculations of [Mo(CO)$_4$(bpy-(**R**)$_2$)] derivatives

Theoretical studies of several [Mo(CO)$_4$(diimine)] complexes have been previously reported .[6, 20-22] In this work, we have focused on the theoretical calculations of **1^{H}**, **1^{tBu}**, **1^{CO2Me}** and **1^{CF3}** [Mo(CO)$_4$(bpy-(**R**)$_2$)] species. Calculation of the structure of the different reduction species was also performed.

The spin densities of the SOMOs of the mono-reduced [Mo(CO)$_4$(bpy-(**R**)$_2$)]$^{\bullet-}$ species are displayed in Figures II.33 and II.34. The electronic calculations localize the extra electronic density over the bipyridine ring with a small contribution on the axial CO ligands. These results are in agreement with a first reduction process consisting of an electron transfer mainly to the bipyridine moiety.[14]

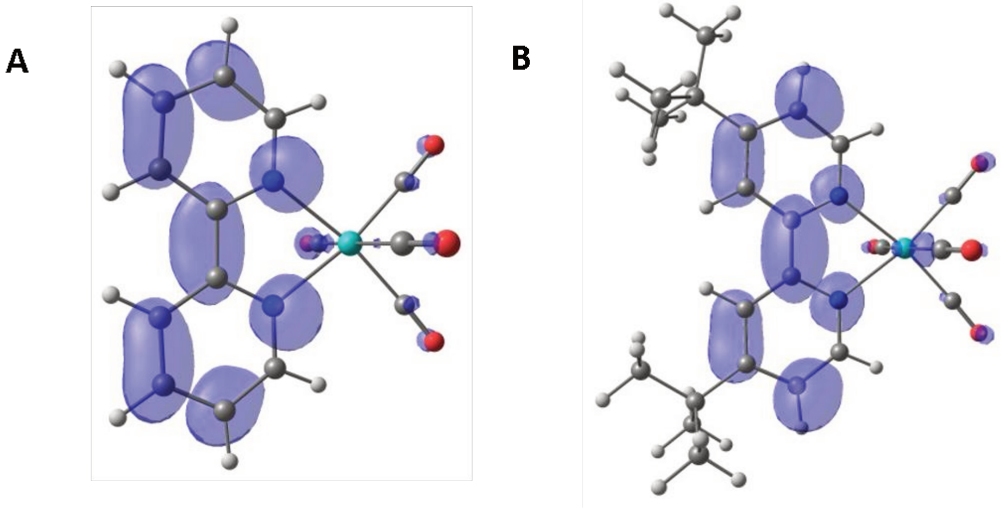

Figure II.33. Spin density plots of the SOMO of [Mo(CO)$_4$(bpy-(**H**)$_2$)]$^{\bullet-}$ (A) and [Mo(CO)$_4$(bpy-(**^{t}Bu**)$_2$)]$^{\bullet-}$ (B). Isosurface value = 0.03.

A slight electronic distribution over the electron-withdrawing substituent groups is observed in mono-reduced species of **1**^{CO2Me} and **1**^{CF3} (Figure II.35). This effect corroborates the positive potential shift observed in cyclic voltammetry experiments (Figure II.7).

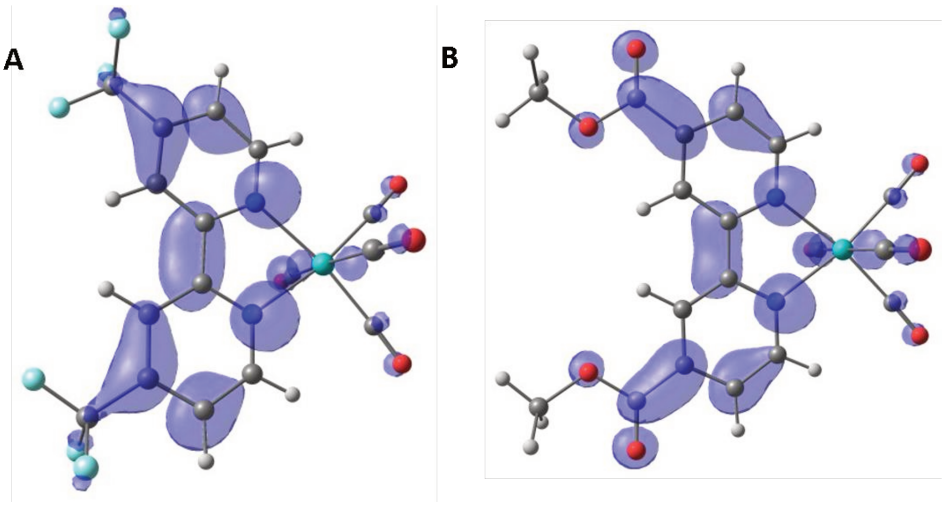

Figure II.34. Spin density plots of the SOMO of [Mo(CO)$_4$(bpy-(**CF$_3$**)$_2$)]$^{\bullet-}$ (A) and [Mo(CO)$_4$(bpy-(**CO$_2$Me**)$_2$)]$^{\bullet-}$ (B). Isosurface value = 0.03.

Theoretical IR data for [Mo(CO)$_4$(bpy-(**R**)$_2$)]$^{\bullet-}$ complexes agree with experimental values. A shift towards lower values in comparison with ν_{CO} neutral species was obtained (Table II.10).

Table II.10. Theoretical and experimental (THF) ν_{CO} values for [Mo(CO)$_4$(bpy-(**R**)$_2$)]$^{\bullet-}$ complexes.

R	ν_{CO} theor. / cm^{-1}	ν_{CO} exp. / cm^{-1}
H	1865, 1890, 1900, 1989	1803, 1841, 1870, 1991
^{t}Bu	1867, 1891, 1900, 1989	1812, 1857, 1878, 1995
CO_2Me	1877, 1902, 1910, 1994	1813, 1856, 1878, 1994
CF_3	1874, 1899, 1909, 1994	1812, 1860, 1881 1997

Modeling of [Mo(CO)$_3$(bpy-(**R**)$_2$)]$^{2-}$ species indicate a shift of the electronic density towards the metal center.[14] The presence of electron-withdrawing groups in [Mo(CO)$_3$(bpy-(**CF$_3$**)$_2$)]$^{2-}$ and [Mo(CO)$_3$(bpy-(**CO$_2$Me**)$_2$)]$^{2-}$ species allows a better distribution of the electronic density, diminishing drastically the electronic density in the Mo-N and Mo-(C)O bonds (Figure II.35.B). This stabilization factor could inhibit partially the catalytic activity towards CO_2 electroreduction of **1^{CO2Me}** and **1^{CF3}**.

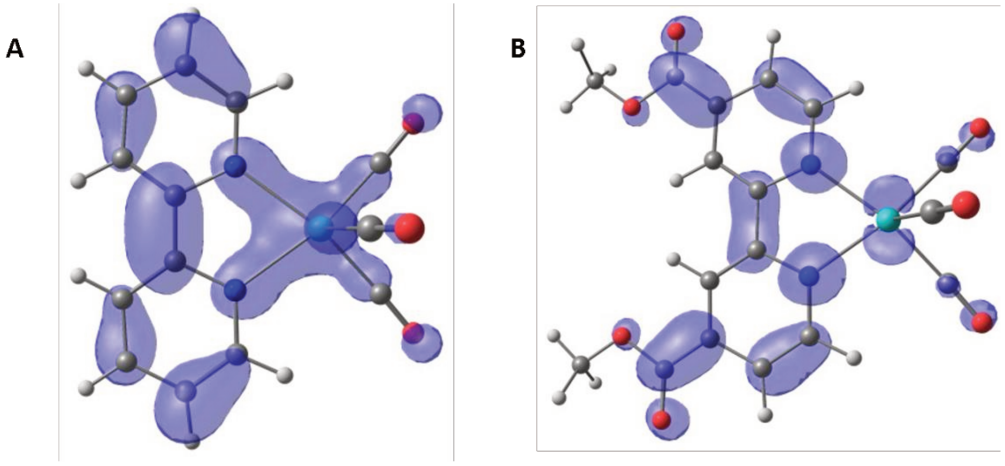

Figure II.35. Spin density plots of the HOMO of **1^{H}** (A) and **1^{CO2Me}** (B) $[Mo(CO)_3(bpy\text{-}(\mathbf{R})_2)]^{2-}$ species. Isosurface value = 0.03.

Theoretical IR data of $[Mo(CO)_3(bpy\text{-}(\mathbf{R})_2)]^{2-}$ species corroborated the IR signature obtained by spectroelectrochemical IR experiments for R = H, ^{t}Bu and CF_3, with two ν_{CO} bands around 1700 and 1850 cm^{-1} (Table II.11). An uniform difference of about 80 cm^{-1} is obtained for each $[Mo(CO)_3(bpy\text{-}(\mathbf{R})_2)]^{2-}$ band in the 1700-1720 cm^{-1} region. However, as previously discussed, the theoretical values did not match with experimental ones for the CO_2Me derivative.

Table II.11. Theoretical ν_{CO} values of $[Mo(CO)_3(bpy\text{-}(\mathbf{R})_2)]^{2-}$ compared to experimental data in THF for the second reduction.

R	ν_{CO} theor. / cm^{-1}	ν_{CO} exp. (in THF) / cm^{-1}
H	1772, 1854	1707, 1843
^{t}Bu	1779, 1859	1712, 1860
CO_2Me	1791, 1871	1829, 1860, 1866, 1974
CF_3	1793, 1871	1700, 1844

Extensive analysis of **1^{CO2Me}** reduction processes was performed by simulating the possible reduced species formed in THF (Table II.12). Comparative theoretical IR data of the different plausible reduced species of **1^{CO2Me}** are gathered in Table II.11. Calculation of $[Mo(CO)_4(bpy\text{-}(\mathbf{CO_2Me})_2)]^{2-}$ species as an equivalent system to $[Mo(CO)_4(H^{+}\text{-}bpy\text{-}(\mathbf{CO_2Me})_2)]^{-}$ was performed. It is remarkable

that [Mo(CO)$_4$(bpy-(**CO$_2$Me**)$_2$)]$^{2-}$ theoretical values for ν_{CO} modes were very close to the experimental ones obtained during the monitoring of **1^{CO2Me}** second reduction process (Figure II.36).

Table II.12. Experimental and theoretical ν_{CO} infrared data of the reduced **1^{CO2Me}** species in THF.

	ν_{CO} theor. / cm^{-1}	ν_{CO} exp. (in THF) / cm^{-1}
[Mo(CO)$_4$(bpy-(**CO$_2$Me**)$_2$)]	1919, 1943, 1950, 2019	1839, 1885, 1911, 2018
[Mo(CO)$_4$(bpy-(**CO$_2$Me**)$_2$)]$^{-}$	1877, 1902, 1910, 1994	1813, 1856, 1878, 1994
[Mo(CO)$_4$(bpy-(**CO$_2$Me**)$_2$)]$^{2-}$	1836, 1861, 1874, 1969	1829, 1860, 1866, 1974
[Mo(CO)$_3$(bpy-(**CO$_2$Me**)$_2$)]$^{2-}$	1670, 1816, 1898	1708, 1851

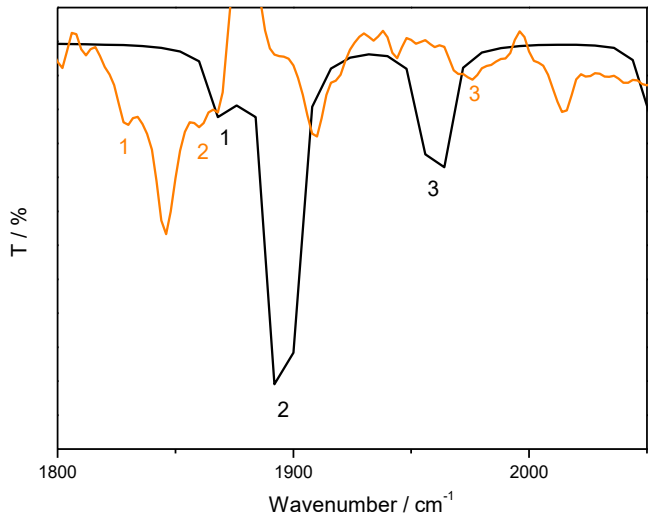

Figure II.36. IR spectra of [Mo(CO)$_4$(bpy-(**CO$_2$Me**)$_2$)]$^{2-}$**.** The black and orange traces represent the theoretical and experimental spectra obtained in THF/ 0.1 M NBu_4PF_6 respectively. The numbers correspond to the main ν_{CO} bands of the species. Conditions: 5 mM of complex, GC (WE).

However, an additional theoretical study of **1^{CO2Me}** and **1^{CF3}** complexes was carried out to comprehend the different redox behavior observed between both complexes. Additional factors

besides the electron-withdrawing character of the complexes should be taken in account. Bond distances and angles of bis-reduced tetracarbonyl **1^{CO2Me}** and **1^{CF3}** species are gathered in Table II.13 and Table II.14. There are no substantially changes in the surroundings of the metal center. Surprisingly, bond distances and angles are not significantly affected from a change of the electron-donating substituent group.

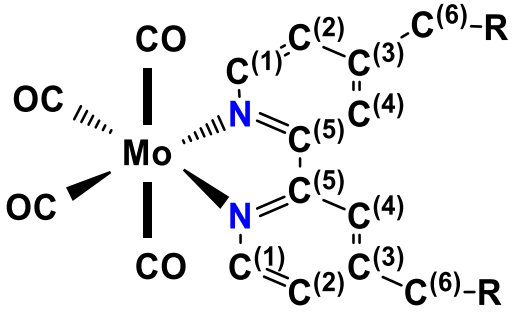

Figure II.37. Atom numbering for the calculated structures of [Mo(CO)$_4$(bpy-(**R**)$_2$)] (**R** = CO_2Me, CF_3) complexes**.**

Table II.13. Calculated bond distances (Å) for bis-reduced tetracarbonyl **1^{CO2Me}** and **1^{CF3}** complexes according to numbering of Figure II.37.

	Mo–N	Mo–CO_{eq}	Mo–CO_{ax}	$C^{(5)}$–$C^{(5)}$	$C^{(5)}$–$C^{(6)}$
[Mo(CO)$_4$(bpy-(**CO_2Me**)$_2$)]$^{2-}$	2.26	1.98	2.05	1.45	1.44
[Mo(CO)$_4$(bpy-(**CF_3**)$_2$)]$^{2-}$	2.25	1.98	2.05	1.42	1.47

Table II.14. Calculated angles (°) for bis-reduced tetracarbonyl **1^{CO2Me}** and **1^{CF3}** complexes according to numbering of Figure II.37.

	$C^{(2)}$–$C^{(3)}$–$C^{(4)}$	N–Mo–C_{eq}	N–Mo–C_{ax}
[Mo(CO)$_4$(bpy-(**CO_2Me**)$_2$)]$^{2-}$	116.1	98.1	93.4
[Mo(CO)$_4$(bpy-(**CF_3**)$_2$)]$^{2-}$	118.3	97.2	93.5

Figure II.38 summarizes the redox mechanism of $[Mo(CO)_4(bpy\text{-}(\mathbf{R})_2)]$ complexes. As mentioned in the beginning of this chapter, the majority of $[Mo(CO)_4(bpy\text{-}(\mathbf{R})_2)]$ derivatives experiences two reduction processes. Hence, an additional pathway is added for $\mathbf{1}^{\mathbf{CO2Me}}$ due to experimental evidences. This pathway is featured by the stabilization of $[Mo(CO)_4(H^+\text{-}bpy\text{-}(\mathbf{CO_2Me})_2)]^-$ species that was characterized during $\mathbf{1}^{\mathbf{CO2Me}}$ spectroelectrochemical experiments. Distribution of the electronic density over the bipyridine moiety seems the main factor of the redox behavior of $[Mo(CO)_4(bpy\text{-}(\mathbf{R})_2)]$ complexes. The capacity of the $\text{-}CO_2Me$ substituting group to accommodate for electronic density as well as proton uptake stands out for $\mathbf{1}^{\mathbf{CO2Me}}$ comparing to $\mathbf{1}^{\mathbf{CF3}}$, inhibiting the latter from following the alternative reduction pathway described in Figure II.38.

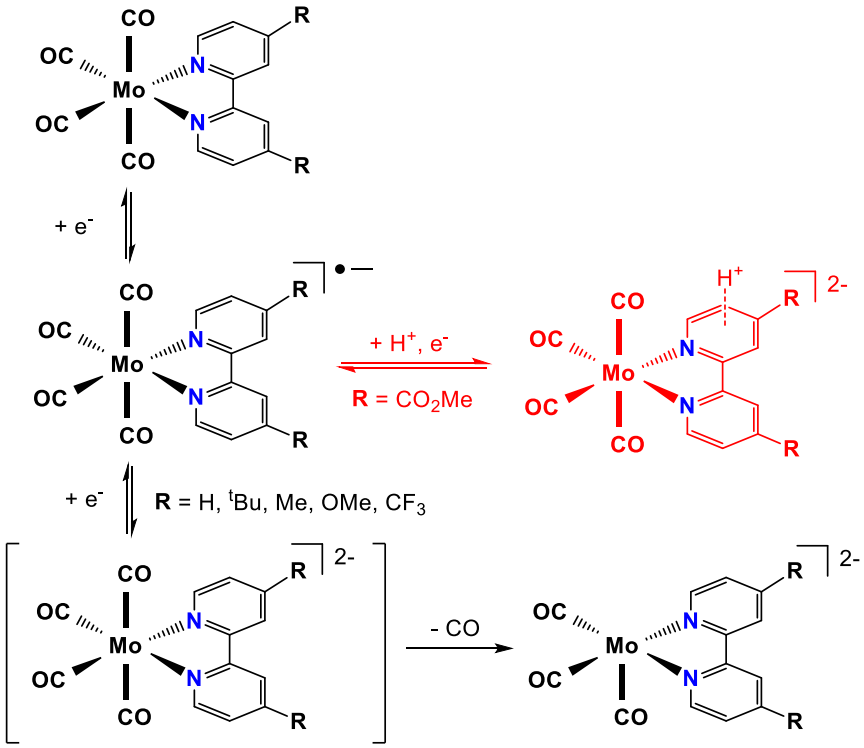

Figure II.38. Proposed redox mechanism for $[Mo(CO)_4(bpy\text{-}(\mathbf{R})_2)]$ (**R** = H, ^{t}Bu, Me, OMe, CO_2Me, CF_3) complexes in THF.

VII. Conclusions

The objective of this chapter was to investigate the influence of the electronic density in [Mo(CO)$_4$(bpy-(**R**)$_2$)] bipyridine moiety on their catalytic role in homogeneous CO_2 electroreduction. Our strategy was to modify the bipyridine ring in the 4-4´position with electron-donating/withdrawing groups. Cyclic voltammetry experiments under an inert atmosphere showed a direct relationship between a potential shift of the reduction processes and a modification of [Mo(CO)$_4$(bpy-(**R**)$_2$)] ligand backbone, in particular the electron-donating or withdrawing properties of the **R** substituent. Notably, an unexpected third reduction was observed with the electron-withdrawing derivatives, **1^{CO2Me}** and **1^{CF3}**. Application of infrared and UV-vis spectroelectrochemical techniques under Ar were useful to determine the nature of the species generated for the reduction processes. All systems studied showed a common pattern, involving the formation of mono-reduced species [Mo(CO)$_4$(bpy-(**R**)$_2$)]$^{\bullet-}$. From the mono-reduced species, going to more negative potentials promoted the formation of [Mo(CO)$_4$(H$^+$-bpy-(**R**)$_2$)]$^-$ or [Mo(CO)$_3$(bpy-(**R**)$_2$)]$^{2-}$ depending on the solvent used. Nevertheless, spectroelectrochemical study of **1^{CO2Me}** second reduction process showed a novel signature, being possible related to the stabilization of bis-reduced [Mo(CO)$_4$(H$^+$-bpy-(**CO$_2$Me**)$_2$)]$^-$ species. In addition, spectroelectrochemical spectra of the third reduction process of **1^{CO2Me}** displayed a signature expected for a tricarbonyl species. Measurements of the catalytic electroreduction of CO_2 by bis-reduced complexes showed a small current enhancement for complexes with electron-donating substituents, generating formate/carbonate in THF as determined by spectroelectrochemical techniques. Noteworthy, an interaction with carbon dioxide was also observed during the first reduction process. DFT calculations were performed in order to better understand the reduction processes. The comparison of the calculated electronic structure of **1^{CO2Me}** with other [Mo(CO)$_4$(bpy-(**R**)$_2$)] derivatives showed the possible formation of tetracarbonyl species during the second reduction process.

Bibliography

[1] R. Francke, B. Schille, M. Roemelt, *Chem. Rev.* **2018**, *118*, 4631-4701.

[2] J. O. Taylor, G. Neri, L. Banerji, A. J. Cowan, F. Hartl, *Inorg. Chem.* **2020**, *59*, 5564-5578.
[3] L. Rotundo, E. Azzi, A. Deagostino, C. Garino, L. Nencini, E. Priola, P. Quagliotto, R. Rocca, R. Gobetto, C. Nervi, *Front. Chem.* **2019**, *7*.
[4] J. O. Taylor, R. D. Leavey, F. Hartl, *ChemElectroChem* **2018**, *5*, 3155-3161.
[5] J. Tory, B. Setterfield-Price, R. A. W. Dryfe, F. Hartl, *ChemElectroChem* **2015**, *2*, 213-217.
[6] M. L. Clark, K. A. Grice, C. E. Moore, A. L. Rheingold, C. P. Kubiak, *Chem. Sci.* **2014**, *5*, 1894-1900.
[7] J. A. Connor, C. Overton, N. El Murr, *J. Organomet. Chem.* **1984**, *277*, 277-284.
[8] M. H. B. Stiddard, *J. Chem. Soc.* **1962**, *0*, 4712-4715.
[9] J. A. Connor, C. Overton, *J. Organomet. Chem.* **1983**, *249*, 165-174.
[10] M. A. Bennett, L. Pratt, G. Wilkinson, *J.Chem.Soc.* **1961**, 2037-2044.
[11] A. Vlček, F. W. Grevels, T. L. Snoeck, D. J. Stufkens, *Inorg. Chim. Acta* **1998**, *278*, 83-90.
[12] D. Guillaumont, C. Daniel, A. Vlček, *Inorg. Chem.* **1997**, *36*, 1684-1688.
[13] S. Záliš, I. R. Farrell, A. Vlček, *J. Am. Chem. Soc.* **2003**, *125*, 4580-4592.
[14] A. Vlček, *Coordin. Chem. Rev.* **2002**, 225-242.
[15] D. M. Manuta, A. J. Lees, *Inorg. Chem.* **1986**, *25*, 1354-1359.
[16] L. P. Hammett, *J. Am. Chem. Soc.* **1937**, *59*, 96-103.
[17] J. O. Taylor, Y. Wang, F. Hartl, *ChemCatChem* **2019**, *12*, 386-393.
[18] S. C. Cheng, C. A. Blaine, M. G. Hill, K. R. Mann, *Inorg. Chem.* **1996**, *35*, 7704-7708.
[19] J. E. Anderson, C. P. Murphy, J. Real, J. Balué, J. C. Bayón, *Inorg. Chim. Acta* **1993**, *209*, 151-160.
[20] L. Rotundo, C. Garino, R. Gobetto, C. Nervi, *Inorg. Chim. Acta* **2018**, *470*, 373-378.
[21] S. Záliš, C. Daniel, A. Vlček, D. A. Chantal Vlček Jr, *Dalton Trans.* **1999**, 3081-3086.
[22] P. Zhang, X. Yang, X. Hou, X. Xu, B. Xiao, J. Huang, C. Stampfl, *Phys. Chem. Chem. Phys.* **2019**, *21*, 23742-23748.

Chapter III

Synthesis, characterization and reactivity towards CO_2 of $[Mo(CO)_4(L)]$ complexes (L = bpy, phen, py-indz)

I. Introduction

In the precedent chapter, we have demonstrated that modulation of electronic density on the Mo-bpy tetracarbonyl complexes could be obtained by variation of the two **R**-substituting groups in 4,4' position on the bipyridine ligand. This strategy was shown to lead to a discrete increment of the catalytic activity for CO_2 reduction by using electron-donating groups (**R** = ^{t}Bu, Me), although this was accompanied by an increase of the overpotential value. In this chapter, we have focused on the effect in the catalytic properties of varying the nature of the diimine ligand, expecting that modification of the coordination sphere would cause a strong change in the electronic and redox properties of the system. Surprisingly, this approach has been poorly developed for the electrocatalytic reduction of CO_2 by group 6 metal-diimine tetracarbonyl complexes.

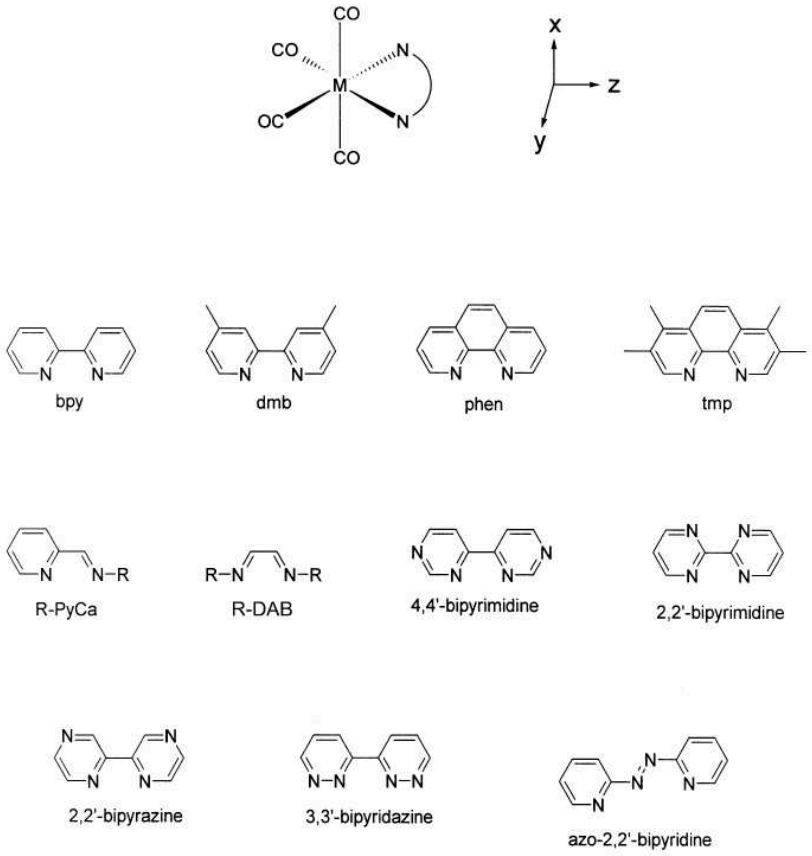

Figure III.1. Schematic representation of $[M(CO)_4(diimine)]$ systems (M = Cr, Mo, W). Reproduced from Ref. [1].

As shown in Figure III.1, many $[M(CO)_4(diimine)]$ complexes (M = Cr, Mo, W) have been synthesized, but mainly for different purposes than catalysis. For instance, molybdenum and tungsten tetracarbonyl phenanthroline (phen) and tetramethylphenanthroline (tmp) complexes (and more generally Mo-dimiine tetracarbonyl derivatives) have been thoroughly investigated because of their fast (ps scale) MLCT (Metal-to-Ligand Charge Transfer) photodissociation upon UV-Vis irradiation, leading to transient tricarbonyl species at the neutral and mono-reduced state. In particular, Vlček *et al.* discussed in a series of reviews on the structural effects of electron transfer reactions triggered by photochemical or electrochemical means in Mo-diimine tetracarbonyl complexes, as well as the localization of electron density upon excitation.[1-3] Electrochemical studies of phenanthroline derivatives phen *vs*. tmp (M = Cr and W, Figure III.1) showed a redox behavior similar to their bipyridine analogues, i.e. a mono-electronic reversible reduction at ca. -2.0 V *vs*. Fc^+/Fc in THF and one or two more chemically irreversible reduction steps at more negative potentials.[4] IR spectroelectrochemistry at an OTTLE cell demonstrated the relative stability of the generated tetracarbonyl radical anions within the experimental timescale. Furthermore, it was shown that subtle structural changes of the diimine ligand from phen to tmp could strongly affect the charge localization on the ligand at the mono-reduced state. Such effect was explained by a switch of LUMO symmetry, as evidenced by EPR spectroelectrochemical studies and supported by DFT.[1] So far, no redox data has been reported for the Mo-phen complexes.

More recently, a comparative study of $[M(CO)_4(dpa)]$ (M = W, Mo; dpa = 2,2´-dipyridylamine) complexes and their bpy analogues has been reported. Electrochemical studies have shown that the former complexes undergo a different redox behavior than $[M(CO)_4(bpy\text{-}R)]$ derivatives since a single and irreversible reduction process at ca. -2.6 V *vs*. Fc^+/Fc was detected. Interestingly, electrocatalytic reduction of CO_2 was shown to occur at this redox potential with production of carbon monoxide and carbonate ions (Figure III.2).[5] DFT calculations performed on the tungsten complex suggested that this untypical behavior was due to a geometry rearrangement upon monoelectronic reduction involving rotation and unbinding of one pyridine ring of the dpa ligand and formation of an hydride intermediate.[6] Furthermore, theoretical calculations indicated the probable formation of a $[M(CO)_3(dpa)(CO_2)]^{2-}$ adduct after metal-CO dissociation and reduction (see Figure III.2). The long-term deactivation of the catalyst observed experimentally was proposed to originate from the deprotonation of the amine separating the pyridyl groups.

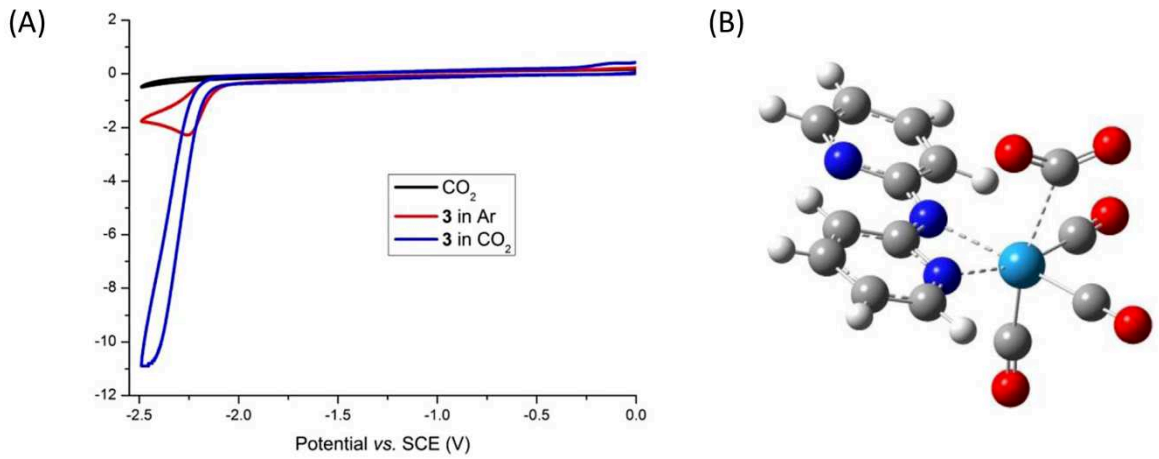

Figure III.2. (A) CVs of the $[Mo(CO)_4(dpa)]$ complex in $MeCN/NBu_4PF_6$ 0.1 M under argon (red) and CO_2 (blue); The black curve is the CV under CO_2 without complex. (B) Calculated structure of the $[Mo(CO)_3(dpa)(CO_2)]^{2-}$ adduct. Reproduced from Ref. [5] and [6].

Another example of group 6 metal tetracarbonyl complexes bearing N-N ligands (other than bpy) was reported by Kubiak and co-workers. These authors investigated the redox properties and reactivity *vs*. carbon dioxide of $[Mo(CO)_4(^{Ar}PMI)]$ (Ar = Ph and *i*Pr_2Ph) complexes featuring a functionalized pyridine monoamine (PMI) ligand.[7] The objective of this work was to shift the reduction potential of the complexes towards more positive values, and consequently to decrease the overpotential for CO_2 reduction as previously observed with analogous rhenium and cobalt complexes. Under inert atmosphere, the complexes displayed a similar electrochemical behavior as $[Mo(CO)_4(bpy)]$ although the first reversible reduction at $E_{1/2}$ = -1.80 V *vs*. Fc^+/Fc was positively shifted by 180 mV compared to $[Mo(CO)_4(bpy)]$. IR spectroelectrochemical studies indicated the loss of one carbonyl group at the second reduction step occurring at -2.35 V and -2.55 V *vs*. Fc^+/Fc for the Ph and *i*Pr_2Ph PMI complexes respectively. Under a saturated CO_2 atmosphere, the $[Mo(CO)_4(^{iPr2Ph}PMI)]$ complex showed a current enhancement when the potential reached the second reduction process (Figure III.3). However, the electrocatalytic activity rapidly decreased upon cycling as shown in Figure III.3.A. This behavior was explained by the generation of a new CO_2 adduct, $[Mo(CO)_3(^{iPr2Ph}PMI)(CO_2)]^{2-}$, for which a C-C bond is formed between the former imine carbon atom and the CO_2 carbon atom (Figure III.3.B). DFT calculations suggested that the highest is mainly centered on the C-C=N imine moiety where CO_2 reacts.

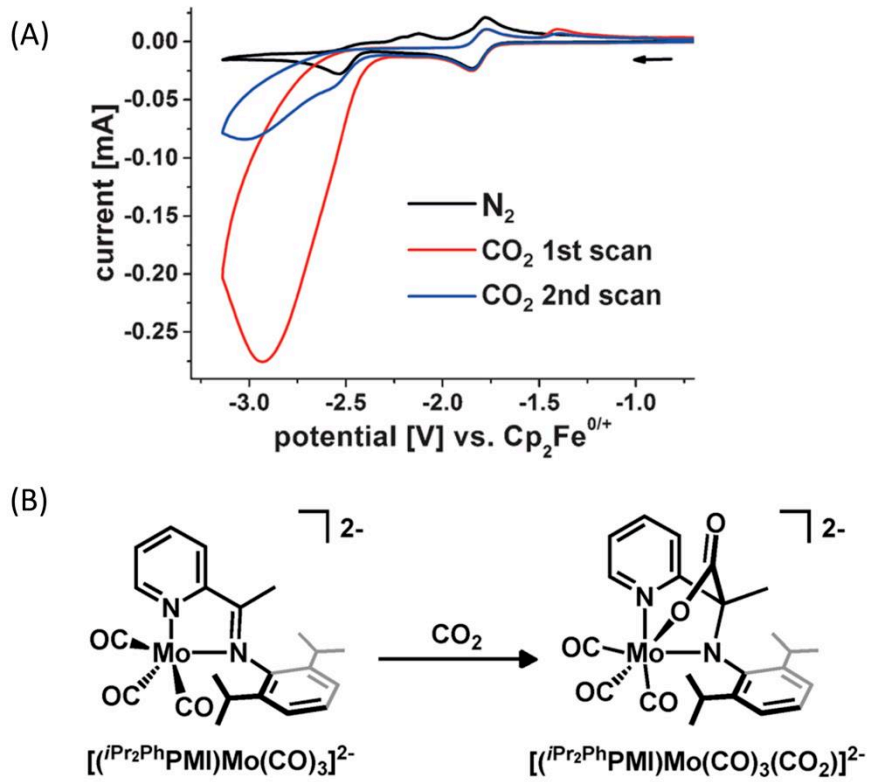

Figure III.3. (A) CVs of $[Mo(CO)_4(^{iPr2Ph}PMI)]$ under Ar (black) and CO_2 (red: 1st scan; blue: 2nd cycle) at v = 200 V s^{-1} in MeCN/NBu_4PF_6 0.1 M. (B) Proposed reaction mechanism of the bis-reduced PMI complex with CO_2. Reproduced from Ref. [7].

Overall, these two recent examples indicate that substitution of the classical bipyridine system by another N-N ligand in $[Mo(CO)_4(diimine)]$ complexes can deeply affect the redox properties and catalytic activity towards CO_2. The variation of the geometrical pattern upon reduction, such as the rotation of the pyridine ring in $[Mo(CO)_4(dpa)]^-$, or the specific localization of charge density due to unsymmetrical ligands, such as in $[Mo(CO)_4(^{iPr2Ph}PMI)]^{2-}$, are two main parameters which can be considered to enhance electrocatalytic properties for CO_2 reduction. Since these two examples remain the only ones reported so far and that more data are needed to fully understand how the ligand topology can impact electrocatalysis, we have focused our work on two different complexes, $[Mo(CO)_4(phen)]$ (**2**) and $[Mo(CO)_4(py\text{-}indz)]$ (py-indz = pyridylindolizine) (**3**) as depicted in Figure III.4. These complexes have been chosen for comparative studies with $[Mo(CO)_4(bpy)]$ (**1**, equivalent to complex $\mathbf{1^H}$ in Chapter II of this work), to rationalize the effect of

a rigid diimine ligand, such as with complex **2**, or the influence of an unsymmetrical pattern such as in **3,** on the redox and catalytic properties towards CO_2. Thus, our objective was to put in perspective the influence of the diimine backbone in the catalytic activity of $[Mo(CO)_4(diimine)]$ systems towards carbon dioxide electroreduction with the help of electrochemical and spectroelectrochemical methods together with DFT calculations. In particular, we have investigated the reactivity of the mono-reduced complexes *vs*. CO_2 and the effect of the solvent by using 1,2 difluorobenzene (DFB) since it is an aprotic and non-coordinating solvent more polar than THF.

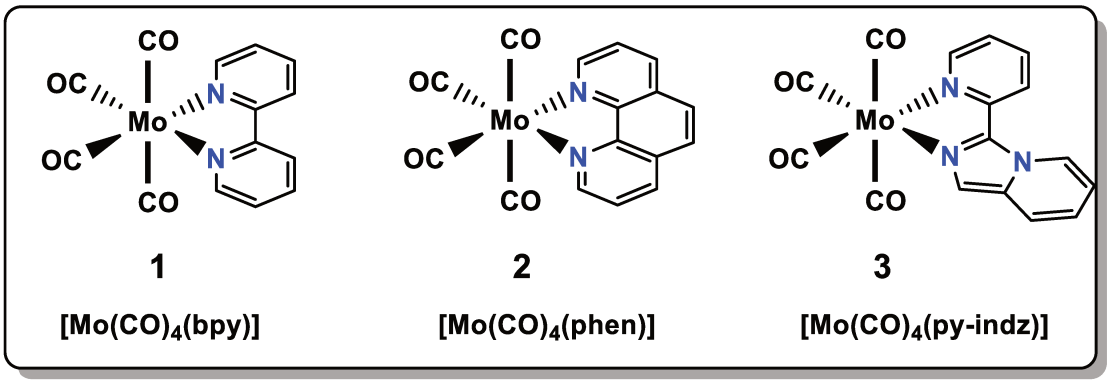

Figure III.4. Structure of $[Mo(CO)_4(bpy)]$ (**1**), $[Mo(CO)_4(phen)]$ (**2**) and $[Mo(CO)_4(py\text{-}indz)]$ (**3**) complexes used in our comparative studies.

II. Synthesis and characterization of complexes **1**, **2** and **3**

The synthesis of complex **1** was carried out according to Stiddard's procedure,[8] as described in Chapter II. The syntheses of complexes **2** and **3** were performed by modification of the synthetic route reported by Ardizzoia. For complex **2**, molybdenum hexacarbonyl and 2,2´-phenanthroline (1 equiv.) were heated at 90°C in toluene overnight (Scheme III.1). The red solution was filtered. The solid was washed with cold toluene and diethyl ether. Recrystallization in 1:1 toluene / dichloro-methane provided a red crystalline solid with good yield (96%).

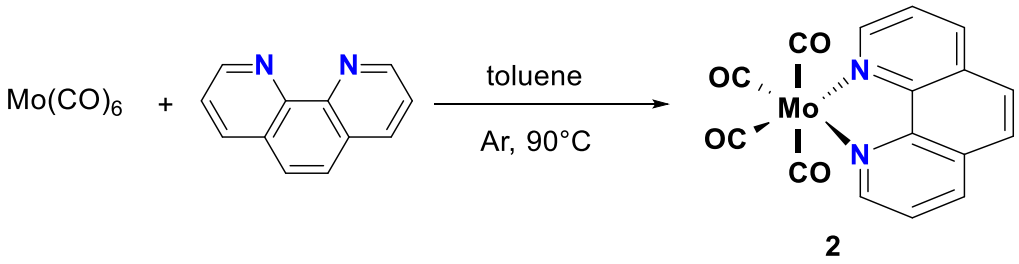

Scheme III.1. Synthetic pathway for complex **2**.

A similar procedure was applied to the synthesis of complex **3**. $[Mo(CO)_6]$ and 3-(Pyridin-2-yl)imidazo[1,5-*a*]pyridine (1 equiv.) were stirred in toluene at 90°C for 6 h. A yellow-orange solution was obtained. After evaporation of the solvent, the material was dissolved in dichloromethane and filtered. Hexane was then added to precipitate the complex. Recrystallization in a 1:1 solution of hexane / dichloromethane gave a yellow crystalline solid with 88 % yield.[9]

Reported XRD structures for the complexes **1**[10], **2**[11] and **3**[9] allowed us to analyze the effect of the diimine ligand on bond distances (Table III.1) and angles (Table III.2) according to the atom numbering in Figure III.5.

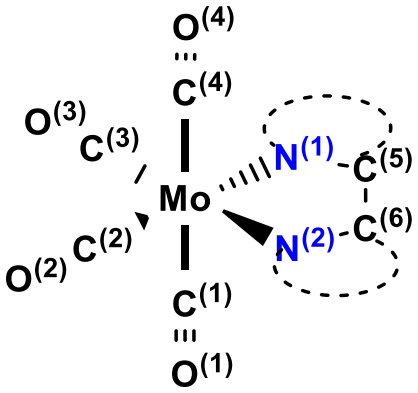

Figure III.5. Atom numbering for the calculated structures of complexes **1**-**3** ($N^{(1)}$ is the N atom of the pyridyl group in complex **3**).

Table III.1. Bond distances (Å) for complexes **1**, **2** and **3** from reported X-Ray data.[9-11]

Atom 1	Atom 2	**1**	**2**	**3**
Mo	$C^{(1)}$	2.056(4)	2.024	2.010(4)
Mo	$C^{(2)}$	1.952(4)	1.959	1.944(4)
Mo	$C^{(3)}$	1.962(3)	1.959	1.951(4)
Mo	$C^{(4)}$	2.022(4)	2.026	2.028(4)
Mo	$N^{(1)}$	2.241(2)	2.243	2.271(3)
Mo	$N^{(2)}$	2.249(3)	2.243	2.200(3)
$C^{(1)}$	$O^{(1)}$	1.135(4)	1.141	1.134(5)
$C^{(2)}$	$O^{(2)}$	1.168(5)	1.154	1.159(5)
$C^{(3)}$	$O^{(3)}$	1.160(4)	1.154	1.160(5)
$C^{(4)}$	$O^{(4)}$	1.151(5)	1.146	1.139(5)
$C^{(5)}$	$C^{(6)}$	1.483(5)	1.439	1.456(5)

Table III.2. Angle (°) values for complexes **1**, **2** and **3** from reported X-Ray data.[9-11]

Atom 1	Atom 2	Atom 3	**1**	**2**	**3**
$C^{(1)}$	Mo	$C^{(2)}$	85.1(1)	85.9	84.0(1)
$C^{(1)}$	Mo	$C^{(3)}$	88.4(1)	85.9	87.0(2)
$C^{(1)}$	Mo	$C^{(4)}$	167.8(1)	167.6	168.6(2)
$C^{(1)}$	Mo	$N^{(1)}$	93.6(1)	95.4	92.3(1)
$C^{(1)}$	Mo	$N^{(2)}$	93.8(1)	95.4	97.0(1)
$C^{(2)}$	Mo	$C^{(3)}$	90.1(1)	93.2	91.0(2)
$C^{(2)}$	Mo	$C^{(4)}$	84.3(1)	85.6	87.7(1)
$C^{(2)}$	Mo	$N^{(1)}$	99.1(1)	96.6	96.5(1)
$C^{(2)}$	Mo	$N^{(2)}$	171.4(1)	170.2	168.3(1)
$C^{(3)}$	Mo	$C^{(4)}$	85.7(1)	85.6	85.4(2)
$C^{(3)}$	Mo	$N^{(1)}$	170.7(1)	170.2	172.4(1)
$C^{(3)}$	Mo	$N^{(2)}$	98.4(1)	96.6	100.7(1)
$C^{(4)}$	Mo	$N^{(1)}$	94.0(1)	94.5	96.3(1)
$C^{(4)}$	Mo	$N^{(2)}$	97.6(1)	94.5	92.7(1)
$N^{(1)}$	Mo	$N^{(2)}$	72.3(9)	73.6	71.8(1)

All complexes display a distorted octahedral geometry featuring two axial and two equatorial CO ligands centered on the metal atom. These complexes show equatorial CO ligands slightly longer than the axial ones (Table III.1). While complexes **1** and **2** display similar Mo-$N^{(1)}$ and Mo-$N^{(2)}$ bond lengths, the unsymmetrical nature of **3** diimine ligand results in different Mo-N values. The shortest bond length is obtained on the indolizine side (Mo-$N^{(2)}$), as a result of a better electronic donation of the py-indz *vs*. py towards the metal center. Table III.2 displays similar $N^{(1)}$-Mo-$N^{(2)}$ angles for all complexes (72.7 +/- 0.9°), hence indicating that the diimine ligand does not impact

the geometrical pattern. In addition, all three complexes show a $C^{(1)}$-Mo-$C^{(4)}$ axis of 168°, which is bent away from the diimine ligand.

All complexes **1**-**3** have been characterized by FTIR, UV-Vis-NIR and ^{1}H-RMN. Table III.3 shows the ν_{CO} frequency obtained from IR analysis of the three complexes in THF and MeCN. The values are typical of $[Mo(CO)_4(diimine)]$ systems with four ν_{CO} bands in the 1800–2020 cm^{-1} range, hence confirming that the coordination sphere of the complexes is maintained while changing from solid-state to the organic solvents.

UV-Vis spectroscopic studies of the complexes in THF and MeCN were also carried out. Absorption maxima of the systems are characterized by a MLCT transition between the diimine ligand and the metal center in the 400-500 nm wavelength region (Table III.4), similar to the behavior observed for other $[M(CO)_4(diimine)]$ systems.[1, 2, 4, 12] No noticeable differences in the absorption spectra between **1**, **2** and **3** systems were observed.

Table III.3. ν_{CO} frequency (in cm^{-1}) of **1**, **2** and **3** in THF and MeCN.

	THF	MeCN
Complex **1**	1840, 1882, 1890, 2012	1831, 1876, 1904, 2012
Complex **2**	1841, 1880, 1896, 2012	1828, 1867, 1902, 2015
Complex **3**	1838, 1877, 1896, 2010	1828, 1870, 1899, 2014

Table III.4. Absorption maxima λ_{max} / nm (ε / M^{-1} cm^{-1}) of **1**, **2** and **3** in THF and MeCN.

	THF	MeCN
Complex **1**	470 (3580)	473 (5320)
Complex **2**	448 (3300)	475 (4920)
Complex **3**	429 (3000)	445 (4000)

III. Electrochemical studies of **1**, **2** and **3** complexes under argon

Electrochemical techniques (essentially cyclic voltammetry (CV)) have been applied to study the redox properties of complexes **1**, **2** and **3**. All CV experiments were performed in a three-electrode cell under an inert atmosphere (argon) in a glovebox. Distilled MeCN, THF and DFB were used as solvents containing 0.1 M NBu_4PF_6 as electrolyte and 1 mM of complex **1**, **2** or **3**. All potentials are reported against the Fc^+/Fc standard potential. A boron-diamond doped (BDD) or glassy carbon (GC) disc were used as a working electrode. Cyclic voltammetry techniques of **1**, **2** and **3** have been applied in MeCN, THF and DFB solvents. While the redox behavior of **1** has already been widely reported in literature, the electrochemical responses of complexes **2** and **3** have not been described so far.[1, 13]

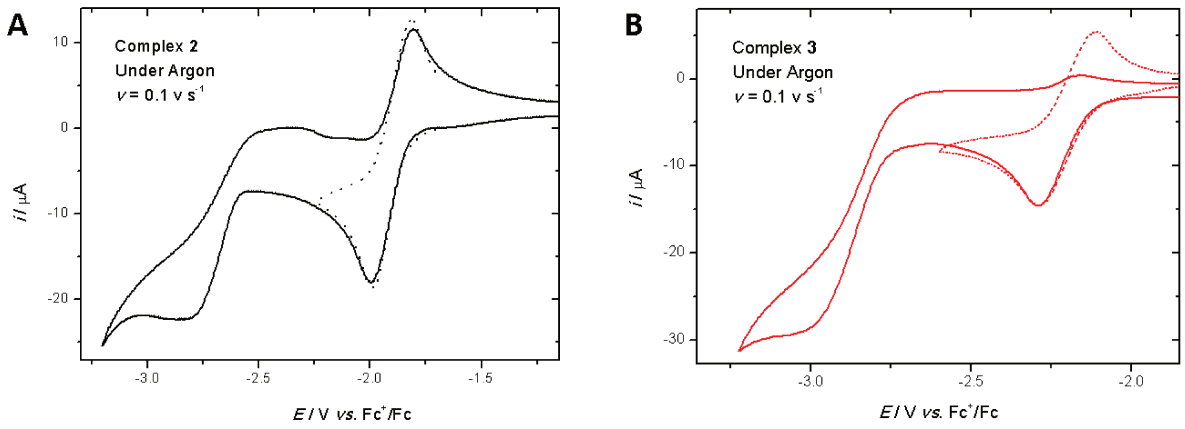

Figure III.6. CVs of complexes **2** (A) and **3** (B) in THF under Ar. Conditions: 1 mM of complex, 0.1 M NBu_4PF_6, BDD working electrode, v = 0.1 V s^{-1}.

Electrochemical data for the reduction processes in different solvents are gathered in Table III.5. No second reduction process could be observed for **3** in DFB due to the restricted potential window of this solvent.

Table III.5. Voltammetric data [$E_{1/2}$ / V *vs.* Fc^+/Fc, v = 0.1 V s^{-1}] for complexes **1**, **2** and **3** (1 mM) in MeCN, THF and DFB. Supporting electrolyte NBu_4PF_6 0.1 M, BDD working electrode.

	Solvent	Complex **1**	Complex **2**	Complex **3**
1st reduction	MeCN	-1.90	-1.98	-2.25
	THF	-1.85	-1.90	-2.20
	DFB	-1.90	-2.00	-2.20
2nd reduction	MeCN	-2.65 [a]	-2.80 [a]	-2.85 [a]
	THF	-2.55 [a]	-2.75 [a]	-2.90 [a]
	DFB	-2.60 [a]	-2.85 [a]	[b]

[a] Irreversible cathodic peak; [b] Not detected because of the restricted potential window of the solvent

The complex **2** displayed a similar CV signature in THF as that reported for **1** under argon, featuring a first reversible reduction at ca. -1.90 V *vs*. Fc^+/Fc and a second irreversible reduction at ca. -2.75 V *vs*. Fc^+/Fc (Figure III.6.A). The same redox behavior was obtained in other solvents or when using a GC working electrode.

The complex **3** (Figure III.6.B) showed a voltammetric response similar to those of **1** and **2**, but at more negative potential values (by ca. -200 mV). This shift can be ascribed to the stronger donor effect of the py-indz moiety compared to phen and bpy. Moreover, while complexes **1** and **2** show similar cathodic peak current values (i_{pc}) for both reduction processes, the current of the second reduction peak for **3** is at least twice that of the first reduction peak. Notably, this current enhancement seemed even more important in MeCN, indicating a possible reaction of the bis-reduced intermediate with the solvent under inert atmosphere.

This assumption was confirmed from the results obtained in cyclic voltammetry of complex **3** at different scan rates in THF (Figure III.7). While the first reduction process remained reversible whatever v in the -1.90 V to -2.60 V potential range (Figure III.7, top), a loss of reversibility was observed for this system when scanning at lower potential values until -2.80 V for low scan rates (10 to 200 mV s^{-1}) as shown in Figure III.7 (bottom). Such as loss of reversibility when reaching the second process was not observed for complexes **2** (Figure III.8, top) and **1** (Figure III.8, bottom).

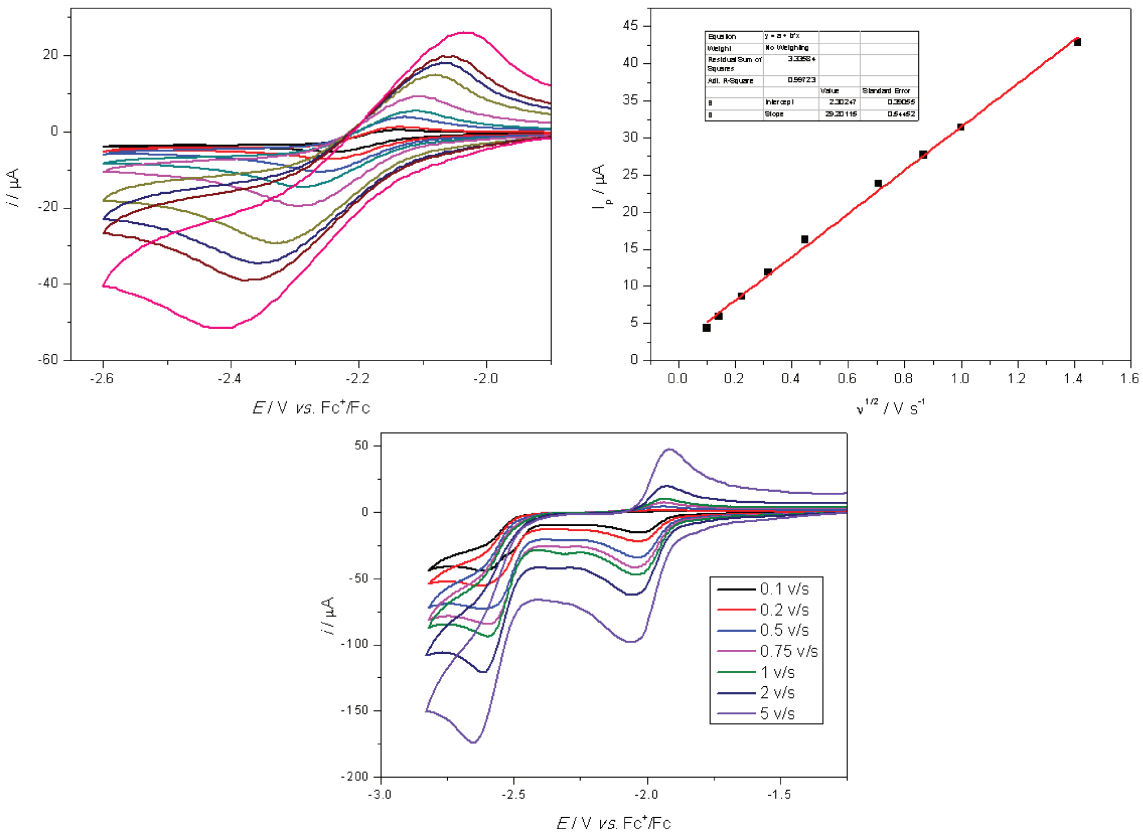

Figure III.7. CVs of complex **3** at 0.01 < *v* < 2 V s^{-1} for different potential range. Top right panel: plots of i_{pc} *vs.* $v^{1/2}$ for the first reversible reduction process. Conditions: 1 mM of complex, THF / NBu_4PF_6 0.1 M, BDD WE, under argon.

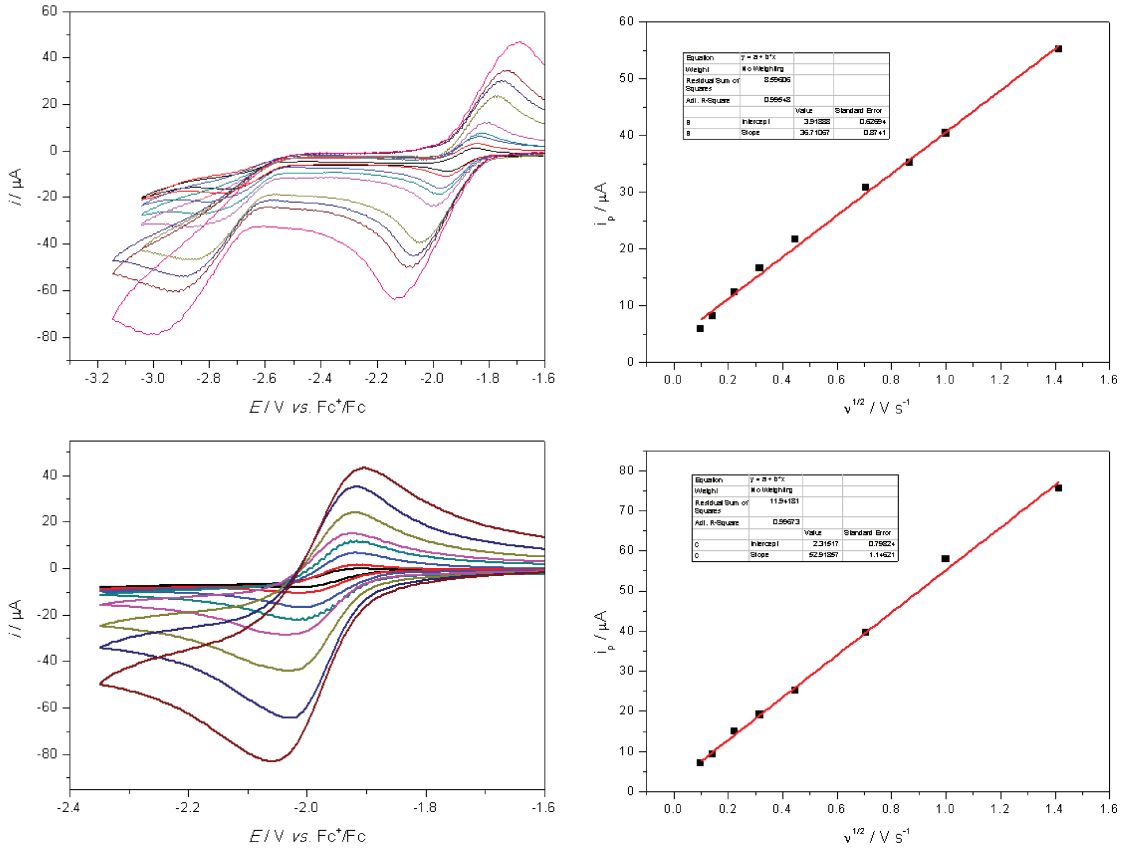

Figure III.8. CVs of complex **2** (top) and **1** (bottom) at 0.01 V s^{-1}< *v* < 2 V s^{-1}. Top right panels: plots of i_{pc} *vs*. $v^{1/2}$ for the first reversible system. Conditions: 1 mM of complex, THF / NBu_4PF_6 0.1 M, BDD WE, under argon.

The reversibility of the first reduction process for complexes **1**, **2** and **3** indicated a simple diffusion limited electron-transfer reaction (E step) with no coupled chemical reaction (C step) occurring at the time scale of the experiment. ^{1}H NMR DOSY experiments in d^8-THF/0.1M KPF_6 (Figure III.9) were carried out to obtain diffusion coefficients *D* of **1**, **2** and **3** (Table III.6). The resulting *D* values were then used to calculate the number of electrons (*n*) involved in the first reduction process by using the Randles-Sevcik equation, from the linear plots of i_{pc} *vs*. $v^{1/2}$ (Figures III.7 and III.8). The calculations indicated that the first reduction is monoelectronic.

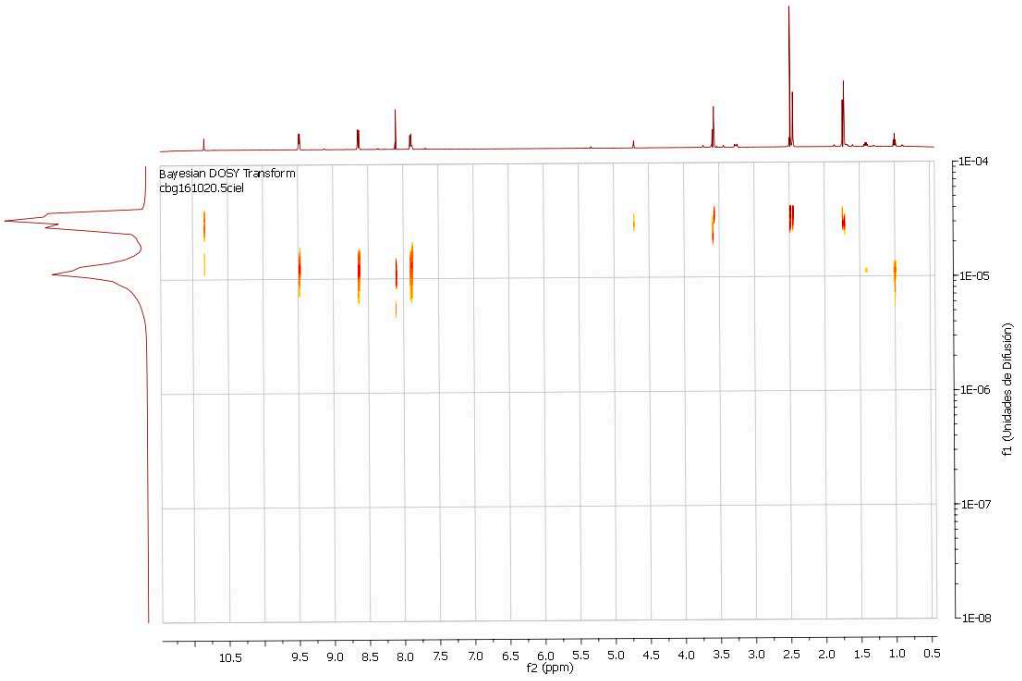

Figure III.9. DOSY ^{1}H NMR spectrum of complex **2** in d^8-THF/0.1 M KPF_6.

Table III.6. Diffusion coefficients *D* ($cm^2\ s^{-1}$) in d^8-THF/0.1M KPF_6 for complexes **1**-**3** from ^{1}H NMR DOSY experiments, and calculated values of the number of electrons *n* for the first reduction process according to the Randles-Sevcik equation.

	D ($10^{-5}cm^2\ s^{-1}$)	*n*
Complex **1**	1.00	1.06
Complex **2**	1.21	1.18
Complex **3**	0.93	1.15

IV. Spectroelectrochemical studies of **1**, **2** and **3** under argon

In order to better characterize the reduced species of complexes **1**, **2** and **3** detected by cyclic voltammetry, IR and UV-vis-NIR spectroelectrochemical experiments were performed under inert atmosphere (argon).

IV.1. UV-vis spectroelectrochemical experiments under Ar

Absorption spectra of THF, MeCN or DFB solutions of **1**, **2** and **3** with 0.1 M NBu_4PF_6 as supporting electrolyte were obtained under thin layer conditions (0.2 mm optical path). Monoelectronic reduction of complexes **2** and **3** induced several changes of the UV-Vis signature (Table III.7). Whatever the solvent, the resulting spectra of **2** and **3** showed several similarities with that obtained for **1**, i.e. two new absorbance bands in the 400 and 600 nm region (Figure III.10). An additional band at 830 nm was detected for complex **2** in THF. Less intense absorption bands together with red-shifted absorption spectrum for complexes $\mathbf{2}^{\bullet-}$ and $\mathbf{3}^{\bullet-}$ *vs*. $\mathbf{1}^{\bullet-}$ could indicate a different charge distribution over the ligand framework.

Table III.7. UV-vis spectroscopic data of neutral and mono-reduced complexes **1**, **2** and **3** in different solvents.

Complexes	λ (nm) / THF	λ (nm) / MeCN	λ (nm) / DFB
1	267, 297, 472	264, 298, 468	294, 471
2	263, 390, 469	260, 393, 451	288, 394, 467
3	255, 340, 444	237, 338, 436	287, 406, 459
$\mathbf{1}^{\bullet-}$	368, 497, 531	367, 492, 526	364, 539, 597, 641
$\mathbf{2}^{\bullet-}$	357, 564, 615, 832	374, 566, 608	385, 578, 625
$\mathbf{3}^{\bullet-}$	260, 410, 595	420, 440, 588	351, 612

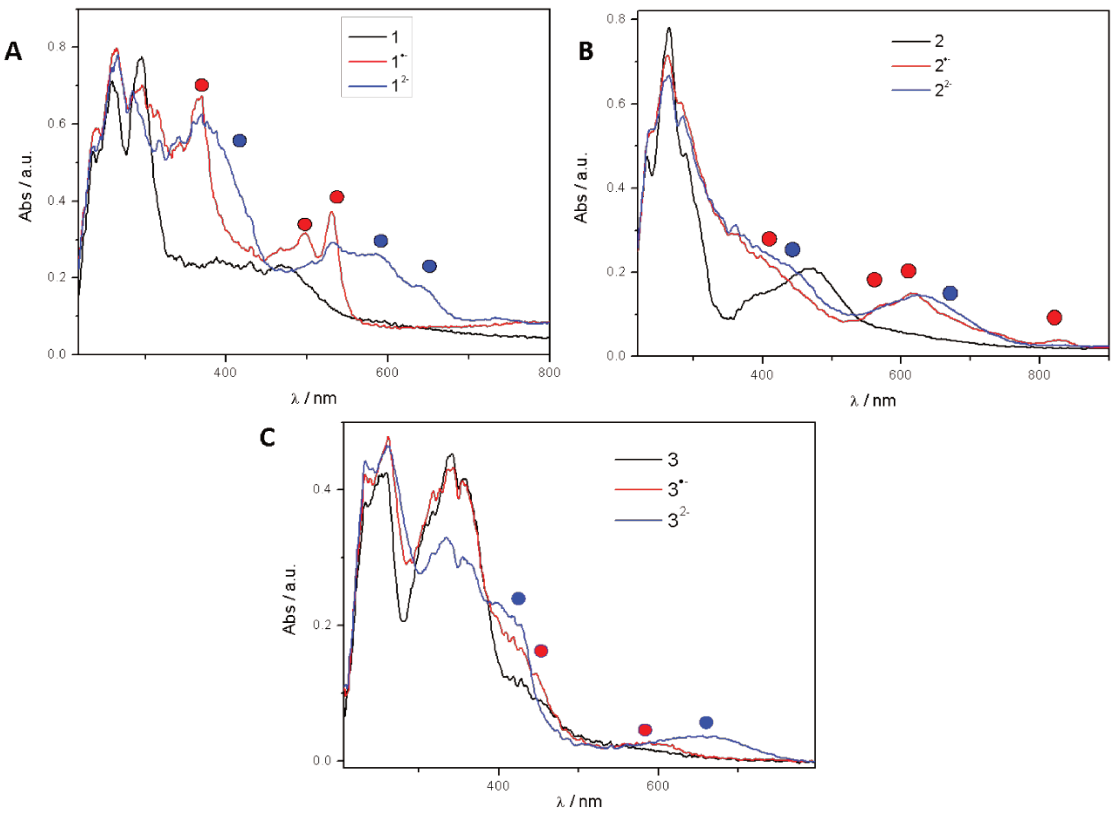

Figure III.10. UV-Vis spectra of neutral (black), mono-reduced (red) and bis-reduced (blue) species generated upon spectroelectrochemical experiments in THF / NBu_4PF_6 0.1 M starting from (A) complex **1**, B) complex **2**, and C) complex **3**. Conditions: 1 mM of complex, BDD working electrode, thin layer condition, 0.2 mm optical path, under Ar.

Figure III.10 shows also the UV-Vis spectra of complexes **1**, **2** and **3** obtained for the second reduction process (blue curves) in THF. As already mentioned in Chapter II, the second reduction of complex **1** was shown to be solvent-dependent since a tricarbonyl $[Mo(CO)_3(bpy)]^{2-}$ species was detected in THF while a protonated tetracarbonyl complex $[Mo(CO)_4(H^+\text{-bpy})]^-$ was rather observed in MeCN. For complexes **2** and **3**, the UV-Vis signatures in THF were similar to that obtained for **1** in THF, thus suggesting the formation of tricarbonyl species $[Mo(CO)_3(phen)]^{2-}$ and $[Mo(CO)_3(py\text{-}indz)]^{2-}$. However, since the bands are not intense, these assumptions have to be taken with caution.

Results using DFB as a solvent did not diverge with the absorption spectrum obtained in THF for all complexes, hence suggesting that the formation of tricarbonyl bis-reduced species formed during the second reduction processes is favored in solvents with a substantial water content.

The UV-Vis signature of complex **2** in acetonitrile did not present any significant differences with the results obtained in THF and DFB (Table III.8). This is however not sufficient to concrete if a protonated tetracarbonyl species $[Mo(CO)_4(H^+\text{-phen})]^-$ was formed. In the case of **3**, the second reduction induced the surge of a considerable band at 280 nm (less intense in THF). This band can be correlated to the increase of current at this potential detected by cyclic voltammetry in MeCN. Possibly, it corresponds to the coordination of a solvent molecule following the loss of one CO ligand.

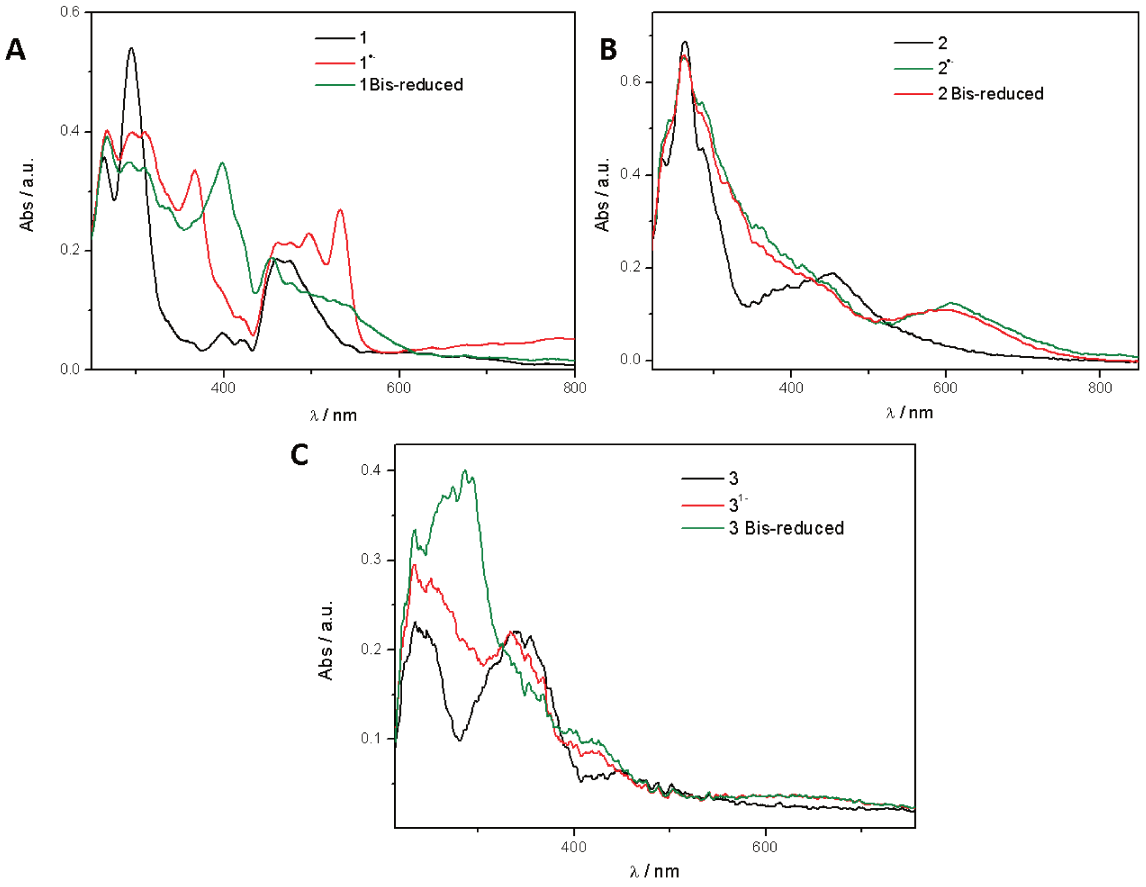

Figure III.11. UV-Vis spectra of neutral (black), mono-reduced (red) and bis-reduced (green) species generated upon spectroelectrochemical experiments in MeCN / NBu_4PF_6 0.1 M starting from A) complex **1**, B) complex **2**, and C) complex **3**. Conditions: 1 mM of complex, BDD working electrode, thin layer condition, 0.2 mm optical path, under Ar.

Table III.8. UV-vis spectroscopic data of the bis-reduced species in THF and DFB.

Complexes	λ (nm) / THF	λ (nm) / DFB
$[Mo(CO)_3(bpy)]^{2-}$	369, 591, 638	400, 587, 635
$[Mo(CO)_3(py\text{-}indz)]^{2-}$	435, 634	369, 614
$[Mo(CO)_3(py\text{-}indz)]^{2-}$	410, 662	361, 607

Table III.9. UV-vis spectroscopic data of the bis-reduced species in MeCN.

Complexes	λ (nm) / MeCN
$[Mo(CO)_4(H^+\text{-}bpy)]^-$	391, 575
$[Mo(CO)_3(phen)]^{2-}$	376, 604
$[Mo(CO)_3(py\text{-}indz)]^{2-}$	288, 422, 665

IV.2. IR spectroelectrochemical experiments under Ar

Infrared spectroelectrochemical experiments in THF or MeCN with 0.1 M NBu_4PF_6 as electrolyte and 5 mM of complex complemented the information obtained from UV-Vis absorption spectra of reduced-species of complexes **1**, **2** and **3**. An ATR-IR probe was incorporated in a modified three-electrode cell such that thin-layer conditions could be obtained. For that purpose, a glassy carbon (GC) working electrode was cone-dipped. Chronoamperometry (CA) techniques were applied at potential values slightly more negative that the peak potentials of each reduction processes to favor fast transformation.

As observed for UV-Vis spectroelectrochemistry experiments, a uniform IR response was detected during the first reduction process for all complexes system whatever the solvent (Table III.10). The 30 cm^{-1} shift of the ν_{CO} bands upon monoelectronic reduction is in agreement with the formation of mono-reduced radical $[M(CO)_4(diimine)]^{\bullet-}$ species,[1, 14] confirming the assignation of the weak absorption spectra obtained for **2** and **3** (Figure III.12) as the formation of tetracarbonyl $[Mo(CO)_4(phen)]^{\bullet-}$ and $[Mo(CO)_4(py\text{-}indz)]^{\bullet-}$ complexes.

Table III.10. Infrared spectroscopic data of neutral and mono-reduced species of complexes **1**, **2** and **3** in THF and MeCN.

Complexes	ν_{CO} (cm^{-1}) / THF	ν_{CO} (cm^{-1}) / MeCN
1	1840,1880,1900,2012	1831, 1876, 1904, 2012
2	1840,1880,1899,2012	1828, 1867, 1902, 2015
3	1836,1877,1895,2012	1828, 1870, 1899, 2014
$\mathbf{1}^{\bullet-}$	1803,1842,1870,1991	1799, 1846, 1871, 1993
$\mathbf{2}^{\bullet-}$	1800,1842,1870,1991	1795, 1844, 1869, 1990
$\mathbf{3}^{\bullet-}$	1800,1839,1863,1989	1797, 1842, 1870, 1989

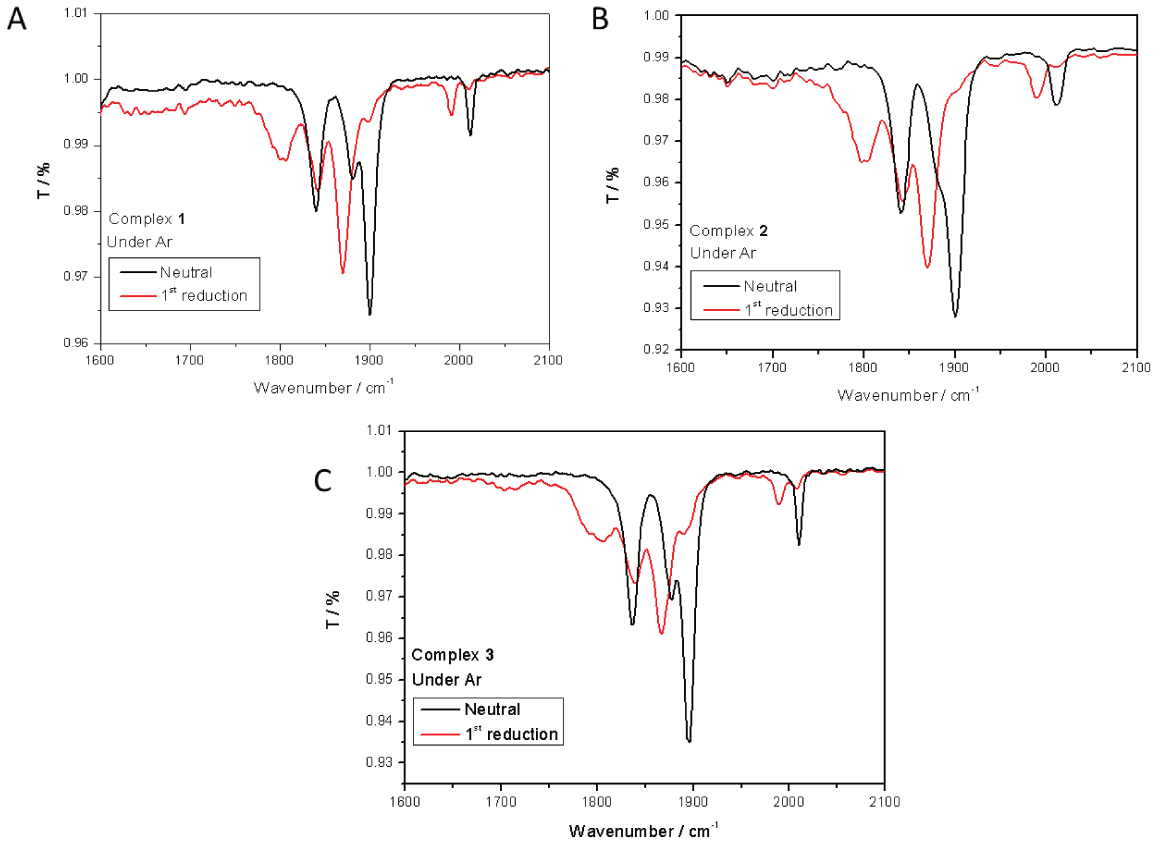

Figure III.12. Infrared spectra of neutral (black) and mono-reduced (red) species obtained from IR-SEC in THF for A) complex **1**, B) complex **2**, and C) complex **3**. Conditions: 5 mM of complex, 0.1 M NBu_4PF_6, GC working electrode, under Ar.

IR spectroelectrochemical studies showed that the second reduction process is solvent dependent, as already observed in UV-vis spectroelectrochemical measurements. In dry THF (in glovebox), ν_{CO} bands assigned to tricarbonyl bis-reduced $[Mo(CO)_3(diimine)]^{2-}$ species were identified (Figure III.13). Interestingly, no protonated tetracarbonyl $[Mo(CO)_4(H^+\text{-phen})]^-$ and $[Mo(CO)_4(H^+\text{-py-indz})]^-$ species were detected when performing experiments with less-dried THF (outside the glovebox) under inert atmosphere. Such a behavior is in strong contrast with complex **1** which showed a switch from $[Mo(CO)_3(bpy)]^{2-}$ to $[Mo(CO)_4(H^+\text{-bpy})]^-$ while increasing water content. This suggests that the charge localization at the doubly-reduced state of bpy may be significantly different than that of phen and py-indz systems.

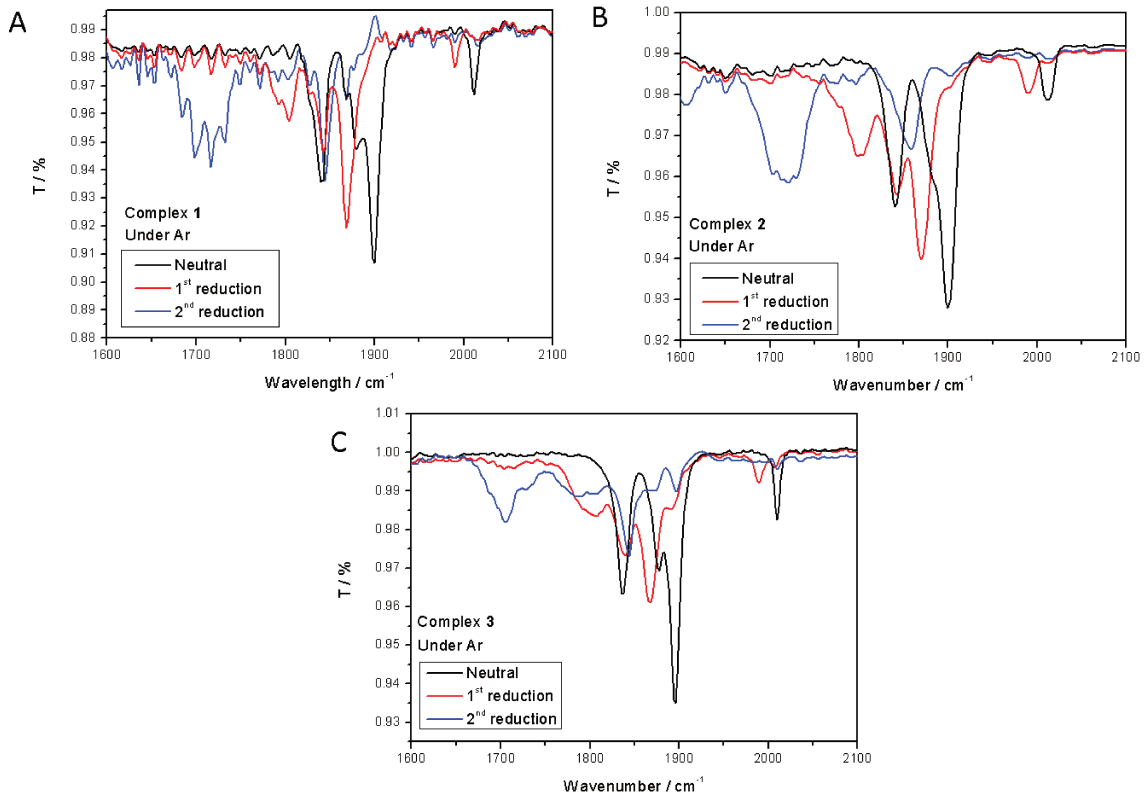

Figure III.13. Infrared spectra of neutral (black), mono-reduced (red) and bis-reduced (blue) and species in THF for A) complex **1**, B) complex **2**, and C) complex **3**. Conditions: 5 mM of complex, 0.1 M NBu_4PF_6, GC working electrode, under Ar.

In MeCN, the second reduction of complexes **2** and **3** led to similar IR spectra as those obtained in THF (Figure III.14.B,C), in contrast to complex **1** (formation of $[Mo(CO)_4(H^+\text{-bpy})]^-$,Figure III.14.A). As observed in Figure III.6, the electrochemical behavior of complexes **2** and **3** during the second reduction processes in MeCN, especially in the case of **3**, could involve an unidentified follow up chemical reaction. In particular, the appearance of an unassigned band at 2244 cm^{-1} in the C≡N region (Figure III.15), could indicate the possible formation of $[Mo(CO)_3(CH_3CN)(diimine)]^-$ species.

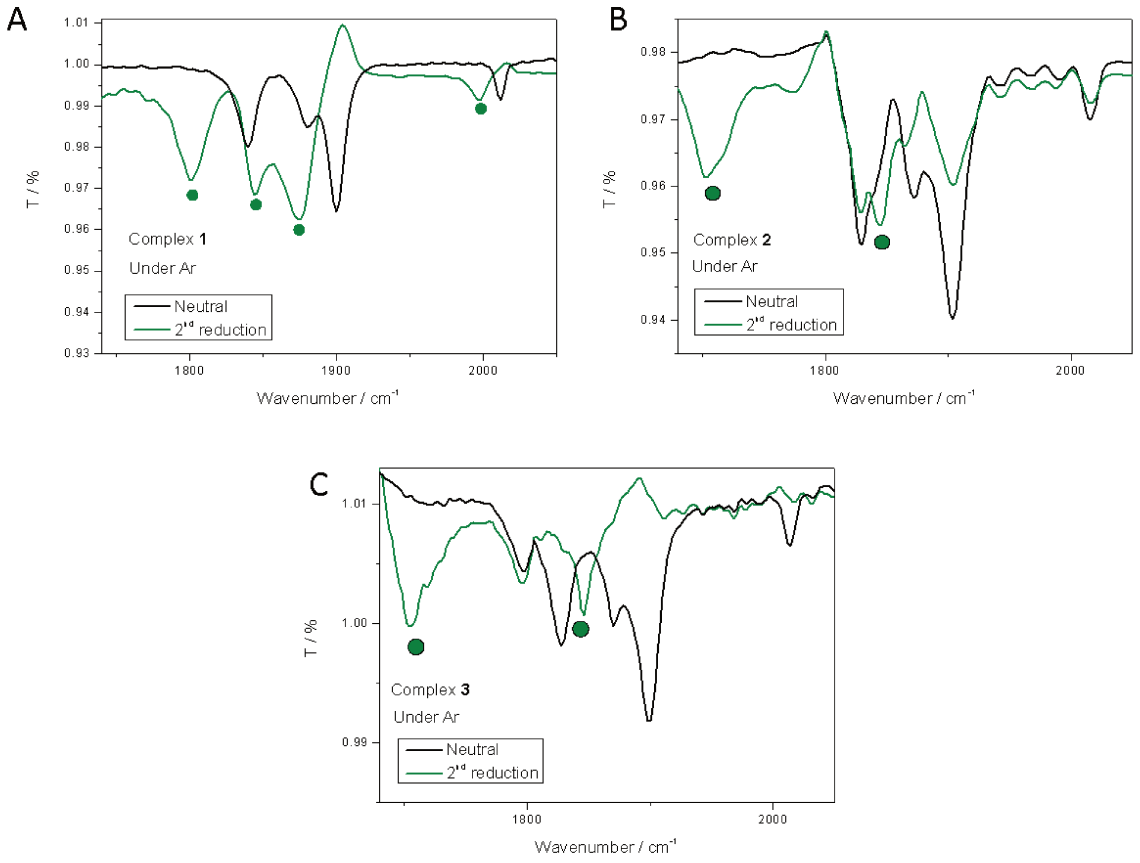

Figure III.14. Infrared spectra of neutral (black) and bis-reduced (green) and species in MeCN for A) complex **1**, B) complex **2**, and C) complex **3**. Conditions: 5 mM of complex, 0.1 M NBu_4PF_6, GC working electrode, under Ar.

Table III.11. Infrared spectroscopic data of bis-reduced species of complexes **1**, **2** and **3** in THF.

Complexes	ν_{CO} (cm^{-1}) / THF
$[Mo(CO)_3(bpy)]^{2-}$	1706, 1725, 1846
$[Mo(CO)_3(phen)]^{2-}$	1702, 1718, 1857
$[Mo(CO)_3(py\text{-}indz)]^{2-}$	1706, 1844

Table III.12. Infrared spectroscopic data of bis-reduced species of complexes **1**, **2** and **3** in MeCN.

Complexes	ν_{CO} (cm^{-1}) / THF
$[Mo(CO)_4(H^+\text{-}bpy)]^-$	1800, 1844, 1874, 1997
$[Mo(CO)_3(phen)]^{2-}$	1703, 1772, 1843
$[Mo(CO)_3(py\text{-}indz)]^{2-}$	1703, 1846

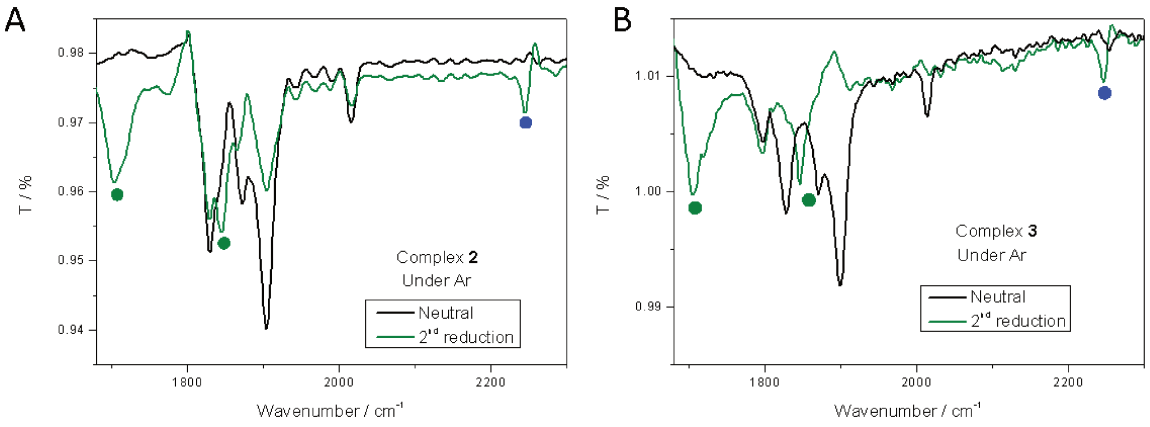

Figure III.15. Infrared spectra of neutral (black) and bis-reduced (green) species in MeCN for A) complex **2** and B) complex **3**. Green and blue dots indicate the novel species formed and the band at 2244 cm^{-1} respectively. Conditions: 5 mM of complex, 0.1 M NBu_4PF_6, GC working electrode, under Ar.

Thus, IR spectroelectrochemistry showed that the stability and reactivity of $[Mo(CO)_4(diimine)]$ bis-reduced species seemed to be affected by the structure of the diimine moiety, as emphasized by the spectroelectrochemical data of **1**, **2** and **3**. While two different bis-reduced species were detected for **1** depending on the solvent, a behavior replicated for $[Mo(CO)_4(bpy\text{-}(\mathbf{R})_2)]$ derivatives (see Chapter II), the tricarbonyl bis-reduced $[Mo(CO)_3(phen)]^{2-}$ and $[Mo(CO)_3(py\text{-}indz)]^{2-}$ were generated independently of the nature of the solvent.

IV.3. Near-IR spectroelectrochemical experiments under Ar

An uncommon characterization technique to study the nature of $[M(CO)_4(diimine)]$ reduced species is the near-IR spectroelectrochemistry, which was recently used for the characterization of group 6 complexes with pyridyl-mesoionic carbene ligands.[15] Here, near-IR spectroelectrochemical experiments have been carried out in solutions of 5 mM of complex in distilled THF / 0.1M NBu_4PF_6 under argon under thin layer conditions with a 0.2 mm optical path.

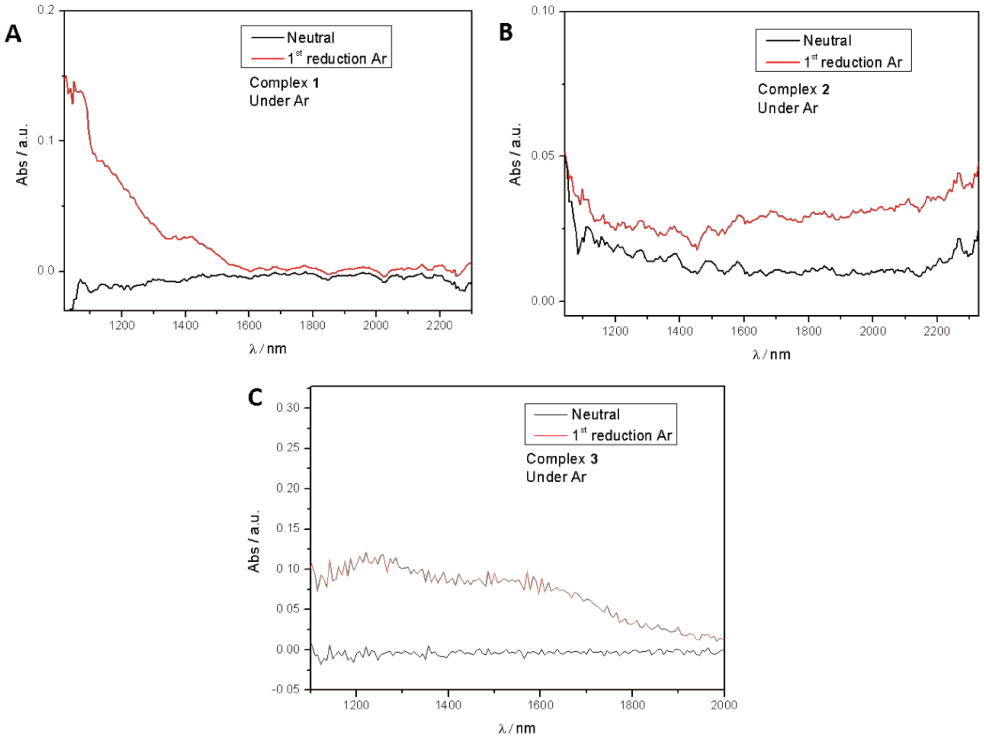

Figure III.16. Near-IR spectra of and neutral (black) and mono-reduced (red) species in THF for A) complex **1**, B) complex **2** (B) and C) complex **3**. Conditions: 5mM of complex, 0.1 M NBu_4PF_6, GC working electrode, 0.2 mm optical path, under Ar.

Figure III.16 confirms the radical nature of the first reduced species formed in THF for each system by the surge of bands in the NIR region. However, the signature significantly diverged with the nature of the complex: while mono-reduced species $\mathbf{1}^{\bullet-}$ and $\mathbf{3}^{\bullet-}$ displayed new bands in the 1100-1600 nm region, the signature of $\mathbf{2}^{\bullet-}$ was found at higher wavelength values (Table III.13). These behaviors can be assigned to an intra-ligand charge transfer transition over the diimine ligand due to the delocalization of the electronic charge provided during the redox process. Interestingly, these NIR bands disappeared when the applied potential reached the second reduction process, as exemplified in Figure III.17 for complex **1**.

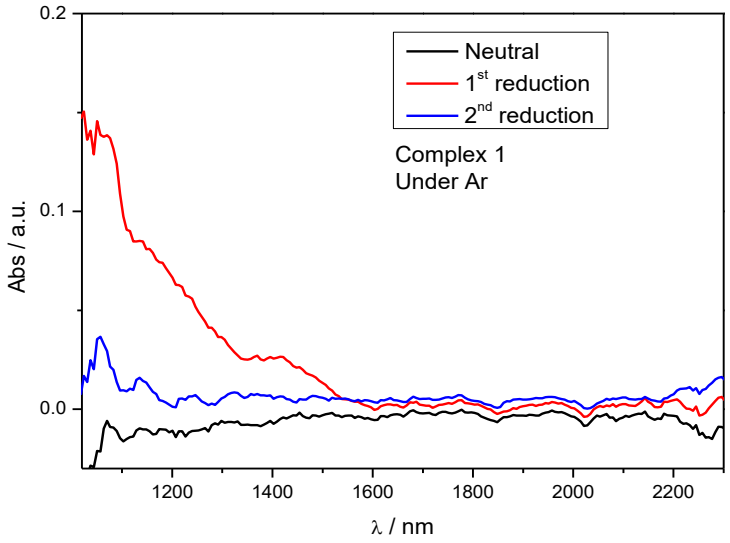

Figure III.17. Near-IR spectra of neutral (black), mono-reduced (red) and bis-reduced (blue) species of complex **1** in THF. Conditions: 5 mM of complex, 0.1 M NBu_4PF_6, GC working electrode, 0.2 mm optical path, under Ar.

Table III.13. Near-IR spectroscopic data of mono-reduced species in THF for complexes **1**, **2** and **3**.

Complexes	λ (nm) / THF
$\mathbf{1}^{\bullet-}$	1156, 1411
$\mathbf{2}^{\bullet-}$	1400-1900
$\mathbf{3}^{\bullet-}$	1228, 1595

V. CO_2 electrochemical catalysis of complexes **1**, **2** and **3**

Bubbling of carbon dioxide using a vacuum schlenk line for pre-purging into a three-electrode cell under an inert atmosphere allowed the study of mono and bis-reduced species of complexes **1**, **2** and **3** by cyclic voltammetry in MeCN, THF or DFB. All the potential values are given against E^0 (Fc^+/Fc). A boron-diamond doped (BDD) was used as working electrode. The comparative CVs of complexes **1**, **2** and **3** at v = 0.1 V s^{-1} in Ar- and CO_2–saturated solutions of THF / NBu_4PF_6 0.1 M are presented in Figure III.18. Clearly, a current enhancement (by approximatively a factor two), assigned to an electrocatalytic reaction, was observed under CO_2 for all complexes at potential values corresponding to the second reduction process. Moreover, a substantial loss of reversibility was observed on the reverse scan for the first reduction process for **2** and **3**.

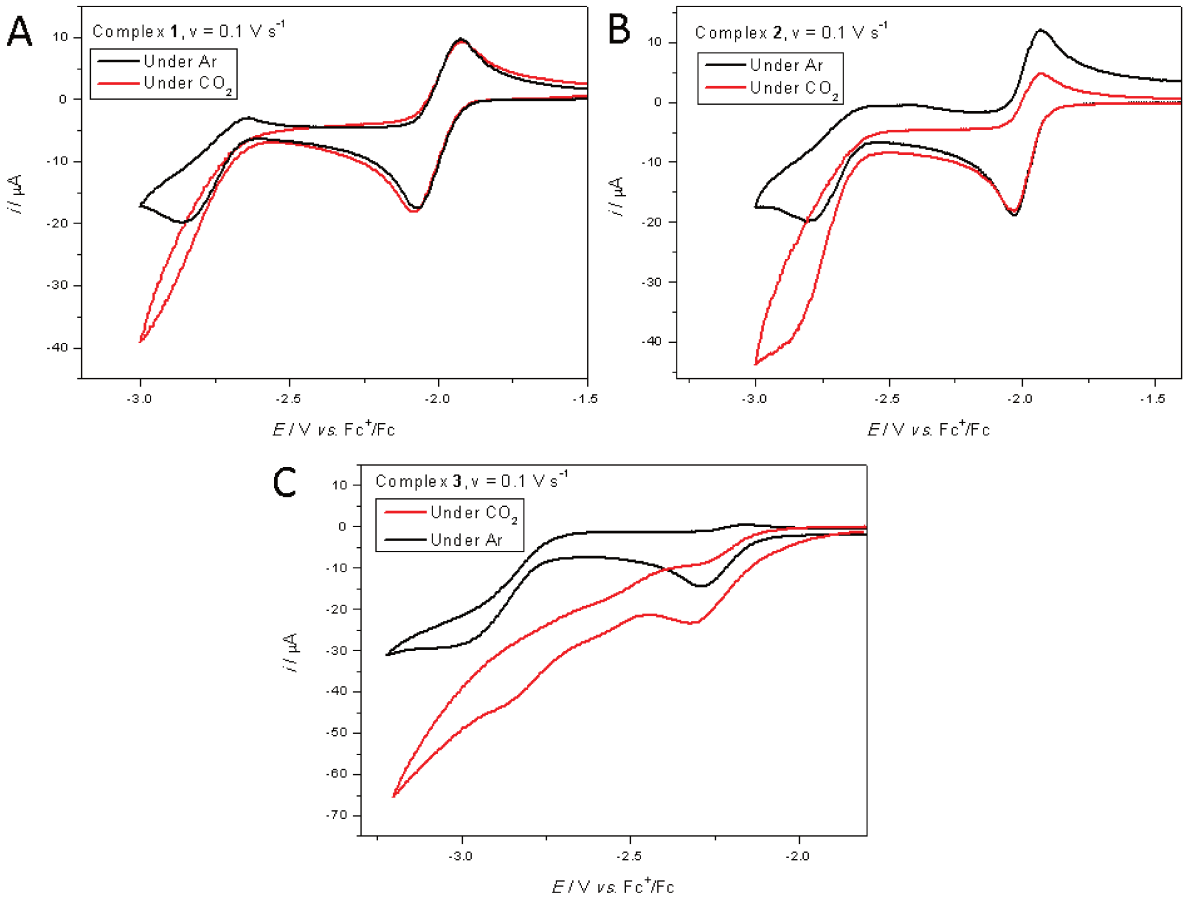

Figure III.18. CVs of A) complex **1**, B) complex **2**, and C) complex **3** in THF/NBu_4PF_6 0.1 M under Ar (black) and CO_2 (red). Conditions: 1 mM of complex, BDD working electrode, v = 0.1 V s^{-1}.

For further analysis, the catalytic current i_{cat} was determined from the peak current value for the second process under CO_2. The "non-catalytic" peak current i_p was taken from experimental data under argon. As shown in Table III.14, values of the i_{cat} / i_p ratio are slightly different depending on both the nature of the ligand and the solvent (note that no result could be obtained for system **3** in DFB due to the insufficient reduction potential window of this solvent).

Table III.14. Calculated values of the i_{cat} / i_p ratio of complexes **1**, **2** and **3** in dry solvents at v = 0.1 V s^{-1} at their respective second reduction potential.

	i_{cat}/i_p in THF	i_{cat}/i_p in MeCN	i_{cat}/i_p in DFB
Complex **1**	1.8	1.6	1.9
Complex **2**	1.9	1.4	1.6
Complex **3**	[a]	[b]	[c]

[a] Not comparable to other complexes because of peak potential shift; [b] No catalytic peak detected but high current increase instead; [c] Peak not detected because of solvent reduction

Overall, the use of MeCN as solvent induced lower catalytic responses for all complexes while higher currents were obtained when using THF or DFB. This effect may result from the competitive role of acetonitrile (*vs*. CO_2) upon coordination to the metal center of $[Mo(CO)_3(diimine)]^{2-}$ species. Noteworthy, the complex **3** displayed a different behavior than the other two complexes at v = 0.1 V s^{-1}. Firstly, a current enhancement was detected at potential values in-between the first and second reduction processes. This effect was not observed under inert atmosphere. In MeCN, this current enhancement was particularly intense and may be associated to the solvent decomposition. Secondly, CV study on the first reduction under CO_2 showed a loss of reversibility as shown in Figure III.19. This redox behavior is an indicator of either an ECE or EC_{cat} molecular process (E = Electrochemical, C = Chemical) which involves the reaction of a transient mono-reduced species with CO_2.

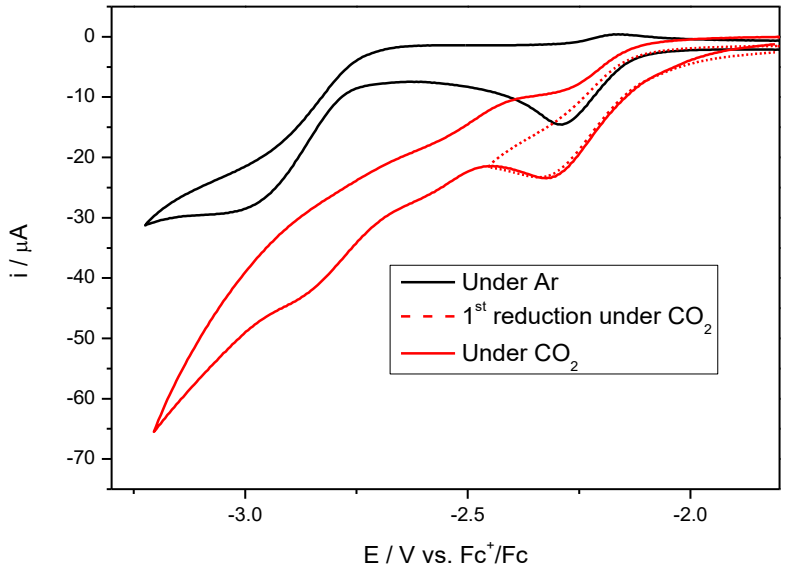

Figure III.19. CVs of complex **3** in THF under Ar (black) and CO_2 (red). The dashed curve corresponds to the CV for the first reduction process only. Conditions: 1 mM of complex, 0.1 M NBu_4PF_6, BDD working electrode, v = 0.1 V s^{-1}.

Consequently, an exhaustive study of the first reduction process was carried out for complexes **1**, **2** and **3** in dry THF under CO_2 and at different scan rates (0.01 V s^{-1} < v < 2 V s^{-1}). While reversibility was maintained for complex **1**, complex **2** (Figure III.20.B) showed a loss of reversibility at low scan rate, hence evidencing a reaction between the mono-reduced species and CO_2. This behavior was even more striking with complex **3** since an anodic peak on the reverse scan could be only detected for v > 1 V s^{-1} (Figure III.20.A).

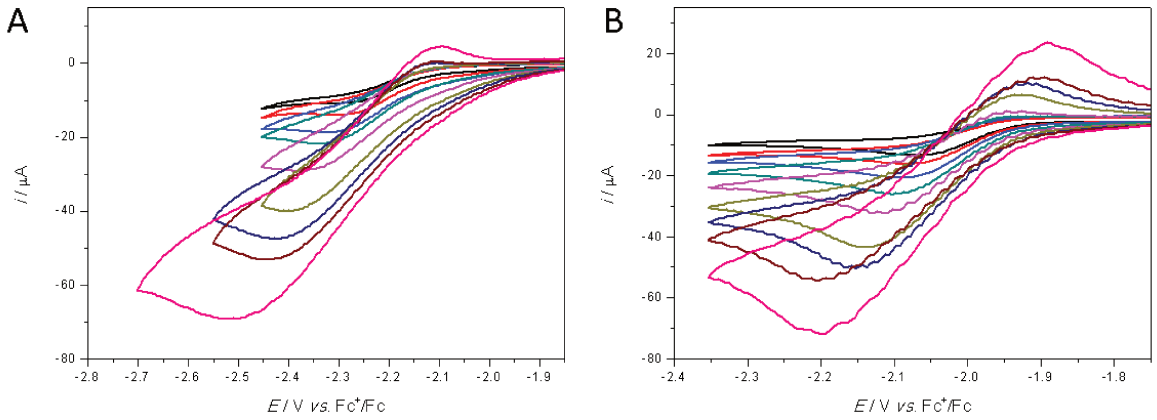

Figure III.20. CVs of A) complex **3** and B) complex **2** in THF under CO_2 at different scan rate (0.01 V s^{-1} < *v* < 2 V s^{-1}) for the first reduction process. Conditions: 1 mM of complex, 0.1 M NBu_4PF_6, BDD working electrode.

Comparison with the studies under argon (see Figures III.7 and III.8) demonstrated that CO_2 induced not only a loss of reversibility but also a net current enhancement at low scan rate for complexes **2** and **3**. Such effect can be more easily comprehended with comparative CVs (Ar/CO_2) for the three complexes for *v* < 0.1 V s^{-1}. As shown in Figure III.21, the current increase was clearly observed for the first reduction process for complexes **2** and **3**, whereas it remained the same for complex **1**. Additionally, the current intensity for the second reduction process was increased for complexes **1** and **2**, as expected for the catalytic reaction of the bis-reduced species with CO_2. However, for complex **3**, the situation was different since a slight current increase was observed at potential values in-between the first and the second reduction process at ca. -2.6 V (Figure III.21.C).

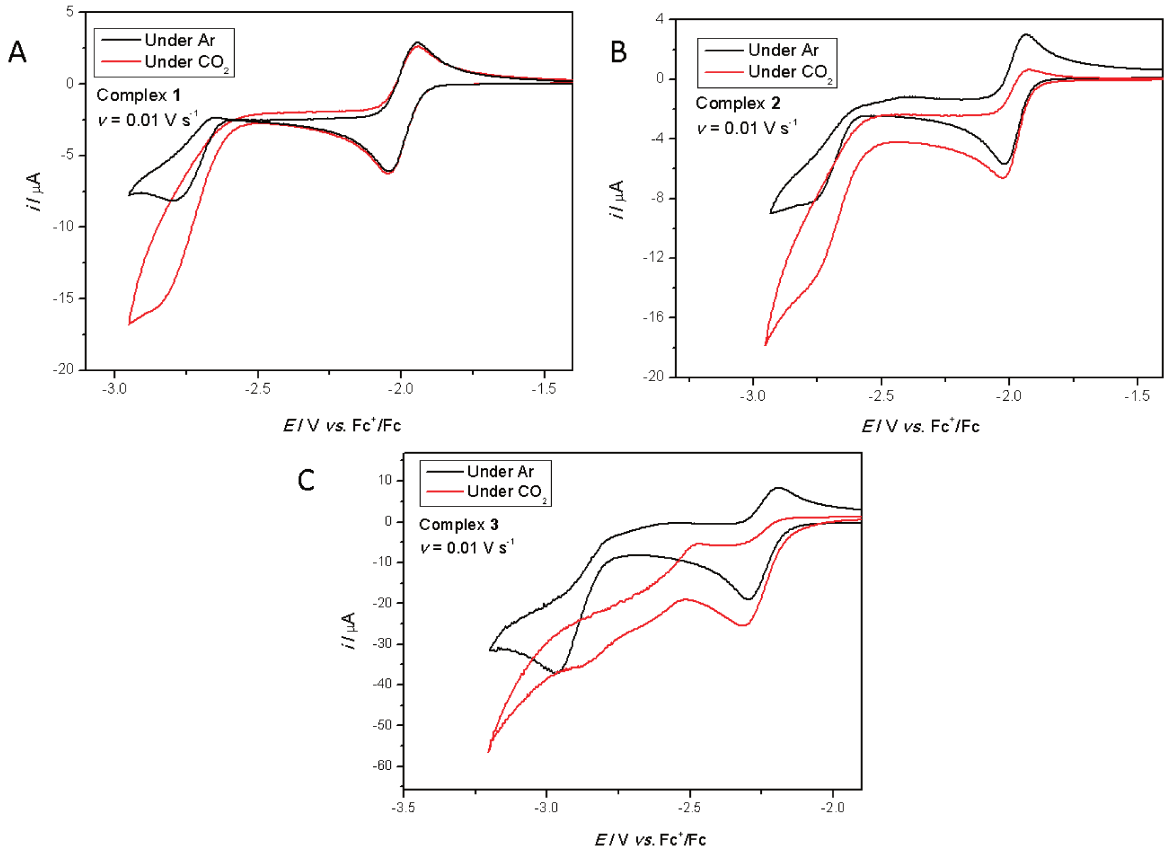

Figure III.21. CVs of A) complex **1**, B) complex **2** and C) complex **3** in THF under Ar (black) and CO_2 (red). Conditions: 1 mM of complex, 0.1 M NBu_4PF_6, BDD working electrode, v = 0.01 V s^{-1}.

In order to better understand this unprecedented reactivity with CO_2, CV studies of complexes **1**, **2** and **3** were carried out in THF at different scan rates in a CO_2 atmosphere under dry and "wet" (0.5 M H_2O) conditions. The aim was to enhance this reactivity by adding a proton source (H_2O) to the solution for a better analysis, and providing the occurrence or not of a potential proton-coupled electron transfer process. At first, control experiments demonstrated that water did not interfere with the mono-reduced complexes under argon. However, in presence of CO_2, a clear enhancement of current intensity as well as a higher loss of reversibility were observed when water was added, as shown by CVs at v = 0.01 V s^{-1} in Figure III.22**.** The same experiments carried out at higher scan rate (v = 0.1 V s^{-1}) showed the same behavior except that current enhancement was lower than at 0.01 V s^{-1} (Figure III.23), as expected for a rate-limited chemical process coupled to the electron transfer (ECE or EC_{cat}).

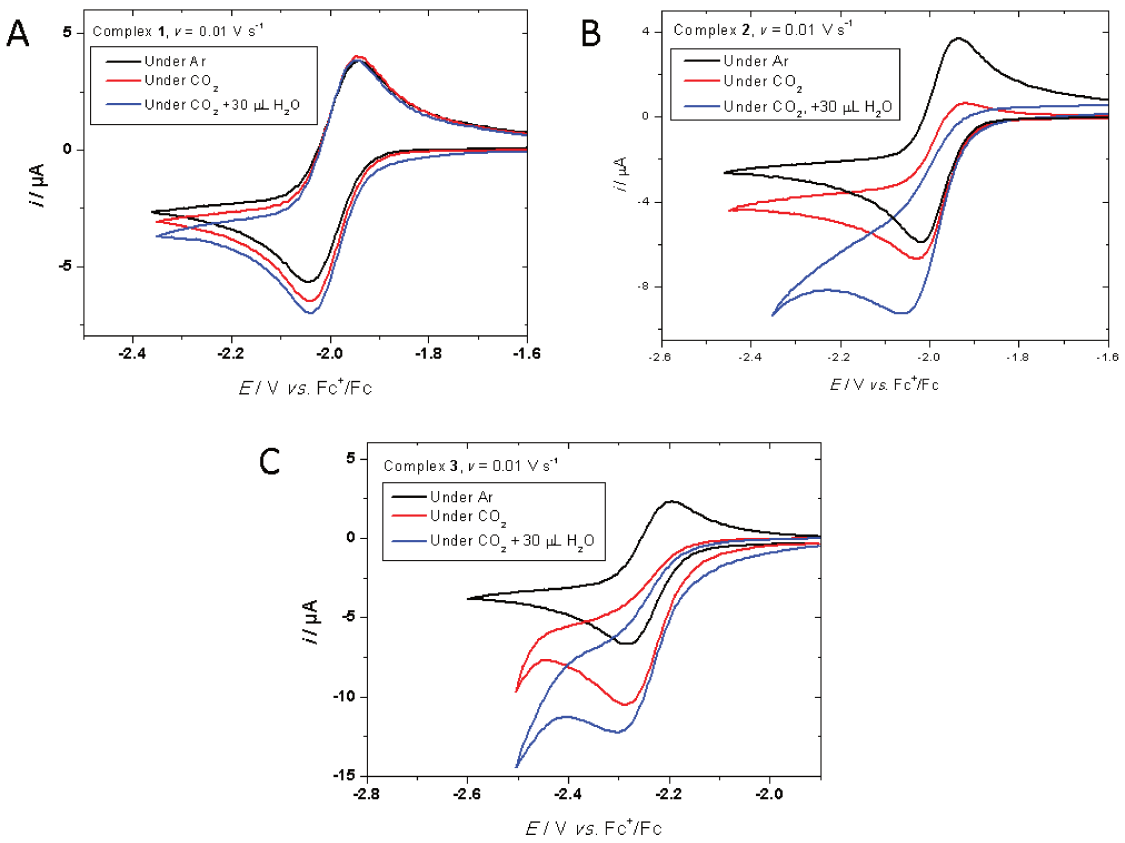

Figure III.22. CVs of A) complex **1**, B) complex **2** and C) complex **3** in THF under Ar (black), under CO_2 (red) and under CO_2 with added water (0.5 M, blue). Conditions: 1 mM of complex, 0.1 M NBu_4PF_6, BDD working electrode, v = 0.01 V s^{-1}.

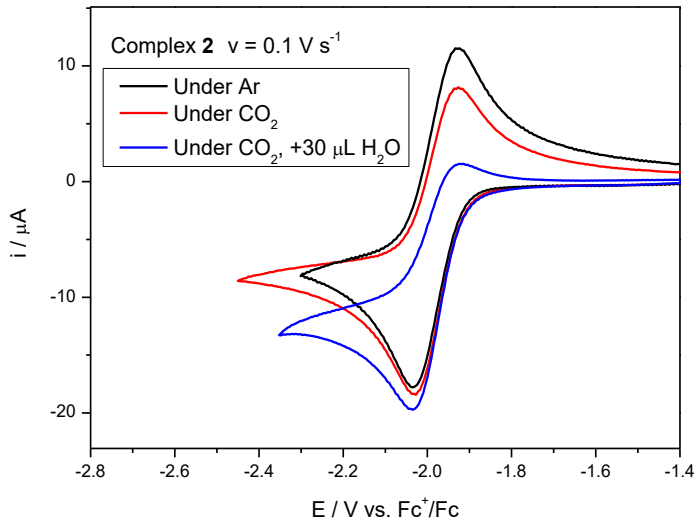

Figure III.23. CV of complex **2** in THF under Ar (black), under CO_2 (red) and under CO_2 with added water (0.5 M, blue). Conditions: 1 mM of complex, 0.1 M NBu_4PF_6, BDD working electrode, v = 0.1 V s^{-1}.

Aiming at determining the nature of this first reduction process, the current function (i_{pc} $v^{-1/2}$) derived from CVs was plotted against v for 0.01 V s^{-1} < v < 0.1 V s^{-1} (Figure III.24). Indeed, the variation of the current function with v is a good indicator of the general mechanistic pathway for chemically-coupled electrochemical processes, such as EC, CE, ECE or E_{cat}. In particular, a significant (> 10%) increase of the current function at low scan rate is indicative of an ECE or EC_{cat} process, the occurrence of this increase being dependent of the rate of the chemical reaction. The Figure III.24 clearly shows the different behavior for the three complexes. For complex **1**, the current function remains quasi-constant with v even in presence of water and CO_2, thus showing the poor reactivity of the mono-reduced species towards carbon dioxide. Conversely, for complexes **2** and **3** (Figures III.24.B and C), the addition of water to a saturated CO_2 solution increases the current function by almost a factor of two at low scan rates.

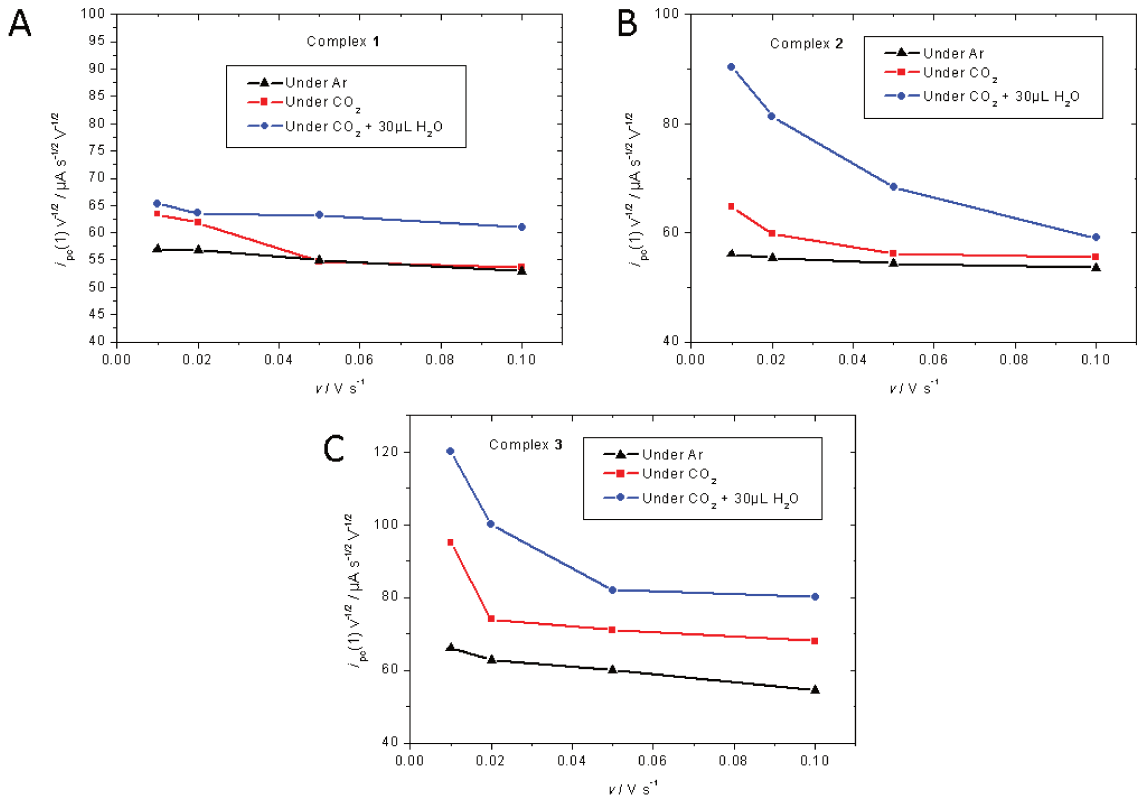

Figure III.24. Plots of $i_p\, v^{1/2}$ *vs.* v taken from CVs of A) complex **1**, B) complex **2** and C) complex **3** in THF under Ar (black), under CO_2 (red) and under CO_2 with added water (0.5 M, blue). Conditions: 1 mM of complex, 0.1 M NBu_4PF_6, BDD working electrode, 0.01 V s^{-1} < v < 0.1 V s^{-1}.

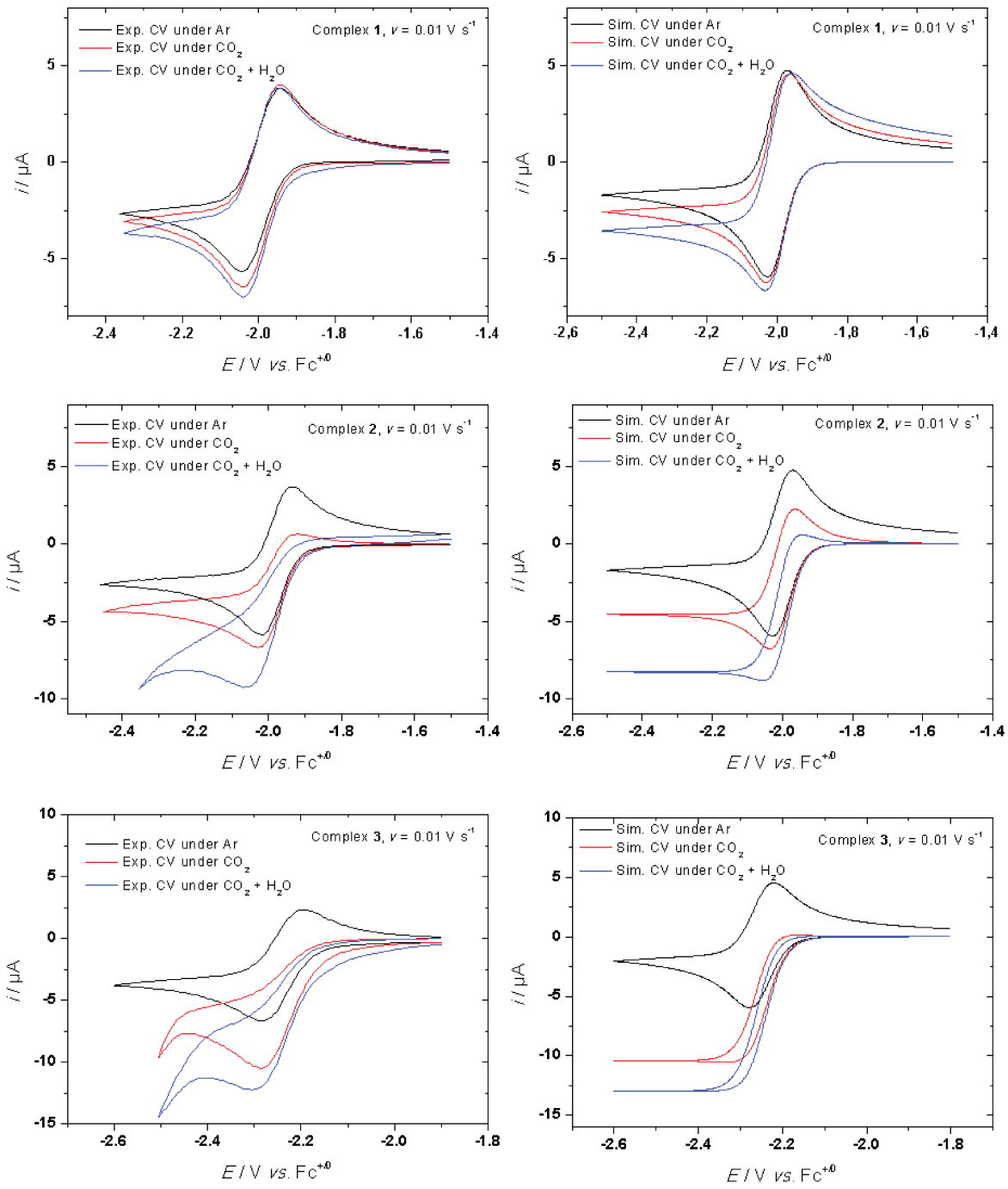

Figure III.25. Experimental (left) and simulated (right) CVs of complexes **1**, **2** and **3** (from top to bottom) in dry THF/NBu_4PF_6 0.1 M under argon (black), under CO_2 (red) and under CO_2 + H_2O (0.5 M, blue). Experimental conditions: 1 mM of complex, BDD working electrode, v = 0.01 V s^{-1}.

In order to better quantify the observed electrochemical changes at the mono-reduced state, simulation of the experimental CVs was carried out by using a voltammetric simulator package according to an EC_{cat} mechanism as shown in Scheme III.2. The experimental curves obtained for the three complexes were satisfactorily reproduced for low and high amounts of water by varying the kinetics of the catalytic reaction (Figure III.25). Interestingly, the cathodic peak current value behavior appeared as mainly controlled by the forward chemical rate constant which increased by a 10-fold manner from complex **1** to complex **3**. Although these data have to be taken with caution, they support the hypothesis that the ligand topology impacts the electron transfer kinetics for CO_2 conversion at the first reduction step.

ET steps:

$[Mo(CO)_4(L)] + e^- = [Mo(CO)_4(L)]^-$ $\quad k^0, E^0$

Homogeneous reactions:

$[Mo(CO)_4(L)]^- + CO_2 = [Mo(CO)_4(L)] + P1$ $\quad k_{f1}, k_{b1}$ (A)

$[Mo(CO)_4(L)]^- + CO_2 + H^+ = [Mo(CO)_4(L)] + P2$ $\quad k_{f2}, k_{b2}$ (B)

Scheme III.2. E_{cat} mechanism used for simulation of CVs obtained with $[Mo(CO)_4(diimine)]$ in dry THF/NBu_4PF_6 0.1 M under argon (black), under CO_2 (red) and under $CO_2 + H_2O$ (H^+).

Table III.15. Electrochemical data obtained from simulated CVs for complexes **1**, **2** and **3** according to Scheme III.2.

	E^0 / V	k_{f1} / M^{-1} s^{-1}	k_{b1} / M^{-1} s^{-1}	k_{f2} / M^{-2} s^{-1}	k_{b2} / M^{-1} s^{-1}
Complex **1**	-2.00	0.06	120	0.15	75
Complex **2**	-2.00	0.15	0.015	0.65	0.65
Complex **3**	-2.25	0.80	0.80	0.80	0.80

In summary, the electrochemical studies have shown that Mo-diimine complexes **1**, **2** and **3** do not work in the same way. Whereas complex **1** displayed a “classical” reactivity at the bis-reduced state towards CO_2, the phen and py-indz complexes **2** and **3** were unexpectedly reactive at the mono-reduced state since a moderate current enhancement was detected. A second information to be taken from electrochemical studies is that the reactivity can be exacerbated by addition of water. At last, these studies have emphasized that complex **3** does not behave as complexes **1** and **2** for the second reduction process since no catalytic wave could be detected.

VI. Spectroelectrochemical studies of **1**, **2** and **3** in CO_2

Electrochemical studies have shown that complexes **1**, **2** and **3** could react with carbon dioxide in THF according to different pathways. In order to clarify these processes and correlate them with the structures of the complexes, IR and UV-vis-NIR spectroelectrochemical techniques have been used to probe the various species generated upon reduction in CO_2-saturated THF solutions.

VI.1. UV-vis spectroelectrochemical experiments under CO_2

The Figure III.26 presents the UV-Vis spectra of complex **1** under Ar and CO_2 for the first and second reduction processes. Clearly, the mono-reduced species generated weakly interacts with CO_2 since a small absorbance loss was obtained under CO_2 compared to Ar (Figure III.26, red and orange curves). This result agrees with electrochemical data, which showed a small reversibility loss of the CV response in CO_2-saturated solution of THF. At the bis-reduced state (green and purple curves), the spectrum under Ar did not match with that under CO_2 as expected from the electrocatalytic behavior observed by CV. In particular, the absorption bands in the 500-600 nm region, shown in Figure III.26.A (green curve), were no longer detected under CO_2 (Figure III.26.B, purple curve).

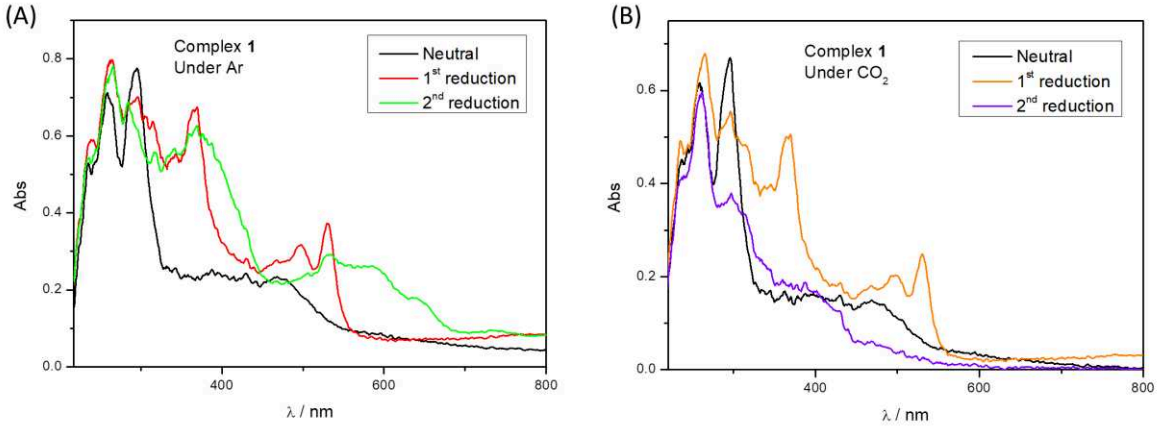

Figure III.26. UV-Vis-SEC spectra of complex **1** in THF A) under Ar at neutral state (black), after the first reduction (red) and second reduction (green), and B) under CO_2 at neutral state (black), after the first reduction (orange) and second reduction (purple). Conditions: 1 mM of complex, 0.1 M NBu_4PF_6, BDD working electrode.

For complex **2**, the situation was different (Figure III.27). A new species was detected after mono-reduction under CO_2, featuring absorption bands at λ_{max} = 396 and 475 nm (Figure III.27.B, orange curve). This was accompanied by the disappearance of the bands between 550 nm and 800 nm region related to mono-reduced $[Mo(CO)_4(phen)]^{\bullet -}$ species detected under Ar (Figure III.27.A, red curve). Such a behavior indicated the reaction of the mono-reduced species with CO_2. Further reduction until the second redox system induced a slight modification of the spectral signature with a decrease of the band at 475 nm (Figure III.27.B, purple curve).

For complex **3**, mono-reduction under CO_2 (Figure III.28.B, orange curve) was characterized by the absence of any new band at ca. λ_{max} = 410 nm, such as observed under Ar (Figure III.28.A, red curve). At the bis-reduced state (Figure III.28.B, purple curve), no species could be longer identified.

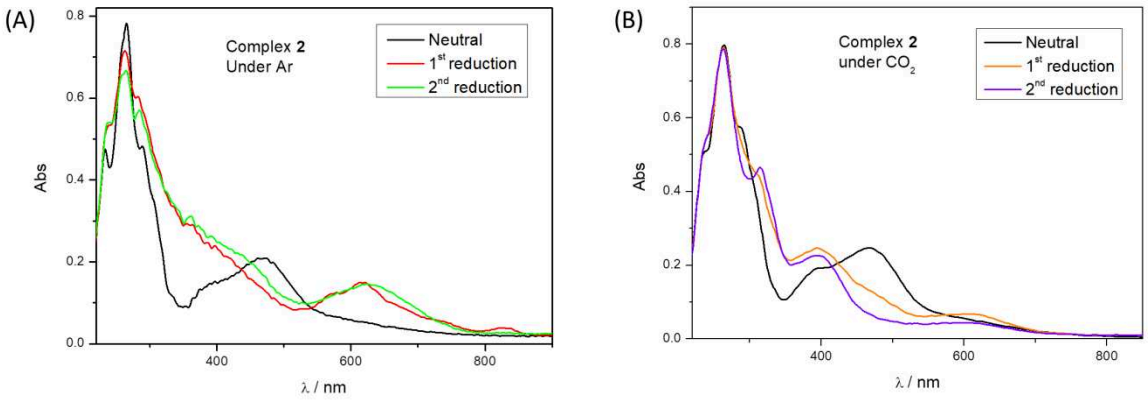

Figure III.27. UV-Vis-SEC spectra of complex **2** in THF A) under Ar at neutral state (black), after the first reduction (red) and second reduction (green), and B) under CO_2 at neutral state (black), after the first reduction (orange) and second reduction (purple). Conditions: 1 mM of complex, 0.1 M NBu_4PF_6, BDD working electrode.

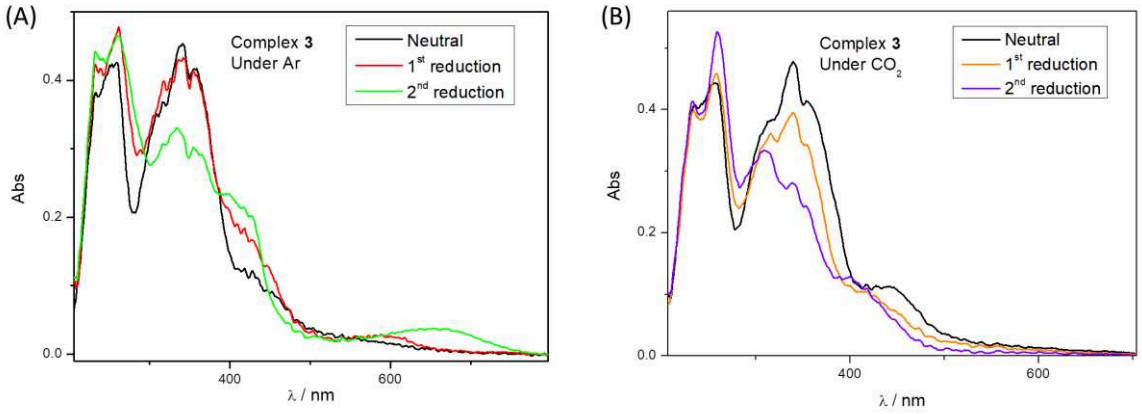

Figure III.28. UV-Vis-SEC spectra of complex **3** in THF A) under Ar at neutral state (black), after the first reduction (red) and second reduction (green), and B) under CO_2 at neutral state (black), after the first reduction (orange) and second reduction (purple). Conditions: 1 mM of complex, 0.1 M NBu_4PF_6, BDD working electrode.

VI.2. IR-SEC spectroelectrochemical experiments under CO_2

To complement the UV-Vis spectroelectrochemical data, IR-SEC experiments were also carried out under CO_2 for the three complexes. The Figure III.29 shows the comparative IR spectra of complex **1** obtained under argon and carbon dioxide. As observed in UV-Vis spectroelectrochemistry, the IR pattern of the mono-reduced species detected under CO_2 was similar to that obtained under Ar, hence in agreement with the formation of $[Mo(CO)_4(bpy)]^{\bullet-}$. However, the IR spectra differed by the presence of new bands in the 1600-1700 cm^{-1} range which can be ascribed to the presence of formate (1610 cm^{-1}) and bicarbonate (1670 cm^{-1}).[16-18] Addition of water to the solution increased the reaction rate of CO_2 consumption (detected at 2340 cm^{-1}, not shown) but no new species could be detected by IR.

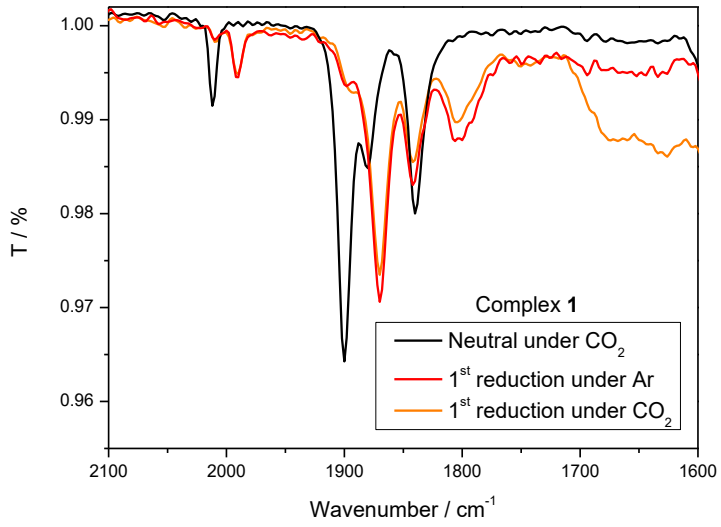

Figure III.29. IR-SEC spectra of complex **1** in THF under Ar at neutral state (black), after the first reduction under Ar (red) and under CO_2 (orange). Conditions: 5 mM of complex, 0.1 M NBu_4PF_6, GC working electrode.

A similar behavior was obtained with complex **2** except that the IR signature of $[Mo(CO)_4(phen)]^{\bullet-}$ was much less intense than under Ar (Figure III.30), together with the presence of new peaks at 1925 and 1743 cm^{-1}. Formate and carbonates ions were also detected in the 1600-1700 cm^{-1} range. This difference between Ar and CO_2 conditions highlights the interaction between the mono-reduced species of complex **2** with carbon dioxide. Interestingly, a similar ν_{CO} band at 1920 cm^{-1} was previously reported for the double reduction of $[Mo(CO)_4(bpy\text{-}(6,6'\text{-}Me)_2]$ under CO_2.[18] Even though, as it will be discussed below, the disappearance of the band at 1743 cm^{-1} during the IR-SEC study of the second reduction process of complex **2** in a saturated CO_2 atmosphere could indicate that the new species observed is not related to any carbonate product.

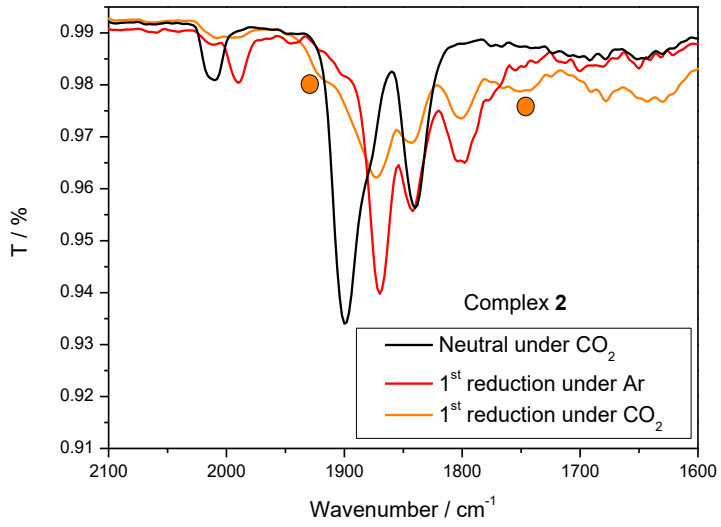

Figure III.30. IR-SEC spectra of complex **2** in THF under Ar at neutral state (black), after the first reduction under Ar (red) and under CO_2 (orange). Orange dots indicate new bands. Conditions: 5 mM of complex, 0.1 M NBu_4PF_6, GC working electrode.

For complex **3**, the situation was more complicated since the resulting IR spectrum obtained under carbon dioxide did not match with that under argon, thus excluding the presence of $[Mo(CO)_4(py\text{-}indz)]^{\bullet-}$ (Figure III.31). Instead, new bands were detected at 2005, 1921, 1887, 1830 and 1740 cm^{-1}. From the previous results with complex **2**, two different species may be likely present in solution. On one hand, the first species would be correlated to that generated during mono-reduction of complex **2** (1920 and 1743 cm^{-1}). On the other hand, the second species would feature the bands at 2005, 1887 and 1830 cm^{-1}.

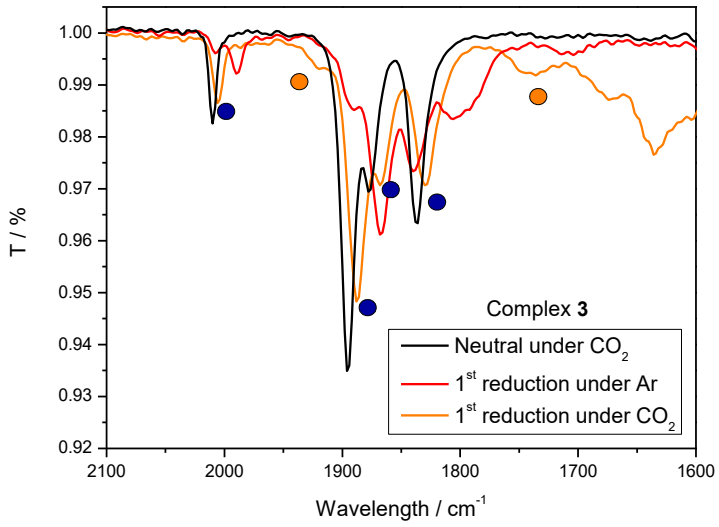

Figure III.31. IR-SEC spectra of complex **3** in THF under Ar at neutral state (black), after the first reduction under Ar (red) and under CO_2 (orange). Conditions: 5 mM of complex, 0.1 M NBu_4PF_6, GC working electrode. Orange and blue dots indicate the new bands.

Further IR-SEC studies were then performed on the second reduction process. The second reduction of complex **1** was characterized by the detection of new bands at 1920 and 1740 cm^{-1} (Figure III.32.A) that were previously observed for the mono-reduced complexes **2** and **3** under CO_2 (Figures III.30 and III.31). In addition, free bicarbonate and formate ions were detected in the 1600-1700 cm^{-1} range. The same conclusions were found for complexes **2** and **3** (Figure III.32.B and C) except that the bands at 1740 and 1920 cm^{-1} decreased for complex **3** whereas it increased for complexes **1** and **2**. Addition of aliquots of water to solution of complexes **1**, **2** and **3** under a CO_2 atmosphere was also monitored by IR-SEC. An enhancement of the catalytic activity along with an increase of carbonate and formate production was observed without detection of any new IR band, hence confirming the exclusive role of water as proton source.

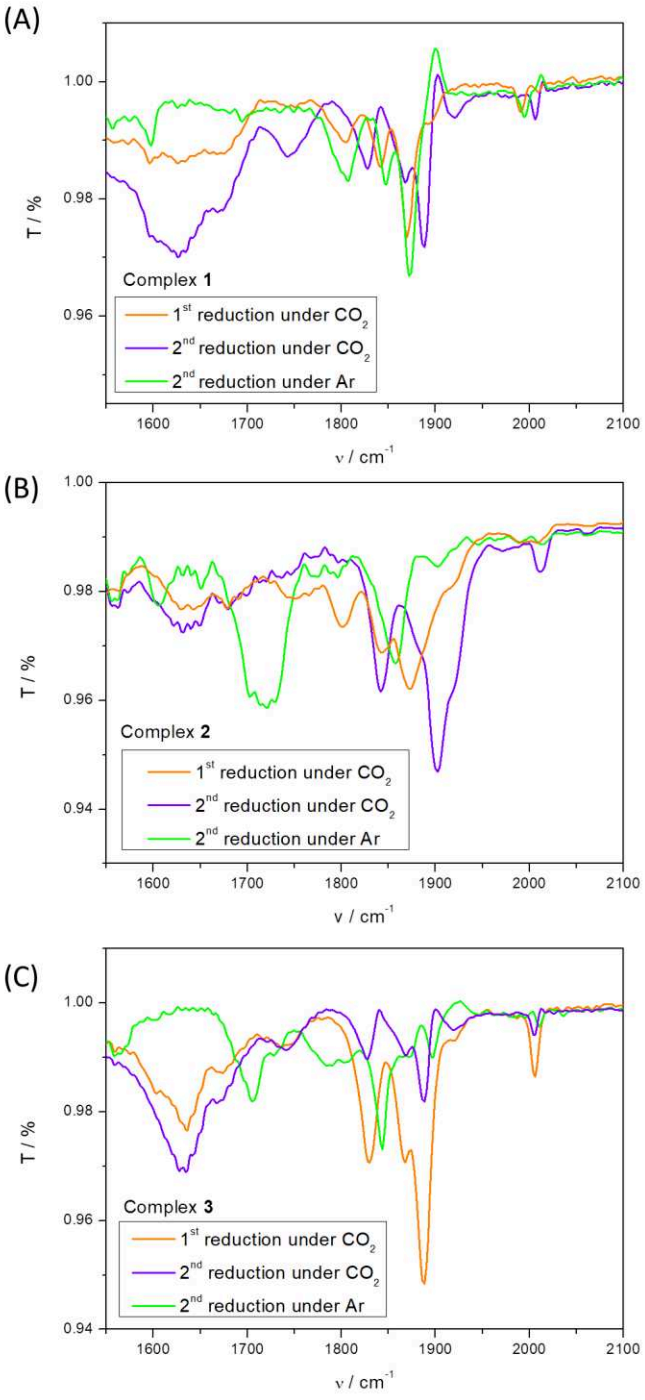

Figure III.32. IR-SEC spectra of A) complex **1**, B) complex **2** and C) complex **3** in THF under Ar at neutral state (black), after the first reduction under CO_2 (orange), after the second reduction under Ar (green) and under CO_2 (purple). Conditions: 5 mM of complex, 0.1 M NBu_4PF_6, GC working electrode.

In conclusion, infrared spectroelectrochemical studies allowed us to characterize the transient species generated upon mono- and bi-reduction of complexes **1**, **2** and **3** under CO_2, and to show the formation of bicarbonate and formate ions. While only one reduced intermediate ($[Mo(CO)_4(bpy)]^{\bullet-}$) was detected by IR in presence of CO_2 for complex **1**, new species were identified upon reduction of complexes **2** and **3**, thus indicating that reactivity can be dependent on the diimine structure.

VI.3. Near-IR spectroelectrochemical experiments under CO_2

Near-IR spectroelectrochemical techniques were applied for probing the mono-reduction of the three complexes under CO_2. The Figure III.33 displays the comparative NIR responses of the mono-reduced species. Clearly, no change was observed for the mono-reduced complex **1** upon gas switching, where loss of the intra-ligand transition band in the 1200-2000 nm region was detected for complexes **2** and **3**. Such a result evidences the direct interaction of the mono-reduced species of complexes **2** and **3** with carbon dioxide, as suggested by UV-SEC, IR-SEC and CV techniques.

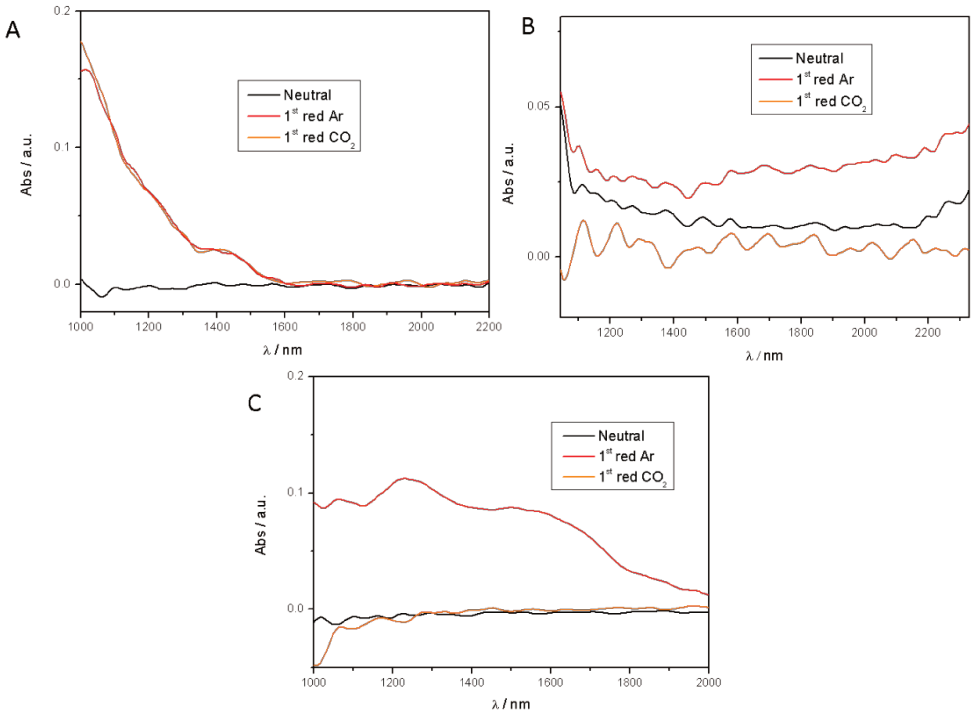

Figure III.33. NIR-SEC spectra of A) complex **1**, B) complex **2** and C) complex **3** in THF under Ar at neutral state (black), after the first reduction under Ar (red) and under CO_2 (orange). Conditions: 5 mM of complex, 0.1 M NBu_4PF_6, GC working electrode.

VII. Infrared spectroscopy under CO_2 of chemically reduced complexes

Chemical reduction was then used as an attempt to obtain information about the species involved in the reaction of reduced complexes with CO_2. Formation of mono-reduced species of complexes **1**, **2** and **3** by chemical means was performed by addition of 1 equivalent of KC_8 in dry THF. The reaction was monitored by IR spectroscopy to achieve near-quantitative yield. The Figure III.34 shows IR spectra of the neutral and chemically mono-reduced species under Ar and CO_2 for the three complexes **1**, **2** and **3**. Clearly, the mono-reduced species displayed four carbonyl bands as expected for $[Mo(CO)_4(diimine)]^{\bullet-}$ complexes, indicating that these species are the stable forms in solution.

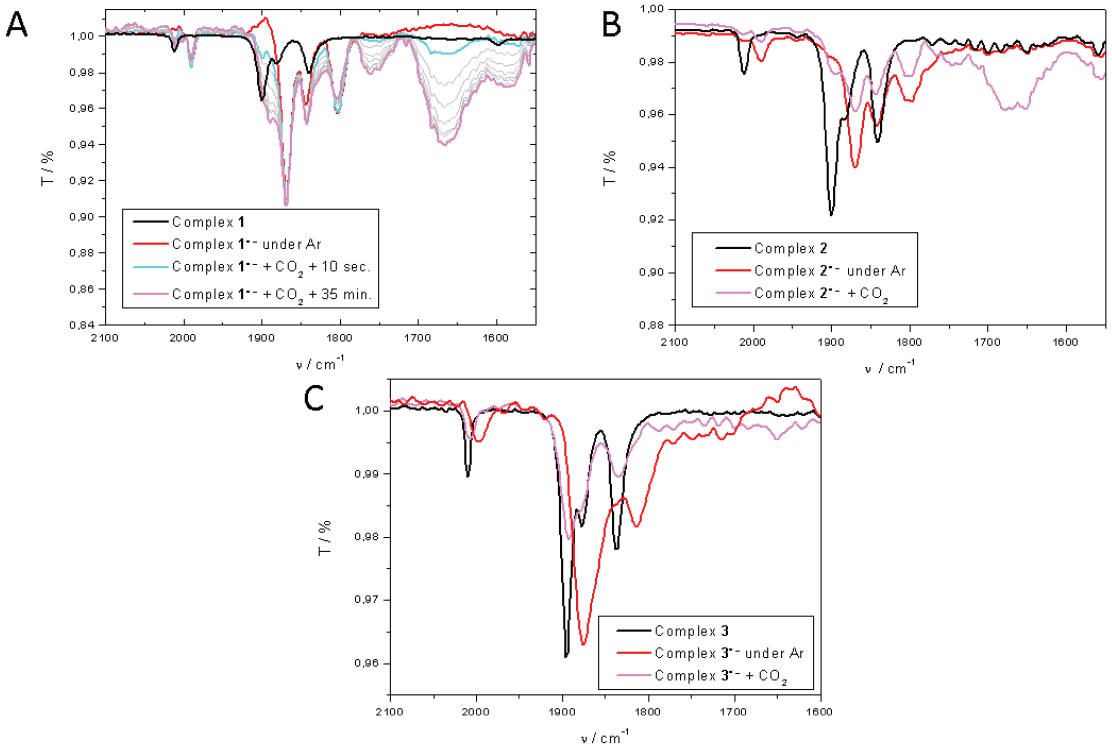

Figure III.34. IR spectra of chemically mono-reduced species under Ar (red) and CO_2 (pink) species in comparison with neutral species under CO_2 (black) in THF for A) complex **1**, B) complex **2** and C) complex **3**. Conditions: 5 mM of complex, 0.1 M NBu_4PF_6, GC working electrode. The cyan and grey curves in A represent intermediates curves during reaction of $\mathbf{1}^{\bullet-}$ with CO_2.

Addition of CO_2 led to sluggish (for complex **1**) to instantaneous (complexes **2** and **3**) modification of the IR spectra with appearance of featuring bands of bicarbonate and formate ions in the 1600-1700 cm^{-1} region. Interestingly, partial recover of the neutral species was observed in every case, suggesting that the enhanced current observed by CV is unlikely due to an ECE mechanism, but rather to an EC_{cat} process as proposed from CV simulations. Moreover, no band at ca. 1910 cm^{-1} could be detected. Addition of water to the solution fastened the formation of bicarbonate and formate ions (see Figure III.35 for complex **2**), evidencing the role of water as a proton source for the reaction of mono-reduced complexes with carbon dioxide, in agreement with spectroelectrochemical and electrochemical studies.

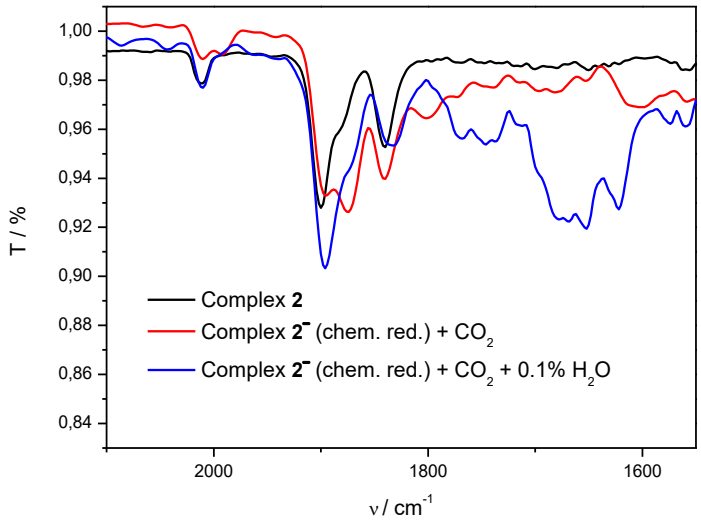

Figure III.35. IR spectra of chemically mono-reduced **2** in distilled THF under Ar (black), under CO_2 (red) and under CO_2 with added water (blue). Conditions: 5 mM of complex, 0.1 M NBu_4PF_6, GC working electrode.

VIII. Theoretical and mechanistic studies of complexes **1**, **2** and **3**

A series of DFT calculations was performed in order to get insights into the generated reduced species reacting with CO_2. For all complexes, calculated structures were optimized starting from X-ray data at neutral state by including a dielectric continuum to model the electrolyte. As shown in Tables III.16 and III.17, calculated structures for complexes **1**-**3** displayed bond distance and angles values which were close to those found experimentally (Tables III.1 and III.2). Mono-reduction of the complexes was shown to have little effect on the whole structure of $[Mo(CO)_4(diimine)]^{\bullet-}$. Electron input induced a slight increase of the C-O and Mo-N bond lengths, as well as a decrease of Mo-C(O) bond lengths. The N-Mo-$C(O)_{ax}$ angle was almost unaffected (-0.5°) by the reduction. Such result is in line with spectroelectrochemical results which suggested a stronger back-bonding of Mo to the CO ligands, and an increase of the electron density on the diimine ligand. The 30 cm^{-1} IR shift of the four carbonyl stretching bands which was detected by IR-SEC was nicely reproduced for the three complexes (Table III.18), thus confirming the good matching of the mono-reduced model with the experimental data. Noteworthy, the calculations indicated that the Mo-$N^{(1)}$ and Mo-$N^{(2)}$ bond lengths for $[Mo(CO)_4(py\text{-}indz)]^{\bullet-}$ are sensibly different (2.293 and 2.248 Å, respectively), in contrast to the two other complexes for which they are strictly identical. This discrepancy, which was already found at neutral state for complex **3**, depicts the better electron-donating property of the indolizine moiety *vs*. pyridyl and unsymmetrical charge localization.

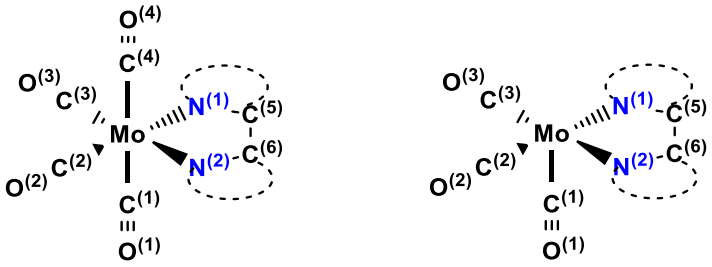

Figure III.36. Atom numbering for tetracarbonyl and tricarbonyl Mo-diimine complexes.

Table III.16. Calculated bond distances (Å) for the neutral and mono-reduced tetracarbonyl complexes and mono-reduced tricarbonyl complexes according to numbering of Figure III.36.

	$Mo–C^{(1)}$	$Mo–C^{(2)}$	$Mo–C^{(3)}$	$C^{(1)}–O^{(1)}$	$C^{(2)}–O^{(2)}$	$Mo–N^{(1)}$	$Mo–N^{(2)}$	$C^{(5)}–C^{(6)}$
Complex **1**	2.047	1.976	1.976	1.164	1.175	2.260	2.260	1.475
Complex **2**	2.047	1.975	1.975	1.164	1.175	2.268	2.268	1.434
Complex **3**	2.046	1.973	1.976	1.165	1.175	2.285	2.238	1.448
Complex $\mathbf{1}^{\bullet-}$	2.044	1.974	1.974	1.169	1.181	2.254	2.254	1.430
Complex $\mathbf{2}^{\bullet-}$	2.045	1.972	1.972	1.169	1.181	2.261	2.261	1.407
Complex $\mathbf{3}^{\bullet-}$	2.044	1.972	1.974	1.169	1.181	2.270	2.231	1.418
$[Mo(CO)_3(bpy)]^{\bullet-}$	1.906	1.955	1.955	1.192	1.189	2.229	2.229	1.438
$[Mo(CO)_3(phen)]^{\bullet-}$	1.907	1.954	1.954	1.192	1.189	2.236	2.236	1.411
$[Mo(CO)_3(py\text{-}indz)]^{\bullet-}$	1.909	1.952	1.956	1.192	1.190	2.243	2.207	1.425

Table III.17. Calculated angles (°) for the neutral and reduced tetracarbonyl complexes and the reduced tricarbonyl complexes according to numbering of Figure III.36.

	$N^{(1)}–Mo–C^{(1)}$	$N^{(2)}–Mo–C^{(1)}$
Complex **1**	93.2	93.2
Complex **2**	93.2	93.2
Complex **3**	93.1	93.6
Complex $\mathbf{1}^{\bullet-}$	93.4	93.4
Complex $\mathbf{2}^{\bullet-}$	93.4	93.4
Complex $\mathbf{3}^{\bullet-}$	93.3	94.3
$[Mo(CO)_3(bpy)]^{\bullet-}$	107.2	107.2
$[Mo(CO)_3(phen)]^{\bullet-}$	107.3	107.3
$[Mo(CO)_3(py\text{-}indz)]^{\bullet-}$	109.2	106.9

The structures of the mono-reduced $[Mo(CO)_3(diimine)]^{\bullet-}$ tricarbonyl complexes were also calculated by DFT. The theoretical structures of $[Mo(CO)_3(diimine)]^{\bullet-}$ indicate that the departure of an axial CO ligand opens a vacant site in axial position while remaining in a pseudo (N-N-C(O)-C(O)) square-based geometry. The comparison with $[Mo(CO)_4(diimine)]^{\bullet-}$ shows that the CO loss induces several modifications in terms of angle and bond lengths values. The main change concerns the substantial shortening of the axial Mo-CO bond together with Mo-N bonds. This is accompanied by an increase of the angle between the axial CO and the Mo-diimine from ca. 93° to 107°. In other words, at the reduced state, CO loss yields a twist of the diimine ligand towards the axial vacant site. These effects are all accentuated for the tricarbonyl doubly-reduced species. In particular, the

$C^{(1)}$-Mo-$N^{(1)}$ angle reaches 120° for $[Mo(CO)_3(L)]^{2-}$, hence emphasizing the distortion form the ideal square-based pyramidal geometry.

Table III.18. Calculated and experimental (in THF) carbonyl stretching energies for neutral and mono-reduced tetracarbonyl complexes.

	ν_{CO} theor. / cm^{-1}	ν_{CO} exp. (in THF) / cm^{-1}
Complex **1**	1911, 1940, 2016	1840, 1882, 1890, 2012
Complex $\mathbf{1}^{\bullet-}$	1868, 1901, 1987	1803, 1842, 1870, 1991
Complex **2**	1913, 1942, 2018	1841, 1880, 1896, 2012
Complex $\mathbf{2}^{\bullet-}$	1865, 1898, 1992	1800, 1842, 1870, 1990
Complex **3**	1912, 1939, 2012	1838, 1877, 1896, 2010
Complex $\mathbf{3}^{\bullet-}$	1871, 1903, 1990	1800, 1839, 1867, 1989

Frontier orbital analysis was then performed in order to gain an insight of the nature of the interaction of mono-reduced species with carbon dioxide. As shown in Figure III.37, calculated structures showed that LUMOs of neutral complexes **1**, **2** and **3** are essentially localized on the diimine ligand, hence favoring a ligand-centered reduction. Accordingly, SOMOs of mono-reduced complexes (Figure III.38) presented a 90% electronic density over the diimine moiety, a behavior coherent with the intra-ligand charge transfer transition detected by near-IR spectroscopy techniques. Furthermore, analysis of bis-reduced $[Mo(CO)_3(diimine)]^{2-}$ HOMOs showed a predominant ligand-based behavior but with a significant metal contribution to the electronic density (Figure III.39). Thus, at a first glance, these calculations suggested no specific influence of the ligand topology that could explain the reactivity at the mono-reduced state with carbon dioxide as observed experimentally by CV and IR-SEC.

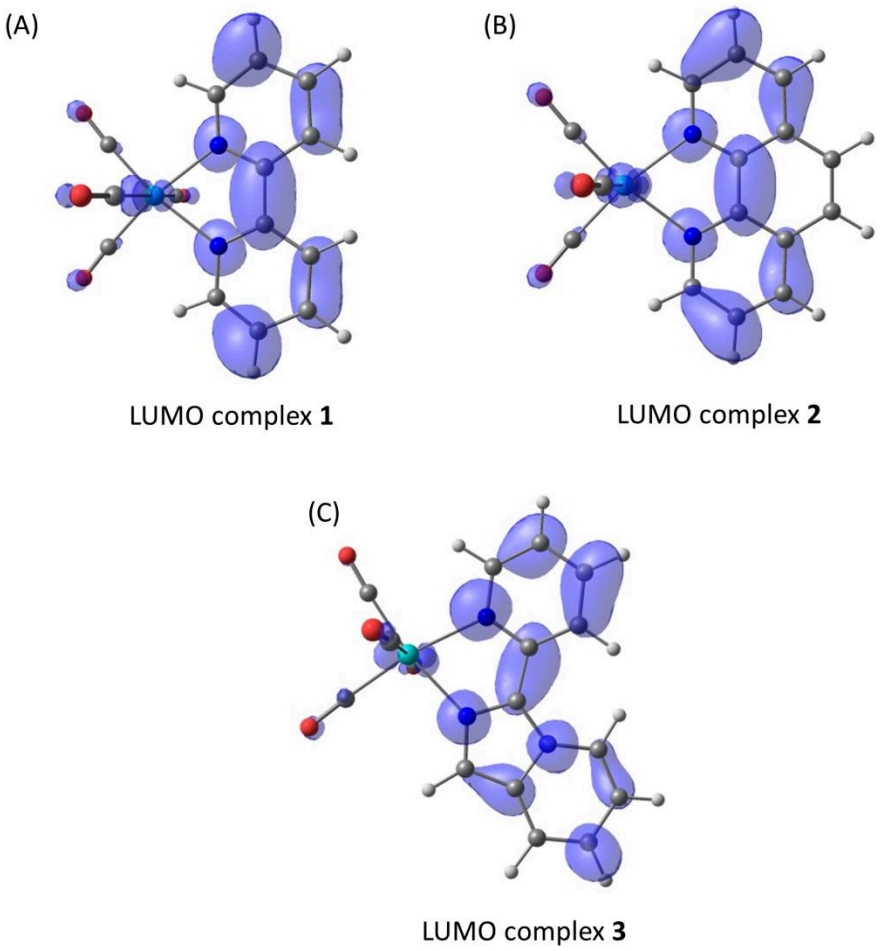

Figure III.37. DFT-calculated LUMO for A) complex **1**, B) complex **2** and C) complex **3**. Isosurface value = 0.03.

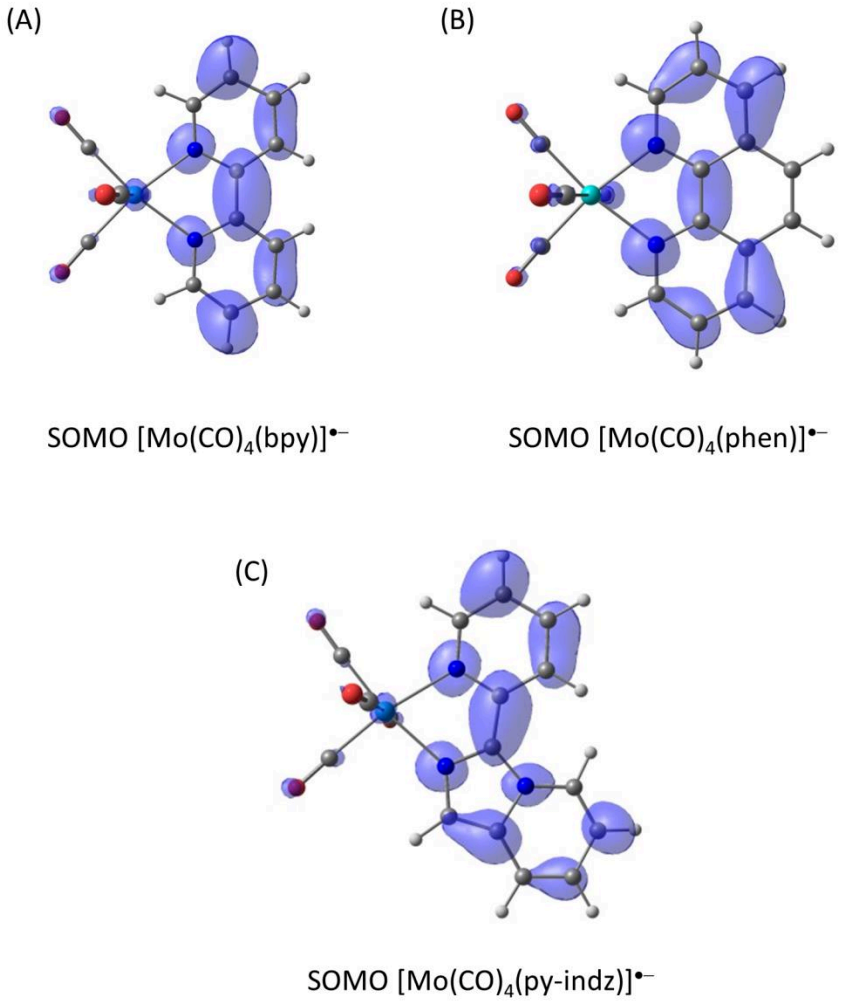

Figure III.38. DFT-calculated SOMO for A) $[Mo(CO)_4(bpy)]^{\bullet-}$, B) $[Mo(CO)_4(phen)]^{\bullet-}$ and C) $[Mo(CO)_4(py\text{-}indz)]^{\bullet-}$ complexes. Isosurface value = 0.03.

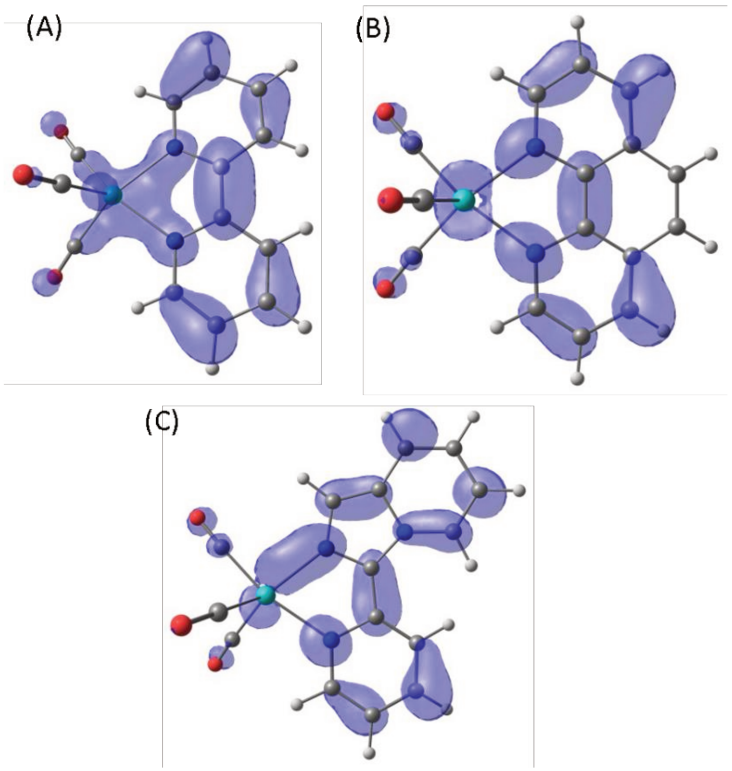

Figure III.39. DFT-calculated HOMO for A) $[Mo(CO)_4(bpy)]^{2-}$, B) $[Mo(CO)_4(phen)]^{2-}$ and C) $[Mo(CO)_4(py\text{-}indz)]^{2-}$ complexes. Isosurface value = 0.03.

On the basis of the results obtained with chemical-reduced complexes and because the rate of the reaction with CO_2 is ligand and water dependent, it is unlikely that the reaction between CO_2 and $[Mo(CO)_4(diimine)]^{\bullet-}$ species occurs through a simple outer-sphere process. This is confirmed by the fact that the calculated standard potential of the $[CO_2]^{0/\bullet-}$ couple was found to be at –2.85 V *vs.* Fc^+/Fc, hence at least 0.8 V more negative than those of $[Mo(CO)_4(dimine)]^{0/\bullet-}$ complexes. From this statement, we investigated a catalytic mechanism in which CO_2 is activated by its association with a reduced form of the complexes possessing a vacant site, i.e. $[Mo(CO)_3(diimine)]^{\bullet-}$ in agreement with previous studies.[14, 19]

Geometry optimization was carried out for the three possible binding modes of CO_2 known for metal-CO_2 complexes (η^1–OCO, η^1–CO_2 and η^2–CO_2)[13] For all complexes, it did not converge to a stable structure when starting from η^1–OCO coordination mode. However, structures in which the

CO_2 ligand could adopt a η^2–CO_2 binding mode were obtained by starting with a CO_2 ligand bound in the η^1–CO_2 mode (Figure III.40). Bond distances and angles obtained for these adducts (see Table III.19) displayed an O–C–O angle in the 141–143°, which is close to the value calculated for an isolated $[CO_2]^{\bullet-}$ radical anion (135°). Moreover, the C–O bonds were elongated by 0.04–0.07 Å which indicated of weaker bond strength. Hence, these calculations clearly demonstrated a significant transfer of electronic density from the $[Mo(CO)_3(diimine)]^{\bullet-}$ moiety to the bound CO_2.

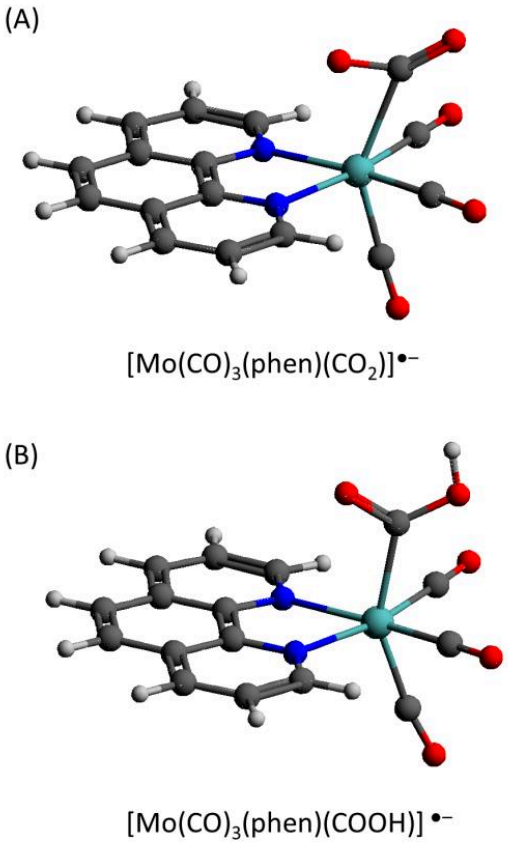

Figure III.40. Calculated structures of (A) $[Mo(CO)_3(phen)(CO_2)]^{\bullet-}$ and (B) $[Mo(CO)_3(phen)(COOH)]^{\bullet-}$.

Table III.19. Calculated bond distances (Å) and angles (°) for the $CO_2^{\bullet-}$ and $COOH^{\bullet-}$ adducts and isolated CO_2 and $[CO_2]^{\bullet-}$ molecules according to numbering of Figure III.36.

	Mo–C(O)$_2$	Mo–O(CO)	O–C(O)	(O)C–O	O–C–O	Mo–N$^{(1)}$	Mo–N$^{(2)}$	C$^{(5)}$–C$^{(6)}$
$[Mo(CO)_3(bpy)(CO_2)]^{\bullet-}$	2.348	2.434	1.240	1.210	142.5	2.221	2.221	1.437
$[Mo(CO)_3(phen)(CO_2)]^{\bullet-}$	2.348	2.439	1.241	1.210	142.4	2.227	2.227	1.411
$[Mo(CO)_3(py\text{-}indz)(CO_2)]^{\bullet-}$	2.364	2.487	1.242	1.214	141.2	2.235	2.198	1.426
$[Mo(CO)_3(bpy)(COOH)]^{\bullet-}$	2.278	3.169	1.238	1.400	115.6	2.331	2.331	1.467
$[Mo(CO)_3(phen)(COOH)]^{\bullet-}$	2.278	3.171	1.238	1.401	115.6	2.238	2.238	1.430
$[Mo(CO)_3(py\text{-}indz)(COOH)]^{\bullet-}$	2.280	3.180	1.239	1.403	115.3	2.259	2.222	1.445
CO_2			1.171		180.0			
$[CO_2]^{\bullet-}$			1.247		134.7			

Table III.20. Theoretical data correlated to the mechanistic pathways depicted in Scheme III.3. E^0 in V *vs*. Fc^+/Fc; ΔG in kcal.mol^{-1}.

	Complex **1**	Complex **2**	Complex **3**
$E^0(1)$	-1.85	-1.88	-2.16
$E^0(3)$	-0.90	-0.91	-0.99
$E^0(4)$	-1.57	-1.58	-1.81
$E^0(5)$	-0.71	-0.72	-0.80
$\Delta G(1)$	+26.7	+26.4	+24.9
$\Delta G(2)$	-17.8	-18.2	-22.8
$\Delta G(3)$	-2.4	-2.4	-2.6
$\Delta G(4)$	-18.1	-18.1	-23.5

Calculations were then performed in order to obtain the redox potentials of the electron transfer reactions and the free energies of the chemical steps involved in the formation and reactivity of CO_2 adducts (see Table III.20). After the first reduction at $E^0(1)$, the CO loss for from the mono-reduced tetracarbonyl species is uphill in energy by $\Delta G(1)$ = +26.7, +26.4 and +24.9 kcal mol^{-1} for complexes **1**$^{\bullet-}$, **2**$^{\bullet-}$ and **3**$^{\bullet-}$ respectively (Scheme III.3 and Table III.20), leading to the tricarbonyl mono-reduced compounds. Starting from this step, two different situations were then considered.

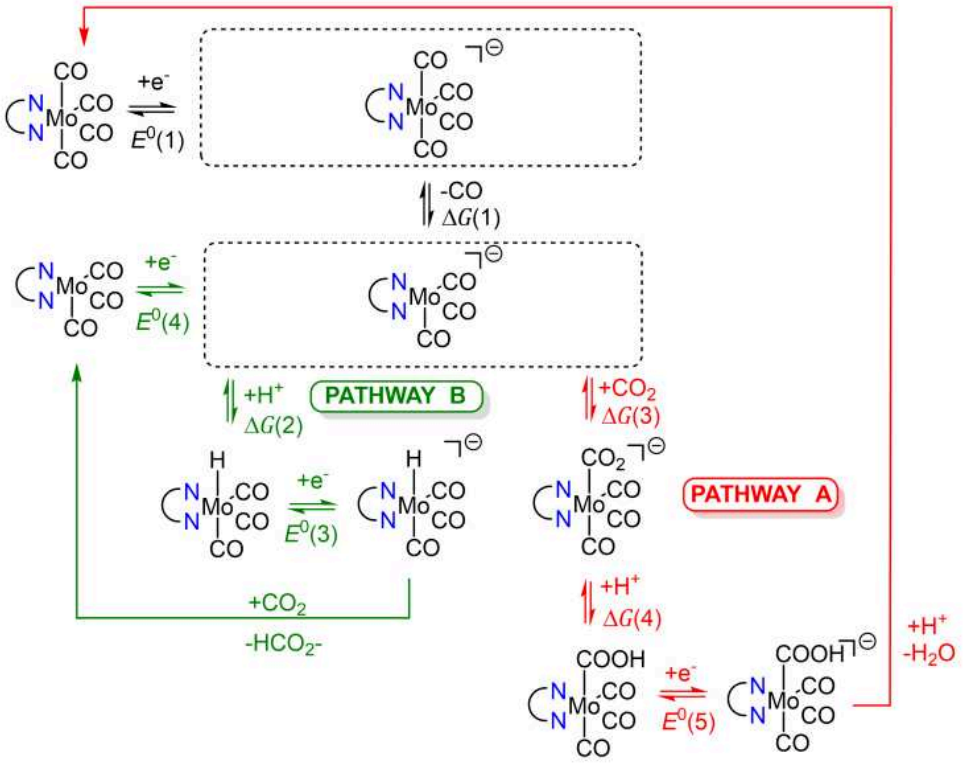

Scheme III.3. Suggested mechanistic pathways for the CO_2 reduction mediated by Mo-diimine complexes **1**, **2** and **3**.

The first one (Pathway A, Scheme III.3) includes the formation of $[Mo(CO)_3(L)(CO_2)]^{\bullet-}$ according to a slightly energetic downhill process ($\Delta G(3)$ = –2.4, –2.4 and -2.6 kcal mol^{-1} for L = bpy, phen and py-indz, respectively, see Table III.20). This reaction is followed by the protonation of the CO_2 ligand leading to the generation of the $[Mo(CO)_3(L)(COOH)]$ adduct. This protonation step was found to occur preferably at the O atom of the CO_2 ligand (and not at the C atom) according to a downhill energetic process as shown by the values of $\Delta G(4)$ in Table III.20. Hence, the overall free energy change for the reaction starting from the mono-reduced tetracarbonyl species ($[Mo(CO)_4(L)]^{\bullet-} + CO_2 + H^+ \longrightarrow [Mo(CO)_3(L)(COOH)] + CO$) was found to be uphill in energy by +6.2 and +5.4 kcal mol^{-1} for L = bpy and phen, while slightly downhill in energy by –1.2 kcal mol^{-1} for L = py-indz. Interestingly, the standard potential values $E^0(5)$ for the $[Mo(CO)_3(L)(COOH)]^{0/-}$ species were found to be significantly less negative than $E^0(1)$ (by ca. 1.2 V, see Table III.20). This result suggested that the protonation step of the $[Mo(CO)_3(L)(CO_2)]^{\bullet-}$ adducts is immediately followed by electrochemical reduction leading to $[Mo(CO)_3(L)(COOH)]^{\bullet-}$ (see Figure III.40 for the phen

derivative). Further calculations showed that subsequent protonation of these intermediates led to C–O(H)$_2$ bond cleavage releasing H_2O and regenerating $[Mo(CO)_4(L)]$ which can be electrochemically reduced into $[Mo(CO)_4(L)]^{\bullet-}$ at $E^0(1)$ (see Figure III.41 for the phen derivative). The overall driving force for CO_2 conversion into CO and H_2O was found to be equal to –20.1, –21.3 and –32.3 kcal mol^{-1} for complexes **1**, **2** and **3**, respectively. The driving force was noticeably larger for complex **3**, which can be explained by a more negative reduction potential value for this derivative. Activation barriers of the chemical steps were not calculated, but the detection of $[Mo(CO)_4(L)]^{\bullet-}$ intermediates under inert atmosphere by IR-SEC experiments have evidenced that the activation barrier for the $[Mo(CO)_3(L)]^{\bullet-} \rightarrow [Mo(CO)_3(L)]^{\bullet-}$ + CO must be significantly larger than that of the first protonation step of bound CO_2.

For the second possible pathway (Pathway B, Scheme III.3), we have considered the direct protonation of $[Mo(CO)_3(L)]^{\bullet-}$, since Pathway A could not support the generation of formate, in contrast to what is observed experimentally. According to Pathway B, the formation of the corresponding hydride derivatives $[Mo(CO)_3(L)(H)]$ was downhill by $\Delta G(2)$ = –17.8, –18.2 and –22.8 kcal mol^{-1} for complexes **1**, **2** and **3**, respectively. In addition, the redox potential $E^0(3)$ for the $[Mo(CO)_3(L)(H)]^{0/-}$ couples was less negative (by ca. 1.0 V, see Table III.20) than $E^0(1)$. This result implied that protonation of $[Mo(CO)_3(L)]^{\bullet-}$ was immediately followed by a reduction step leading to $[Mo(CO)_3(L)(H)]^{\bullet-}$. Structure calculations showed that the reaction of CO_2 with these reduced hydrides led to Mo–H bond cleavage then formate and $[Mo(CO)_3(L)]$ (Figure III.41.B), the latter being immediately reduced back to $[Mo(CO)_3(L)]^{\bullet-}$ at $E^0(4)$ (see Table III.20). The overall driving force for the production of formate according to pathway B was found to be equal to –19.5, –20.6 and –32.9 kcal mol^{-1} for L = bpy, phen and py-indz, respectively. These free energy values are comparable to those calculated for the production of CO and H_2O according to Pathway A. The mechanism leading to the production of formate is likely favored in the presence of added water. In addition, once initiated, this mechanism bypasses the CO loss reaction of the mono-reduced tetracarbonyl species. However, the formation of the $[Mo(CO)_3(L)(H)]$ hydride from $[Mo(CO)_3(L)]^{\bullet-}$ in Pathway B has most likely a higher energy barrier than the protonation of the partly reduced bound CO_2 in $[Mo(CO)_3(L)(CO_2)]^{\bullet-}$ in Pathway A, which might explain the low catalytic activity experimentally measured.

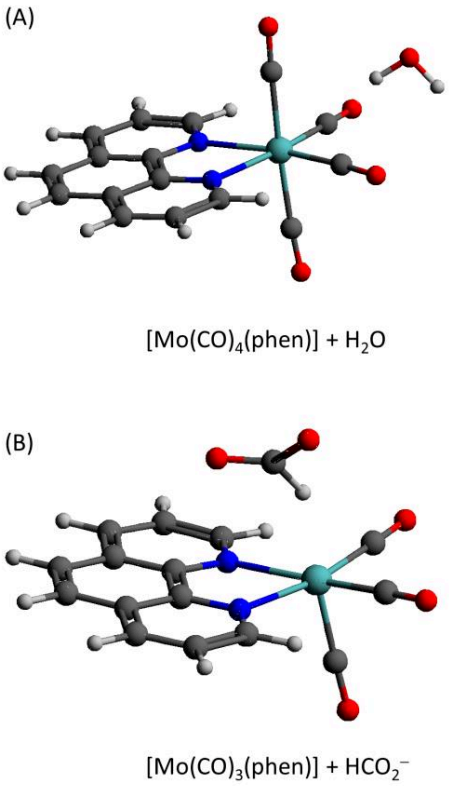

Figure III.41. Calculated structures (A) upon protonation of $[Mo(CO)_3(phen)(COOH)]^{\bullet-}$ leading to the release of water and generation of $[Mo(CO)_4(phen)]$ according to Pathway A, and (B) reaction of $[Mo(CO)_3(phen)(H)]^{\bullet-}$ with CO_2 leading to the release of formate and $[Mo(CO)_3(phen)]$ according to pathway A.

Since bicarbonate ions were detected by IR-SEC experiments, their formation may be explained by the reaction of a transient reduced metal-CO_2 adducts with a supplementary carbon dioxide molecule in pathway A.[6, 20] This reaction may lead to C-O bond cleavage and release of bicarbonate while a carbonyl ligand remains attached to the metal ion. Possibly, bicarbonate production during electrochemical reduction of the complexes may be due to the reductive disproportionation of CO_2 into carbonate and CO, which usually occurs in presence of Lewis acids such as Mg^{2+} or other metal ions.[13, 21, 22] Alternatively, the acid-base equilibria $CO_2 + H_2O \rightarrow H^+ + HCO_3^-$ and $CO_2 + H_2O \rightarrow 2H^+ + CO_3^{2-}$ may also explain the increase of carbonates content since pathway A favors the formation of water.

IX. Conclusion

This chapter aimed at performing comparative electrocatalytic studies of three different $[Mo(CO)_4(diimine)]$ complexes mainly in order to rationalize the impact of a rigid diimine ligand or an unsymmetrical pattern on the catalytic properties towards CO_2. Redox properties of the three complexes **1**, **2** and **3** were first investigated in different solvents under an inert atmosphere. Monoelectronic reduction led to the formation of $[Mo(CO)_4(diimine)]^{\bullet-}$ species as confirmed by near-IR spectroelectrochemical techniques. Further reduction led to the generation of a tricarbonyl $[Mo(CO)_3(diimine)]^{2-}$ species, although the complex **1** led also to the $[Mo(CO)_4(H^+\text{-bpy})]^{2-}$ complex in MeCN, as shown by different spectroelectrochemical techniques.[23] Electrochemical studies of each redox process under CO_2 led to the observation of current enhancements unexpectedly at the first reduction processes at low-to-moderate scan rate, hence indicating a reactivity of the mono-reduced species with CO_2. So far, this redox behavior was not reported for similar systems. Thorough analysis of the CVs according to an EC_{cat} mechanism further supported a ligand and water dependent rate of reaction. IR-SEC spectroelectrochemical experiments further showed the formation of carbonate and formate ions upon monoelectronic reduction under CO_2. Theoretical calculations corroborated the diimine-localized nature of first reduction processes, delocalizing the electronic density towards the metal center during the second reduction processes. A mechanistic proposal of the interaction between $[Mo(CO)_4(diimine)]^{\bullet-}$ species with carbon dioxide was presented, suggesting two possible pathways.

Nevertheless, the discrete catalytic activity of **1**, **2** and **3** bis-reduced species make them unattractive compared to other metallic complexes. The generation of more active complexes by modification of the ligand backbone should be attempted as the main goal after the experimental evidences exposed during this chapter. An interesting strategy would be the exchange of a CO ligand with a more labile group, such as a pseudo-halide molecule.[24] Immobilization of the complex over an electrode surface could diminish the high overpotential values, an alternative that will be explored during Chapter IV.

Bibliography

[1] A. Vlček Jr, *Coord. Chem. Rev.* **2002**, *230*, 225-242.
[2] I. R. Farrell, A. Vlcek, *Coord. Chem. Rev.* **2000**, *208*, 87-101.
[3] I. R. Farrell, J. van Slageren, S. Zalis, A. Vlcek, *Inorg. Chim. Acta* **2001**, *315*, 44-52.
[4] I. R. Farrell, F. Hartl, S. Záliš, T. Mahabiersing, J. A. Vlček, *Dalton Trans.* **2000**, 4323-4331.
[5] F. Franco, C. Cometto, F. Sordello, C. Minero, L. Nencini, J. Fiedler, R. Gobetto, C. Nervi, *ChemElectroChem* **2015**, *2*, 1372-1379.
[6] L. Rotundo, C. Garino, R. Gobetto, C. Nervi, *Inorg. Chim. Acta* **2018**, *470*, 373-378.
[7] D. Sieh, D. C. Lacy, J. C. Peters, C. P. Kubiak, *Chem. Eur. J.* **2015**, *21*, 8497-8503.
[8] M. H. B. Stiddard, *J. Chem. Soc.* **1962**, *0*, 4712-4715.
[9] C. M. Álvarez, L. Álvarez-Miguel, R. García-Rodríguez, J. M. Martín-Álvarez, D. Miguel, *Eur. J. Inorg. Chem.* **2015**, *2015*, 4921-4934.
[10] S. S. Braga, A. C. Coelho, I. S. Gonçalves, F. A. Almeida Paz, *Acta Cryst.* **2007**, *63*, m780-m782.
[11] H. J. Bruins Slot, N. W. Murrall, A. J. Welch, *Acta Cryst.* **1985**, *41*, 1309-1312.
[12] S. Záliš, C. Daniel, A. Vlček, D. A. Chantal Vlček Jr, *Dalton Trans.* **1999**, 3081-3086.
[13] R. Francke, B. Schille, M. Roemelt, *Chem. Rev.* **2018**, *118*, 4631-4701.
[14] J. Tory, B. Setterfield-Price, R. A. W. Dryfe, F. Hartl, *ChemElectroChem* **2015**, *2*, 213-217.
[15] T. Bens, P. Boden, P. Di Martino-Fumo, J. Beerhues, U. Albold, S. Sobottka, N. I. Neuman, M. Gerhards, B. Sarkar, *Inorg. Chem.* **2020**, *59*, 15504-15513.
[16] J. D. Froehlich, C. P. Kubiak, *J. Am. Chem. Soc.* **2015**, *137*, 3565-3573.
[17] F. Franco, C. Cometto, L. Nencini, C. Barolo, F. Sordello, C. Minero, J. Fiedler, M. Robert, R. Gobetto, C. Nervi, *Chem. Eur. J.* **2017**, *23*, 4782-4793.
[18] J. O. Taylor, R. D. Leavey, F. Hartl, *ChemElectroChem* **2018**, *5*, 3155-3161.
[19] G. Neri, P. M. Donaldson, A. J. Cowan, *J. Am. Chem. Soc.* **2017**, *139*, 13791-13797.
[20] A. L. Ostericher, T. M. Porter, M. H. Reineke, C. P. Kubiak, *Dalton Trans.* **2019**, *48*, 15841-15848.
[21] M. D. Sampson, C. P. Kubiak, *J. Am. Chem. Soc.* **2016**, *138*, 1386-1393.
[22] C. Costentin, S. Drouet, M. Robert, J. M. Saveant, *Science* **2012**, *338*, 90-94.
[23] M. L. Clark, K. A. Grice, C. E. Moore, A. L. Rheingold, C. P. Kubiak, *Chem. Sci.* **2014**, *5*, 1894-1900.
[24] J. O. Taylor, F. L. P. Veenstra, A. M. Chippindale, M. J. Calhorda, F. Hartl, *Organometallics* **2019**, *38*, 1372-1390.

Chapter IV

Immobilization of Mo-diimine tetracarbonyl complexes onto electrode surfaces for CO_2 electroreduction

I. Introduction

Three main strategies are generally considered for the development of efficient electrocatalysts for the CO_2 reduction reaction (CO_2RR). As shown in Figure IV.1, they include (a) homogeneous molecular catalysis with metal complexes, (b) supported molecular catalysis with metal complexes or metal-organic frameworks (MOFs), and (c) heterogeneous catalysis with bulk metals. As previously mentioned in Chapter I, most of the reported molecular metal electrocatalysts for the CO2RR are able to generate carbon monoxide (CO) or formic acid (HCOOH) with relatively high efficiency and selectivity. So far, a great majority of these electrocatalysts have been developed for homogeneous reactions, i.e. the metal complex is dissolved in the electrolytic solution in low concentration (*v*s. substrate and proton source) as shown in Figure IV.1. Although these systems can display outstanding results at the laboratory scale, they cannot be envisaged yet for industrial purposes, mainly because they are unable to provide high current densities and their development as supported catalysts remains still at its infancy. In contrast, bulk heterogeneous catalysts based on metals (Au, Ag, Zn, Cu, Pt, Ni….) have shown remarkable catalytic properties in terms of current densities, but they clearly suffer from poor selectivity since H_2 is usually co-produced with other CO_2 reduction products. Moreover, the rationalization of the different catalytic pathways occurring with bulk materials remains highly challenging. The recent investigations in that domain have highlighted the possible enhancement of their catalytic performance through single atom catalyst approaches or by finely controlling the size and shape of *in-situ* generated metal nanoparticles.

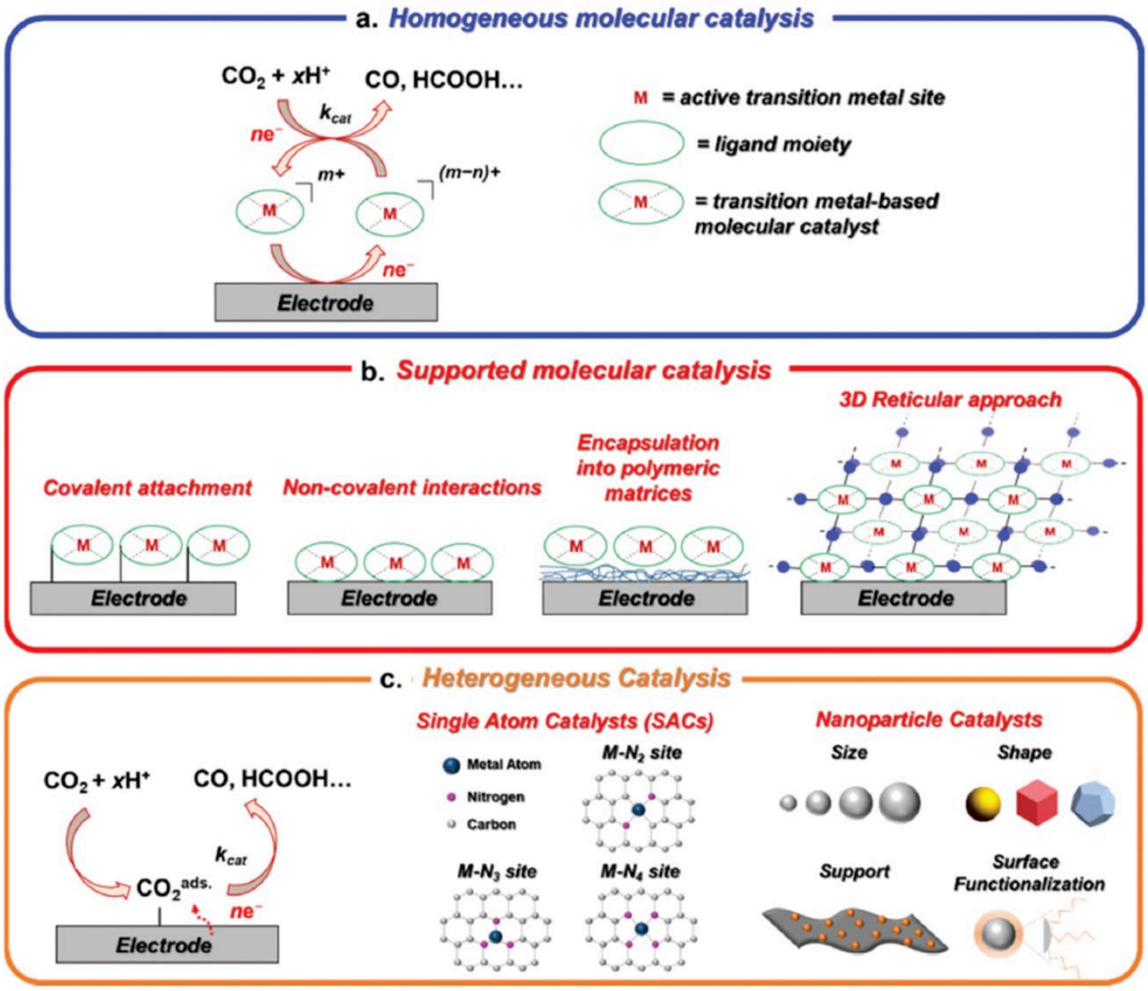

Figure IV.1. Current strategies for CO_2RR: (a) homogeneous molecular catalysis, (b) surface-anchored molecular catalysis by using several immobilization strategies and (c) heterogeneous catalysis. Reproduced from Ref. [1].

From this statement, it appears that the development of supported molecular metal catalysts, as depicted in Figure IV.1.b, is a promising approach to enhance catalytic properties of metal complexes. Indeed, it gives the opportunity to significantly increase current density mainly by using porous or 3D materials while keeping the advantageous versatile properties of complexes by variation of the ligand topology. One main advantage of supported catalysis is that different media can be used since there is no need to solubilize the catalysts. Hence, aqueous media such as $KHCO_3$ are commonly used for carbon dioxide electrocatalysis,[2] although CO_2 remains much less soluble in water than in organic solvents.[3]

Several strategies have been developed to immobilize molecular complexes onto electrode surfaces, such as covalent or non-covalent attachment, encapsulation into polymeric matrices or by forming 3D frameworks (Figure IV.1.b).[4, 5] Among them, covalent and non-covalent immobilization methodologies have been widely applied for CO_2RR according to several methods (Figure IV.2), including chemical immobilization[6] or π-π stacking hybridization techniques.[7]

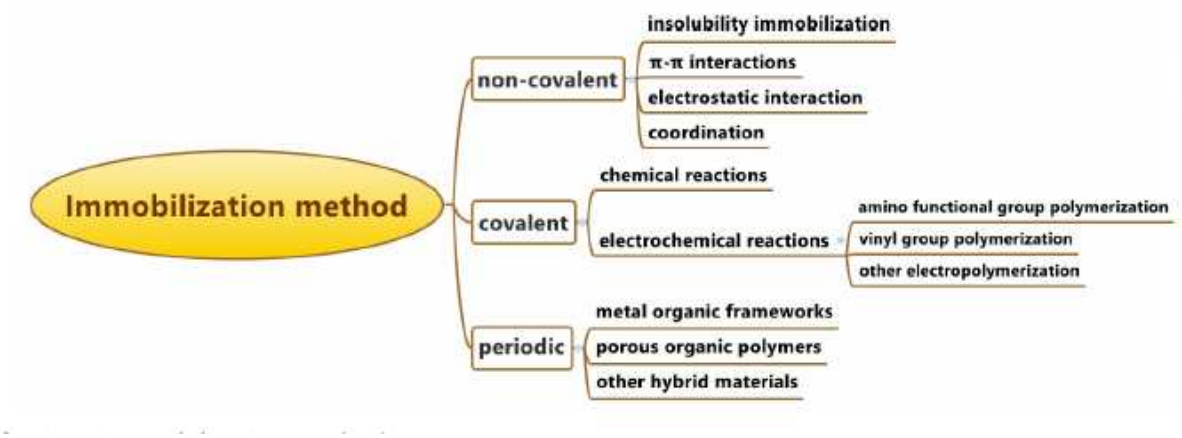

Figure IV.2. Current methodologies for immobilization of molecular metal complexes onto electrode surfaces. Reproduced from Ref. [5].

One of the first example of covalent immobilization of transition metal complexes for the electrocatalytic reduction of CO_2 was reported in 1985 by Meyer and co-workers.[6] The $[Re(Cl)(CO)_3(vbpy)]$ (vbpy = 4-vinyl-4'-methyl-2,2´-bipyridine) complex was electropolymerized onto Pt by application of a reductive potential. The electropolymerization process was monitored by CV as shown in Figure IV.3.A. The modified electrode displayed an electrocatalytic activity in acetonitrile at ca. -1.4 V *vs*. SCE (Figure IV.3.B). Notably, the authors emphasized that CO formation was 30-fold higher by site compared to the results obtained from the same complex in solution. Moreover, the generation of oxalate which was observed in homogeneous electrochemical experimental conditions could be avoided.

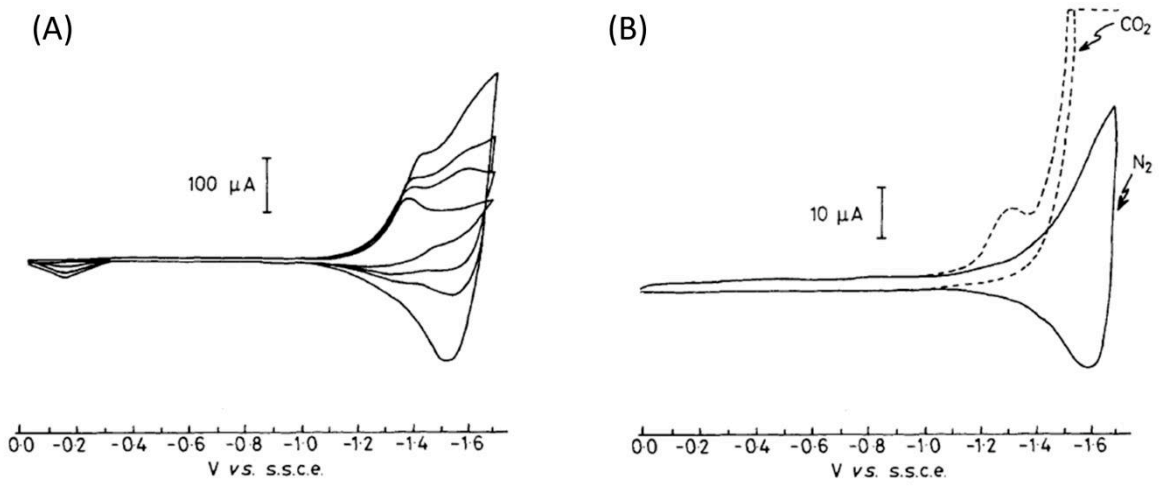

Figure IV.3. A) CV of the electropolymerization of [Re(vbpy)$(CO)_3$Cl] in MeCN/NBu_4ClO_4 0.1 M onto Pt; B) CV under N_2 (-) and CO_2 (---) of the resulting poly-rhenium Pt electrode in MeCN/NBu_4ClO_4 0.1 M. Reproduced from Ref. [6].

Since, many other metal complexes have been immobilized onto electrode surfaces or metal nanoparticles for CO_2RR, as detailed in recent reviews.[2, 8, 9] Among them, several [$M(CO)_4$(tpy)] (M = Fe, Co, Cr, Ni, Ru, Os; tpy = vinylterpyridine) systems were immobilized by electropolymerization onto glassy carbon surfaces. Electrocatalytic reduction of carbon dioxide in H_2O/$NaClO_4$ by using these modified electrodes yielded an unique product, formaldehyde, at ca. -1.1 V *vs*. Ag/AgCl with high TON (up to 15000 for the iron complex) and moderate-to-high faradic efficiency (30% to 80%).[10]

More recently, an alternative strategy based on the *in-situ* electrochemical reduction of diazonium salts has been reported for the covalent immobilization of metal complexes onto electrode surfaces. This approach was successfully used for group 7 tetracarbonyl diimine species. For instance, Nervi and co-workers described the grafting of [$Mn(CO)_4$(apbpy)] (apbpy = 4-(4-aminophenyl)2,2´-bipyridine) systems onto a carbon cloth (Figure IV.4).[11] The modified electrode displayed remarkable catalytic properties in CO_2-saturated $KHCO_3$ in terms of selectivity and efficiency. Indeed, carbon monoxide was the only product generated for -1.0 V < E_{app} < -1.4 V *vs*. Ag/AgCl. Moreover, a 33200 TON value for CO was found together with a 60% faradaic efficiency at -1.35 V *vs*. Ag/AgCl for 600 min. Interestingly, the authors suggested that the electrocatalytic

mechanism of CO production may imply bromide substitution by water in the first stages of the electrocatalytic cycle followed by the dimerization of the Mn-based complex. Their statement was supported by the absence of formate after 10 hours of CO_2 electrolysis, hence suggesting the occurrence of a dimer pathway instead of a hydride pathway.

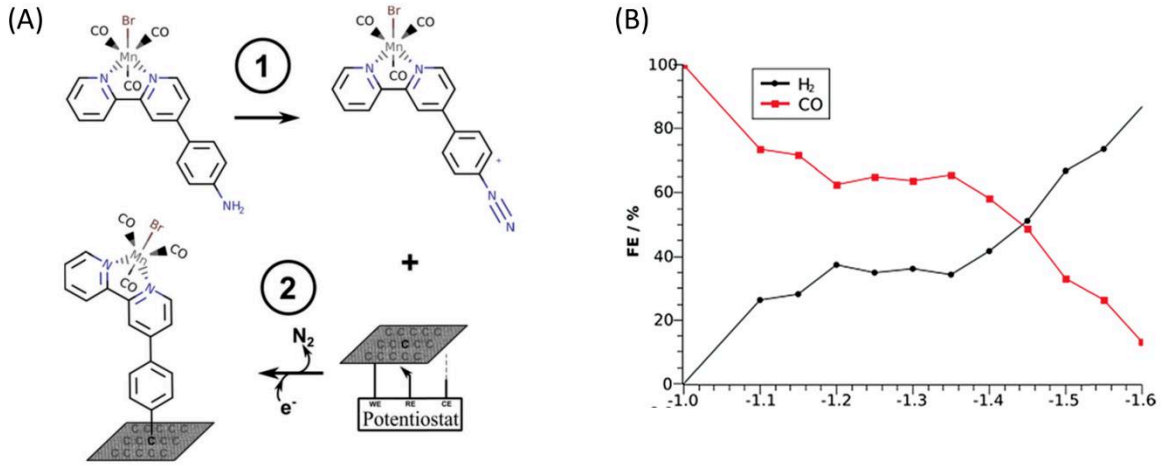

Figure IV.4. A) Preparation of the fac-Mn(apbpy)$(CO)_3$Br/CC electrode *via* diazonium salt reduction; (1) *in-situ* preparation of the diazonium salt and (2) direct electrochemical reduction on carbon cloth. B) H_2 and CO Faradaic efficiency against applied potential for the reduction of CO_2 with a modified fac-Mn(apbpy)$(CO)_3$Br carbon cloth electrode in $KHCO_3$. Reproduced from Ref. [11].

The same research group reported in 2017 the immobilization of two metal amino-phenyl diimine complexes (M = Re, Mn) onto carbon surfaces by using two different methods (reduction of *in-situ* generated diazonium species or oxidation of the amine).[12] Electrocatalytic studies for carbon dioxide reduction in acetonitrile/methanol by these supported catalysts showed that the heterogeneous catalysts were much more efficient than the corresponding homogeneous solutions. Moreover, the functionalized electrodes obtained by reducing the diazonium salts displayed better durability than the ones obtained by oxidizing the amino moiety. Analogously, Zhou *et al.* reported the synthesis and immobilization of 4-amino bpy – Re and Mn complexes by diazonium grafting on graphene oxide. [13] The electrocatalytic activity towards CO_2 of the grafted

complexes was investigated in acetonitrile by using water as proton source. The Re catalyst displayed a turnover frequency (TOF) for the generation of CO up to 4.44 s^{-1} with a H_2/CO ratio of 0.71 by applying a potential of ca. -2.0 V *vs*. Ag/AgCl.

The examples above-described are concerned with covalent attachment of molecular complexes *via* electrochemical activation. Alternatively, non-covalent grafting of metal complexes for CO_2 reduction has been also reported. The approach involves highly aromatic ligands, such as porphyrins or pyrene groups, which can interact with the electrode surface via π-π interactions. Also, ligand backbones which can favor electrostatic interactions or coordination to the electrode surface have been envisaged.[5] For that purpose, multi-walled carbon nanotubes (MWCNTs) have gained attention because they display excellent electric conductivity and high active surfaces.[14] These properties allow the formation of heterogeneous systems which maintain the main structural features of the molecular complex while increasing the surface concentration. Noteworthy, MWCNTs are compatible with hybrid covalent/noncovalent procedures (such as diazonium grafting on nanotubes).[15, 16]

An example of immobilization of a molecular electrocatalyst onto carbon nanotubes was reported by Reisner and co-workers in 2017.[17] In their paper, a *fac*-[MnBr(Me-bpy_{pyr})$(CO)_3$] complex was grafted on CNTs *via* interaction of a pyrene moiety attached to a bipyridine (Figure IV.5). This complex was shown to be an active electrocatalyst for CO_2 reduction in H_2O / $KHCO_3$ 0.5 M since product formation was increased by 10 times compared to the results obtained with similar systems in homogeneous conditions.[18, 19]

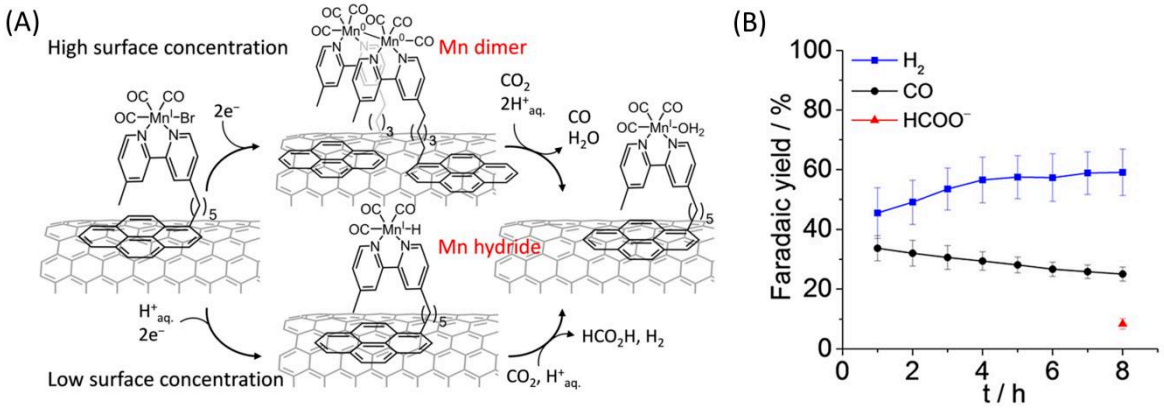

Figure IV.5. General scheme of selective carbonate product formation induced by different Mn species depending on the catalyst loading over the surface. Reproduced from Ref. [17].

The authors observed that product selectivity (CO/formate) could be driven by modification of the complex concentration over the CNT surface: at low concentration, Mn-hydride species were detected by IR-spectroelectrochemistry and promoted the formation of formate. In contrast, an increase of the complex concentration over the surface favored the formation of a Mn-Mn dimer and shifted the selectivity towards CO (Figure IV.5). Nevertheless, CNTs also produced a significant amount of H_2 as shown by the Faradaic efficiency in Figure IV.5.

In summary, the electrocatalytic reduction of CO_2 by supported molecular complexes appears as very promising since it provides better catalytic activities than in the homogeneous case and gives the possibility of working in aqueous phases with better recyclability.[5] The significant improvements achieved for transition metal molecular catalysts suggest that the catalytic activity found for the different [$Mo(CO)_4$(diimine)] complexes described in Chapters II and III could be enhanced by their immobilization onto electrode surfaces. So far, there is no report on any grafted [$Mo(CO)_4$(diimine)] complex for CO_2 reduction.

Thus, this chapter shows preliminary results obtained from the functionalization of carbon electrodes by two different [$Mo(CO)_4$(diimine)] complexes, namely, [$Mo(CO)_4(bpy_{pyr})$] (bpy_{pyr} = 4-Methyl-4'-(5-(pyren-1-yl)pentyl)-2,2'-bipyridine) (**4**) and [$Mo(CO)_4$(4-$PhNH_2$-phen)] (**5**) (Figure IV.6) It includes the synthesis of the ligand and complexes, their characterization, the grafting methods and their studies as electrocatalysts for CO_2 reduction. While the complex **4** can be immobilized over a MWCNT-functionalized surface thanks to non-covalent π-π interactions with the pyrene moiety, the complex **5** is merely grafted by *in-situ* generation of diazonium ions.

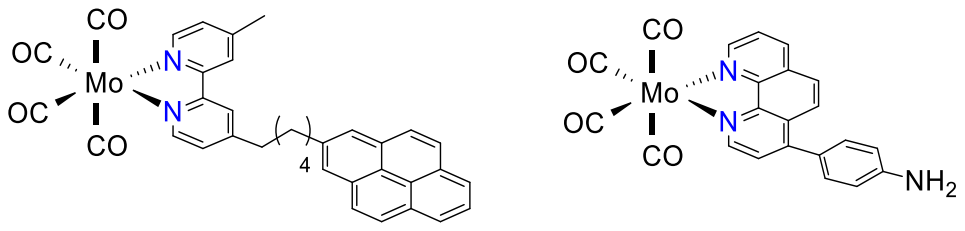

Complex **4** Complex **5**

Figure IV.6. Schematic representation of complexes **4** and **5** investigated in this chapter.

II. Synthesis and electrochemical studies of complex **4**

*II.1. Synthesis and characterization of complex **4***

Synthesis of the ligand bpy-C_5-(pyrene,methyl) (Scheme IV.1) was carried out following a reported procedure by Reisner and co-workers.[17] The ligand was obtained in good yield (64 %). The synthesis of complex **4** was inspired from the synthetic procedure reported by Connor.[20] $[Mo(CO)_4(nbd)]$ (nbd = norbornadiene) was reacted with the functionalized bipyridine in an equimolar reaction at room temperature in THF (Scheme IV.1). An orange solid was obtained in good yields after recrystallization in CH_2Cl_2/THF (Scheme IV.1). IR and ^{1}H-NMR spectroscopic techniques confirmed the nature of the product formed (Figure IV.7).

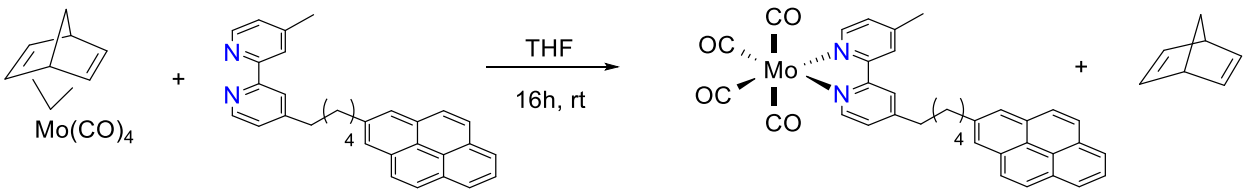

Scheme IV.1. Synthetic pathway for complex **4**.

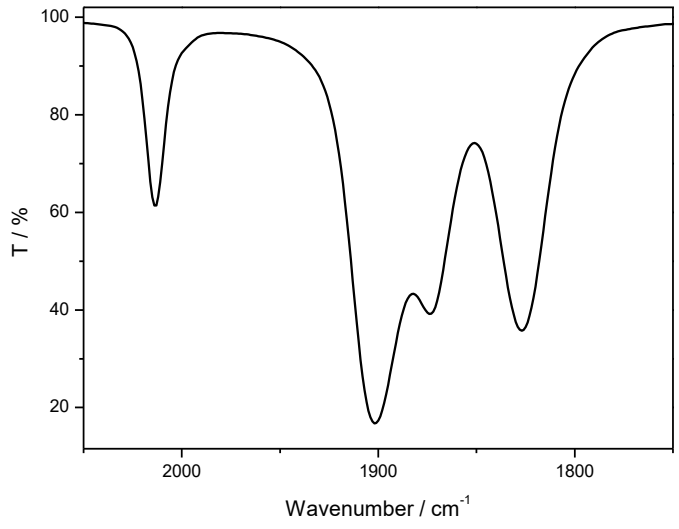

Figure IV.7. IR spectra of complex **4** in THF.

*II.2. Electrochemical studies of complex **4** under Ar and CO_2 in solution*

The redox properties of complex **4** were first investigated by cyclic voltammetry (CV) under argon in THF/NBu_4PF_6 0.1 M by using a boron-diamond doped (BDD) working electrode. All redox potentials are given against the ferrocenium/ferrocene (Fc^+/Fc) redox couple. The Figure IV.8 shows both cathodic and anodic electrochemical responses for the complex at v = 0.1 V s^{-1}. On one hand, a reversible reduction system was detected at -2.05 V *vs*. Fc^+/Fc followed by an irreversible peak at -2.55 V (Figure IV.8, left). On the other hand, several irreversible oxidation processes were observed (Figure IV.8., right). This CV signature is similar to those found for group 6 tetracarbonyl diimine complexes such as [$Mo(CO)_4$(bpy)]. This suggests that reduction processes observed are mainly ligand-based, while oxidation processes are centered in the metal center.[21] Notably, we have observed a 2-fold current difference between the second and first reduction processes, as previously found for the unsymmetrical pyridylindolizine complex [$Mo(CO)_4$(py-indz)] (see Chap. III). This current increase may be ascribed to an ECE or EC_{cat} process occurring between the bis-reduced species and the solvent. It may also be due to a dimerization process.

Under CO_2, a significant increase of the current intensity was detected at the second reduction process whereas the first remained as found under argon (Figure IV.9). This CV behavior is reminiscent to that observed for group 6 tetracarbonyl systems. The modest value of the i_{cat}/i_p ratio (1.6) suggested that the interaction of carbon dioxide with the doubly-reduced complex is hindered by the pyrene group.

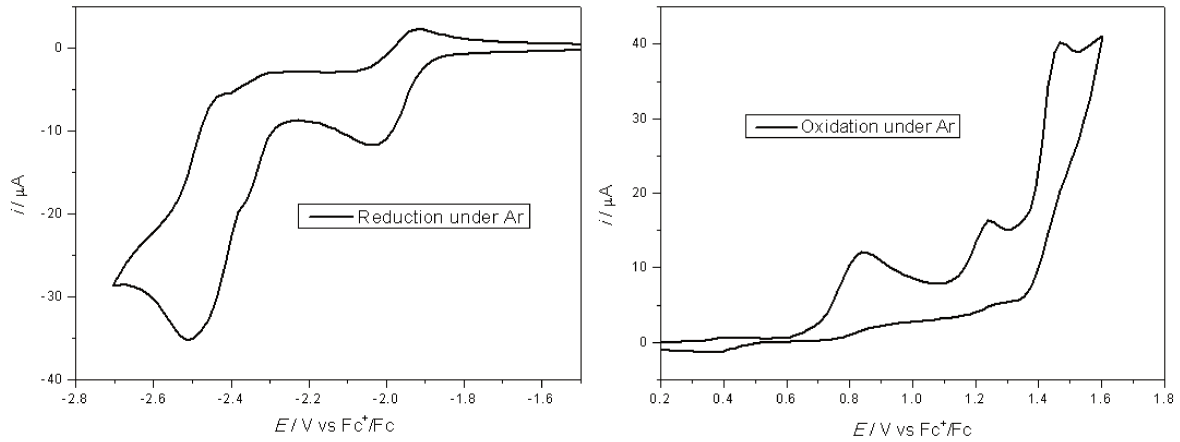

Figure IV.8. CV of complex **4** at a BDD working electrode in THF/NBu_4PF_6 0.1 M under Ar. Conditions: 1 mM of complex, v = 0.1 V s^{-1}.

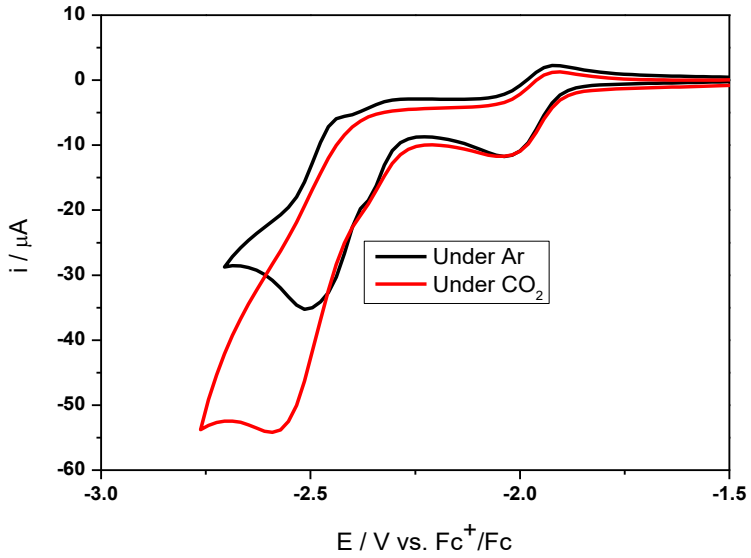

Figure IV.9. CV of complex **4** at a BDD working electrode in THF/NBu_4PF_6 0.1 M under CO_2 (sat.). Conditions: 1 mM of complex, v = 0.1 V s^{-1}.

*II.3. Electrochemical studies of functionalized MWCNT-**4** electrodes under argon and CO_2*

The immobilization of complex **4** onto MWCNTs was carried out according to a previously-described procedure:[22] first, 2 µl of a solution of carbon nanotubes was drop-casted on the surface of a glassy carbon electrode. A 5 µm thick MWCNT film was obtained after solvent (NMP) evaporation under vacuum for 12 h. Second, a solution of complex **4** was then deposited on the functionalized MWCNT electrode.

The resulting modified electrode (**4**-MWCNTs) was then studied by cyclic voltammetry in THF/NBu_4PF_6 0.1 M under argon (Figure IV.10). During the first scan, several reduction processes were detected upon cycling (red curve, Figure IV.10) which may be ascribed to the reduction of poorly attached molecules of Mo complex. After 10 cycles, a stable voltammetric signal was obtained (blue curve, Figure IV.10) with a single reduction peak at -2.55 V *vs*. Ag/$AgNO_3$. For comparison, this reduction peak was not observed with a glassy carbon electrode covered by MWCNTs only (black curve, Figure IV.10).

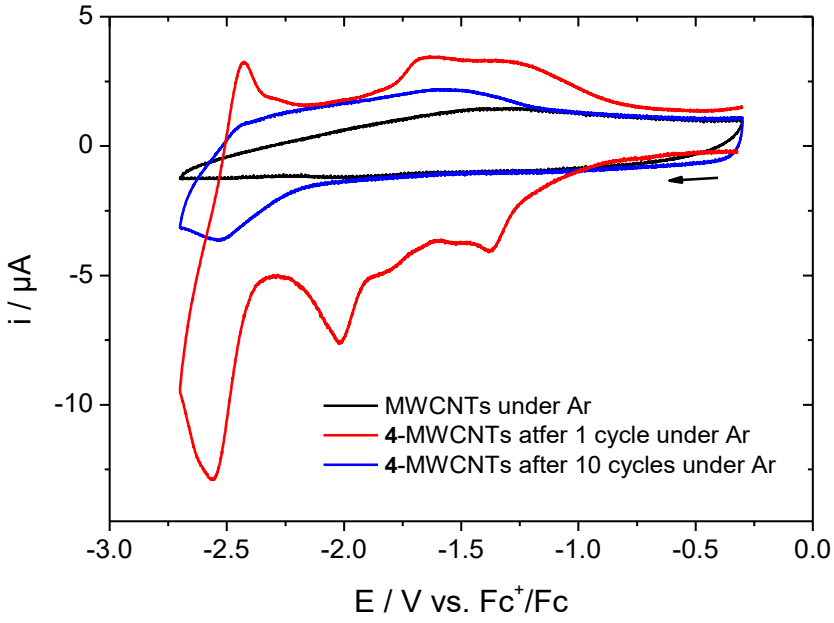

Figure IV.10. CV at a **4**-MWCNTs modified glassy carbon electrode in THF/NBu_4PF_6 0.1 M under Ar Red: first cycle: Blue: after 10 cycles. The black line shows the CV of a bare MWCNTs glassy carbon electrode in the same conditions. Conditions: Ag/$AgNO_3$ (RE), 0.1 V s^{-1}.

Under CO_2 (Figure IV.11), a large current increase was detected at -2.50 V, a potential value related to the second reduction process under Ar, which could be interpreted as an electrocatalytic curve. However, the same experiment carried out with a bare MWCNTs-modified electrode showed almost the same current enhancement, hence clearly indicating that the electrocatalytic behavior found with the **4**-MWCNTs electrode is likely due to CO_2 reduction by carbon nanotubes.

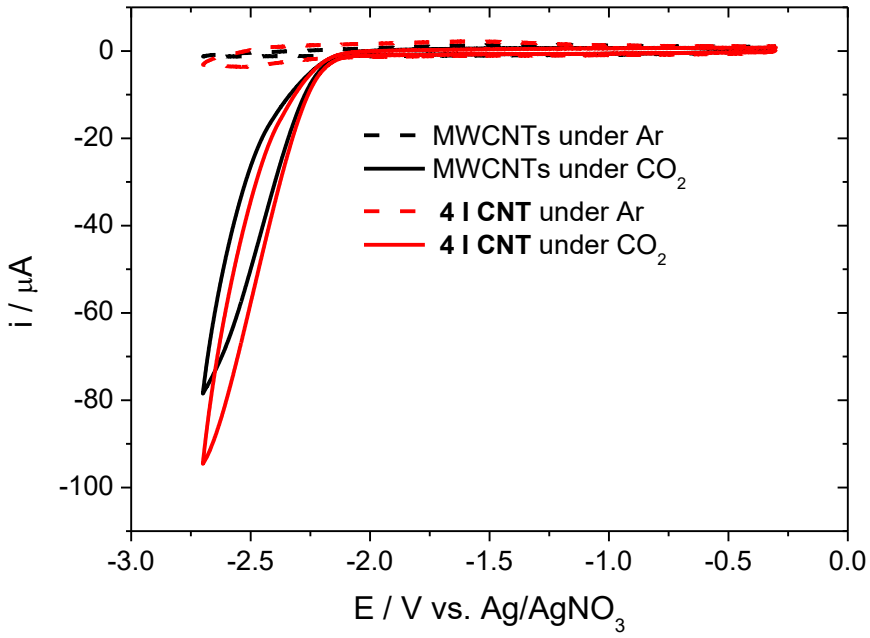

Figure IV.11. CVs of **4**|**CNT** modified glassy carbon electrodes (red) and bare MWCNT GC electrodes (black) under Ar (dashed) and CO_2 (plain) in THF / NBu_4PF_6, 0.1 M. Ref: $Ag/AgNO_3$, v = 0.1 V s^{-1}.

III. Synthesis and electrochemical studies of complex **5**

*III.1. Synthesis and characterization of complex **5***

The synthesis of complex **5** [$Mo(CO)_4$(4-$PhNH_2$-phen)] was performed following the procedure reported by Ardizzoia *et al*.[23] It was the same as that used for the synthesis of [$Mo(CO)_4$(phen)] (see Chapter III). The orange crystalline solid obtained after recrystallization with toluene / dichloromethane was characterized by IR and ^{1}H-NMR spectroscopies. The infrared signature was typical of a tetracarbonyl complex with ν_{CO} bands in the 1900-2100 cm^{-1} region (Figure IV.12).

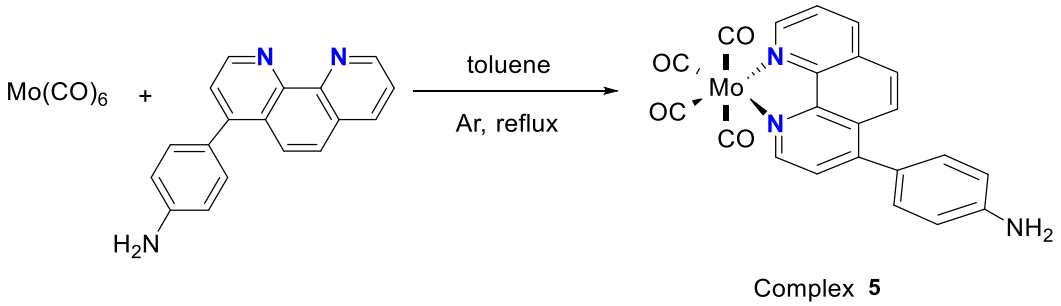

Scheme IV.2. Synthetic pathway for complex **5**.

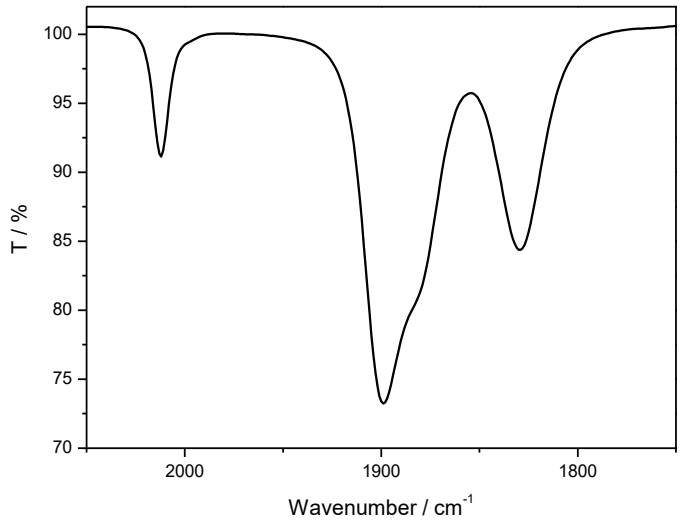

Figure IV.12. IR spectra of complex **5** in THF.

*III.2. Electrochemical studies of complex **5** under Ar*

As shown in Figure IV.13, the complex **5** displayed an electrochemical behavior in acetonitrile which is analogous to that obtained for $[Mo(CO)_4(phen)]$ (**2**) (see Tables IV.1 and IV.2 for comparative electrochemical data). Indeed, a one-electron reversible reduction was detected at $E_{1/2}(1) = -1.85$ V *vs*. Fc^+/Fc, followed by an irreversible second reduction at $E_{pc}(2) = -2.40$ V. Noteworthy, the current for this irreversible process appeared as twice more intense than that detected for the first. This result supports the idea that the bis-reduced species of complex **5**

reacts with a solvent molecule as observed for complex **4**. Comparison with complex **2** clearly showed a positive shift by 130 mV and 400 mV for the first and second process, respectively (Table IV.1). This potential drift was analogously observed for a phenyl-substituted bipyridine derivative, $[Mo(CO)_4(Ph_2\text{-bpy})]$, compared to $[Mo(CO)_4(bpy)]$.[24] This effect might be due to the extent of delocalization of the charge at the reduced states thanks to the phenyl groups. Higher delocalization may induce better stability of the reduced species, hence consequently a positive shift of the redox potential. When scanning positively, the complex **5** exhibited several oxidation peaks which were all irreversible at v = 0.1 V s^{-1} (Figure IV.13). This behavior is also similar to that found for complex **2** (Table IV.2), except that supplementary peaks were detected, likely resulting from the oxidation of the amino group.

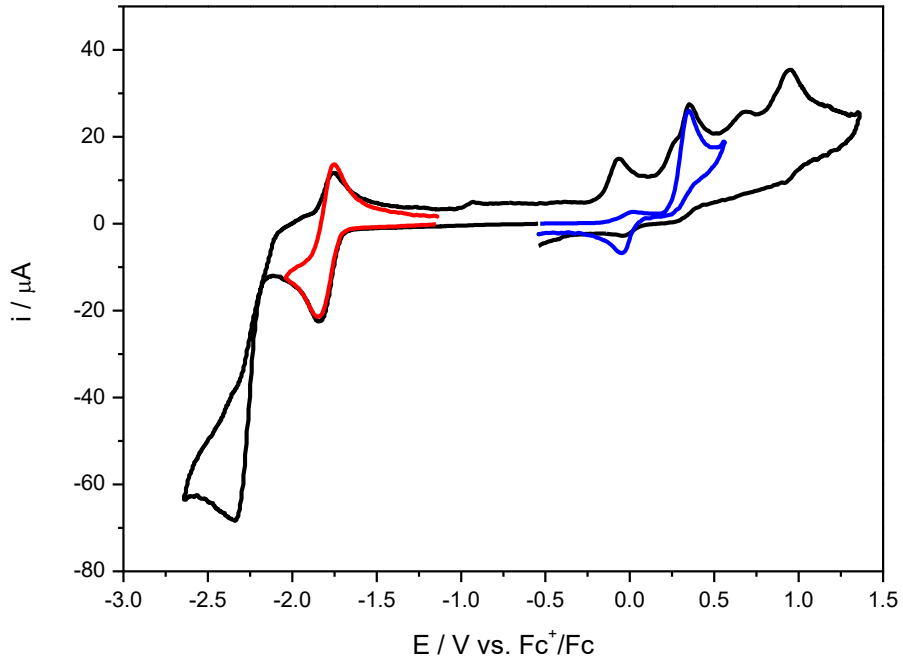

Figure IV.13. CV of complex **5** at a GC working electrode in $MeCN/NBu_4PF_6$ 0.1 M under Ar. Conditions: 1mM of complex, 0.1 V s^{-1}.

Table IV.1. Electrochemical data ($E_{1/2}$/V *vs.* Fc^+/Fc) of complex **5** and **2** (for comparison) in MeCN / NBu_4PF_6 0.1 M for the reduction processes.

	$E_{1/2}(1)$	$E_{1/2}(2)$ [a]
Complex **5**	-1.85	-2.40
Complex **2**	-1.98	-2.80

[a] Irreversible peak at v = 0.1 V s^{-1}

Table IV.2. Electrochemical data ($E_{1/2}$/V *vs.* Fc^+/Fc) of complex **5** and **2** (for comparison) in MeCN / NBu_4PF_6 0.1 M for the oxidation processes.

	$E_{pa}(3)$ [a]	$E_{pa}(4)$ [a]	$E_{pa}(5)$ [a]	$E_{pa}(6)$ [a]
Complex **5**	-0.05[a]	0.35[a]	0.70[a]	0.95[a]
Complex **2**	0.30	0.74	-	-

[a] Irreversible peak at v = 0.1 V s^{-1}

*III.3. Immobilization of complex **5** onto a glassy carbon electrode via in-situ diazonium reduction*

The grafting of complex **5** onto a GC working electrode was performed according to the well-known diazonium approach.[4] The principle is to generate the diazonium salt from the aminophenyl derivative by addition of nitrite ions in presence of acid. The resulting diazonium is then reduced electrochemically into an aryl radical which undergoes a C-C bond making with the carbon surface together with N_2 evolution. More specifically for complex **5**, the procedure was similar to that reported by Nervi and co-workers for a Mn-bby complex.[11] The complex **5** (1.4 mg) was initially dissolved in cold acetonitrile (2 mL, 0°C) containing NBu_4PF_6 (0.1 M) under Ar. Addition of trichloroacetic acid (40 mg) then tert-butyl nitrite (12 µL) led to the formation of the diazonium salt. CV of the solution displayed an irreversible reduction peak at -0.67 V *vs*. Ag/AgCl for the first scan (Figure IV.14). Further cycling from 1.0 to -0.90 V *vs*. Ag/AgCl led to the fast disappearance of this peak, which was indicative of the formation of a layer on the electrode, as usually observed for diazonium grafting.

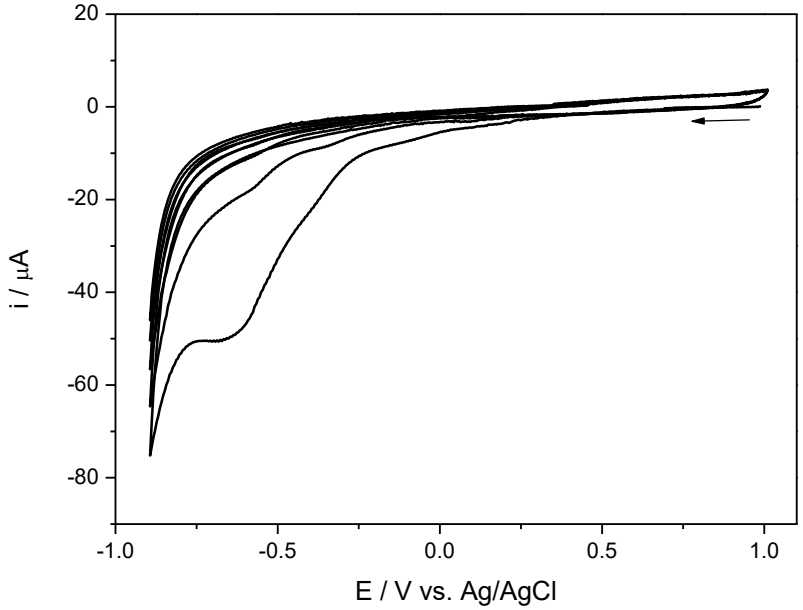

Figure IV.14. CVs of the diazonium solution of complex **5** at a GC working electrode in MeCN / NBu_4PF_6 0.1 M (0 °C) under Ar. Conditions: v = 0.1 V s^{-1}. See text for details.

After cleaning the modified glassy carbon electrode with acetonitrile, an electrochemical study was performed in a solution of MeCN / NBu_4PF_6 0.1 M free of any complex. As shown in Figure IV.15, an irreversible peak was detected at −1.70 V *vs*. Fc^+/Fc for the functionalized electrode. The absence of peak when using a bare GC electrode in the same conditions strongly suggested that the grafting of complex **5** was successful. Furthermore, the redox potential value was consistent with a reduction process centered on the grafted complex, since solution studies showed that the first reduction process occurred at -1.85 V in acetonitrile (Table IV.1).

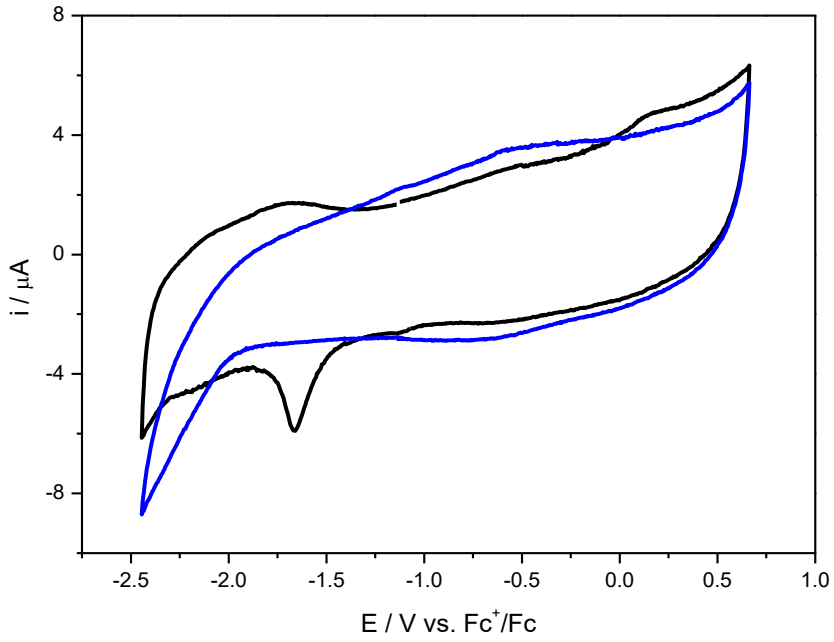

Figure IV.15. CV of bare (blue) and complex **5**-functionalized (black) glassy carbon electrodes in MeCN / NBu_4PF_6 0.1 M under Ar at v = 0.1 V s^{-1}.

*III.4. Voltammetric response of immobilized complex **5** under CO_2*

As shown in Figure IV.16, exposition of the functionalize GC electrode to carbon dioxide in MeCN induced two new reduction peaks at -1.45 V and -1.79 V *vs*. Fc^+/Fc. While the first peak remained undetermined and may be due to solution impurities or dioxygen (as it was present also at a bare electrode), the second reduction peak observed at -1.79 V *vs*. Fc^+/Fc may be certainly ascribed to an electron transfer reaction for complex **5**. Comparison of the peak current obtained under Ar at -0.6 V indicates no real enhancement of the current at this scan rate (v = 0.1 V s^{-1}), hence no catalytic reaction. Nevertheless, the slight negative potential shift (90 mV) may correspond to the formation of a novel metal-CO_2 adduct which would be reduced at a lower potential. However, supplementary studies are necessary to better understand these processes.

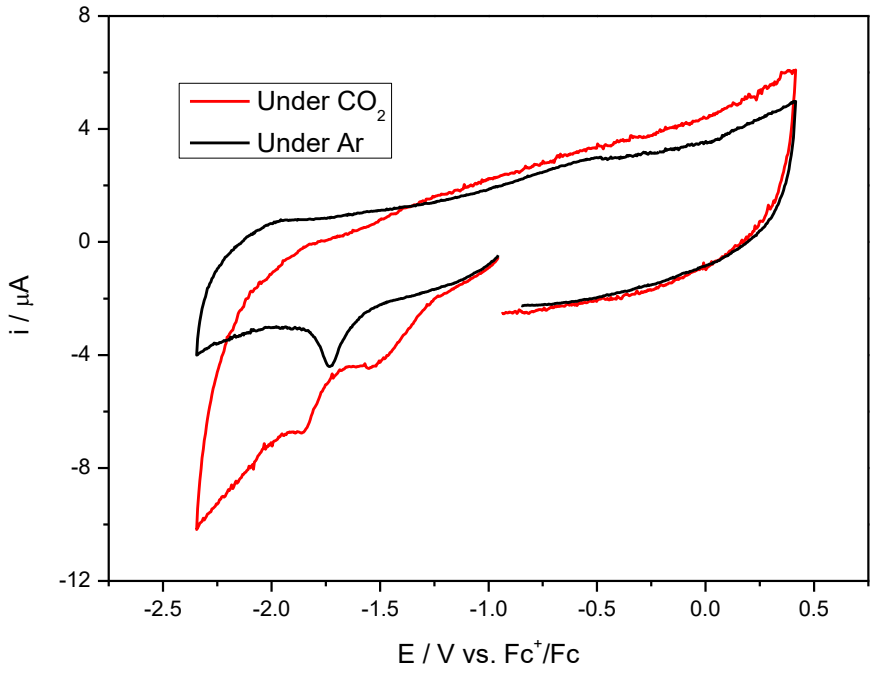

Figure IV.16. CV of a complex **5**-functionalized glassy carbon electrode in MeCN / NBu_4PF_6 0.1 M under Ar (black) and under CO_2 (red) at v = 0.1 V s^{-1}.

IV. Conclusions

In summary, two novel Mo-diimine tetracarbonyl complexes which can be grafted onto electrode surfaces have been successfully synthesized. Electrochemical studies have shown that the complex **4** bearing a pyrene-modified bipyridine ligand behaved similarly to $[Mo(CO)_4(bpy)]$, since a significant catalytic current was detected at the second reduction. Grafting of this complex onto MWCNTs was operated by π-π stacking thanks to the pyrene moiety. The resulting modified electrode was tested under CO_2 in THF. A large current enhancement was found at ca. −2.3 V *vs*. Fc^+/Fc which was further ascribed to CO_2 electroreduction mediated by carbon nanotubes. Hence, these first studies have led to the main conclusion that the use of MWNTCs as grafting support is possible only if the MO-diimine complex displays an onset of catalysis above -2.0 V *vs*. Fc^+/Fc.

The complex **5**, $[Mo(CO)_4(phen\text{-}PhNH_2)]$, was also studied in solution by CV in an organic solvent. The redox behavior was similar to that of $[Mo(CO)_4(phen)]$. However, the two reduction processes occurred at slightly more positive potential values and the second electron transfer was characterized by a chemical-coupled reaction. Immobilization of complex **5** onto GC electrode was carried out by electrochemical reduction of *in-situ* generated diazonium derivatives. CVs under argon demonstrated that the grafting led to the deposition of a new species on the surface which was ascribed to the Mo complex. Electrochemical studies under CO_2 showed a slight shift of the reduction peak without real current enhancement. Nevertheless, these first experiments need being reproduced and completed by surface analyses (IR, XPS).

From these preliminary results, several strategies can be envisaged. The first one would be to change the nature of the supporting material such that it does not interfere with the electrocatalytic properties of the complex. A second approach would be to design new metal complexes which able to perform electrocatalysis at higher potential values than -2.0 V *vs.* Fc^+/Fc. This would be possible by modification of the ligand framework for example by insertion of withdrawing groups, or by variation of the metal center (W, Cr). Alternatively, new ligands such as hydroxybenzene-bipyridine which was recently shown to be of high interest for CO_2 electrocatalysis as Cr complexes,[25] could be modified for further grafting onto electrode surfaces.

Bibliography

[1] F. Franco, C. Rettenmaier, H. S. Jeon, B. Roldan Cuenya, *Chem. Soc. Rev.* **2020**, *49*, 6884-6946.

[2] K. E. Dalle, J. Warnan, J. J. Leung, B. Reuillard, I. S. Karmel, E. Reisner, *Chem. Rev.* **2019**, *119*, 2752-2875.

[3] M. König, J. Vaes, E. Klemm, D. Pant, *iScience* **2019**, *19*, 135-160.

[4] D. Belanger, J. Pinson, *Chem. Soc. Rev.* **2011**, *40*, 3995-4048.

[5] L. Sun, V. Reddu, A. C. Fisher, X. Wang, *Energy Environ. Sci.* **2020**, *13*, 374-403.

[6] T. R. O'Toole, L. D. Margerum, T. D. Westmoreland, W. J. Vining, R. W. Murray, T. J. Meyer, *J. Chem. Soc. Chem. Commun.* **1985**, 1416.

[7] X. Zhang, Z. Wu, X. Zhang, L. Li, Y. Li, H. Xu, X. Li, X. Yu, Z. Zhang, Y. Liang, H. Wang, *Nat. Commun.* **2017**, *8*, 14675.

[8] E. Boutin, L. Merakeb, B. Ma, B. Boudy, M. Wang, J. Bonin, E. Anxolabehere-Mallart, M. Robert, *Chem. Soc. Rev.* **2020**.

[9] N. Elgrishi, M. B. Chambers, X. Wang, M. Fontecave, *Chem. Soc. Rev.* **2017**, *46*, 761-796.

[10] J. A. Ramos Sende, C. R. Arana, L. Hernandez, K. T. Potts, M. Keshevarz-K, H. D. Abruna, *Inorg. Chem.* **1995**, *34*, 3339-3348.

[11] L. Rotundo, J. Filippi, R. Gobetto, H. A. Miller, R. Rocca, C. Nervi, F. Vizza, *Chem. Commun.* **2019**, *55*, 775-777.

[12] C. Sun, L. Rotundo, C. Garino, L. Nencini, S. S. Yoon, R. Gobetto, C. Nervi, *Chemphyschem* **2017**, *18*, 3219-3229.

[13] X. Zhou, D. Micheroni, Z. Lin, C. Poon, Z. Li, W. Lin, *ACS Appl. Mater. Interfaces* **2016**, *8*, 4192-4198.

[14] S. Iijima, *Nature* **1991**, *354*, 56-58.

[15] A. Maurin, M. Robert, *Chem. Commun.* **2016**, *52*, 12084-12087.

[16] X. Zhang, Z. Wu, X. Zhang, L. Li, Y. Li, H. Xu, X. Li, X. Yu, Z. Zhang, Y. Liang, H. Wang, *Nat. Commun.* **2017**, *8*, 14675-14683.

[17] B. Reuillard, K. H. Ly, T. E. Rosser, M. F. Kuehnel, I. Zebger, E. Reisner, *J. Am. Chem. Soc.* **2017**, *139*, 14425-14435.

[18] S. Sinha, A. Sonea, W. Shen, S. S. Hanson, J. J. Warren, *Inorg. Chem.* **2019**, *58*, 10454-10461.

[19] J. D. Blakemore, A. Gupta, J. J. Warren, B. S. Brunschwig, H. B. Gray, *J. Am. Chem. Soc.* **2013**, *135*, 18288-18291.

[20] J. A. Connor, C. Overton, *J. Organomet. Chem.* **1983**, *249*, 165-174.

[21] M. L. Clark, K. A. Grice, C. E. Moore, A. L. Rheingold, C. P. Kubiak, *Chem. Sci.* **2014**, *5*, 1894-1900.

[22] M. Bourourou, K. Elouarzaki, N. Lalaoui, C. Agnes, A. Le Goff, M. Holzinger, A. Maaref, S. Cosnier, *Chem. Eur. J.* **2013**, *19*, 9371-9375.

[23] G. A. Ardizzoia, M. Bea, S. Brenna, B. Therrien, *Eur. J. Inorg. Chem.* **2016**, *2016*, 3829-3837.

[24] D. Miholová, B. Gaš, S. Záliš, J. Klíma, A. A. Vlček, *J. Organomet. Chem.* **1987**, *330*, 75-84.

[25] S. L. Hooe, J. M. Dressel, D. A. Dickie, C. W. Machan, *ACS Catal.* **2019**, 1146-1151.

Conclusions and perspectives

Conclusions and perspectives

The main objective of this PhD work was the study of group 6 tetracarbonyl diimine systems as molecular electrocatalysts for CO_2 reduction. Our first approach has been to modify the diimine moiety in $[Mo(CO)_4(bpy\text{-}(\mathbf{R})_2)]$ complexes by introduction of either electron-donating or electron-withdrawing substituting groups **R** on the bipyridine backbone. Two new complexes, bearing CO_2Me and CF_3 moieties were thus synthesized and characterized by spectroscopic and electrochemical methods. Comparative voltammetric and spectroelectrochemical (UV-Vis-IR) studies in different media allowed us to better comprehend the effect of the **R** group on the redox properties under argon and CO_2. All complexes have shown a first reduction process taking place on the bipyridine ligand, leading to a Mo-bipyridyl radical species whose reduction potential value was R-dependent. The second reduction event was found to lead to tricarbonyl $[Mo(CO)_3(bpy\text{-}(\mathbf{R})_2]^{2-}$ species in THF for all complexes except that bearing CO_2Me moieties according to spectroelectrochemical results. Indeed, a putative protonated tetracarbonyl complex was likely generated for that compound (Figure V.1). Electrocatalytic studies of this family of complexes demonstrated that the highest catalytic current could be obtained for complexes bearing electron-donating groups (**R** = Me, ^{t}Bu), but this gain was overcompensated by higher overpotential values. Inversely, $[Mo(CO)_4(bpy\text{-}(\mathbf{R})_2)]$ complexes bearing electron-withdrawing moieties, $\mathbf{1}^{CO2Me}$ and $\mathbf{1}^{CF3}$, displayed poor CO_2 activity at the second reduction. Nevertheless, a current increase was detected at potential values in-between the second and third cathodic processes.

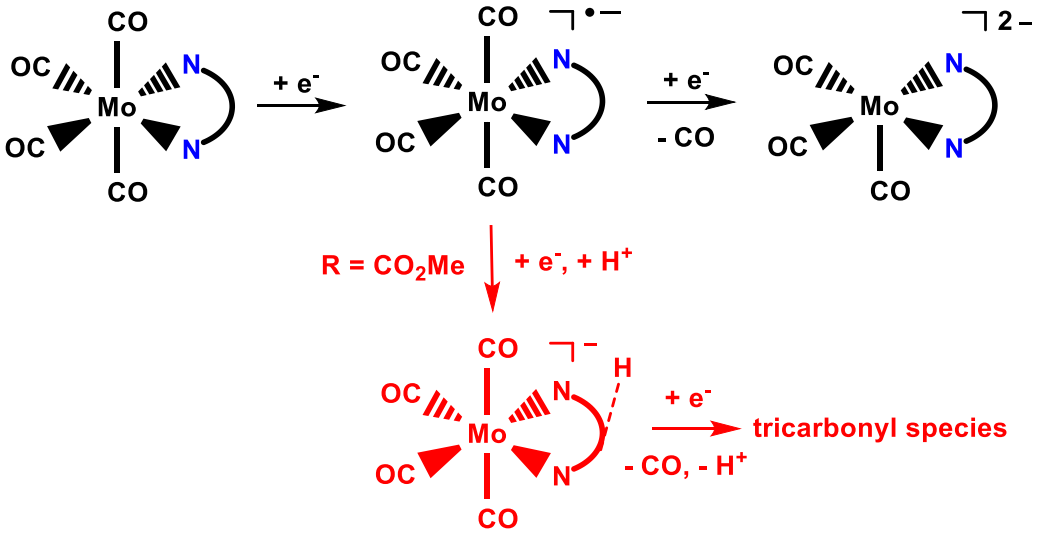

Figure V.1. Reduction pathways of $[Mo(CO)_4(bpy\text{-}(\mathbf{R})_2]$ complexes.

Our second strategy has been to study the redox properties and reactivity *vs*. CO_2 of two other Mo complexes bearing phen (complex **2**) or py-indz (complex **3**) diimine ligand instead of bpy. The complexes have displayed an electrochemical signature similar to $[Mo(CO)_4(bpy)]$. An unexpected interaction with carbon dioxide was detected for complexes **2** and **3** at their first reduction processes at low-to-moderate scan rate. The reaction rate was dependent on the nature of the diimine ligand, obtaining the highest i_{cat} / i_p ratio value for the py-indz complex **3**. Noteworthy, IR-spectroelectrochemical results showed the formation of carbonate and formate ions upon reduction under CO_2 atmosphere (Figure V.2). In addition, water was found to play an active role in the reaction rate. Experimental data supported by theoretical calculations allowed us to propose different mechanistic pathways based on the assumption that the tetracarbonyl mono-reduced species could loss one CO and lead to the active $[Mo(CO)_3(diimine)]^{\bullet-}$ species. Two main catalytic pathways were the considered, one involving a first reaction with CO_2 and H^+, the other with H^+. According to DFT calculations, both CO_2 and hydride transient adducts may be reduced at more positive potential than the $[Mo(CO)_4(diimine)] \rightarrow [Mo(CO)_4(diimine)]^{\bullet-}$ reaction, thus explaining the current enhancement observed experimentally. Even though, modification of the diimine ligand in $[Mo(CO)_4(diimine)]$ complexes did not provide any considerable catalytic enhancement comparing to other systems already described.[1-3]

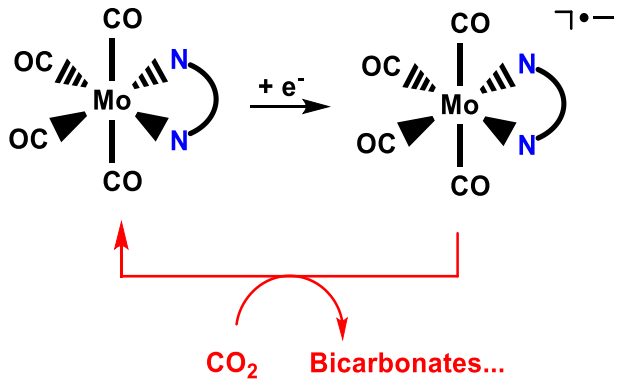

Figure V.2. Interaction of $[Mo(CO_4(diimine)]$ mono-reduced species with carbon dioxide.

At last, another proposed strategy was to functionalize glassy carbon electrodes with $[Mo(CO)_4(diimine)]$ complexes in order to perform supported electrocatalysis for CO_2 reduction .[4]

Two novel complexes, [($Mo(CO)_4(bpy_{pyr})$] (**4**) and [$Mo(CO)_4$(4-$PhNH_2$-phen)] (**5**), were designed to afford immobilization onto electrode surfaces by either non-covalent π-π interactions (with carbon nanotubes) or covalent diazonium grafting respectively, on the basis of previous results obtained with other metals.[5, 6] The preliminary studies showed that functionalization of the electrodes with these complexes was successful. However, in the case of complex **4**, the presence of CNTs hindered the electrocatalytic signal, hence not allowing to give a definitive conclusion of the activity of the metal complex towards CO_2. For the complex **5**, no real current enhancement could be evidenced, requiring further trials with various experimental conditions.

To summarize, we have developed different electrochemical strategies around [$Mo(CO)_4$(diimine)] catalytic properties towards carbon dioxide transformation. Mechanistic details about the interaction of mono-reduced [$Mo(CO)_4$(diimine)] species with carbon dioxide were proposed.[7] Although no great enhancement of catalytic activity could be achieved, two interesting and unexpected results were obtained. The first one concerns the putative tetracarbonyl species obtained at the second reduction of the complex $\mathbf{1}^{\mathbf{CO2Me}}$ which might result from electron-withdrawing and H-bonding effects of the ester group. The second point concerns the detection of a current enhancement under CO_2 at the first reduction step for complexes **2** and **3**. This result may be exploited by combining this ligand architecture with a right surface material (such as gold) in order to favor CO unbinding from the mono-reduced tetracarbonyl species, which is the rate determining step of the CO_2 conversion. Alternatively, a deeper modification of the ligand framework should be enough to increase the results reported in this work, improving considerably the lability necessary to habilitate an easier interaction with carbon dioxide. This strategy is exemplified in the study of the complex [Mo(η^3-allyl)$(CO)_2$(x,x'-dimethyl-2,2'-bipyridine)(NCS)] (x = 4–6) reported by Taylor *et al.*[7] Again, the use of photoelectrochemical techniques could be considered as the next step in the study of [$Mo(CO)_4$(diimine)] complexes as catalysts. Labilization of an axial CO ligand by photo-irradiation should reduce the overpotentials and improve the catalytic activity of these systems. Indeed, the efficiency of this strategy was reported by Hartl *et al.* in the study of [$Mo(CO)_4$(6,6´-dimethyl-2,2´-bipyridine)] complexes, achieving a ca. 500 mV positive shift of the catalytic onset.[8]

Bibliography

[1] M. L. Clark, K. A. Grice, C. E. Moore, A. L. Rheingold, C. P. Kubiak, *Chem. Sci.* **2014**, *5*, 1894-1900.

[2] J. O. Taylor, R. D. Leavey, F. Hartl, *ChemElectroChem* **2018**, *5*, 3155-3161.

[3] J. Tory, B. Setterfield-Price, R. A. W. Dryfe, F. Hartl, *ChemElectroChem* **2015**, *2*, 213-217.

[4] X. Zhang, Z. Wu, X. Zhang, L. Li, Y. Li, H. Xu, X. Li, X. Yu, Z. Zhang, Y. Liang, H. Wang, *Nat. Commun.* **2017**, *8*, 14675.

[5] S. Sinha, A. Sonea, W. Shen, S. S. Hanson, J. J. Warren, *Inorg. Chem.* **2019**, *58*, 10454-10461.

[6] C. Sun, L. Rotundo, C. Garino, L. Nencini, S. S. Yoon, R. Gobetto, C. Nervi, *Chemphyschem* **2017**, *18*, 3219-3229.

[7] J. O. Taylor, F. L. P. Veenstra, A. M. Chippindale, M. J. Calhorda, F. Hartl, *Organometallics* **2019**, *38*, 1372-1390.

[8] J. O. Taylor, Y. Wang, F. Hartl, *ChemCatChem* **2019**, *12*, 386-393.

APPENDIX

General synthetic methods

All starting materials (bipyridine, functionalized bipyridines, phenanthroline, $Mo(CO)_6$, KC_8) were commercially available and used as purchased, unless stated otherwise. Synthesis of functionalized bipyridines 4-Methyl-4'-(5-(pyren-1-yl)pentyl)-2,2'-bipyridine and 4-(1,10-phenanthrolin-4-yl) aniline were performed following the experimental procedure reported by Gunnlangson.[1] Solvents were purified by standard methods (CaH_2 or Na/benzophenone) before use. All syntheses were conducted under inert atmosphere of dry argon by using standard Schlenk techniques. For electrochemical and spectroelectrochemical measurements, tetrahydrofuran was passed over activated basic alumina before distillation over sodium. The solvent was collected under inert atmosphere and stored into glovebox under molecular sieves (3 Å) several days before use. The supporting salt NBu_4PF_6 was synthesized from NBu_4OH (Fluka) and HPF_6 (Aldrich). It was then purified, dried under vacuum for 48 hours at 100°C, and then kept under Ar in the glovebox. Solution of THF/NBu_4PF_6 0.1 M was dried for two days under 3 Å molecular sieves before use. Characterization via ^{1}H-RMN have been performed in deuterated chloroform or tetrahydrofuran, while IR spectroscopic data have been obtained in THF for each system.

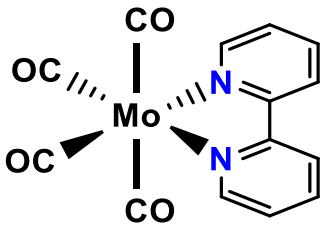

Tetracarbonyl(2,2´-bipyridine)molybdenum(0).**1^H**,**1**.

Molybdenum hexacarbonyl (0.7 g, mmol) and 2,2´-bipyridine (0.4 g, mmol) were refluxed in toluene for 90 minutes in the absence of light. The solution goes from a strong violet to red, forming a precipitate that is filtered and washed with cold toluene and diethyl ether, obtaining a red powder. Recrystallization in 1:1 diethyl ether / dichloromethane provides red crystalline

solid.[2] Yield: 0.77 g (81%). ^{1}H RMN (300 MHz, d8-THF): 9.11 (d, J=4.99 Hz, 2 H), 8.44 (d, J=8.17 Hz, 2H), 7.94 (td, J=8.04, 1.45 Hz, 2H), 7.52 (t, J=5.91 Hz, 2H). IR (THF, cm^{-1}): 2012, 1890, 1882, 1840.

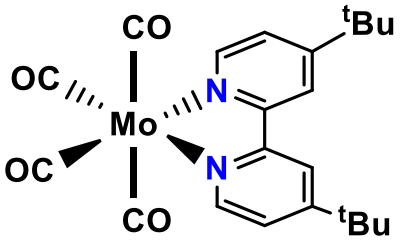

Tetracarbonyl(4,4´-ditertbutyl-2,2´-bipyridine)molybdenum(0).**1^{tBu}**.

Molybdenum hexacarbonyl (0.7 g, 2.65 mmol) and 4,4´-ditertbutyl-2,2´-bipyridine (0.71 g, 2.65 mmol) were refluxed in toluene for 90 minutes under reflux in the absence of light. The solution goes from a strong violet to red, forming a precipitate that is filtered and washed with cold toluene and diethyl ether, obtaining a red powder. Recrystallization in 1:1 diethyl ether / dichloromethane provides red crystalline solid.[2, 3] Yield: 0.81 g (70%). ^{1}H RMN (300 MHz, Chloroform-d): 8.93 (d, J=5.77, 2H), 8.07 (s, 2H), 7.38 (d, J=5.77, 2H), 1.41 (s, 18H). IR (THF, cm^{-1}): 2015, 1908, 1889, 1846.

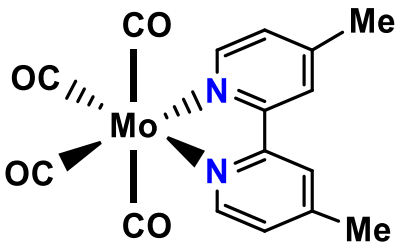

Tetracarbonyl(4,4´-dimethyl-2,2´-bipyridine)molybdenum(0).**1^{Me}**.

[Mo(CO)$_4$(bicyclo[2,2,1]hepta-2,5-diene)] (0.55 g, 1.66 mmol) and 4,4'-dimethyl-2,2'-bipyridine (0.3 g , 1.65 mmol) were dissolved in THF (30 ml) at room temperature, obtaining a dark red

solution. After stirring overnight, the solution was filtered and a red residue was obtained after solvent evaporation at reduced pressure, washing with light petroleum ether. Recrystallization in a 1:1 light petroleum ether / dichloromethane solution provides a brown crystalline solid after storing the solution at 0°C.[3] Yield: 0.25 g (72%) ^{1}H RMN (300 MHz, Chloroform-d): 7.84 (d, J = 7.55 Hz, 2H), 7.74 (d, J = 7.12 Hz, 2H), 7.32 (d, J = 7.55 Hz, 2H), 2.95 (s, 6H). IR (THF, cm^{-1}): 2013, 1908, 1890, 1847.

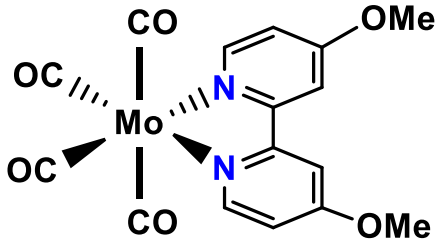

Tetracarbonyl(4,4´-dimethoxy-2,2´-bipyridine)molybdenum(0).**1^{OMe}**.

[Mo(CO)$_4$(bicyclo[2,2,1]hepta-2,5-diene)] (0.5 g, 1.66 mmol) and 4,4'-dimethoxy-2,2'-bipyridine (0.35 g , 1.65 mmol) were dissolved in THF (30 ml) at room temperature, obtaining a dark red solution. After stirring overnight, the solution was filtered and an orange residue was obtained after solvent evaporation at reduced pressure, washing with light petroleum ether. Recrystallization in a 1:1 light petroleum ether / dichloromethane solution provides orange crystals after storing the solution at 0°C.[3] Yield: 0.27 g (75%) ^{1}H RMN (300 MHz, Chloroform-d): 8.89 (d, J = 6.24 Hz, 2H), 7.48 (s, 2H), 6.88 (d, J = 6.29 Hz, 2H), 4.01 (s, 6H). IR (THF, cm^{-1}): 2011, 1895, 1872, 1832.

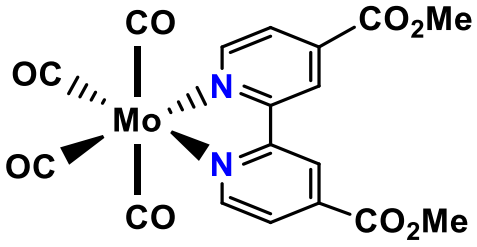

Tetracarbonyl(4,4´-dicarboxy-2,2´-bipyridine)molybdenum(0).**1**^{CO2Me}.

[Mo(CO)$_4$(bicyclo[2,2,1]hepta-2,5-diene)] (0.110 g, 0.37 mmol) and 4,4'-dicarboxy-2,2'-bipyridine (0.1 g , 0.37 mmol) were dissolved in THF (30 ml) at room temperature, obtaining a dark solution. After stirring overnight, the solution was filtered and a purple residue was obtained after solvent evaporation at reduced pressure, washing with light petroleum ether. Recrystallization in a 1:1 light petroleum ether / dichloromethane solution provides purple crystalline solid after storing the solution at 0°C.[3] Yield: 0.08 g (75%) ^{1}H RMN (300 MHz, Chloroform-d): 9.24 (d, J = 5.61 Hz, 2H), 8.85 (s, 2H), 7.94 (d, J = 5.59 Hz, 2H), 2.14 (s, 6H). IR (THF, cm^{-1}): 2011, 1895, 1872, 1832.

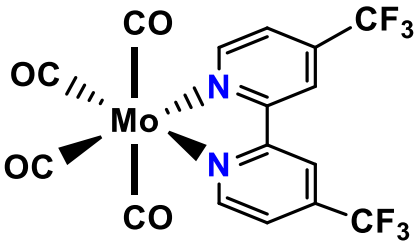

Tetracarbonyl[4,4´-bis(trifluoromethyl)-2,2´-bipyridine)]molybdenum(0).**1**^{CF3}.

[$Mo(CO)_4$(bicyclo[2,2,1]hepta-2,5-diene)] (0.1 g, 0.33 mmol) and 4,4'-bis(trifluoromethyl)-2,2'-bipyridine (0.01 g , 0.34 mmol) were dissolved in THF (30 ml) at room temperature, obtaining a dark solution. After stirring overnight, the solution was filtered and a purple residue was obtained after solvent evaporation at reduced pressure, washing with light petroleum ether. Recrystallization in a 1:1 light petroleum ether / dichloromethane solution provides purple crystalline solid after storing the solution at 0°C.[3] Yield: 0.054 g (85%) ^{1}H RMN (300 MHz, Chloroform-d): 9.40 (d, J = 5.02 Hz, 2H), 8.62 (d, J = 8.22, 2H), 8.08 (d, J=5.0, 2H). IR (THF, cm^{-1}): 2016, 1911, 1891, 1846.

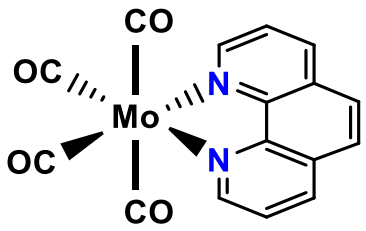

Tetracarbonyl(2,2´-phenanthroline)molybdenum(0).**2**.

Molybdenum hexacarbonyl (1 g, 3.79 mmol) and 2,2´-phenanthroline (0.68g, 3.79 mmol) were refluxed in 25 mL of toluene overnight at 90°C. The red solution is filtered, obtaining a red solid that is washed with cold toluene and diethyl ether. Recrystallization in 1:1 toluene / dichloromethane provides red crystalline solid.[4] Yield: 0.94 g (96%). ^{1}H RMN (300 MHz, d8-THF): 9.48 (dd, J=5.07,1.32 Hz, 2H), 8.63 (dd, J=8.12,1.35 Hz, 2H), 8.15 (s, 2H), 7.88 (dd, J=8.14,5.02 Hz, 2H). IR (THF, cm^{-1}): 2012, 1896, 1880, 1841.

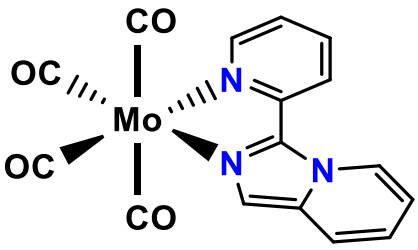

Tetracarbonyl(2,2´-pyridylindolizine)molybdenum(0).**3.**

$[Mo(CO)_6]$ (0.264 g, 1 mmol) and 3-(pyridin-2-yl)imidazo[1,5-*a*]pyridine (0.195 g, 1 mmol) was stirred in toluene (20 mL) at reflux for 6 h. A yellow to orange solution is obtained, evaporating the toluene and filtrating the precipitate after dissolving in dichloromethane. Recrystallization in a solution 1:1 hexane / dichloromethane gives a yellow crystalline solid.[5] Yield = 0.356 (88%). ^{1}H RMN (300 MHz, d8-THF): 9.14 (d, J=4.75 Hz, 1H), 8.93 (d, J=7.34 Hz, 1H), 8.19 (d, J=8.26 Hz, 1H), 8.07 (td, J=6.68,1.62 Hz, 1H), 7.96 (s, 1H), 7.81 (d, J=9.16 Hz, 1H), 7.36 (m, 1H), 7.15 (td, J=8.98,6.71 Hz, 1H), 7.07 (t, J=6.90 Hz, 1H). IR (THF, cm^{-1}): 2014, 1899, 1870, 1828.

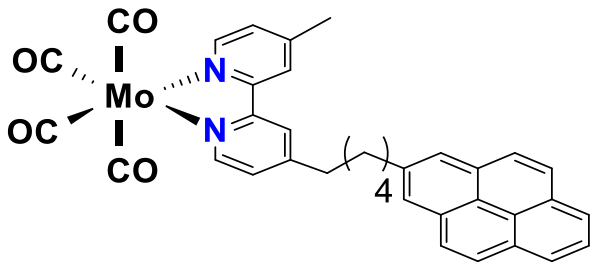

Tetracarbonyl(4-Methyl-4'-(5-(pyren-1-yl)pentyl)-2,2'-bipyridine)molybdenum(0).**4**.

$[Mo(CO)_4$(bicyclo[2,2,1]hepta-2,5-diene)] (0.05 g, 0.17 mmol) and 4-Methyl-4'-(5-(pyren-1-yl)pentyl)-2,2'-bipyridine (0.08 g , 0.17 mmol) were dissolved in THF (10 ml), obtaining an orange to red solution. After stirring overnight, the solution was filtered by cannula and the solution was evaporated at reduced pressure, obtaining a red solid residue and that was washed with light petroleum ether. Recrystallization in a 1:1 light petroleum ether / dichloromethane solution provides orange crystalline solid after storing the solution at 0°C and washing with hexane.[3] Yield: 0.05 g (35%) ^{1}H RMN (300 MHz, Chloroform-d): 8.95 (m, 2H), 8.29-8.19 (m, 1H), 8.12-8.03 (d, 4H), 7.86 (m, 3H), 7.19 (m, 3H), 7.13 (m, 2H), 3.40 (m, 2H), 2.76 (m, 2H), 1.96 (m, 2H), 1.80 (m, 2H), 1.28 (s, 2H). IR (THF, cm^{-1}): 2013, 1901, 1873, 1826.

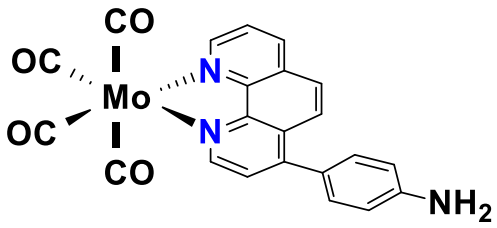

Tetracarbonyl(4-aminophenyl-2,2'-phenanthroline)molybdenum(0).**5**.

$[Mo(CO)_4$(bicyclo[2,2,1]hepta-2,5-diene)] (0.05 g, 0.17 mmol) and 4-(1,10-phenanthrolin-4-yl) aniline (0.05 g , 0.17 mmol) were dissolved in THF (10 ml), obtaining a dark brown solution. After stirring overnight, the solution was filtered by cannula and the solution was evaporated at reduced pressure, obtaining a brown solid residue that was washed with light petroleum ether. Recrystallization in a 1:1 light petroleum ether / dichloromethane solution provides a brown solid after storing the solution at 0°C and washing with hexane. Yield: 0.06 g (70%) ^{1}H RMN (300 MHz, Chloroform-d): 9.83 (m, 2H), 9.14 (d, J=8.26 Hz, 2H), 9.08 (s, 2H), 8.24 (d, J=7.57 Hz, 1H), 7.94 (dd, J=4.35,7.97, 2H), 7.66 (d, J=4.35, 2H), 3.95 (s, 2H). IR (THF, cm^{-1}): 2012, 1897, 1880, 1828.

Electrochemical methods

Electrochemistry is a relevant technique that can be used to study the reactivity caused by the combination of chemical and electrical effects. Electrochemical techniques allow removing (oxidation) or adding (reduction) electrons in a controlled manner, causing chemical changes in the substrate such as the cleavage of chemical bonds or the formation of new ones.

Electrochemical measurements are commonly performed in a three-electrode electrochemical cell, involving the use of working electrode (WE), counter electrode (CE) and reference electrode (RE) (Figure A.1). Redox reaction of interest takes place at the working electrode surface, measuring the current (*i*) and desired potential (*E*) in accordance to the reference electrode that is used as a reference to measure the voltage supplied in the working electrode. Counter electrode

closes the electrical circuit, providing the counter reaction necessary to equilibrate the redox reaction that is taking action in the WE.

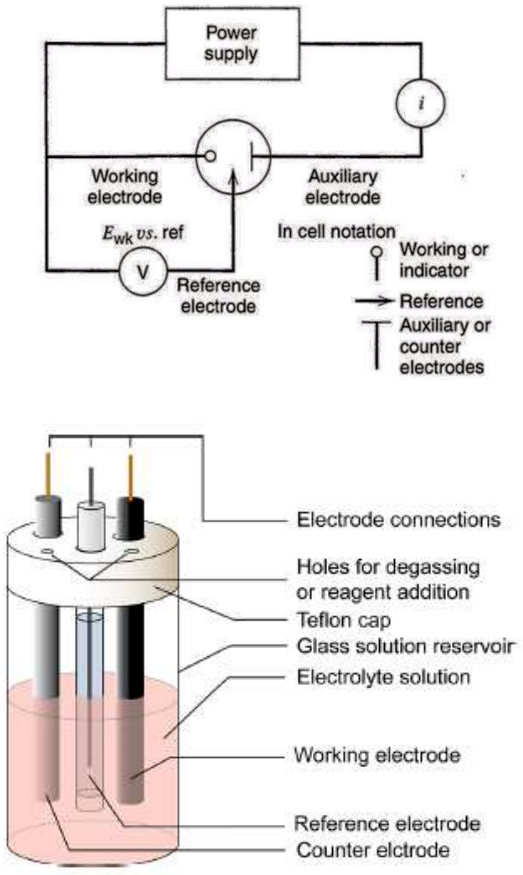

Figure A.1. Schematic representation of a three-electrode cell. Reproduced from Ref. [6, 7].

Cyclic voltammetry (CV) has been mainly used in this work, a technique included in the linear sweep voltammetry set where a variation of the potential in a defined rate is performed, according to two different scanning directions. The *i-E* curve obtained gives detailed information about the number of electrons involved in the redox reaction, kinetic information about the rate of the electron transfers as well as thermodynamic details such as the redox potential of the electroactive species in solution.

Electrochemical studies

Electrochemical experiments have been performed using a home-made 3-electrode cell in inert conditions (O_2 < 1 ppm, H_2O < 1 ppm) by using a glovebox (Jacomex). 3 mm boron diamond-doped (BDD) working electrode have been mainly used, polishing before each measurement with 1 mm alumina powder, sonicated in water and washed with acetone. While Pt wires are used as reference electrode (in a Fc^+/Fc solution) and as counter electrode during electrochemical characterization and spectroelectrochemical experiments, catalytic electrochemical experiments are carried out using a $Ag/AgNO_3$ reference electrode. Ferrocene was added at the end of each experiment as an internal reference. When necessary, carbon dioxide (Alphagaz 1, Air Liquide) was introduced directly in the cell inside the glovebox by using a home-made set-up which includes a vacuum purge line. Distilled (THF/MeCN) or commercial (DFB) solvents were stored in a dry glovebox under Ar. The potential of the WE was controlled by an AUTOLAB PGSTAT 100 (Metrohm) potentiostat controlled by the NOVA 1.11 software.

Spectroelectrochemical studies

All spectroelectrochemical experiments have been carried out in a modified home-made 3-electrode cell (Figure A.2). Thin layer near-IR and UV-vis spectroscopic measurements have been performed with Ocean Optics apparatus, using a deuterium-halogen light source (DH-2000-Bal, 230-2500 nm), Near-IR (NQ256-2.5 model, 900-2500 nm, minimum integration time: 1 ms) and UV-vis (MAYA or QUEPRO models, 200-1100 nm, minimum integration time: 8 ms) detectors. Transmission of the optical signed during spectroelectrochemical measurements by optic fibers (UV/SR-VIS and VIS/Nir), UV-vis and NIR probes (Ocean Optics T300 model).

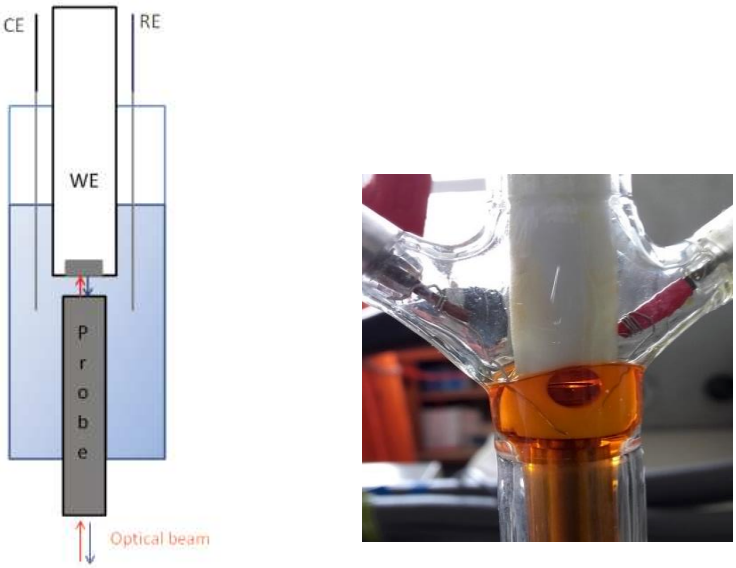

Figure A.2. Spectroelectrochemical three-electrode cell set-up.

Thin layer IR spectroelectrochemistry was carried out with an ATR-Si IR optic-fiber-probe purchased from Art Photonics (ATR-P-Si-6-15-150-Lab). A glassy carbon WE electrode was finely modified to allow inclusion of the Si tip to achieve thin layer conditions. Detection of the IR signal (2 cm^{-1} resolution, one spectrum every 10 sec.) was obtained by using a FT-IR- FC model purchased from Arcoptix (FTMIR-FC-120-LN2).

Computational methods

All DFT calculations were performed with the Orca[8] package (version 3.03) using the PBE functional and a mixed basis set (TZVP for H, C, N and O and LANL2DZ for Mo). The calculations were accelerated with the resolution of identity (RI) approximation in conjunction with an appropriate auxiliary basis set. Vibrational frequency calculations were performed to ensure that each geometry optimization converged to a real minimum. The geometry optimizations and frequency calculations were carried out using the conductor-like screening model (COSMO) to account for the solvation effects of THF. The Avogadro software (version 1.2.0) was used to prepare the Cartesian coordinate inputs and to analyze the results.[9]

CV simulations

Voltametric simulations were performed by using the Kissa 1D software (Amatore, C.; Klymenko, O.; Svir, I.; A new strategy for simulation of electrochemical mechanisms involving acute reaction fronts in solution: Principle, *Electrochem.Commun.* **2010**, *12*, 1170-1173).

Bibliography

[1] R. B. P. Elmes, M. Erby, S. A. Bright, D. C. Williams, T. Gunnlaugsson, *Chem. Commun.* **2012**, *48*, 2588-2590.

[2] M. H. B. Stiddard, *J. Chem. Soc.* **1962**, *0*, 4712-4715.

[3] J. A. Connor, C. Overton, *J. Organomet. Chem.* **1983**, *249*, 165-174.

[4] G. A. Ardizzoia, M. Bea, S. Brenna, B. Therrien, *Eur. J. Inorg. Chem.* **2016**, *2016*, 3829-3837.

[5] C. M. Álvarez, L. Álvarez-Miguel, R. García-Rodríguez, J. M. Martín-Álvarez, D. Miguel, *Eur. J. Inorg. Chem.* **2015**, *2015*, 4921-4934.

[6] N. Elgrishi, K. J. Rountree, B. D. McCarthy, E. S. Rountree, T. T. Eisenhart, J. L. Dempsey, *J. Chem. Educ.* **2017**, *95*, 197-206.

[7] A. J. Bard, L. R. Faulkner, *Electrochemical Methods: Fundamentals and Applications, 2nd Edition*, John Wiley & Sons, Incorporated, **2000**.

[8] F. Neese, *WIRES Comp.Mol.Sci.* **2018**, *8*, 1327.

[9] M. D. Hanwell, D. E. Curtis, D. C. Lonie, T. Vandermeersch, E. Zurek, G. R. Hutchison, *J.Cheminformatics* **2012**, *4*, 17.

Published article

Electrochemically-driven reduction of carbon dioxide mediated by mono-reduced Mo-diimine tetracarbonyl complexes: electrochemical, spectroelectrochemical and theoretical studies

Carlos Garcia Bellido,[a] Lucia Álvarez-Miguel,[a] Daniel Miguel,[b] Noémie Lalaoui,[a] Nolwenn Cabon,[a] Frédéric Gloaguen*[a] and Nicolas Le Poul*[a]

Dedicated to Jean-Michel Savéant

[a] C. Garcia Bellido, Dr. L. Álvarez-Miguel, Dr. N. Lalaoui, Dr. F. Gloaguen, Dr. N. Le Poul
Laboratoire de Chimie, Électrochimie Moléculaires et Chimie Analytique (UMR CNRS 6521)
Université de Bretagne Occidentale
6 Avenue Le Gorgeu 29238 Brest (France)
E-mail: frederic.gloaguen@univ-brest.fr; nicolas.lepoul@univ-brest.fr
[b] Prof. D. Miguel
GIR MIOMET-IU CINQUIMA, Química Inorgánica, Facultad de Ciencias,
Universidad de Valladolid,
7 Paseo de Belén 47011 Valladolid (Spain)
[c] Dr. N. Cabon
CNRS UMR 6226, Institut des Sciences Chimiques de Rennes,
Université de Rennes
1 Rue Edouard Branly 22300 Lannion (France)

Supporting information for this article is given via a link at the end of the document.

Abstract: The activation of carbon dioxide by three different Mo-diimine complexes $[Mo(CO)_4(L)]$ (L = bipyridine (bpy), 1,10-phenantroline (phen) or pyridylindolizine (py-indz)) has been investigated by electrochemistry and spectroelectrochemistry. Under inert atmosphere, monoreduction of the complexes is ligand-centred and leads to tetracarbonyl $[Mo(CO)_4(L)]^{\bullet-}$ species, whereas double reduction induces CO release. Under CO_2, $[Mo(CO)_4(L)]$ complexes undergo unexpected coupled chemical-electrochemical reactions at the first reduction step, leading to the formation of reduced CO_2 derivatives. The experimental results obtained from IR, NIR and UV-Vis spectroelectrochemistry, as well as DFT calculations, demonstrate an electron-transfer reaction whose rate is ligand-dependent.

Introduction

Extensive efforts towards the transformation of carbon dioxide into valuable fuels have been carried out during the last decades, achieving promising results by the development of photocatalytic,[1] electrocatalytic[2] and photoelectrochemical[3] devices. Molecular catalysts involving transition metals have been extensively investigated because metal-based systems are easily tunable and offer the possibility to directly rationalize the structure-reactivity relationships by simple variation of the ligand topology and/or the nature of the metal.[4] First molecular metal-based catalysts were predominantly developed with Ni[5] or Co[6] metal centers, and more heavy metals such as Re[7] or Ir[8]. This family of complexes was more recently supplanted by molecular catalysts based on more abundant and cheaper metals such as Mn[9] or Fe[10]. The two latter systems have been widely studied and still exhibit the best performances amongst reported molecular catalysts, although their use as heterogeneous catalysts in aqueous media remains scarce.[11] In contrast, group 6 (Cr, Mo, W) metal-based systems have received less attention as homogeneous catalysts[4c, 12] despite the presence of Mo and W centers in biological CO_2/CO processes.[13] Among them, metal-carbonyl derivatives bearing redox non-innocent 2,2'-bipyridine (bpy) ligands $[M(CO)_4(bpy)]$ (M = Mo, W, Cr) have shown remarkable properties for the electrocatalytic CO_2 to CO transformation in terms of faradaic efficiency and turn-over frequency.[12k, 12m] However, the negative redox potential necessary to achieve electrocatalysis in organic solvents is still an obstacle to their prospective development as CO_2 catalysts. For instance, the proposed catalytic active species, $[Mo(CO)_3(bpy)]^{2-}$, is generated at E = -2.7 V *vs.* Fc^+/Fc in acetonitrile at a Pt or glassy carbon electrode, a potential value which is significantly more negative than those reported for analogous Mn or Fe complexes. Interestingly, recent works have demonstrated that a significant positive shift (up to 600 mV) of the catalytic potential could be achieved by using a gold electrode instead of Pt or carbon materials.[12j, 12m] Such enhancement was suggested to be due to interfacial processes favoring the formation of the tricarbonyl-reduced species $[Mo(CO)_3(bpy)]^{\bullet-}$ and its electrochemical reduction at higher potential than usually found with Pt and C. Although modification of ligand topology by either introduction of adequate substituents on the backbone, or substitution by an analogous ligand is common in molecular electrocatalysis, this approach has been scarcely applied to molybdenum tetracarbonyl 2,2' bipyridine species for CO_2 reduction. So far, only $[M(CO)_4(x,x'\text{-}R_2\text{-}bpy)]$ (x = x'=4, 5 or 6, R = Me, *t*Bu, M = Mo, W) complexes were investigated, and their electrocatalytic properties were quite similar to the parent $[M(CO)_4(bpy)]$ complex.[12k, 12l] Alternatively, an unsymmetrical mono-imine molybdenum complex was shown

to be reactive towards CO_2 when doubly-reduced. The resulting adduct featured C-C binding between CO_2 and the imine.[12f] More recently, Mo and W dipyridylamine (dpa) tetracarbonyl complexes showed an unexpected catalytic behavior at the mono-reduced state.[12c] DFT calculations suggested a strong ligand reorganization prior to reaction with CO_2.[12g]

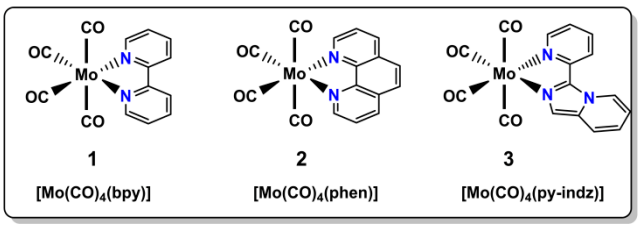

Scheme 1. Mo-diimine complexes 1, 2 and 3 studied for the electrochemically-driven, CO_2 reduction and schematic atom numbering.

In this context, we have focused our research on two analogues of the well-studied $[Mo(CO)_4(bpy)]$ catalyst (**1**), by considering the substitution of the bipyridyl ligand by 1,10 phenantroline (phen) or pyridylindolizine (py-indz) scaffolds, leading to $[Mo(CO)_4(phen)]$ (**2**) and $[Mo(CO)_4(py\text{-}indz)]$ (**3**) complexes, respectively (see Scheme 1). The choice of these two ligands was motivated by the possibility to rationalize the effect of rigid (phen) and unsymmetrical (py-indz) ligands on the electrochemical properties for CO_2 reduction, by comparison to the bpy parent complex **1**. Meanwhile the synthesis and characterization of both complexes **2** and **3** were previously reported,[14] their reactivity towards CO_2 has never been explored. This paper thus reports the electrochemical, UV-Vis, near-IR and IR spectroelectrochemical studies of the reduction of three molybdenum complexes in organic media under inert and CO_2 atmosphere, together with DFT studies and chemical reduction experiments.

Results and Discussion

Synthesis and solid-state characterization

The complexes **1**, **2** and **3** were prepared following previously described procedures and characterized by ^{1}H NMR and IR spectroscopy (see Supplementary Information).[14a, 14b, 14e, 15] The solids were analyzed by solid state IR spectroscopy using an ATR detector. IR spectra for complexes **1**, **2** and **3** displayed the characteristic four-signal pattern of tetracarbonyl diimine systems in the 1800-2050 cm^{-1} region, corresponding to ν(CO) frequency modes (Table S1).[16] Stretching energies did not significantly vary within the series, in agreement with X-ray data. The already-published XRD structures[14a, 14d, 14f] offer the possibility to analyze bond lengths and angles at solid state for **1**, **2** and **3** (Tables S2 and S3). The three molybdenum complexes exhibit a pseudo-octahedral geometry centered on the metal atom, with two axial and two equatorial carbonyl ligands. X-ray data suggest a shorter Mo-C(O) axial bond for complex **3** in comparison to complex **1** (Scheme 1). Moreover, whereas both Mo-N bond lengths are similar in the cases of **1** and **2**, they are very different for **3.** The shortest Mo-N bond is found for the nitrogen atom of the indolizine moiety, consistent with a better donation compared to pyridine.

Spectroscopic characterization

^{1}H NMR, FTIR and UV-Visible spectroscopies were carried out for the characterization of the synthesized complexes in solution. NMR spectroscopy allows accurate assignment of the hydrogen atoms of the bpy, phen, and py-indz groups in the aromatic region (7-8 ppm, see Supplementary Information). As found at solid state, IR spectroscopy in tetrahydrofuran (THF) displayed four main bands in the 1800-2050 cm^{-1} range corresponding to carbonyl stretching vibration modes (Figure 2, black curves). The values for the energy are somewhat similar to those found with solids, despite being up-shifted by 30 cm^{-1} for some frequency modes (Tables 1 and S1). This result suggests that while the pseudo-octahedral symmetry is preserved in THF, it is nevertheless varied due probable electrostatic interactions of the solvent with carbonyl groups.[14c] In particular, the lowest values of wavenumber were found for complex **3** as in solid state. Moreover, stretching energies for complexes **1** and **2** are similar to reported data in organic solvents.[16] UV-vis spectroscopy experiments exhibit several absorption bands in the 250-300 nm region assigned to π-π* transitions within the diimine framework (Table 1). Electronic transitions at lower energies (330 < λ < 490 nm) result from d(Mo)→π*(diimine) and d(Mo)→ (COax) metal-to-ligand (MLCT) charge transfer transitions.[14c, 16a, 17] Noteworthy, the absorption band at ca. 470 nm for complexes **1** and **2** is blue-shifted by 25 nm for complex **3**.

Table 1. UV-Vis (λ_{max} / nm) and IR (ν_{CO} / cm^{-1}) spectroscopic data for complexes **1**, **2** and **3**.[a]

Complex	λ_{max} / nm	ν_{CO} / cm^{-1}
$[Mo(CO)_4(bpy)]$ (**1**)	267, 297, 472	1840, 1880, 1900, 2012
$[Mo(CO)_4(phen)]$ (**2**)	263, 390, 469	1840, 1880, 1899, 2012
$[Mo(CO)_4(py\text{-}indz)]$ (**3**)	255, 340, 428	1836, 1877, 1895, 2010
$[Mo(CO)_4(bpy)]^{\bullet-}$	261, 297, 368, 497, 531, 854	1803, 1842, 1870, 1991
$[Mo(CO)_4(phen)]^{\bullet-}$	263,284, 357, 564, 615, 832	1800, 1842, 1870, 1990
$[Mo(CO)_4(py\text{-}indz)]^{\bullet-}$	260, 345, 418, 595	1800, 1839, 1867, 1989
$[Mo(CO)_3(bpy)]^{2-}$	260, 369, 591, 638	1706, 1725, 1846
$[Mo(CO)_3(phen)]^{2-}$	264, 435, 634	1702, 1718, 1857
$[Mo(CO)_3(pyindz)]^{2-}$	261, 410, 662	1706, 1727, 1844

[a] Data obtained from spectroelectrochemical measurements in THF/NBu_4PF_6 0.1 M.

Electrochemical and spectroelectrochemical characterization under argon

Cyclic voltammetry experiments were performed in dry THF/NBu_4PF_6 0.1M at room temperature with a boron-doped diamond (BDD) working electrode. Similar results were obtained at a glassy carbon electrode (GC, see Figure S15). Electrochemical data are gathered in Table 2. First experiments were carried out under argon in order to decipher the chemically-coupled reactions which can occur upon

reduction. All complexes display two cathodic processes which can be ascribed to two successive monoelectronic reductions, according to previous studies on complex **1**.[12k, 18] The first process occurring at $E_{1/2}(1)$ (ca. -2.0 V *vs.* Fc^+/Fc, see Table 2) is reversible for all complexes (0.02 V s^{-1} < *v* < 1 V s^{-1}). Randles-Ševčik analysis ($i_{pc}(1)$ *vs.* $v^{1/2}$, Figure S18) indicated that the first reduction is a diffusion-limited process. The formal potential varied with the nature of the diimine ligand, the most negative value being detected for complex **3**, as probably resulting from a stronger donating effect of the py-indz ligand (*vs.* phen and bpy). Further scanning towards more negative values led to the appearance of an irreversible cathodic peak at ca. $E_{pc}(2)$ whose value varies with the ligand (Table 2). Increasing of the scan rate or decreasing of the temperature did not induce any better reversibility. Here, the doubly-reduced Mo complexes are unstable as tetracarbonyl species and undergo probable CO loss or protonation as previously suggested for complex **1**.[12k, 12m]

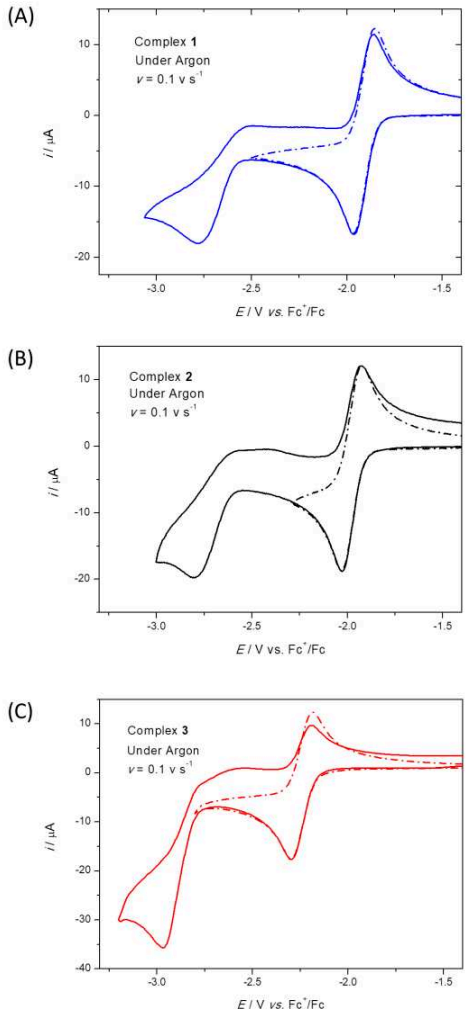

Figure 1. CVs at a BDD electrode (*v* = 0.1 V s^{-1}, *E* / V *vs.* Fc^+/Fc) of complexes **1** (Panel A), **2** (Panel B), and **3** (Panel C) in THF/NBu_4PF_6 0.1 M. *C* (complex) = 1 mM.

Table 2. Experimental electrochemical data (*E* / V *vs.* Fc^+/Fc) for complexes **1**, **2** and **3** (1 mM) in THF/NBu_4PF_6 0.1 M.

Complex	$E_{1/2}$ (1)	E_{pc}(2)
1	-1.85	-2.55
2	-1.90	-2.75
3	-2.20	-2.90

In-situ IR and UV-Vis spectroelectrochemistry (SEC) measurements were then carried out in order to identify the species generated during the reduction. An IR-SEC setup based on an ATR Si-probe in close contact to a glassy carbon conical electrode was designed for these experiments (Figure S8). It allowed *in-situ* probing of the redox species which were electrochemically generated within the thin layer separating the probe and the electrode surface. Potential-step methods such as chronoamperometry were preferred to low scan-rate CV for fast generation of these species. Typically, full transformation was obtained after 100 sec. of applied potential.

The Figure 2 displays the IR-SEC monitoring of both reduction processes for **1**, **2** and **3** under argon (subtracted from the solvent and electrolyte signature). For all complexes, the IR pattern obtained at the first reduction was typical of a tetracarbonyl molybdenum adduct, as previously reported for complex **1** (Figure 2, red curves).[12m] This is in agreement with the reversible redox behavior of the complexes at $E_{1/2}(1)$, thus strongly suggesting the formation of the mononuclear $[Mo(CO)_4(L)]^{\bullet-}$ species (L= bpy, phen, py-indz). The shift of the four IR bands by ca. 30 cm^{-1} towards lower frequencies upon reduction is consistent with a lengthening of the CO bonds due to stronger back-bonding of the metal to the carbonyl moieties. It advocates for an increase of the electron density on the diimine ligand as well as on equatorial and axial CO moieties (see DFT studies, *vide supra*).[14c, 19]

Investigation of the first reduction process was also carried out by *in-situ* time-resolved UV-Visible spectroelectrochemistry. New absorption bands at ca. 350-400 nm and 530-600 nm were detected (Figure S4), as previously found for mono-reduced metal-bound diimine species.[12l, 12m] Remarkably, low-energy broad bands were detected in the NIR region for $\mathbf{1}^{\bullet-}$, $\mathbf{2}^{\bullet-}$ and $\mathbf{3}^{\bullet-}$ (1200-2000 nm) (Figure S6). These bands may be ascribed to an intra-ligand charge-transfer transition and thus confirm the diimine character of the first cathodic process.[20] Further reduction of the complexes **1-3** until $E_{pc}(2)$ under argon led to a modification of the IR and UV-Vis spectra. On one hand, the four ν_{CO} bands found for the neutral and mono-reduced species evolved towards a 3-bands signature at ca. 1850 and 1700 cm^{-1} (Figure 2, green curves, and Table 1). Such a behavior was previously described for the bpy-Mo complex and is diagnostic of a tricarbonyl molybdenum-diimine species, namely $[Mo(CO)_3(L)]^{2-}$. On the other hand, UV-Vis spectroelectrochemical measurements showed the appearance of broad peaks centered at λ_{max} = 638, 634 and 662 nm for complexes **1**, **2** and **3**, respectively (Figure S4). Moreover, the double-reduction was accompanied with the disappearance of the 1200-2000 nm NIR band found for the complexes (Figure S6). The latter result hence suggests that injection of a second electron induces the loss of electronic delocalization on the diimine backbone.

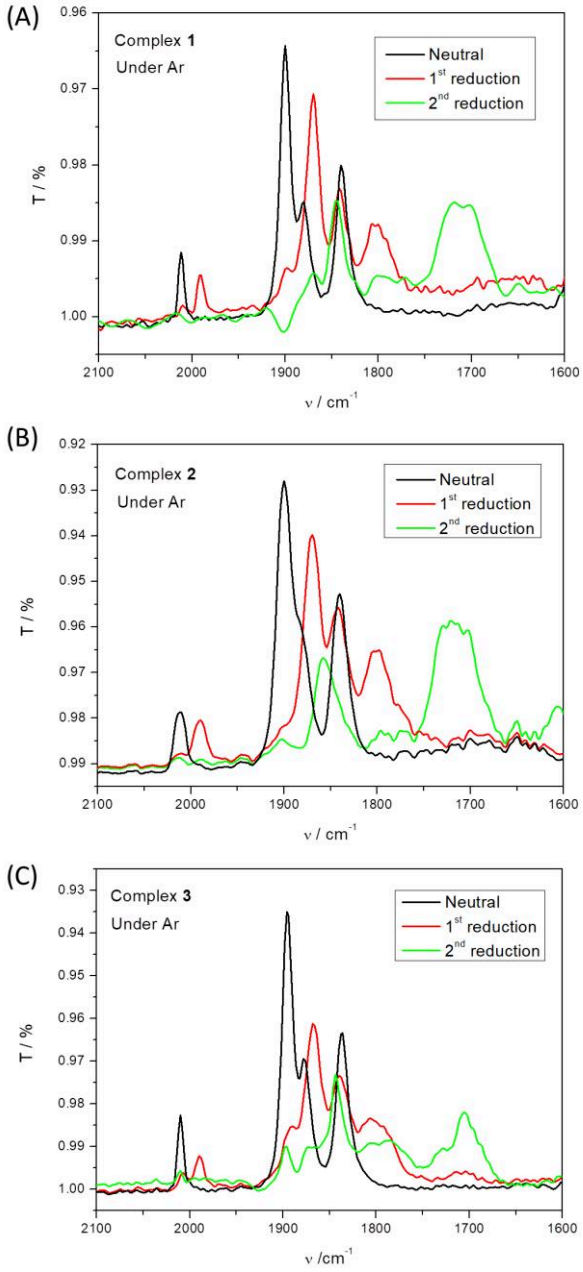

Figure 2. IR-SEC spectra of complexes **1** (Panel A), **2** (Panel B), and **3** (Panel C) in dry THF/NBu_4PF_6 0.1 M under Ar. Black curve: neutral complexes; Red curve: after the 1st reduction; Green curve: after the second reduction.

Thus, experimental data clearly indicate that electrochemical reduction under argon induces the same processes for the three complexes, independently of the nature of the diimine ligand i.e. (i) a monoelectronic reduction leading to the formation of a tetracarbonyl $[Mo(CO)_4(L)]^{\bullet-}$ species whose spin density is essentially localized on the diimine scaffold and (ii) a bi-electronic reduction yielding a tricarbonyl $[Mo(CO)_3(L)]^{2-}$ species with rapid loss of one CO ligand in dry THF.

Electrochemical and spectroelectrochemical characterization under CO_2

Electrochemical properties of the complexes **1**-**3** were then investigated in a CO_2-saturated THF/NBu_4PF_6 0.1 M solution. BDD or glassy carbon working disc electrodes were preferred to metal (Pt, Au) materials in order to avoid direct CO_2 electroreduction given the negative values of $E_{pc}(2)$ for complexes **1**-**3,** or surface-mediated effects.[12j, 12m] Cyclic voltammetry was first carried out in dry THF. At v = 0.1 V s^{-1}, complexes **1** and **2** did not exhibit any significant increase of the peak current $i_{pc}(1)$ or shift of $E_{pc}(1)$ (Figure S13A and B) in contrast to complex **3** (Figure S13C). Moreover, on this first reduction system, complexes **2** and **3** displayed a loss of reversibility (total loss for **3**) whereas CV of complex **1** was the same as under Ar.

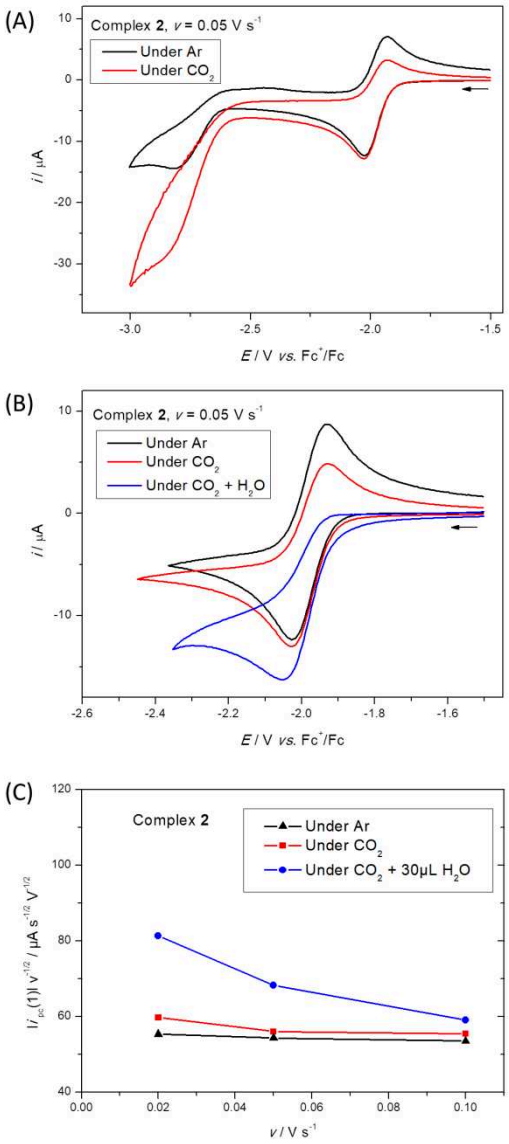

Figure 3. CVs (E / V *vs.* Fc^+/Fc) at a BDD working electrode of complex **2** (1 mM), in dry THF/NBu_4PF_6 0.1 M; Panel A: For v = 0.05 V s^{-1} under argon (black) and CO_2 (red); Panel B: For v = 0. 05 V s^{-1} under argon (black), under CO_2 (red), and under CO_2 + 0.1% H_2O (v) (blue); Panel C: Plots of $I i_{pc}(1) I\ v^{1/2}$ against v under Ar (black), under CO_2 (red), and under CO_2 + 0.1% H_2O (blue).

At more negative potential values, two different redox behaviors were found depending on the nature of the diimine ligand. For complexes **1** and **2**, a significant increase of the peak current at $E_{pc}(2)$ was observed (Figure S13A and B), which likely

corresponds to the reaction of CO_2 with $[Mo(CO)_3(L)]^{2-}$.[12k, 12m] In contrast, for the complex **3**, two broad and undefined peaks of low intensity were detected at potential values ranging between $E_{pc}(1)$ and $E_{pc}(2)$ (Figure S13C), whereas the peak at $E_{pc}(2)$ was no longer identified.

Lowering the scan rate was shown to have a significant effect on the first reduction process. Indeed, a substantial increase of the peak current at $E_{pc}(1)$ and a loss of reversibility were observed, as shown in Figure 3B for complex **2** at $v = 0.05$ V s^{-1} (red curve). Under strictly identical conditions, this current increase was higher for complexes **2** and **3** than for complex **1**, as shown by plots of the current function $i_{pc}(1)\ v^{1/2}$ against v under Ar and CO_2 (red curve in Figure 3C for complex **2**, and Figure S14 for complexes **1** and **3**). Addition of aliquots of water under CO_2 was accompanied by an increase of the peak current (Figures 3B-C, S14 and S17). A maximum peak current value was obtained after addition of ca. 0.1 % H_2O (vol.). Control experiments revealed no effect of water on the peak potential or current at this redox potential under argon (Figure S16).

In order to better quantify the observed electrochemical changes at the mono-reduced state for complexes **1** and **2**, simulation of the experimental CVs was carried out by using a voltammetric simulator package (see Supplementary Information). Only a EC_{cat} mechanism (E = electrochemical, C = chemical) was considered since IR spectroscopic studies with chemically-reduced complexes showed the back generation of the neutral complexes **1**-**3** by reaction with CO_2 (*vide supra*), hence discriminating an ECE process (which would have not led back to the neutral species) or an EC process (which would have induced a minor (10%) increase of the peak current).[21] The experimental curves obtained under Ar and CO_2 at $v = 0.05$ V s^{-1}(with and without added water) for the two complexes were satisfactorily reproduced by varying kinetics of the chemical reaction (Figure S19). Interestingly, the cathodic peak current value behavior appeared as mainly controlled by both the forward and the backward rate constants (see Supplementary Information). Although these data have to be taken with caution, they support the hypothesis that the ligand topology impacts the electron transfer kinetics for CO_2 conversion at the first reduction step. This redox behavior is reminiscent to that observed for Mo and W tetracarbonyl dipyridylamine (dpa) complexes which underwent substantial current increase at the first reduction step after strong ligand reorganization.[12c, 12g] However, in our case, IR- and UV-Vis-SEC of complexes **1**-**3** under Ar were not indicative of any specific conformational change upon monoelectronic reduction.

Bulk electrolysis experiments under CO_2 followed by analysis of the gaseous products by chromatography was not conducted (see experimental section). However, aiming at better rationalizing this discrepancy and qualitatively analyze the products of the reaction, IR and UV-Vis-NIR spectroelectrochemical studies were performed under CO_2 for the three complexes. As shown in Figure 4A, the electrochemical reduction under CO_2 of complex **1** led to the appearance of ν_{CO} bands typically ascribed to the mono-reduced tetracarbonyl species $[M(CO)_4(bpy)]^{\bullet-}$ (**1**$^{\bullet-}$). The same conclusion could be drawn for complex **2,** except that only low intensity bands featuring **2**$^{\bullet-}$ were found (Figure 4B). The complex **3** did not exhibit any IR response corresponding to **3**$^{\bullet-}$ but rather a new spectrum typical of a tetracarbonyl Mo species (Figure 4C). In addition, all complexes showed supplementary bands (not observed under argon, see red curves in Figure 4) in the 1550-1700 cm^{-1} region, which were ascribed to carbonate and formate ions as previously reported,[12l, 22] and in agreement with our control experiments (Figure S11). Further IR measurements also demonstrated that these bands were not detected at the resting potential of the neutral species (see for instance Figure S12 for complex **2**), thus showing the need for electron source. Furthermore, IR-SEC experiments performed in the dark yielded similar results to those carried out in daylight, thus excluding a photoactivated process. Noteworthy, complexes **2** and **3** displayed two new bands at 1920 and 1750 cm^{-1}, which were previously reported for the electrocatalytic reduction of CO_2 by Mo-diimine complexes.[12e, 12m] The amplitude of these supplementary bands was shown to increase with water content.

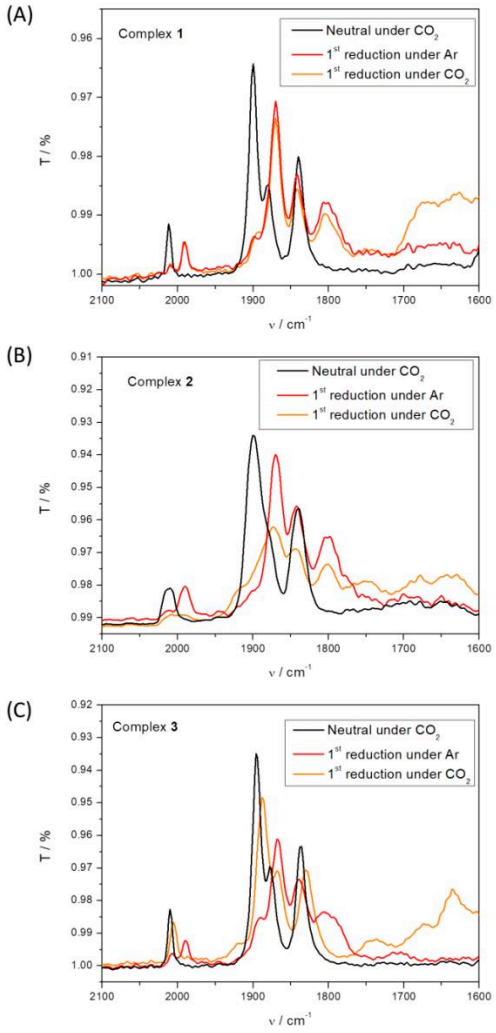

Figure 4. IR-SEC spectra of complexes **1** (Panel A), **2** (Panel B), and **3** (Panel C) in dry THF/NBu_4PF_6 0.1 M before (black) and after (orange) reduction at $E_{1/2}(1)$ under CO_2. For comparison, IR spectra after reduction at $E_{1/2}(1)$ under Ar (red) are given.

UV-Vis spectroelectrochemistry was also carried out for CO_2 reactivity for the first reduction process, revealing the presence of the mono-reduced species **1**$^{\bullet-}$ and **2**$^{\bullet-}$ (partially) whereas the complex **3**$^{\bullet-}$ was not identified, in agreement with IR data (Figure

S5). NIR-spectroelectrochemistry was also consistent with IR and UV-Vis spectroscopic results since low-energy intra-ligand charge transfer absorption bands detected under argon were no longer observed for complexes **2** and **3** under CO_2, whereas it remained the same for complex **1** (Figure S7). Thus, this clearly evidences that mono-reduced species $\mathbf{2}^{\bullet-}$ and $\mathbf{3}^{\bullet-}$ reacted instantly with CO_2.

Chemical generation and reactivity *vs.* CO_2 of mono- and bis-reduced species.

In complement to spectroelectrochemical studies, mono-reduced complexes were prepared by reacting complexes **1**-**3** with one equivalent of chemical reductant KC_8 in THF under argon. The resulting complexes displayed similar IR signatures to those found by spectroelectrochemistry (Figure S10, red curves), thus confirming the formation of tetracarbonyl species $\mathbf{1}^{\bullet-}$, $\mathbf{2}^{\bullet-}$ and $\mathbf{3}^{\bullet-}$. Reaction of the mono-reduced species with carbon dioxide was monitored by IR spectroscopy (Figure S10). For all complexes, the resulting spectra indicated the back and partial generation of the neutral complexes **1**-**3**, together with new species displaying stretching bands in the 1600-1750 cm^{-1} region, which can be ascribed to C-O vibrations of bicarbonate and formate anions as seen by IR-SEC.[12l, 22] Noteworthy, formation of these new species was revealed to be significantly accelerated in presence of 0.1% water in dry THF. These results evidenced the participation of protons/water to CO_2 reduction by the mono-reduced Mo complexes in good agreement with electrochemical and spectroelectrochemical data.

DFT calculations

A series of DFT calculations were performed in order to get insights into the reaction of the mono-reduced species with CO_2. Preliminary calculations allowed the determination the standard potential of the $[CO_2]^{0/\bullet-}$ couple. The resulting value (–2.85 V *vs.* $Fc^{+/0}$) was at least 0.8 V more negative than those of $[Mo(CO)_4L]^{0/\bullet-}$, thus ruling out the possibility of CO_2 activation at the mono-reduced state through an outer sphere electron transfer (no bond making/cleavage). From this result, we investigated a catalytic mechanism in which CO_2 is activated by its association with a reduced form of the complexes possessing a vacant site, i.e. $[Mo(CO)_3(L)]^{\bullet-}$ according to previous studies.[12j, 12m]

A series of geometry optimization was performed for the three different binding modes of CO_2 that have been reported in mononuclear transition metal complexes, i.e. η^1–OCO, η^1–CO_2 and η^2–CO_2.[2d] Formation of a η^1–OCO adduct and subsequent protonation of the C atom is thought to favor the production of formate, one of the products detected by IR-SEC experiments.[2d] However, for all complexes, geometry optimization starting with a CO_2 ligand bound in the η^1–OCO mode did not converged to a stable structure. On the other hand, when starting with a CO_2 ligand bound in the η^1–CO_2 mode, structures in which the CO_2 ligand can adopt a η^2–CO_2 binding mode were obtained (Figure 5A).

Relevant bond distances and angles are listed in Table S5. In the CO_2 adducts, the O–C–O angle is the range 141–143°, close to the value of 135° calculated for an isolated $[CO_2]^{\bullet-}$ radical anion. Besides, the C–O bonds are elongated by 0.04–0.07 Å as compared to those in an isolated CO_2 molecule, indicative of a weakening of the bond strength. These geometric features clearly demonstrate a significant transfer of electronic density from the $[Mo(CO)_3(L)]^{\bullet-}$ moiety to the bound CO_2 (*vide infra*).

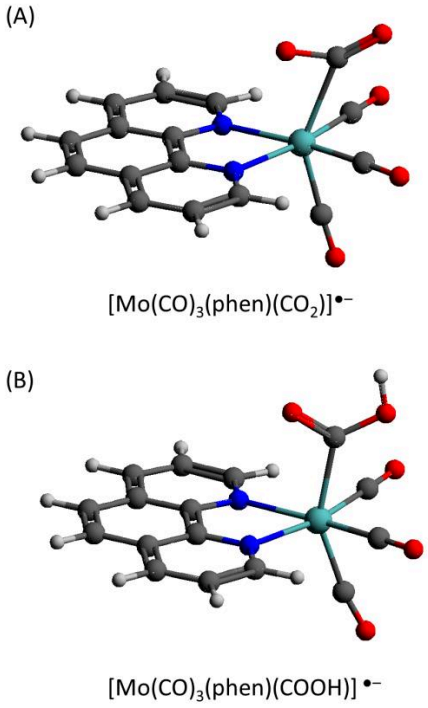

Figure 5. Calculated structures of (A) $[Mo(CO)_3(phen)(CO_2)]^{\bullet-}$ and (B) $[Mo(CO)_3(phen)(COOH)]^{\bullet-}$. Atom colors: H (white), C (grey), N (blue), O (red) and Mo (green).

Our next set of analyses was hence devoted to the calculations of the redox potentials of the electron transfer steps and of the free energies of the chemical steps involved in the formation and reactivity of CO_2 adducts. The resulting thermodynamic data are gathered in Table 3. Starting from $[Mo(CO)_4(L)]^{\bullet-}$, the CO loss is uphill in energy by $\Delta G(1)$ = +26.7, +26.4 and +24.9 kcal mol^{-1} for L = bpy, phen and py-indz, respectively (Schemes 2-3, and Table 3).Two different situations may be then considered.

The first one includes the binding of CO_2 to $[Mo(CO)_3(L)]^{\bullet-}$, yielding the corresponding $[Mo(CO)_3(L)(CO_2)]^{\bullet-}$ adduct according to Pathway A (Scheme 2). This reaction was recently discussed in the frame of DFT studies for a series metal-bipyridine tetracarbonyl complexes.[12d] This process is slightly downhill in energy ($\Delta G(3)$ = –2.4, –2.4 and -2.6 kcal mol^{-1} for L = bpy, phen and py-indz, respectively (see Table 3). The next step is most likely the protonation of the CO_2 ligand even in the absence of added proton source (residual water in the medium may be sufficient to trigger the reaction). Since production of formate was detected by IR-SEC experiments, we first considered that protonation could occur at the C atom of the CO_2 ligand according to this pathway. However, all attempted calculations aimed at optimizing the geometry of such intermediates failed to converge. On the other hand, protonation at the O atom of the CO_2 ligand was found to be downhill in energy as shown by the values of $\Delta G(4)$ in Table 3. Summing values of $\Delta G(1)$, $\Delta G(3)$ and $\Delta G(4)$ indicated that the reaction $[Mo(CO)_4(L)]^{\bullet-} + CO_2 + H^+ \rightarrow [Mo(CO)_3(L)(COOH)] + CO$ following pathway A is uphill in energy by +6.2 and +5.4 kcal

mol^{-1} for L = bpy and phen, while slightly downhill in energy by –1.2 kcal mol^{-1} for L = py-indz. In addition, the calculated reduction potentials $E^0(5)$ of the $[Mo(CO)_3(L)(COOH)]$ intermediates are significantly less negative than the reduction potential of the $[Mo(CO)_4(L)]$ complexes (by ca. 1.2 V, see Table 3). This result implies that the protonation step of the $[Mo(CO)_3(L)(CO_2)]^{\bullet-}$ adducts is immediately followed by a reduction step leading to $[Mo(CO)_3(L)(COOH)]^{\bullet-}$ (see Figure 5B for the phen derivative). Structure calculations showed that subsequent protonation of these negatively charged intermediates leads to C–O(H)$_2$ bond cleavage releasing H_2O and regenerating $[Mo(CO)_4(L)]$ which is electrochemically reduced into $[Mo(CO)_4(L)]^{\bullet-}$ at $E^0(1)$ (see Figure 6A for the phen derivative). The conversion of CO_2 into CO and H_2O activated by the reduction of $[Mo(CO)_4(L)]$ complexes has thus an overall driving force of –20.1, –21.3 and –32.3 kcal mol^{-1} for L = bpy, phen and py-indz, respectively (Scheme 3). The driving force is noticeably larger for L = py-indz, which can be explained by a more negative reduction potential value for this derivative. We did not calculate the activation barriers of the chemical steps described above. However, the detection of $[Mo(CO)_4(L)]^{\bullet-}$ intermediates under inert atmosphere by IR-SEC experiments indicates that the activation barrier of the CO loss to give $[Mo(CO)_3(L)]^{\bullet-}$ must be significantly larger than that of the first protonation step of bound CO_2.

Table 3. Theoretical data correlated to the mechanistic pathways depicted in Scheme 3. E^0 in V *vs.* Fc^+/Fc; ΔG in kcal.mol^{-1}.

Complex	**1**	**2**	**3**
$E^0(1)$	-1.85	-1.88	-2.16
$E^0(3)$	-0.90	-0.91	-0.99
$E^0(4)$	-1.57	-1.58	-1.81
$E^0(5)$	-0.71	-0.72	-0.80
$\Delta G(1)$	+26.7	+26.4	+24.9
$\Delta G(2)$	-17.8	-18.2	-22.8
$\Delta G(3)$	-2.4	-2.4	-2.6
$\Delta G(4)$	-18.1	-18.1	-23.5

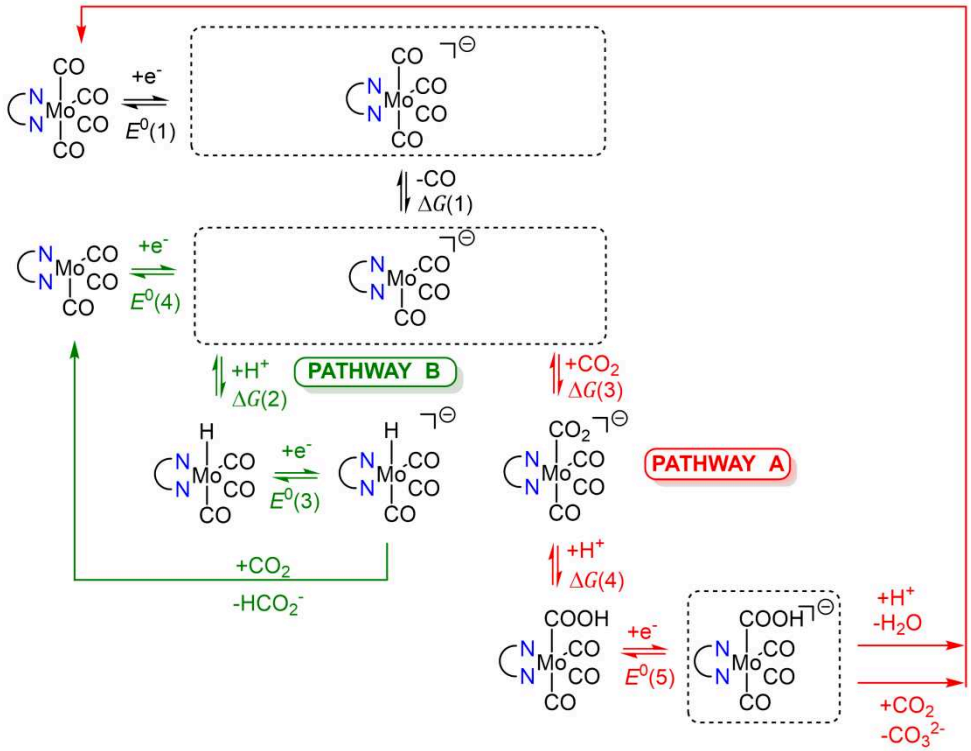

Scheme 2. Suggested mechanistic pathways for the CO_2 reduction mediated by Mo-diimine complexes **1**, **2** and **3**.

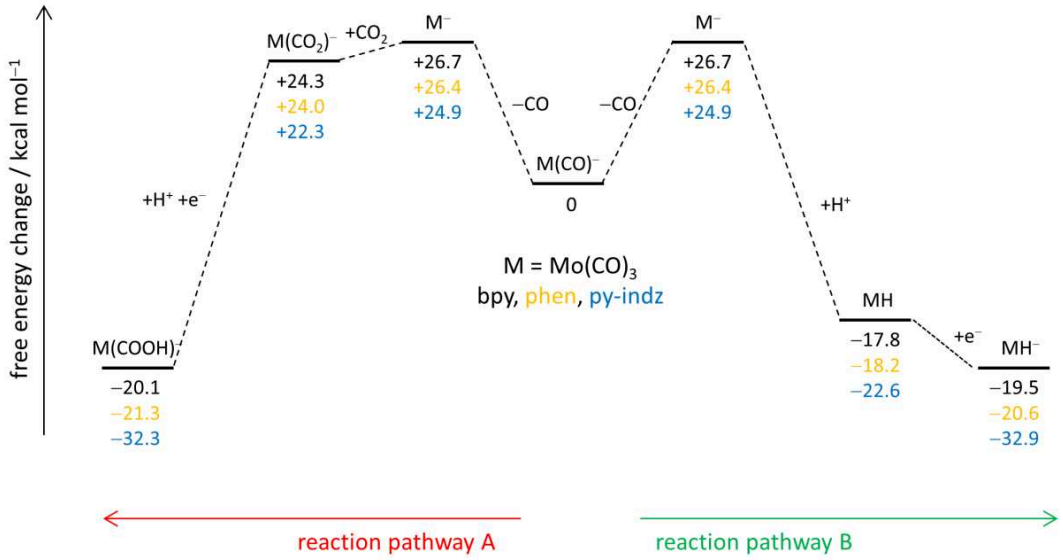

Scheme 3. Energy profile for the CO_2 reduction mediated by Mo-diimine complexes **1**, **2** and **3** for the reactions pathways A and B.

The second situation that we have considered is the direct protonation of the $[Mo(CO)_3(L)]^{\bullet-}$ intermediate according to Pathway B in Scheme 2. Such a possibility was envisaged because Pathway A cannot support the generation of formate, in contrast to what is observed experimentally. Formation of hydride-Mo carbonyl complexes was previously reported, but resulting from the reaction of the bis-reduced $Mo(CO)_6$ species with protons.[12h] According to Pathway B, the formation of the corresponding hydride derivatives $[Mo(CO)_3(L)(H)]$ is downhill by $\Delta G(2)$ = –17.8, –18.2 and –22.8 kcal mol^{-1} for L = bpy, phen and py-indz, respectively. In addition, the reduction potential $E^0(3)$ of these hydrides is significantly less negative (by ca. 1.0 V, see Table 3) than $E^0(1)$. This result implies that the protonation of $[Mo(CO)_3(L)]^{\bullet-}$ is immediately followed by a reduction step leading to $[Mo(CO)_3(L)(H)]^{\bullet-}$. Structure calculations showed that the reaction of these reduced hydrides with CO_2 leads to Mo–H bond cleavage leading to formate and $[Mo(CO)_3(L)]$ (Figure 6B), the latter being immediately reduced back to $[Mo(CO)_3(L)]^{\bullet-}$ at $E^0(4)$ (see Table 3). Overall, the production of formate by the reduction of $[Mo(CO)_4(L)]$ in the presence of CO_2 and a proton source has thus a driving force of –19.5, –20.6 and –32.9 kcal mol^{-1} for L = bpy, phen and py-indz, respectively (Scheme 3). These free energy values are comparable to those calculated for the production of CO and H_2O according to Pathway A (*vide infra*) (Scheme 3). The mechanism leading to the production of formate should however be favored in the presence of added water, which is what was observed experimentally. In addition, once initiated, this mechanism bypasses the CO loss reaction $[Mo(CO)_4(L)]^{\bullet-} \rightarrow [Mo(CO)_3(L)]^{\bullet-} + CO$. However, the protonation of the metal center in $[Mo(CO)_3(L)]^{\bullet-}$ yielding a $[Mo(CO)_3(L)(H)]$ hydride has most likely a higher energy barrier than the protonation of the partly reduced bound CO_2 in $[Mo(CO)_3(L)(CO_2)]^{\bullet-}$, which might explain the low catalytic activity experimentally measured.

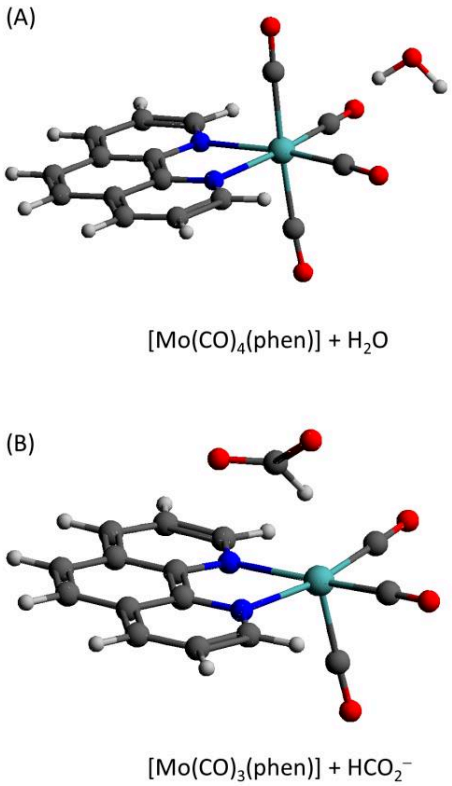

Figure 6. Calculated structures (A) upon protonation of $[Mo(CO)_3(phen)(COOH)]^{\bullet-}$ leading to the release of water and generation of $[Mo(CO)_4(phen)]$ according to Pathway A, and (B) reaction of $[Mo(CO)_3(phen)(H)]^{\bullet-}$ with CO_2 leading to the release of formate and $[Mo(CO)_3(phen)]$ according to pathway A. Atom colors: H (white), C (grey), N (blue), O (red) and Mo (green).

Generation of CO_3^{2-} ions is generally explained by the reaction of a transient reduced metal-CO_2 adduct with a supplementary carbon dioxide molecule,[12g, 23] leading to C-O bond cleavage and release of bicarbonate while a carbonyl ligand remains attached to the metal ion (Scheme 2). According to DFT studies, the binding of a supplementary CO_2 molecule to $[Mo(CO)_3(L)(COOH)]^{\bullet-}$ yields a stable $[Mo(CO)_3(L)(COOH)(CO_2)]^{\bullet-}$ adduct (see Figure S21 for L = phen) through a thermodynamically uphill process (ΔG = +13.8 kcal mol^{-1} for L = phen). Another possible explanation for carbonate production during electroreduction can be the reductive disproportionation of CO_2 into carbonate and CO, which usually occurs in presence of Lewis acids such as Mg^{2+} or other metal ions.[2d, 9b, 24] Alternatively, the acid-base equilibria $CO_2 + H_2O \rightarrow H^+ + HCO_3^-$ and $CO_2 + H_2O \rightarrow 2H^+ + CO_3^{2-}$ may also explain the increase of carbonates content since pathway A favors the formation of water. This assumption is supported by DFT calculations, which show that protonation of $[Mo(CO)_3(L)(CO_2)]^{\bullet-}$ by displacement of the dioxide-carbonate acid-base equilibrium and further reduction of the protonated intermediates at $E^0(1)$ has an overall driving force of −13.5, −14.3 and −23.8 kcal mol^{-1} for for L = bpy, phen and py-indz, respectively (Table S11). Moreover, the protonation and further reduction of $[Mo(CO)_3(L)]^{\bullet-}$ following the same pathway has an overall driving force of −8.6, −9.5 and −18.8 kcal mol^{-1} for for L = bpy, phen and py-indz, respectively (Table S12).

Electronic structures. In order to gain insight on the localization of the electronic density in the catalytic intermediates, we first analyzed selected bond lengths and angles of the calculated structures (Tables S5-S7). For all complexes, calculated structures were optimized starting from X-ray data at neutral state by including a dielectric continuum to model the electrolyte (see experimental section for details).

The calculated structures of the tetracarbonyl complexes $[Mo(CO)_4(L)]$ display bond distance and bond angle values that are in good agreement with those determined from the X-ray data. Noteworthy, the two Mo–N bond lengths are sensibly different in $[Mo(CO)_4$(py-indz)] (2.285 and 2.238 Å, respectively), in contrast to the bpy and phen derivatives in which they are strictly identical (Tables S6 and S7). The shortening of one of the two Mo–N bonds depicts the better electron donating property of the indolizine *vs*. pyridyl moiety and an unsymmetrical charge location. The structures of the reduced tetracarbonyl intermediates $[Mo(CO)_4(L)]^{\bullet-}$ are similar to those of the corresponding neutral complexes (Tables S6 and S7). Electron input induces a slight increase of the C-O and Mo-N bond lengths, as well as a shortening of Mo-C(O) bonds. Moreover, a significant decrease of the (N)C–C(N) bond length by 0.030–0.045 Å was found, hence indicating that the π* orbital of the non-innocent ligands L is now occupied. These results are in line with spectroelectrochemical data which suggest a stronger back-bonding of Mo to the CO ligands, and an increase of the electron density on the diimine ligand. The 30 cm^{-1} IR shift of the four carbonyl stretching bands which was detected by IR-SEC was nicely reproduced for the three complexes (Figure S20 and Table S8), thus confirming the good matching of the mono-reduced model with the experimental data.

The calculated structures of the $[Mo(CO)_3(L)]^{\bullet-}$ intermediates show that the departure of a CO ligand opens a vacant site in axial position. The CO loss induces a substantial shortening of the axial Mo–CO bond together with that of the two Mo–N bonds (Table S6). This is accompanied by an increase of the angle between the axial CO and the Mo-diimine moiety from ca. 93° to 107°. The CO loss yields thus a twist of the diimine ligand towards the axial vacant site, emphasizing a distortion from the ideal square-based pyramidal geometry. Besides, a slight but noticeable lengthening of the (N)C–C(N) bond was found suggesting that some electronic density has been transferred from the π* orbital of the diimine ligand to the $Mo(CO)_3$ moiety (*vide infra*).

Additional calculations were carried out on the $[Mo(CO)_3(L)(CO_2)]^{\bullet-}$ adducts proposed for the Pathway A. Theoretical structures show evidence for a transfer of electronic density to the CO_2 ligand (*vide infra*). However, the (N)C–C(N) bond lengths are quite similar in $[Mo(CO)_3(L)]^{\bullet-}$ and $[Mo(CO)_3(L)(CO_2)]^{\bullet-}$ suggesting that the electronic density is mostly transferred from the $Mo(CO)_3$ moiety (Tables S5 and S6). Interestingly, the $[Mo(CO)_3(L)(CO_2)]^{\bullet-}$ and $[Mo(CO)_3(L)(COOH)]^{\bullet-}$ complexes display significant structural differences (Figure 5, Tables S5-S7). The Mo–C(OOH) bond is indeed shorter than the Mo–C(O_2) bond by 0.070–0.084 Å, indicating a stronger Mo-C binding. In the meantime, the C–O(H) bond is longer than the C–O bond by 0.19 Å, evidencing a weakening of the C-O bond strength. Importantly, the (N)C–C(N) bond in $[Mo(CO)_3(L)(COOH)]^{\bullet-}$ is elongated by 0.019–0.030 Å compared to this bond in $[Mo(CO)_3(L)(CO_2)]^{\bullet-}$, indicating less electronic density in π* orbital of the L ligands. These observations are consistent with a transfer of electronic density from the diimine moiety to the COOH ligand which may favor C-O bond cleavage and water formation.

Electronic structures of $[Mo(CO)_3(L)(H)]^{\bullet-}$ were also calculated to better investigate the Pathway B (see Figure 7 for the phen derivative structure). The Mo–H bond lengths are in the range 1.84–1.85 Å (Table S9). Compared to their respective values in $[Mo(CO)_4(L)]^{\bullet-}$, the Mo–N bonds are shorter and the (N)C–C(N) bond is longer in the reduced metal hydrides, consistent with a transfer of electronic density from the diimine moiety to the hydride ligand, thus activating the site for further reaction with carbon dioxide.

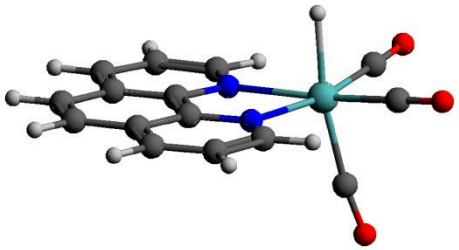

$[Mo(CO)_3(phen)(H)]^{\bullet-}$

Figure 7. Calculated structure of $[Mo(CO)_3(phen)(H)]^{\bullet-}$. Atom colors: H (white), C (grey), N (blue), O (red) and Mo (green).

To complement the analysis of the structures, we now discuss the Mulliken charges for several catalytic intermediates listed in Table S10. On the average, in $[Mo(CO)_3(L)]^{\bullet-}$, the Mo center carries a positive charge of +1.09, while the tricarbonyl fragment

carries a negative charge of –1.52 and the non-innocent ligand L a negative charge of –0.57. In $[Mo(CO)_3(L)(CO_2)]^{\bullet-}$ adducts, the CO_2 ligand carries a negative charge of –0.32 which comes from both the $Mo(CO)_3$ fragment (–0.18) and the non-innocent ligand L (–0.14), as shown by the comparison with the charge distribution in $[Mo(CO)_3(L)]^{\bullet-}$. Importantly, in the CO_2 bound-ligand of $[Mo(CO)_3(L)(CO_2)]^{\bullet-}$, the two O atoms carry a negative charge, while the C atom carries a positive charge. Going from $[Mo(CO)_3(L)(CO_2)]^{\bullet-}$ to $[Mo(CO)_3(L)(COOH)]^{\bullet-}$ by protonation and reduction steps leads to a transfer of negative charges from the L ligand to the $Mo(CO)_3$ and COOH moieties by –0.28 and –0.13, respectively. A similar trends is observed when going from $[Mo(CO)_3(L)]^{\bullet-}$ to $[Mo(CO)_3(L)(H)]^{\bullet-}$, which also entails a protonation and reduction steps. This emphasizes the beneficial role of the non-innocent ligands bpy, phen and py-indz in the electrochemical activation of CO_2 and H^+. When looking at the Mulliken charge on the non-innocent ligands in the course of catalysis, the transfer of electronic density is slightly more pronounced for L = py-indz, but the discrepancy seems too small to explain a difference in reactivity between the complexes.

Conclusion

In summary, the studied diimine $[Mo(CO)_4(L)]$ complexes have shown similar redox properties under inert atmosphere, but somewhat different behavior in presence of carbon dioxide. In particular, low scan-rate cyclic voltammetry have revealed that reactivity with CO_2 occurs already at the mono-reduced state. Spectroelectrochemical data supported by DFT calculations suggest that the tricarbonyl $[Mo(CO)_3(L)]^{\bullet-}$ species originating from $[Mo(CO)_4(L)]^{\bullet-}$ is the key reactive species for further CO_2 activation. Two different mechanistic pathways have been identified depending on the reactivity of the tricarbonyl mono-reduced complexes with protons or carbon dioxide. Strikingly, the experimental data demonstrate that the rate of CO_2 conversion is ligand-dependent, the highest rate being obtained for the unsymmetrical py-indz Mo species.

Beyond the reactivity of the mono-reduced species towards CO_2, which remains very modest compared to other molecular metal complexes, these results fill out the idea that alternative strategies than those classically carried out for molecular electrocatalysis (i.e. donor effect of the ligand *vs.* redox potential) can be of high interest to enhance reactivity. In the particular case of group 6 metal carbonyl complexes, the combination of photochemistry with electrochemical methods appears as one of the most promising approach to lower the overpotential for CO_2 reduction by generating reactive species such as the putative $[Mo(CO)_3(L)]^{\bullet-}$ complex.[12e]

Experimental Section

Experimental Details. All starting materials (bipyridine, phenanthroline, $Mo(CO)_6$, KC_8) were commercially available and used as purchased, unless stated otherwise. Solvents were purified by standard methods (CaH_2 or Na/benzophenone) before use. All syntheses were conducted under inert atmosphere of dry argon by using standard Schlenk techniques. For electrochemical and spectroelectrochemical measurements, tetrahydrofuran was passed over activated basic alumina before distillation over sodium. The solvent was collected under inert atmosphere and stored into glovebox under molecular sieves (3 Å) several days before use. The supporting salt NBu_4PF_6 was synthesized from NBu_4OH (Fluka) and HPF_6 (Aldrich). It was then purified, dried under vacuum for 48 hours at 100°C, and then kept under Ar in the glovebox. Solution of THF/NBu_4PF_6 0.1 M was dried for two days over 3 Å molecular sieves before use.

Characterization methods. Infrared spectra were recorded on a PerkinElmer Spectrum Two FTIR using a low-volume transmittance cell with CaF_2 windows from PIKE. ^1H NMR spectra were recorded at the "Services communs" of the University of Brest with a Bruker Avance 400 (400 MHz), or Bruker AMX-3 300 (300 MHz) spectrometers. All NMR data are reported in ppm (δ) relative to tetramethylsilane as external reference. Coupling constants are reported in Hertz. Electrochemical studies were performed in a glovebox (Jacomex) (O_2 < 1 ppm, H_2O < 1 ppm) with a home-made 3-electrode cell (WE: BDD or glassy carbon, RE: Pt wire in a 1 mM Fc^+/Fc THF/NBu_4PF_6 solution, CE: Pt). Ferrocene was added at the end of each experiment to determine the exact redox potential values. The potential of the cell was controlled by an AUTOLAB PGSTAT 100 (Metrohm) potentiostat monitored by the NOVA© software (Metrohm). The working electrodes were polished over a 1 µm alumina slurry with water, sonicated in H_2O (18.2 Ω.cm) and acetone, then dried with N_2 flush. Thin layer UV-Vis-NIR spectroelectrochemistry was performed with a specific home-designed cell in a reflectance mode (WE: glassy carbon or BDD, RE: Pt wire, CE: Pt wire).[25] The UV-Vis and Vis-NIR optic-fiber probes were purchased from Ocean Optics. Time-resolved UV-Vis-NIR detection was performed with a QEPro and NIRQuest spectrometers (Ocean optics). Thin layer IR spectroelectrochemistry was carried out with a home-made cell (WE: glassy carbon, RE: Pt wire, CE: Pt wire) and an ATR-Si IR optic-fiber-probe purchased from Art Photonics (ATR-P-Si-6-15-150-Lab). The WE electrode was finely modified to allow inclusion of the Si tip to achieve thin layer conditions (Figure S5). Detection of the IR signal (2 cm^{-1} resolution, one spectrum every 10 sec.) was obtained by using a FT-IR-FC model purchased from Arcoptix (FTMIR-FC-120-LN2). UV-Vis-NIR and FTIR measurements were performed in the glovebox under inert and dry atmosphere. When necessary, carbon dioxide (Alphagaz 1, Air Liquide) was introduced directly in the cell inside the glovebox by using a home-made set-up which includes a vacuum purge line. Saturation, of the THF solution with CO_2 was monitored by FTIR spectroscopy (2340 cm^{-1}). Bulk electrolysis experiments under CO_2 followed by analysis of the gaseous products by chromatography was not conducted because upon decomposition, one equivalent of Mo complex could also release up to four equivalent of CO. Accordingly, a TON value significantly larger than 4 with a faradaic efficiency of 100% must be achieved in the course of an electrolysis experiment to safely conclude to an electrocatalytic conversion of CO_2 to CO. However, the rate of the electrochemically driven reduction of CO_2 by the Mo complexes at $E_{1/2}(1)$ is modest and achieving a TON value larger than 4 will require conducting the electrolysis over a very long period of time (i.e. several hours), favoring thus the occurrence of side reactions (e.g. decomposition) that are not observed at the CV timescale.

Computational method. All DFT calculations were performed with the Orca package (version 3.03)[26] using the PBE functional[27] and a mixed basis set (TZVP for H, C, N and O and LANL2DZ for Mo)[28]. The calculations were accelerated with the resolution of identity (RI) approximation in conjunction with an appropriate auxiliary basis set. The geometry optimizations and frequency calculations were carried out using the conductor-like screening model (COSMO) to account for the solvation effects of THF.[29] Vibrational frequency analyses allowed us to confirm that the optimized geometries were actual minima (no imaginary frequencies) on the potential energy surface (PES) and to calculate the free energies. The calculations of the redox potentials using well established thermodynamic cycles require the use of the solvation energy of the electron in THF, which value is not known. We overcame this issue by using an internal reference and relative redox potentials. The experimental value of the reduction potential of $[Mo(CO)_4(bpy)]$ ($E_{1/2}(1)_{exp}$ = –1.85 V *vs.* $Fc^{+/0}$) was chosen as an internal reference, and all the calculated potentials reported here are relative to that value. A

difference lower than 50 mV was thus found between the calculated and experimental potentials of the $[Mo(CO)_4(phen)]^{0/\bullet-}$ and $[Mo(CO)_4(py\text{-}indz)]^{0/\bullet-}$ redox couples, which validated our approach. It is important to point out that many properties of transition metal complexes calculated by DFT are sensitive to the choice of the functional, and in particular of the amount of Hartree-Fock exchange.[30] For the systems investigated here, we found that, compared to the B3LYP hybrid functional, the PBE functional gives better agreements between calculated and experimental redox potentials, which justified our choice. Similarly, we used the estimated value of the solvation energy of H^+ in acetonitrile (–264.6 kcal mol^{-1}) to calculate the free energy of the protonation steps.[31] Importantly, the conductor-like screening model corresponds to a pure solution of THF (ε = 7.25), whereas the electrochemical measurements were carried in the presence of electrolyte at a concentration of 0.1 M in solutions saturated with CO_2 and, in some cases, with added water. Thus, we anticipate a large difference between the calculated and the actual values of the acidity constant of the possible intermediates. As a result, the values of the free energy of protonation reported in this work should only be compared against each other. The Avogadro software (version 1.2.0) was used to prepare the Cartesian coordinate inputs and to analyze the results.[32]

Synthetic procedures and complexes characterization. Complexes **1**, **2** and **3** were synthesized according to reported procedures.[14a, 14e, 33] The detailed synthesis and spectroscopic characterization of the complexes are given in the electronic supplementary information part.

Acknowledgements

Nicolas Le Poul is grateful to Gaël Le Roux (UBO) for his participation to the building of the IR spectroelectrochemical cell. Financial support was provided by UBO for a PhD grant (Carlos Garcia Bellido), by FEDER UE Interreg Atlantic Area (HYLANTIC, EAPA204/2016) for a post-doctoral fellowship (Lucia Alvarez Miguel) and by ANR (CATHOMIX, 19-CE43-0013-02).

Conflicts of Interest

The authors declare no conflict of interest.

Keywords: Mo-diimine complexes • CO_2 reduction • spectroelectrochemistry • electrochemistry • DFT calculations

[1] E. Boutin, L. Merakeb, B. Ma, B. Boudy, M. Wang, J. Bonin, E. Anxolabehere-Mallart, M. Robert, *Chem. Soc. Rev.* **2020**, *49*, 5772-5809.
[2] a) J. M. Savéant, *Chem. Rev.* **2008**, *108*, 2348-2378; b) K. E. Dalle, J. Warnan, J. J. Leung, B. Reuillard, I. S. Karmel, E. Reisner, *Chem. Rev.* **2019**, *119*, 2752-2875; c) W. Zhang, Y. Hu, L. Ma, G. Zhu, Y. Wang, X. Xue, R. Chen, S. Yang, Z. Jin, *Adv. Sci.* **2018**, *5*, 1700275; d) R. Francke, B. Schille, M. Roemelt, *Chem. Rev.* **2018**, *118*, 4631-4701.
[3] V. Kumaravel, J. Bartlett, S. C. Pillai, *ACS Energy Letters* **2020**, *5*, 486-519.
[4] a) F. Franco, C. Rettenmaier, H. S. Jeon, B. Roldan Cuenya, *Chem. Soc. Rev.* **2020**, *49*, 6884-6946; b) C.-F. Leung, P.-Y. Ho, *Catalysts* **2019**, *9*, 760; c) C. Jiang, A. W. Nichols, C. W. Machan, *Dalton Trans.* **2019**, *48*, 9454-9468.
[5] a) M. Beley, J.-P. Collin, R. Ruppert, J.-P. Sauvage, *J. Chem. Soc., Chem. Commun.* **1984**, 1315; b) J. Collin, *Coord. Chem. Rev.* **1989**, *93*, 245-268.
[6] a) S. Meshitsuka, M. Ichikawa, K. Tamaru, *J. Chem. Soc. Chem. Commun.* **1974**, 158; b) C. M. Lieber, N. S. Lewis, *J. Am. Chem. Soc.* **1984**, *106*, 5033-5034.
[7] a) J. Hawecker, J.-M. Lehn, R. Ziessel, *J. Chem. Soc., Chem. Commun.* **1984**, 328-330; b) J. Hawecker, J.-M. Lehn, R. Ziessel, *Helv. Chim. Acta* **1986**, *69*, 1990-2012.
[8] C. M. Bolinger, N. Story, B. P. Sullivan, T. J. Meyer, *Inorg. Chem.* **2002**, *27*, 4582-4587.
[9] a) M. Bourrez, F. Molton, S. Chardon-Noblat, A. Deronzier, *Angew. Chem. Int. Ed.* **2011**, *50*, 9903-9906; b) M. D. Sampson, C. P. Kubiak, *J. Am. Chem. Soc.* **2016**, *138*, 1386-1393.
[10] a) M. Hammouche, D. Lexa, J. M. Savéant, M. Momenteau, *J. Electroanal. Chem.* **1988**, *249*, 347-351; b) C. Costentin, S. Drouet, G. Passard, M. Robert, J. M. Savéant, *J. Am. Chem. Soc.* **2013**, *135*, 9023-9031; c) C. Costentin, G. Passard, M. Robert, J. M. Savéant, *Proc. Natl. Acad. Sci. USA* **2014**, *111*, 14990-14994; d) J. Bonin, A. Maurin, M. Robert, *Coord. Chem. Rev.* **2017**, *334*, 184-198.
[11] a) L. Rotundo, J. Filippi, R. Gobetto, H. A. Miller, R. Rocca, C. Nervi, F. Vizza, *Chem. Commun.* **2019**, *55*, 775-777; b) B. Reuillard, K. H. Ly, T. E. Rosser, M. F. Kuehnel, I. Zebger, E. Reisner, *J. Am. Chem. Soc.* **2017**, *139*, 14425-14435; c) S. Sato, K. Saita, K. Sekizawa, S. Maeda, T. Morikawa, *ACS Catal.* **2018**, *8*, 4452-4458; d) A. Maurin, M. Robert, *J. Am. Chem. Soc.* **2016**, *138*, 2492-2495; e) J. Choi, J. Kim, P. Wagner, S. Gambhir, R. Jalili, S. Byun, S. Sayyar, Y. M. Lee, D. R. MacFarlane, G. G. Wallace, D. L. Officer, *Energy Environ. Sci.* **2019**, *12*, 747-755.
[12] a) S. L. Hooe, J. M. Dressel, D. A. Dickie, C. W. Machan, *ACS Catal.* **2019**, *10*, 1146-1151; b) J. O. Taylor, F. L. P. Veenstra, A. M. Chippindale, M. J. Calhorda, F. Hartl, *Organometallics* **2018**, *38*, 1372-1390; c) F. Franco, C. Cometto, F. Sordello, C. Minero, L. Nencini, J. Fiedler, R. Gobetto, C. Nervi, *ChemElectroChem* **2015**, *2*, 1372-1379; d) P. Zhang, X. Yang, X. Hou, X. Xu, B. Xiao, J. Huang, C. Stampfl, *PCCP* **2019**, *21*, 23742-23748; e) J. O. Taylor, Y. Wang, F. Hartl, *ChemCatChem* **2019**, *12*, 386-393; f) D. Sieh, D. C. Lacy, J. C. Peters, C. P. Kubiak, *Chem. Eur. J.* **2015**, *21*, 8497-8503; g) L. Rotundo, C. Garino, R. Gobetto, C. Nervi, *Inorg. Chim. Acta* **2018**, *470*, 373-378; h) K. A. Grice, C. Saucedo, *Inorg. Chem.* **2016**, *55*, 6240-6246; i) K. A. Grice, *Coord. Chem. Rev.* **2017**, *336*, 78-95; j) G. Neri, P. M. Donaldson, A. J. Cowan, *J. Am. Chem. Soc.* **2017**, *139*, 13791-13797; k) M. L. Clark, K. A. Grice, C. E. Moore, A. L. Rheingold, C. P. Kubiak, *Chem. Sci.* **2014**, *5*, 1894-1900; l) J. O. Taylor, R. D. Leavey, F. Hartl, *ChemElectroChem* **2018**, *5*, 3155-3161; m) J. Tory, B. Setterfield-Price, R. A. W. Dryfe, F. Hartl, *ChemElectroChem* **2015**, *2*, 213-217.
[13] a) R. Hille, J. Hall, P. Basu, *Chem. Rev.* **2014**, *114*, 3963-4038; b) A. C. Ghosh, C. Duboc, M. Gennari, *Coord. Chem. Rev.* **2021**, *428*, 213606.
[14] a) C. M. Álvarez, L. Álvarez-Miguel, R. García-Rodríguez, J. M. Martín-Álvarez, D. Miguel, *Eur. J. Inorg. Chem.* **2015**, *2015*, 4921-4934; b) S. L. Mukerjee, S. P. Nolan, C. D. Hoff, R. Lopez de la Vega, *Inorg. Chem.* **2002**, *27*, 81-85; c) A. Vlček Jr, *Coord. Chem. Rev.* **2002**, *230*, 225-242; d) H. J. Bruins Slot, N. W. Murrall, A. J. Welch, *Acta Cryst.* **1985**, *41*, 1309-1312; e) M. H. B. Stiddard, *J. Chem. Soc.* **1962**, *0*, 4712-4715; f) S. S. Braga, A. C. Coelho, I. S. Gonçalves, F. A. Almeida Paz, *Acta Cryst.* **2007**, *63*, m780-m782.
[15] T. S. A. Hor, S.-M. Chee, *J. Organomet. Chem.* **1987**, *331*, 23-28.
[16] a) J. A. Connor, C. Overton, *J. Organomet. Chem.* **1983**, *249*, 165-174; b) R. Johnson, H. Madhani, J. P. Bullock, *Inorg. Chim. Acta* **2007**, *360*, 3414-3423.
[17] L. Yang, J. K. Feng, A. M. Ren, *Synth. Met.* **2005**, *152*, 265-268.
[18] a) D. Miholová, A. A. Vlček, *J. Organomet. Chem.* **1985**, *279*, 317-326; b) D. Miholová, B. Gaš, S. Záliš, J. Klíma, A. A. Vlček, *J. Organomet. Chem.* **1987**, *330*, 75-84.
[19] J. A. Vlček, F. Baumann, W. Kaim, F.-W. Grevels, F. Hartl, *J. Chem. Soc., Dalton Trans.* **1998**, 215-220.
[20] T. Bens, P. Boden, P. Di Martino-Fumo, J. Beerhues, U. Albold, S. Sobottka, N. I. Neuman, M. Gerhards, B. Sarkar, *Inorg. Chem.* **2020**, *59*, 15504-15513.
[21] J.-M. Savéant, *Elements of molecular and biomolecular electrochemistry*, John Wiley & Sons, **2006**.
[22] a) J. D. Froehlich, C. P. Kubiak, *J. Am. Chem. Soc.* **2015**, *137*, 3565-3573; b) F. Franco, C. Cometto, L. Nencini, C. Barolo, F. Sordello, C. Minero, J. Fiedler, M. Robert, R. Gobetto, C. Nervi, *Chem. Eur. J.* **2017**, *23*, 4782-4793.
[23] A. L. Ostericher, T. M. Porter, M. H. Reineke, C. P. Kubiak, *Dalton Trans.* **2019**, *48*, 15841-15848.
[24] C. Costentin, S. Drouet, M. Robert, J. M. Savéant, *Science* **2012**, *338*, 90-94.
[25] a) I. Lopez, R. Cao, D. A. Quist, K. D. Karlin, N. Le Poul, *Chem. Eur. J.* **2017**, *23*, 18314-18319; b) A. Thibon-Pourret, F. Gennarini, R. David, J. A. Isaac, I. Lopez, G. Gellon, F. Molton, L. Wojcik, C. Philouze, D. Flot, Y. Le Mest, M. Reglier, N. Le Poul, H. Jamet, C. Belle, *Inorg. Chem.* **2018**, *57*, 12364-12375.
[26] F. Neese, *WIREs Comput. Mol. Sci.* **2011**, *2*, 73-78.
[27] J. P. Perdew, K. Burke, M. Ernzerhof, *Phys. Rev. Lett.* **1996**, *77*, 3865-3868.
[28] a) A. Schäfer, H. Horn, R. Ahlrichs, *J. Chem. Phys.* **1992**, *97*, 2571-2577; b) P. J. Hay, W. R. Wadt, *J. Chem. Phys.* **1985**, *82*, 270-283.
[29] A. Klamt, G. Schüürmann, *J. Chem. Soc., Perkin Trans. 2* **1993**, 799-805.
[30] K. A. Moltved, K. P. Kepp, *J. Chem. Theory Comput.* **2018**, *14*, 3479-3492.
[31] C. P. Kelly, C. J. Cramer, D. G. Truhlar, *J. Phys. Chem. B* **2007**, *111*, 408-422.
[32] M. D. Hanwell, D. E. Curtis, D. C. Lonie, T. Vandermeersch, E. Zurek, G. R. Hutchison, *J. Cheminform.* **2012**, *4*, 17.
[33] G. A. Ardizzoia, M. Bea, S. Brenna, B. Therrien, *Eur. J. Inorg. Chem.* **2016**, *2016*, 3829-3837.

Résumé en Français

Principaux résultats des travaux de thèse

I. Introduction

La transformation du dioxyde de carbone a attiré l'attention de plusieurs groupes de recherche en raison de l'augmentation des émissions anthropiques de gaz à effet de serre au cours des dernières décennies, ce qui contribue à l'augmentation du réchauffement de la planète (+1°C au cours de la dernière décennie). [1-3] La Figure VI.1. montre comment l'accroissement des émissions de gaz à effet de serre tels que le CO_2 ou le méthane accentue le forçage radiatif à la surface de la Terre.

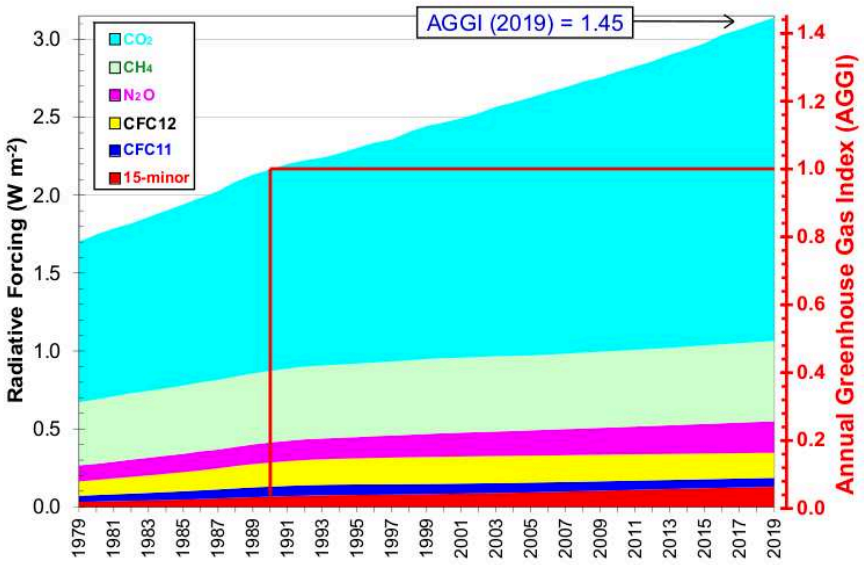

Figure VI.1. Forçage radiatif des gaz à effet de serre corrélée à l´accumulation de la valeur AGGI.[4]

Différentes stratégies ont été envisagées afin de parvenir à une transformation efficace des gaz à effet de serre présents dans l'atmosphère. Elles allient des stratégies chimiques[5] à une perspective plus biomimétique basée sur l'étude de la photosynthèse, celle-ci étant le processus de transformation du dioxyde de carbone le plus efficace connu à ce jour. [6-8] Par conséquent, il devient nécessaire d'investir des ressources dans le développement de technologies de capture et de stockage qui pourraient offrir la possibilité d'un recyclage des émissions de gaz à effet de serre.[9]

Il est également envisageable d'adopter une perspective biomimétique, en remarquant le rôle essentiel des réactions d'oxydoréduction dans chaque réaction naturelle qui implique la transformation du dioxyde de carbone, de la photosynthèse[7] aux processus catalytiques trouvés dans différentes enzymes présentes dans les plantes et autres organismes.[10] En conséquence du traitement très efficace des gaz émis dans l'atmosphère par les organismes biologiques, le développement de stratégies photo-, électro- et photoélectrocatalytiques biomimétiques a attiré l'attention de plusieurs groupes de recherche dans le monde (Figure VI.2.).

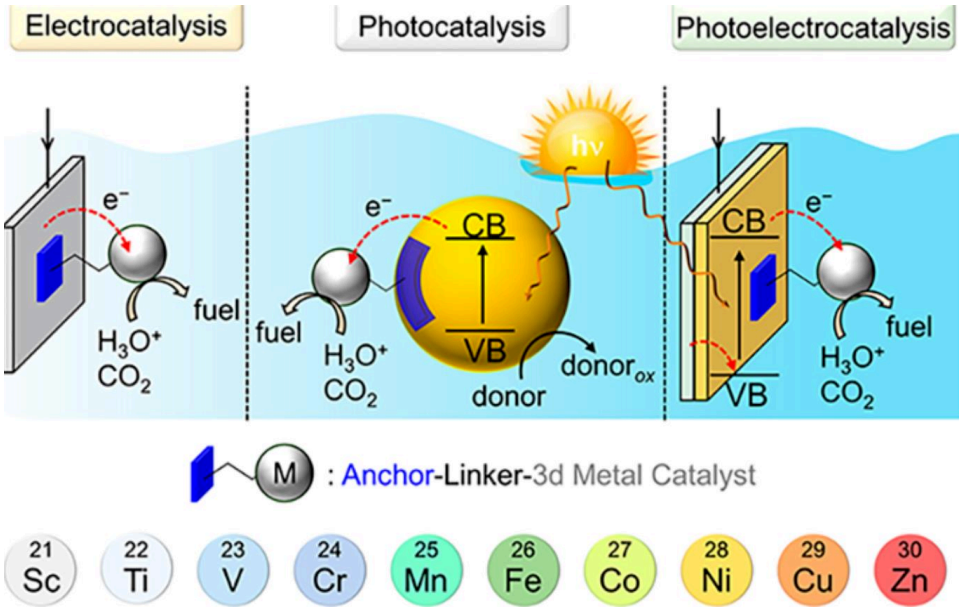

Figure VI.2. Représentation schématique des stratégies électrocatalytique (à gauche), photocatalytique (centre) et photoélectrocatalytique (à droite) pour la transformation du CO_2.[11]

La transformation du dioxyde de carbone par des méthodologies électrochimiques présente des caractéristiques intéressantes. Ces techniques permettent de produire des produits chimiques à forte valeur ajoutée grâce à l'utilisation de cellules électrolytiques où un transfert d'électrons vers le substrat est effectué sur la surface d'une électrode. Cependant, les surtensions et les énergies de réorganisation élevées, ainsi que la cinétique lente de l'électroréduction directe du dioxyde de

carbone (Tableau VI.1), rendent nécessaire l'utilisation d'un système catalytique capable d'améliorer les taux de réaction et la sélectivité du transfert d'électrons vers le substrat.

Tableau VI.1. Potentiels de réduction de la transformation directe du dioxyde de carbone en produits monocarbonés par rapport à l'électrode normale à hydrogène (ENH).

Réactions	E^0 (V *vs.* ENH)
$CO_2 + 2H^+ + 2e^- \rightarrow HCOOH + H_2O$	-0,61
$CO_2 + 2H^+ + 2e^- \rightarrow CO + H_2O$	-0,53
$CO_2 + 4H^+ + 4e^- \rightarrow HCHO + H_2O$	-0,48
$CO_2 + 6H^+ + 6e^- \rightarrow CH_3OH + H_2O$	-0,38
$CO_2 + 8H^+ + 8e^- \rightarrow CH_4 + 2H_2O$	-0,24
$CO_2 + e^- \rightarrow CO_2^{\bullet -}$	-1,90

Un système catalytique est caractérisé par la sélectivité et l'efficacité de l'électroréduction catalysée du CO_2. L'utilisation d'électrocatalyseurs moléculaires permet une haute sélectivité et une simple modification de la structure du système catalytique. En contrepartie, ces catalyseurs montrent une mauvaise recyclabilité du catalyseur et d'un faible “turnover number” (TON). Le dioxyde de carbone se coordine par des modes de liaison métal (M) - CO_2 principalement η^1-C, η^1-O ou η^2-CO.[12] L´utilisation de Re et d´Ir comme centre métallique pour les catalyseurs moléculaires pour l'électroréduction du CO_2 a été prédominante au cours des dernières décennies, [13, 14] des métaux abondants tels que Mn et Fe ont attiré l'attention, car ils présentent d'excellents taux de conversion et une grande sélectivité. Seuls quelques rares cas de catalyseurs moléculaires ont été étudiés.[15, 16] On ne trouve que quelques exemples de complexes de métaux de transition du groupe 6 (Cr, Mo, W) comme catalyseurs actifs pour l'électroréduction du CO_2 dans la littérature, même s'ils sont présents dans plusieurs systèmes enzymatiques capables de transformer le dioxyde de carbone en d'autres molécules via des processus naturels.[10] Ces complexes ont généralement besoin de ligands redox non-innocents pour être catalytiquement actifs.[17] $[Mo(CO)_4(bpy)]$ reste l'un des systèmes catalytiques du groupe 6 les plus discutés ces dernières années, montrant une activité catalytique médiocre pour la réduction du CO_2 dans des

solvants organiques en plus de surtensions élevées, ce qui rend ce complexe moins attractif et inexploré que d'autres systèmes similaires.[18, 19] La caractérisation par des techniques (spectro)électrochimiques attribue le rôle catalytique aux espèces bis-réduites $[Mo(CO)_4(bpy)]^{2-}$ dans une atmosphère saturée de dioxyde de carbone.[20] La modification de la structure du ligand des complexes de métaux de transition du groupe 6 a été tentée afin d'améliorer l'activité catalytique.[21-23] Néanmoins, l'amélioration modeste de l'activité catalytique ainsi que l'absence de détails mécanistiques sur l'interaction avec le dioxyde de carbone rendent ces complexes peu étudiés par rapport à d'autres complexes moléculaires.

Dans cette perspective, l'objectif principal de cette thèse était l'étude de plusieurs complexes $[Mo(CO)_4(diimine)]$ comme systèmes catalytiques pour la transformation du dioxyde de carbone. La caractérisation du comportement redox du $[Mo(CO)_4(diimine)]$ *via* le couplage des techniques spectroscopiques UV-Vis-NIR et IR avec l'électrochimie permet de déterminer les intermédiaires formés dans les processus redox des complexes $[Mo(CO)_4(diimine)]$. Les résultats (spectro)électrochimiques dans des atmosphères inertes/CO_2 ainsi que les calculs théoriques ont été considérés pour comprendre l'activation du dioxyde de carbone dans des conditions homogènes.

La modulation de la densité électronique sur la structure du ligand est *a priori* un facteur clé de l'activité catalytique des complexes $[Mo(CO)_4(diimine)]$. La première stratégie envisagée est l'addition de groupes donneurs/attracteurs d´électrons au ligand bipyridine de $[Mo(CO)_4(bpy\text{-}(\mathbf{R})_2)]$ (**R** = H, ^{t}Bu, Me, OMe, CO_2Me, CF_3). La présence de groupements substituants devrait affecter le comportement redox et catalytique de ces complexes. L'accent a été mis sur les conditions expérimentales telles que le choix du solvant en raison de l'observation de différentes espèces bis-réduites en fonction de la quantité d´eau résiduelle dans le solvant utilisé.[20]

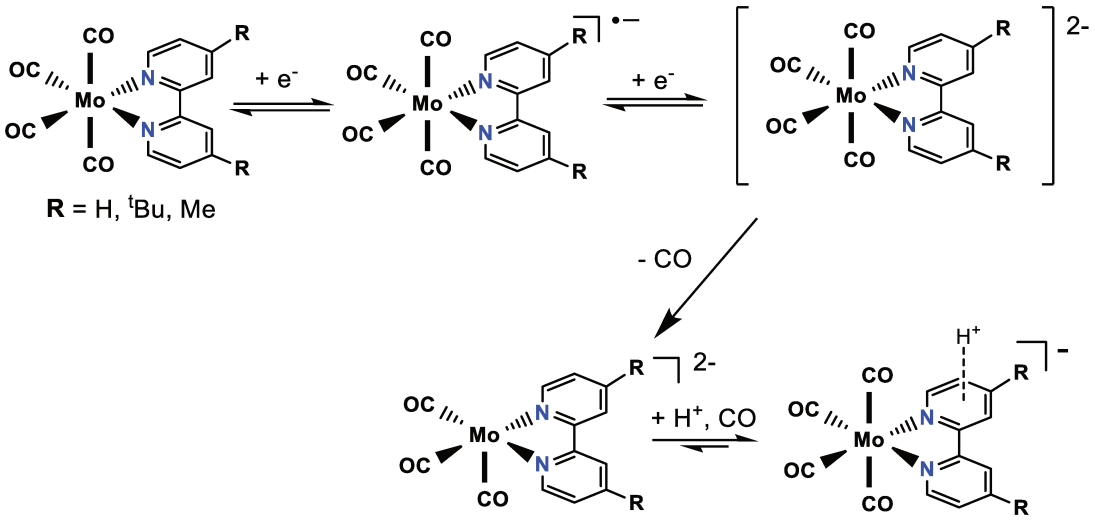

Schéma VI.1. Processus de réduction des systèmes $\mathbf{1}^{H}$, $\mathbf{1}^{tBu}$ et $\mathbf{1}^{Me}$ dans MeCN et THF.

Une deuxième stratégie concernant une modification structurelle plus importante des complexes $[Mo(CO)_4(diimine)]$ a également été proposée. La caractérisation (spectro)électrochimique des complexes $[Mo(CO)_4(bpy)]$ (**1**), $[Mo(CO)_4(phen)]$ (**2**) et $[Mo(CO)_4(py\text{-}indz)]$ (**3**) est envisagée (Figure VI.3). L'influence d'un ligand diimine plus rigide dans le complexe **2** ou la présence d'un motif asymétrique pour le complexe **3** par rapport au complexe **1** sont les principaux facteurs de l'étude comparative. En particulier, nous avons étudié la réactivité des complexes mono-réduits par rapport au CO_2 et l'effet du solvant.

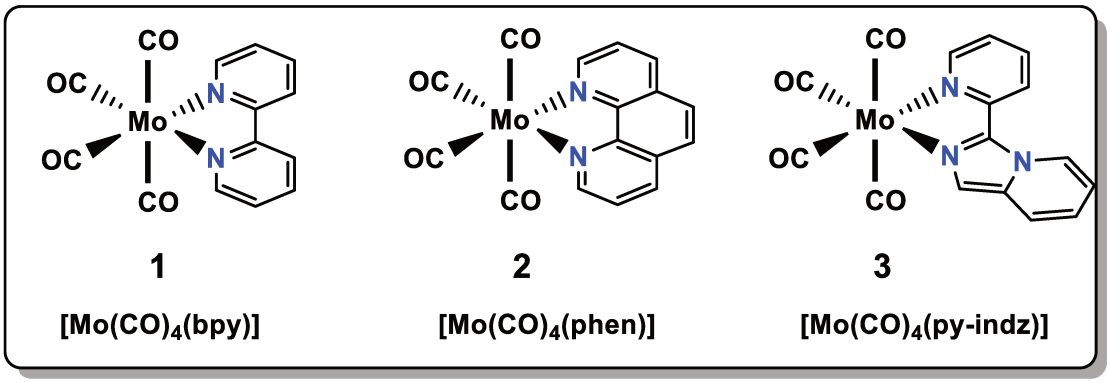

Figure VI.3. Structure des complexes $[Mo(CO)_4(bpy)]$ (**1**), $[Mo(CO)_4(phen)]$ (**2**) et $[Mo(CO)_4(py\text{-}indz)]$ (**3**) utilisés dans nos études comparatives.

La dernière stratégie poursuivie concerne l'immobilisation de complexes [Mo(CO)4(diimine)] sur la surface de l'électrode. Cette technique a montré une amélioration de l'activité catalytique et de la sélectivité d'autres systèmes (Figure VI.4). Nous présentons l'étude électrochimique des complexes [($Mo(CO)_4(bpy_{pyr})$] (bpy_{pyr} = 4-Méthyl-4'-(5-(pyren-1-yl)pentyl)-2,2'-bipyridine) (**4**) et [$Mo(CO)_4$(4-$PhNH_2$-phen)] (**5**) comme électrocatalyseurs pour la réduction du CO_2 (Figure VI.4). Alors que le complexe **4** peut être immobilisé sur une surface fonctionnalisée par des nanotubes de carbone grâce à des interactions π-π non covalentes avec la partie pyrène, le complexe **5** a été greffé par la génération *in-situ* d'ions diazonium.

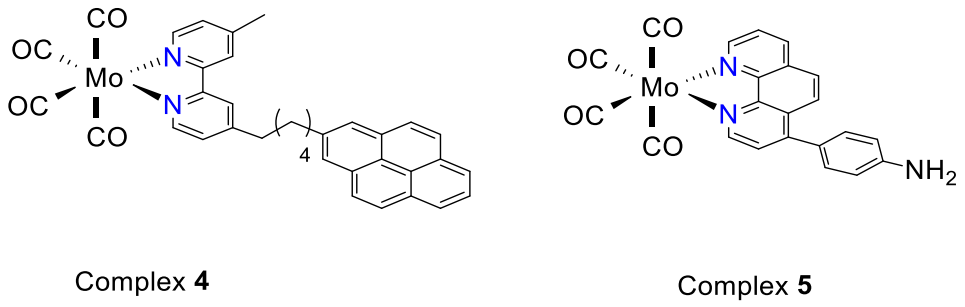

Complex **4** Complex **5**

Figure VI.4. Représentation schématique des complexes **4** et **5**.

II. Étude de l'effet des substituants sur les systèmes [$Mo(CO)_4$(bpy-(**R**)$_2$)]

La synthèse et la caractérisation (spectro)électrochimique des complexes [$Mo(CO)_4$(bpy-(**R**)$_2$)] (**R** = H, ^{t}Bu, Me, OMe, CO_2Me, CF_3) décrits dans la Figure VI.5 ont été réalisées. L'utilisation de techniques spectroélectrochimiques, appuyée par des calculs DFT, nous a permis de corréler le caractère électronique des substituants R avec les propriétés spectroscopiques et redox des complexes correspondants.

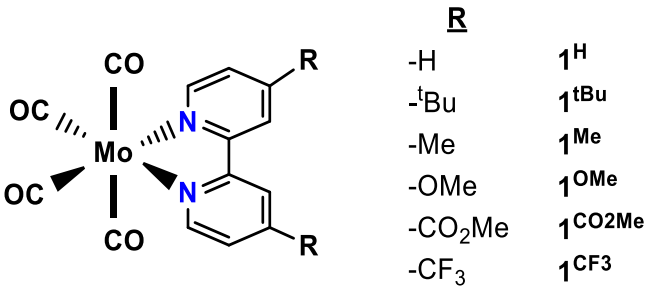

Figure VI.5. Structure générale des dérivés $[Mo(CO)_4(bpy\text{-}(\mathbf{R})_2)]$.

Comme prévu, nous avons observé un décalage de la signature spectroscopique et redox des complexes $[Mo(CO)_4(bpy\text{-}(\mathbf{R})_2)]$ en fonction du groupe substituant sur le ligand bipyridine. Les expériences électrochimiques dans les solvants THF/MeCN ont montré un décalage de potentiel négatif pour les dérivés donneurs d'électrons ($\mathbf{1^{tBu}}$, $\mathbf{1^{Me}}$, $\mathbf{1^{OMe}}$) par rapport à $\mathbf{1^{H}}$. L'effet inverse est observé pour les complexes $\mathbf{1^{CF3}}$et $\mathbf{1^{CO2Me}}$ avec des groupes attracteurs d'électrons (Tableau VI.2). Curieusement, ce dernier présente un processus de réduction supplémentaire par rapport aux autres complexes $[Mo(CO)_4(bpy\text{-}(\mathbf{R})_2)]$ (Figure VI.6).

Tableau VI.2. Potentiel de réduction des systèmes $[Mo(CO)_4(bpy\text{-}(\mathbf{R})_2)]$ en fonction de Fc^+/Fc dans le THF.

$E_{1/2}$ *vs*. Fc^+/Fc	1ère red.	2nde red.	3ème red.
$\mathbf{1^{H}}$	-1,90	-2,50[a]	-
$\mathbf{1^{tBu}}$	-2,06	-2,70[a]	-
$\mathbf{1^{Me}}$	-2,05	-2,65[a]	-
$\mathbf{1^{OMe}}$	-2,06	-2,65[a]	-
$\mathbf{1^{CO2Me}}$	-1,54	-1,98	-2,65
$\mathbf{1^{CF3}}$	-1,55	-2,05[a]	-2,94[a]

[a] Pic cathodique irréversible

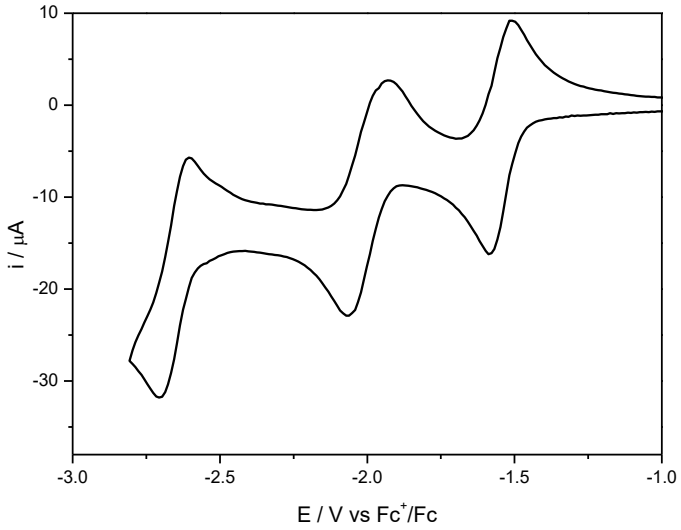

Figure VI.6. Voltammétrie cyclique de $\mathbf{1}^{\mathbf{CO2Me}}$ dans THF / 0.1 M NBu_4PF_6 sous Ar. Conditions : 1 mM de complexe, électrode de travail BDD, v = 0,1 V s^{-1}.

Les expériences électrochimiques de $[Mo(CO)_4(bpy\text{-}(\mathbf{R})_2)]$ sous une atmosphère saturée en dioxyde de carbone montrent une augmentation modeste de l'activité catalytique pour les complexes avec substituants électrodonneurs pendant son second processus de réduction. Néanmoins, la réactivité des complexes $\mathbf{1}^{\mathbf{CO2Me}}$ et $\mathbf{1}^{\mathbf{CF3}}$ diminue sensiblement (Figure VI.7). Des études IR-spectroélectrochimiques dans une atmosphère de dioxyde de carbone ont confirmé la formation de formate/carbonate dans le THF et de monoxyde de carbone dans le MeCN comme principaux produits carbonatés.

Tableau VI.3. Rapport i_{cat}/i_p pour les systèmes $[Mo(CO)_4(bpy\text{-}(\mathbf{R})_2)]$ au second potentiel de réduction dans le THF et le MeCN.

	i_{cat}/i_p dans THF	i_{cat}/i_p dans MeCN
$\mathbf{1}^{\mathbf{H}}$	1,8	1,6
$\mathbf{1}^{\mathbf{tbu}}$	2,3	1,7
$\mathbf{1}^{\mathbf{Me}}$	2,6	2,3
$\mathbf{1}^{\mathbf{OMe}}$	2,8	2,6
$\mathbf{1}^{\mathbf{CO2Me}}$	1,3	1,1
$\mathbf{1}^{\mathbf{CF3}}$	[a]	[a]

[a] Pic non détecté

Les études spectroélectrochimiques des complexes $[Mo(CO)_4(bpy\text{-}(\mathbf{R})_2)]$ ont confirmé le comportement redox présenté dans la figure VI.4 pour presque tous les complexes à l'exception de $\mathbf{1}^{\mathbf{CO2Me}}$. La nature atypique de la forme bis-réduite de $\mathbf{1}^{\mathbf{CO2Me}}$ a été étudiée. La signature IR/UV-vis suggère la formation de $[Mo(CO)_4(H^+\text{-}bpy\text{-}(CO_2Me)_2]^-$ (Figure VI.7). Le caractère électroattracteur de $\mathbf{1}^{\mathbf{CO2Me}}$ permet une augmentation de la stabilité de l'espèce bis-réduite formée. Cependant, ce comportement n'a pas été observé pour $\mathbf{1}^{\mathbf{CF3}}$. Les calculs théoriques ont confirmé que la caractéristique clé est la localisation de la densité électronique sur le groupe substituant.

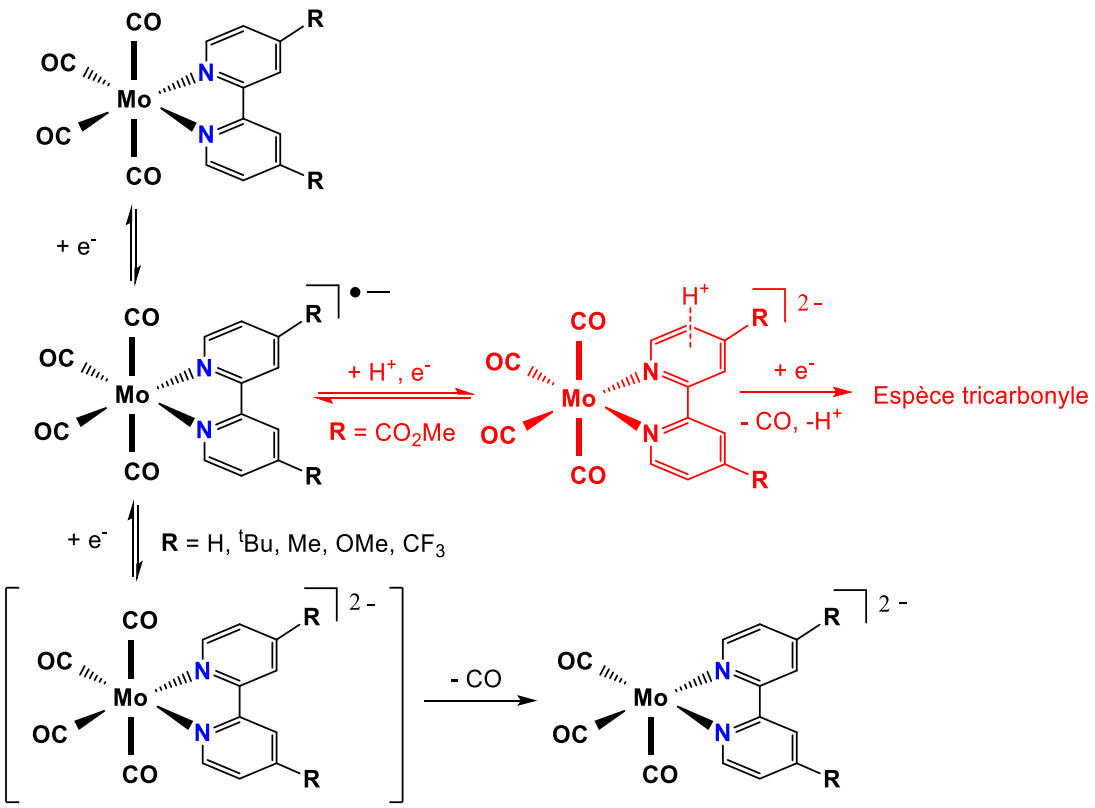

Figure VI.7. Proposition de mécanisme redox pour les complexes $[Mo(CO)_4(bpy\text{-}(\mathbf{R})_2)]$ (**R** = H, ^{t}Bu, Me, OMe, CO_2Me, CF_3) dans le THF.

III. Systèmes $[Mo(CO)_4(L)]$ (L = bpy, phen, py-indz)] pour l'électroréduction catalytique du CO_2

Les résultats obtenus dans l'étude des complexes $[Mo(CO)_4(bpy\text{-}(\mathbf{R})_2)]$ (**R** = H, ^{t}Bu, Me, OMe, CO_2Me, CF_3) montrent l'importance de la distribution électronique sur la structure du ligand. Ainsi, une étude électrochimique et spectroscopique des complexes $[Mo(CO)_4(bpy)]$ (**1**), $[Mo(CO)_4(phen)]$ (**2**) et $[Mo(CO)_4(py\text{-}indz)]$ (**3**) a été réalisée dans différents solvants. L'influence d'un ligand diimine plus rigide dans le complexe **2** ou la présence d'un motif asymétrique pour le complexe **3** par rapport au complexe **1** sont les principaux facteurs de l'étude comparative.

La réponse voltammétrique sous Ar des complexes **1**, **2** et **3** est résumée dans le Tableau VI.4. Le complexe **2** présente une signature CV dans le THF similaire à celle rapportée pour le **1** sous argon, avec une première réduction réversible à environ -1,90 V par rapport au Fc^+/Fc et une seconde

réduction irréversible à environ -2,75 V. Le même comportement redox a été obtenu dans d'autres solvants ou en utilisant une électrode de travail de carbone vitreux. Le complexe **3** a montré une réponse voltampérométrique similaire à celles de **1** et **2**, mais à des valeurs de potentiel plus négatives (d'environ -200 mV). Ce décalage peut être attribué à l'effet donneur plus fort de la fraction py-indz par rapport à phen et bpy. De plus, alors que les complexes **1** et **2** présentent des valeurs de courant de pic cathodique (i_{pc}) similaires pour les deux processus de réduction, le courant du second pic de réduction pour **3** est au moins deux fois supérieur à celui du premier pic de réduction. Notamment, cette augmentation du courant semble encore plus importante dans MeCN, indiquant une possible réaction de l'intermédiaire bis-réduit sous atmosphère inerte.

Tableau VI.4. Données voltamétriques [$E_{1/2}$ / V *vs*. Fc^+/Fc, v = 0,1 V s^{-1}] for complexes **1**, **2** and **3** (1 mM) pour les complexes **1**, **2** et **3** (1 mM) dans MeCN, THF et DFB. Electrolyte de support NBu_4PF_6 0.1 M, électrode de travail BDD.

	Solvant	Complexe **1**	Complexe **2**	Complexe **3**
1ère réduction	MeCN	-1,90	-1,98	-2,25
	THF	-1,85	-1,90	-2,20
	DFB	-1,90	-2,00	-2,20
2nde réduction	MeCN	-2,65 [a]	-2,80 [a]	-2,85 [a]
	THF	-2,55 [a]	-2,75 [a]	-2,90 [a]
	DFB	-2,60 [a]	-2,85 [a]	[b]

[a]Pic cathodique irréversible; [b] Non détecté car au-delà de la fenêtre de potentiel du solvant

Les expériences spectroélectrochimiques ont montré que la stabilité et la réactivité des espèces bis-réduites [$Mo(CO)_4$(diimine)] sont affectées par la structure de la partie diimine, comme observé dans les différences significatives trouvées dans les données spectroélectrochimiques de **1**, **2** et **3**. Alors que deux espèces bis-réduites différentes sont détectées pour **1** en fonction du solvant, la formation de $[Mo(CO)_3(phen)]^{2-}$ et $[Mo(CO)_3(py\text{-}indz)]^{2-}$ bis-réduits espèces semble indépendante du solvant.

Une augmentation du courant, attribuée à une réaction électrocatalytique, a été observée dans une atmosphère saturée du CO_2 pour tous les complexes à des valeurs de potentiel correspondant au second processus de réduction (Figure VI.9). De plus, une perte substantielle de réversibilité a été observée sur le scan inverse pour le premier processus de réduction pour **2** et **3**.

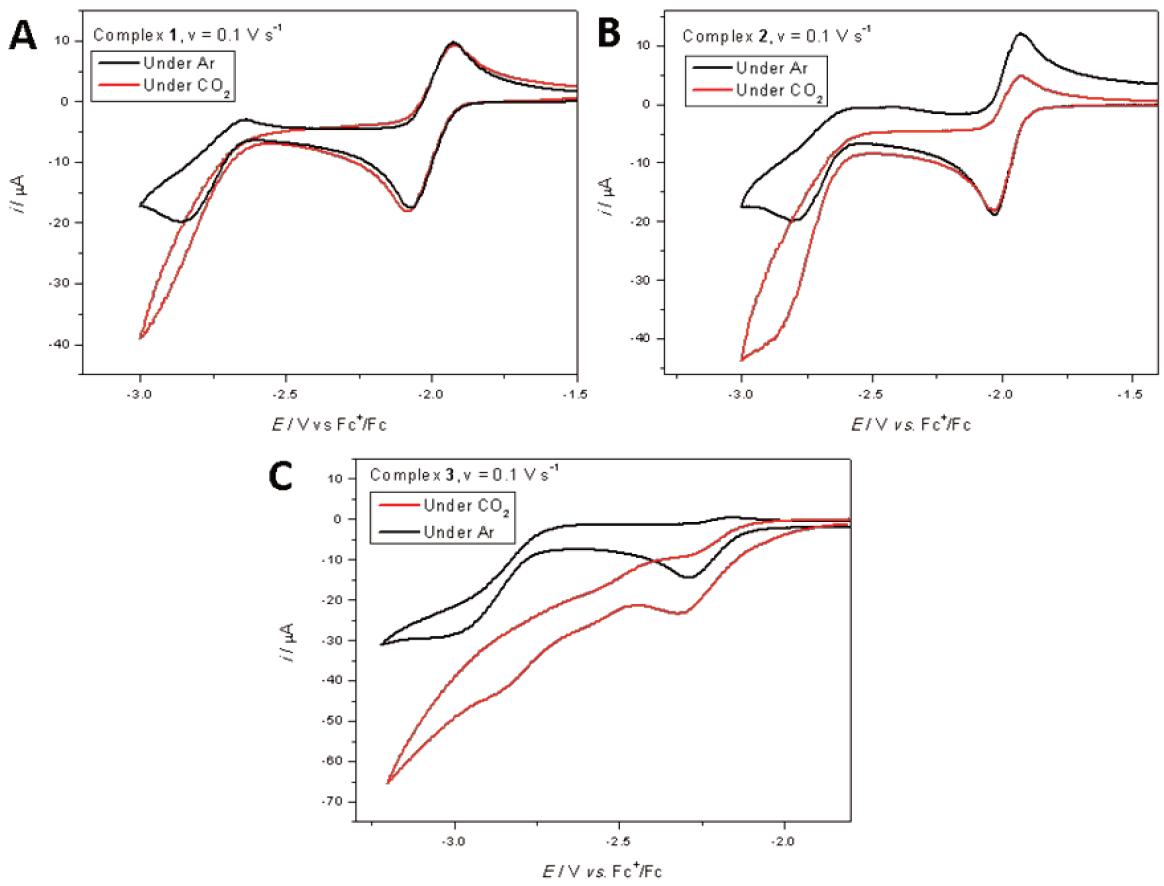

Figure VI.8. Voltammétries cycliques des complexes A) **1**, B) **2**, et C) **3** dans THF/,1 M NBu_4PF_6 sous Ar (noir) et CO_2 (rouge). Conditions : 1 mM de complexe, électrode de travail BDD, v = 0,1 V s^{-1}.

Afin de mieux comprendre cette réactivité sans précédent avec le CO_2, des études voltammétriques des complexes **1**, **2** et **3** ont été réalisées dans le THF à différentes vitesses de balayage dans une atmosphère de CO_2 dans des conditions sèches et "humides" (0,5 M H_2O). L'objectif était d'améliorer cette réactivité en ajoutant une source de protons (H_2O) à la solution pour une meilleure analyse, et de prouver l'existence d'un processus potentiel de transfert d'électrons couplé à des protons. Dans un premier temps, des expériences de contrôle ont démontré que l'eau n'interférait pas avec les complexes mono-réduits sous argon. Cependant, en présence de CO_2, une nette augmentation de l'intensité du courant ainsi qu'une plus grande perte de réversibilité a été observées lorsque de l'eau a été ajoutée, comme le montrent les CV à v = 0,01 V s^{-1} dans la Figure VI.10. Les mêmes expériences réalisées à une vitesse de balayage plus élevée (v = 0,1 V s^{-1}) ont montré le même comportement, sauf que l'augmentation du courant

était plus faible qu'à 0,01 V s^{-1}, comme prévu pour un processus chimique à vitesse limitée couplé au transfert d'électrons (ECE ou EC_{cat}).

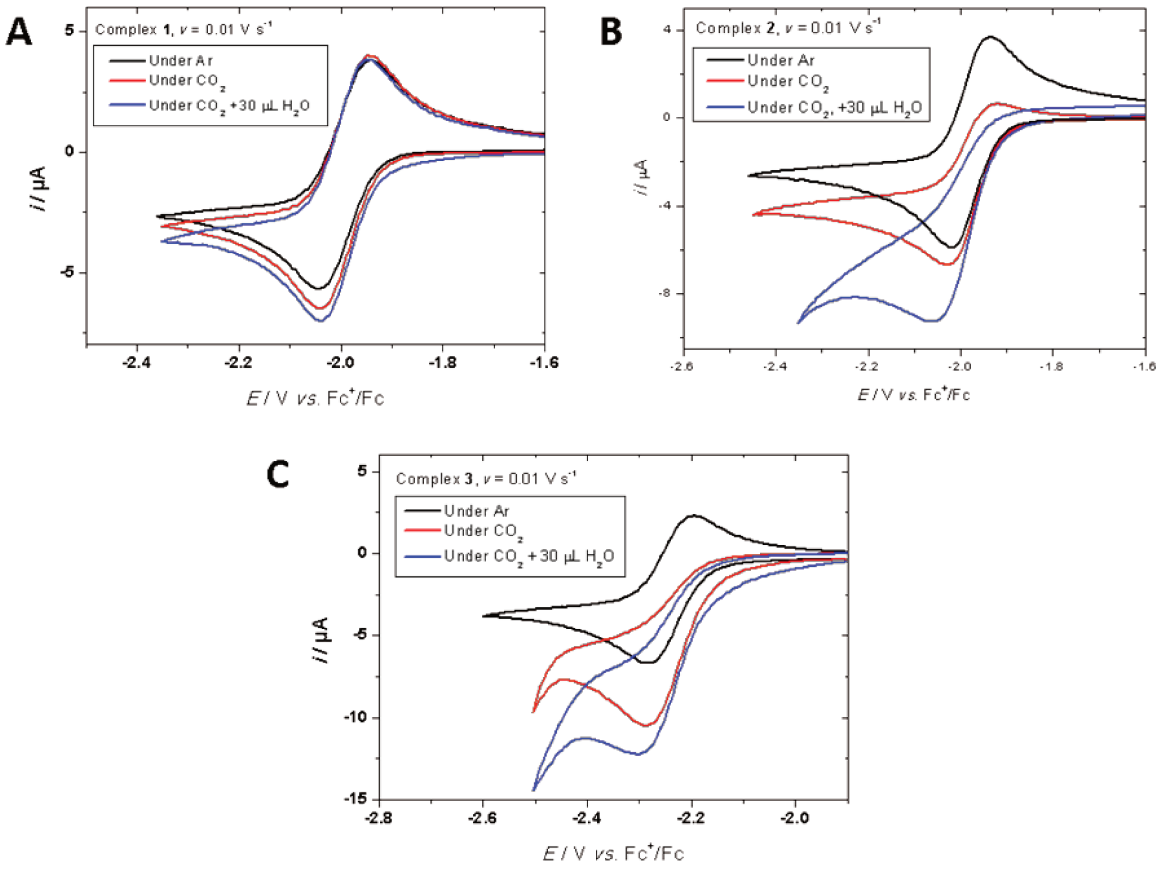

Figure VI.9. Voltammétries cycliques du A) complexe **1**, B) complexe **2** and C) complexe **3** dans le THF sous Ar (noir), sous CO_2 (rouge) et sous CO_2 avec ajout d'eau (0,5 M, bleu). Conditions : 1 mM de complexe, 0.1 M NBu_4PF_6, électrode de travail BDD, v = 0,01 V s^{-1}.

Une analyse approfondie du premier processus de réduction des complexes $[Mo(CO)_4(diimine)]$ dans une atmosphère de CO_2 a permis de proposer un mécanisme EC_{cat} tout en soulignant que la vitesse de réaction dépend du ligand et de la présence d´eau. Les calculs théoriques ont corroboré le fait que la réduction a lieu sur le ligand diimine. La densité électronique est délocalisée vers le centre métallique pour le second processus de réduction. Par conséquent, une proposition mécanistique de l'interaction entre les espèces $[Mo(CO)_4(diimine)]^{\bullet-}$ avec le dioxyde de carbone a

été présentée, suggérant deux voies possibles qui sont soutenues par la formation d'ions carbonate et formate observée dans les expériences spectroélectrochimiques IR.

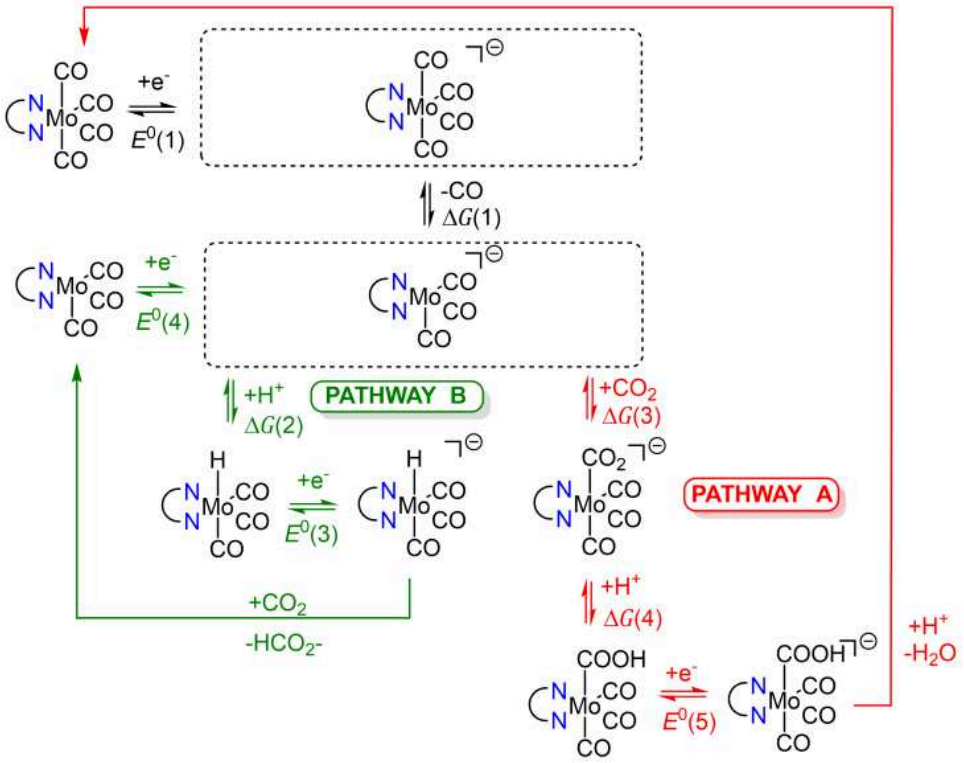

Figure VI.10. Voies mécanistiques suggérées pour la réduction du CO_2 par les complexes Mo-diimine **1**, **2** et **3**.

IV. Immobilisation de complexes Mo-diimine tétracarbonyle sur surface d'électrode pour l'électroréduction du CO_2

Malgré les résultats obtenus dans les Chapitres II et III, aucune amélioration significative de l'activité catalytique n'a été obtenue. Ainsi, dans le Chapitre IV, nous présentons les résultats obtenus à partir de la fonctionnalisation d'électrodes de carbone par deux complexes $[Mo(CO)_4(diimine)]$ différents, à savoir, $[(Mo(CO)_4(bpy_{pyr})]$ (bpy_{pyr} = 4-Méthyl-4'-(5-(pyren-1-yl)pentyl)-2,2'-bipyridine) (**4**) et $[Mo(CO)_4(4\text{-}PhNH_2\text{-}phen)]$ (**5**) (Figure IV.6). Alors que le complexe **4** peut être immobilisé sur une surface fonctionnalisée par des nanotubes de carbone (MWCNTs) grâce à des interactions π-π non covalentes avec la partie pyrène, le complexe **5** est simplement greffé par génération *in-situ* d'ions diazonium. Cette stratégie apparaît comme une stratégie

prometteuse car elle fournit de meilleures activités catalytiques que dans le cas homogène et donne la possibilité de travailler en phase aqueuse avec une meilleure recyclabilité.[27]

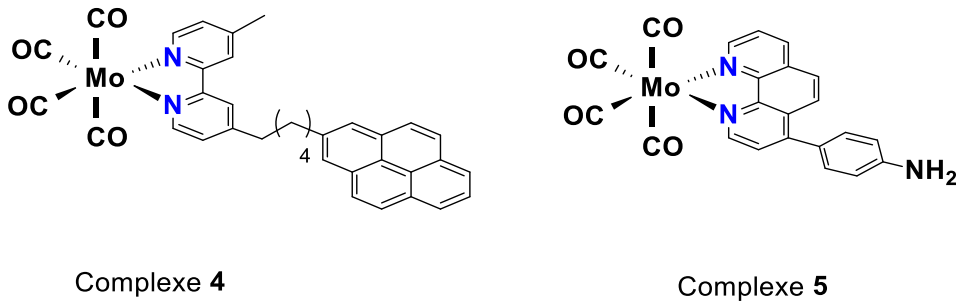

Complexe **4** Complexe **5**

Figure VI.11. Représentation schématique des complexes **4** et **5** étudiés dans ce chapitre.

Des études électrochimiques en phase homogène ont montré que le complexe **4** portant un ligand bipyridine modifié par du pyrène se comportait de manière similaire à $[Mo(CO)_4(bpy)]$, puisqu'un courant catalytique significatif a été détecté lors de la seconde réduction. L'électrode modifiée **4**ICNT a été testée sous CO_2 dans THF. Une augmentation importante du courant a été trouvée à environ -2,0 V par rapport à $Ag/AgNO_3$, ce qui a été attribué à l'électroréduction du CO_2 médiée par les nanotubes de carbone. Ainsi, ces premières études ont mené à la conclusion principale que l'utilisation des nanotubes de carbone comme support de greffage est possible seulement si le complexe Mo-diimine montre un début de catalyse à des valeurs plus positives que -2,0 V *vs.* $Ag/AgNO_3$.

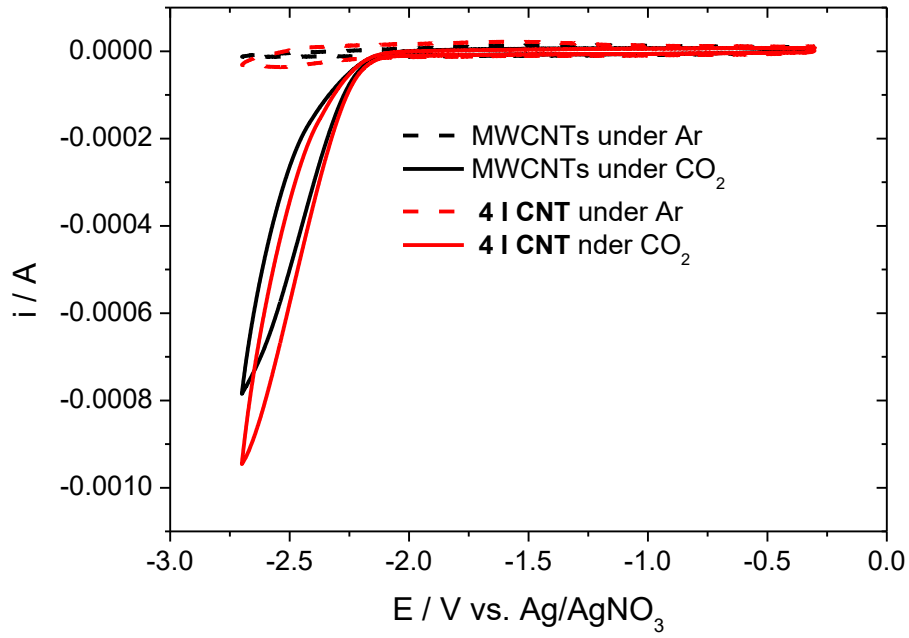

Figure VI.12. Voltammétries cycliques des assemblages **4**|CNT accrochés sur des électrodes de carbone vitreux (rouge) et des électrodes GC MWCNT nues (noir) sous Ar (pointillés) et CO_2 (simple) dans THF / 0,1 M NBu_4PF_6. Ref. : $Ag/AgNO_3$, v = 0,1 V s^{-1}.

Le comportement redox du complexe **5**, $[Mo(CO)_4(phen\text{-}PhNH_2)]$, est similaire à celui du $[Mo(CO)_4(phen)]$. Cependant, les deux processus de réduction se sont produits à des valeurs de potentiel légèrement plus positives et le second transfert d'électrons a été caractérisé par une réaction chimique couplée. L'immobilisation du complexe **5** sur l'électrode GC a été réalisée par réduction électrochimique de dérivés de diazonium générés *in-situ*. Les voltammétries cycliques sous argon ont démontré que le greffage a conduit au dépôt d'une nouvelle espèce sur la surface qui a été attribuée au complexe $[Mo(CO)_4(4\text{-}PhNH_2\text{-}phen)]$. Les études électrochimiques sous CO_2 ont montré un léger déplacement du pic de réduction sans réelle augmentation du courant. Néanmoins, ces premières expériences demandent à être reproduites et complétées par des analyses de surface (XPS).

A partir de ces résultats préliminaires, plusieurs stratégies peuvent être envisagées. La première consisterait à modifier la nature du matériau de support de manière à ce qu'il n'interfère pas avec les propriétés électrocatalytiques des complexes. Une deuxième approche consisterait à concevoir de nouveaux complexes métalliques capables de réaliser l'électrocatalyse à des valeurs de potentiel supérieures à -2,0 V par rapport à Fc^+/Fc. Cela serait possible en modifiant la structure du ligand, par exemple par l'insertion de groupes attracteurs, ou par la variation du centre métallique (W, Cr). Alternativement, de nouveaux ligands pourraient être utilisés, tels que l'hydroxybenzène-bipyridine qui s'est récemment avéré être d'un grand intérêt pour l'électrocatalyse du CO_2 avec des complexes de Cr.[24]

V. Conclusions

L'objectif principal de ce travail de doctorat était l'étude des systèmes tétracarbonyle diimine du groupe 6 en tant qu'électrocatalyseurs moléculaires pour la réduction du CO_2. Notre première approche a été la modification de la partie diimine sur les complexes $[Mo(CO)_4(bpy\text{-}(\mathbf{R})_2)]$ (**R** = H, ^{t}Bu, Me, OMe, CO_2Me, CF_3) par l'addition de groupes substituants donneurs ou attracteurs d'électrons. L'utilisation de techniques (spectro)électrochimiques permet de comprendre la répercussion causée par les ligands sur les propriétés redox de chaque système sous différentes atmosphères. La meilleure activité catalytique en termes de courant a été obtenue pour les dérivés possédant des groupes électrodonneurs. Cependant, ils montrent une valeur de surtension plus élevée. Nous observons l'effet inverse pour les dérivés $[Mo(CO)_4(bpy\text{-}(\mathbf{R})_2)]$ avec des groupements attracteurs d'électrons. Les complexes $\mathbf{1}^{\mathbf{CO2Me}}$ et $\mathbf{1}^{\mathbf{CF3}}$ présentent un troisième processus de réduction. Néanmoins, cette réduction n'a été observée pour aucun autre système $[Mo(CO)_4(bpy\text{-}(\mathbf{R})_2)]$. Nous avons pu confirmer par des techniques spectroélectrochimiques la formation d'espèces réduites tricarbonyles pour le complexe $\mathbf{1}^{\mathbf{CO2Me}}$.

Une autre stratégie envisagée a été d'étudier l'influence de la structure diimine sur les propriétés redox de trois systèmes différents ; $[Mo(CO)_4(bpy)]$ (**1**), $[Mo(CO)_4(phen)]$ (**2**) et $[Mo(CO)_4(py\text{-}indz)]$ (**3**). Les trois systèmes présentent une signature électrochimique similaire, caractérisée par un premier pic de réduction réversible localisée sur le ligand diimine. Une interaction inattendue avec le dioxyde de carbone pour le premier processus de réduction a été détectée pour les complexes **2** et **3** en particulier. Ce type d'interaction n'a pas été décrite pour des complexes similaires.[25] Les résultats spectroélectrochimiques IR montrent la formation de carbonates pendant ces processus. Le courant catalytique est dépendant de la structure du ligand diimine, obtenant la valeur i_{cat}/i_p la plus élevée pour le complexe **3**. En outre, la confirmation du rôle actif de l'eau dans l'activité catalytique a été confirmée. Les évidences expérimentales ainsi que les résultats obtenus par les calculs théoriques nous ont permis de proposer un mécanisme catalytique. Deux voies différentes ont été proposées en fonction du produit formé, établissant $[Mo(CO)_3(diimine)]^{\bullet-}$ comme l'espèce active.

Cependant, la modification du ligand diimine dans les complexes $[Mo(CO)_4(diimine)]$ n'a pas apporté d'amélioration catalytique considérable par rapport aux autres systèmes déjà décrits.[20, 21, 25] Une autre stratégie proposée dans le chapitre IV de cette thèse est l'immobilisation de complexes $[Mo(CO)_4(diimine)]$ sur la surface d´une électrode de carbone vitreux. [26] Deux

nouveaux systèmes, [($Mo(CO)_4(bpy_{pyr})$] (**4**) et [$Mo(CO)_4$(4-$PhNH_2$-phen)] (**5**), ont été préparés pour être immobilisés par interactions non-covalentes π-π ou greffage de sels de diazonium, en espérant une amélioration de l'activité catalytique déjà montrée pour des systèmes similaires.[27, 28] Un décalage positif d'environ 0,4 V a été atteint pour les deux complexes. Cependant, les surtensions élevées obtenues pour chaque système inhibent toute activité catalytique pour le second processus de réduction.

En résumé, dans ce manuscrit, nous avons développé différentes stratégies électrochimiques autour des propriétés catalytiques du [$Mo(CO)_4$(diimine)] pour la transformation du dioxyde de carbone. Des détails mécanistiques sur l'interaction des espèces monoréduites de [$Mo(CO)_4$(diimine)] avec le dioxyde de carbone ont été proposés. Cependant, une amélioration significative de l'activité catalytique n'a pas été obtenue avec les stratégies électrochimiques explorées. Une modification plus importante de la topologie du ligand devrait permettre une amélioration des propriétés catalytiques, notamment en privilégiant des ligands induisant une meilleure labilité des groupements carbonyles pour une interaction plus facile du métal avec le dioxyde de carbone. Cette stratégie est par exemple illustrée dans l'étude du complexe [Mo(η^3-allyl)$(CO)_2$(x,x'-dimethyl-2,2'-bipyridine)(NCS)] (x = 4-6) rapporté par Taylor *et al*.[22]

Bibliographie

[1] *IPCC, 2019: Climate Change and Land*, **2019**.
[2] H. Ritchie, Published online at OurWorldInData.org, **2017**.
[3] H. Ritchie, M. Roser, *Published online at OurWorldInData.org*, **2020**.
[4] J. H. Butler, S. A. Montzka, *Published online at esrl.noaa.gov*, **2020**.
[5] W. Wang, S. Wang, X. Ma, J. Gong, *Chem. Soc. Rev.* **2011**, *40*, 3703-3727.
[6] I. Gamba, *Bioinorg. Chem. Appl.* **2018**, *2018*, 2379141.
[7] M. P. Johnson, *Essays Biochem.* **2016**, *60*, 255-273.
[8] X. Sala, A. Llobet, *Eur. J. Inorg. Chem.* **2019**, *2019*, 2017-2019.
[9] M. Bui, *Energ. Environ. Sci.* **2018**, *11*, 1062-1176.
[10] R. Hille, J. Hall, P. Basu, *Chem. Rev.* **2014**, *114*, 3963-4038.
[11] K. E. Dalle, J. Warnan, J. J. Leung, B. Reuillard, I. S. Karmel, E. Reisner, *Chem. Rev.* **2019**, *119*, 2752-2875.
[12] D. H. Gibson, *Chem. Rev.* **1996**, *96*, 2063-2096.
[13] P. Kang, C. Cheng, Z. Chen, C. K. Schauer, T. J. Meyer, M. Brookhart, *J. Am. Chem. Soc.* **2012**, *134*, 5500-5503.
[14] N. P. Liyanage, H. A. Dulaney, A. J. Huckaba, J. W. Jurss, J. H. Delcamp, *Inorg. Chem.* **2016**, *55*, 6085-6094.
[15] C. Costentin, J. M. Saveant, C. Tard, *P. Natl. Acad. Sci. USA* **2018**, *115*, 9104-9109.
[16] F. Franco, e. al., *Chem. Eur. J.* **2017**, *23*, 4782-4793.
[17] R. Francke, B. Schille, M. Roemelt, *Chem. Rev.* **2018**, *118*, 4631-4701.
[18] J. M. Smieja, C. P. Kubiak, *Inorg. Chem.* **2010**, *49*, 9283-9289.
[19] J. M. Smieja, M. D. Sampson, K. A. Grice, E. E. Benson, J. D. Froehlich, C. P. Kubiak, *Inorg. Chem.* **2013**, *52*, 2484-2491.
[20] M. L. Clark, K. A. Grice, C. E. Moore, A. L. Rheingold, C. P. Kubiak, *Chem. Sci.* **2014**, *5*, 1894-1900.
[21] J. O. Taylor, R. D. Leavey, F. Hartl, *ChemElectroChem* **2018**, *5*, 3155-3161.
[22] J. O. Taylor, F. L. P. Veenstra, A. M. Chippindale, M. J. Calhorda, F. Hartl, *Organometallics* **2019**, *38*, 1372-1390.
[23] J. O. Taylor, Y. Wang, F. Hartl, *ChemCatChem* **2019**, *12*, 386-393.
[24] S. L. Hooe, J. M. Dressel, D. A. Dickie, C. W. Machan, *ACS Catal.* **2019**, 1146-1151.
[25] J. Tory, B. Setterfield-Price, R. A. W. Dryfe, F. Hartl, *ChemElectroChem* **2015**, *2*, 213-217.
[26] X. Zhang, Z. Wu, X. Zhang, L. Li, Y. Li, H. Xu, X. Li, X. Yu, Z. Zhang, Y. Liang, H. Wang, *Nat. Commun.* **2017**, *8*, 14675.
[27] S. Sinha, A. Sonea, W. Shen, S. S. Hanson, J. J. Warren, *Inorg. Chem.* **2019**, *58*, 10454-10461.
[28] C. Sun, L. Rotundo, C. Garino, L. Nencini, S. S. Yoon, R. Gobetto, C. Nervi, *Chemphyschem* **2017**, *18*, 3219-3229.

Titre : Complexes tétracarbonyles diimine du molybdène pour la reduction électrocatalytique du CO_2

Mots clés : Complexes de molybdène, Réduction du CO_2, spectroélectrochemie, électrocatalyse, ligand diimine, greffage

Résumé : Au cours des dernières décennies, la transformation du dioxyde de carbone est devenue un enjeu important pour la diminution de l'effet de serre sur Terre. Dans cet objectif, l'utilisation de techniques électrochimiques peut être envisagée pour générer des produits chimiques à haute valeur ajoutée par réduction électrocatalytique du CO_2. Ces dernières années, de nombreux complexes moléculaires à base de métaux de transition ont été proposés comme catalyseurs potentiels pouvant permettre une réduction sélective et efficace du dioxyde carbone.
Dans ce contexte, l'objectif de cette thèse a été de synthétiser de nouveaux complexes du molybdène porteurs de ligands carbonyles et diimine afin de déterminer leurs propriétés électrocatalytiques du CO_2.

Cette famille de complexes reste à ce jour très peu étudiée malgré le fait que le molybdène soit utilisé au niveau biologique par des enzymes deshydrogénases pour la conversion réversible de dioxyde de carbone en formate. Pour ce travail, différentes séries de complexes de molybdène ont été étudiées *via* des techniques spectroélectrochimiques et des calculs théoriques. Nous avons ainsi pu corréler les propriétés catalytiques des complexes à différents paramètres tels que la nature des groupements substituants donneurs/attracteurs d'électrons sur le ligand bipyridine, ou bien le type de ligand diimine (bipyridine, phenanthroline, pyridylindolizine) coordonné au métal. Enfin, l'immobilisation sur surface d'électrode de cette famille de complexes a été initiée selon deux méthodes de greffage différentes.

Title : Molybdenum diimine tetracarbonyl complexes for the electrocatalytic reduction of CO_2

Keywords : CO_2 reduction, molybdenum complexes, spectroelectrochemistry, electrocatalysis, diimine ligand, grafting

Abstract : In the last decades, transformation of carbon dioxide has become an important issue due to its impact Earth´s enhanced greenhouse effect. Electrochemical techniques are promising tools to produce valuable chemicals through CO_2 electrocatalytic reduction. Different molecular catalysts based on transition metal have been reported over the last years, with the objective of improving both selectivity and efficiency of the reduction process.
The objective of this work is the preparation and study of several molybdenum diimine complexes as catalysts towards the electrocatalytic reduction of CO_2. The utility of molybdenum as metal center has been evidenced by its presence in several enzymes capable of transforming carbon dioxide in nature.

Three different families of molybdenum diimine complexes were studied via spectroelectrochemical techniques and theoretical calculations. We have investigated the influence of electron-donating/electron-withdrawing substituting groups on the catalytic activity displayed for these complexes. In a second strategy we have performed a deeper study of the coordination sphere in molybdenum diimine complexes (bipyridine, phenanthroline, pyridyl-indazoline), with a more detailed description of their first reduction process.
Lastly, the study of supported molecular molybdenum diimine complexes over electrode´s surfaces was carried out.